FRIEDRICH-SCHILLER-UNIVERSITÄT JENA

Probing Strong-field Photoionization of Atoms and Diatomic Molecules with Short-wave Infrared Radiation

Dissertation zur Erlangung des akademischen Grades

doctor rerum naturalium (Dr. rer. nat.)

Vorgelegt dem Rat der Physikalisch-Astronomischen Fakultät der Friedrich-Schiller Universität Jena

von Dipl.-Phys. Max Möller

geboren am 13.01.1987 in Jena

Gutachter:

    1. Prof. Dr. Gerhard G. Paulus, Friedrich-Schiller Universität Jena

    2. Prof. Dr. Reinhard Dörner, Goethe-Universität Frankfurt am Main

    3. Prof. Dr. Dieter Bauer, Universität Rostock

Tag der Disputation: 29.08.2017

Content

Content

Abstract

The availability of pico- and femtosecond laser pulses, which can be focused to peak intensities in the range between 10^{12} and 10^{16} W/cm^2, allows the investigation of the interaction between atoms or diatomic molecules with strong laser fields. It has revealed fascinating phenomena such as above-threshold ionization (ATI) [1], high energy above-threshold ionization (HATI) [2], non-sequential ionization (NSDI) [3], high-harmonic generation (HHG) [4] and, most recently, frustrated tunnel ionization (FTI) [5]. Today, these characteristic strong-field phenomena are the backbone of the burgeoning field of attosecond science. Derived applications presently mature to standard techniques in the field of ultrafast atomic and molecular dynamics. Examples are HHG as table-top source of coherent extreme ultraviolet radiation with attosecond duration or the application of HATI for the characterization of few-cycle laser pulses [6] [7]. Although experimental and theoretical considerations have shown that using longer laser wavelength is interesting for applications as well as for fundamental aspects [8], primary due to technological limitations, the vast majority of measurements has been performed at laser wavelengths below 1.0 μm.

In this thesis, an optic parametric amplification laser source of intense femtosecond laser pulses with short-wave infrared (SWIR) and infrared (IR) wavelength is put to operation, characterized and compressed to intense few-cycle pulses. Further, it is applied to investigate strong-field photoionization (SFI) of atoms and diatomic molecules using two different experimental techniques for momentum spectroscopy of laser-induced fragmentation processes.

For SFI of atoms, the velocity map imaging technique is used to measure three-dimensional momentum distributions from strong-field photoionization of Xenon by strong SWIR fields with different pulse duration. Besides observation of the pulse duration dependence of characteristic features, like the low-energy structures [9], which are particularly pronounced in the SWIR, an eye-catching off-axis low-energy feature, called the "fork", which appears close to right angle to the polarization axis of the laser, is investigated in detail [10]. The corresponding modeling with an improved version of the semi-classical model [11] [12] [13], demonstrates that on- and off-axis low-energy features can be traced to rescattering between the laser-driven photoelectron and the remaining ion. They can, thus, be understood on the same footing as HATI [2], where the electron scatters into high energy states.

SFI of diatomic molecules is investigated using an apparatus for Ion Target Recoil Ion Momentum Spectroscopy (ITRIMS) [14] [15]. Besides measuring intensity dependent vector momentum distributions of the protons from SFI of the hydrogen molecular ion, H_2^+ ($H_2^+ \rightarrow H^+ + H^+ + e^-$), it is shown that momentum conservation can be used to extract the correlated electron momentum from the measured data, although the electron is not detected. The capability of having experimental access to the momenta of all fragments, i.e. two protons and one electron, enables the analysis of correlated electron-nuclear momentum distributions. Together, with a one-dimensional two-level model, this sheds light on correlated electron-nuclear ionization dynamics during SFI of diatomic molecules by SWIR fields.

Kurzfassung

Die Verfügbarkeit von Laserpulsen mit Pulsdauern im Piko- und Femtosekundenbereich, die auf Spitzenintensitäten zwischen 10^{12} and 10^{16} W/cm^2 fokussiert werden können, hat die Untersuchung der Wechselwirkung zwischen Atomen oder zweiatomigen Molekülen mit starken Laserfeldern ermöglicht und führte zur Entdeckung faszinierender Phänomene wie Above-Threshold Ionisation (ATI) [1], hoch energetische Above-Threshold Ionisation (HATI) [2], nichtsequentielle Ionisation (NSDI), die Erzeugung hoher Harmonischer (HHG) [4] und, zuletzt, frustrierte Tunnelionisation [5]. Heute sind diese charakteristischen Starkfeldeffekte das Rückgrat des der Attosekundenwissenschaft, wo derzeit abgeleitete Anwendungen zu Standardmethoden für die Untersuchung extrem schneller atomarer und molekularer Dynamik heranwachsen. Beispiele dafür sind die Erzeugung hoher Harmonischer als Laborquelle für kohärenter Strahlung im extrem ultravioletten Wellenlängenbereich sowie als Quelle für Attosekundenpulse oder die Anwendung von HATI zur Vermessung von Einzelzyklenlaserpulsen [6] [7]. Obwohl experimentelle und theoretische Betrachtungen gezeigt haben, dass die Verwendung längerer Laserwellenlänge für Anwendungen und fundamentale Aspekte von Interesse ist, wurde aufgrund technologischer Beschränkungen der allergrößte Teil der Messungen bei Laserwellenlängen unterhalb von 1.0 µm durchgeführt.

In dieser Arbeit wird eine optisch-parametrische Laserquelle intensiver Femtosekundenlaserpulse mit Wellenlängen im kurzwelligen Infrarotbereich (SWIR) und Infrarotbereich (IR) in Betrieb genommen, charakterisiert und zu Pulsdauern im Einzelzyklenbereich komprimiert. Weiterhin wird diese Quelle verwendet um die Starkfeldionisation (SFI) von Atomen und zweiatomigen Molekülen in diesem Wellenlängenbereich zu untersuchen. Dazu werden zwei verschiedene Techniken der Impulsspektroskopie lasergetriebener Fragmentierung verwendet.

Zur Untersuchung der SFI von Atomen wird die Velocity-Map-Imaging Technik benutzt um dreidimensionale Photoelektronenimpulsverteilungen von Xenon nach Ionisation durch SWIR-Felder bei verschiedenen Pulsdauern zu vermessen. Neben der Beobachtung der Pulsdauerabhängigkeit charakteristischer Strukturen, die im SWIR-Bereich besonders stark hervortreten, z. B. die Low-Energy-Struktur [9], wird eine interessante Struktur mit dem Namen „Gabel", die in nahezu rechtwinkliger Emissionsrichtung zur Laser Polarisation auftritt, im Detail untersucht [10]. Die zugehörige Modellierung mit einem verbesserten halbklassischen Modell [11] [12] [13] zeigt, dass auch niederenergetische Strukturen auf Rückstreuung zwischen dem lasergetriebenen Elektron und dem verbliebenen Ion erklärt werden können. Dies führt den Ursprung der niederenergetischen Strukturen auf dasselbe Konzept zurück, das zum Verständnis der HATI Strukturen bei hohen Elektronenenergien verwendet wird.

Die SFI zweiatomiger Moleküle wird mit Hilfe einer Anlage für Ion Target Recoil Ion Momentum Spectroscopy (ITRIMS) untersucht [14] [15]. Neben der intensitätsabhängigen Messung von Vektorimpulsverteilungen der Protonen nach SFI des Wasserstoffmolekülions, H_2^+ ($H_2^+ \rightarrow H^+ + H^+ + e^-$), durch SWIR-Felder, wird gezeigt, dass Impulserhaltung verwendet werden kann um den korrelierten Elektronenimpuls aus den Messdaten zu extrahieren, obwohl das Elektron nicht detektiert wurde. Die experimentelle Verfügbarkeit der Impulse aller Fragmente, nämlich von zwei Protonen und eines Elektrons, erlaubt die Analyse korrelierter Elektron-Kern-Impulsverteilungen. Gemeinsam mit einem eindimensionalen Zweiniveau-Modell können so korrelierte Elektron-Kern-Ionisationsdynamiken während der SFI zweiatomiger Moleküle beleuchtet werden.

1 Motivation and Document Structure

1.1 Motivation

The availability of energetic laser pulses with pulse durations in pico- and femtosecond domain which can be focused to peak intensities in the range between 10^{12} and 10^{16} W/cm^2, enabled the investigation of the interaction between strong laser fields and matter since of the end of the 1970s. Since then, the combined experimental and
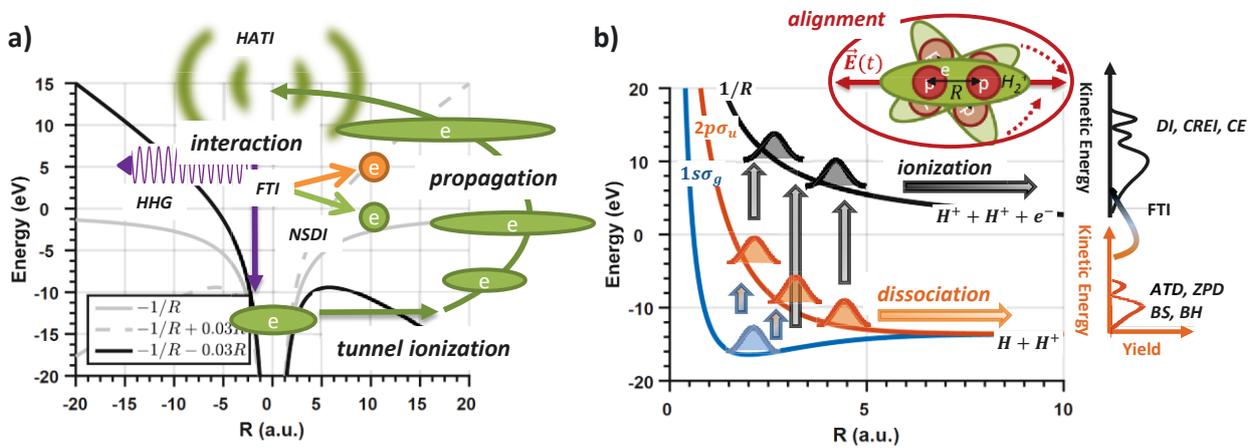
Figure 1.1: a) Illustration of the semi-classical model of the interaction between a strong-field and an atom The characteristic processes of ATI, HATI, NSDI, FTI and HHG are shown see text for details. b) in addition to the molecular versions of ATI, HATI, NSDI, FTI and HHG, coupled electron-nuclear dynamics lead to additional phenomena which are relevant for ionization and dissociation of diatomic molecules, see text for details.

For atoms this includes classical and quantum mechanical aspects of the characteristic processes like above-threshold ionization (ATI) [1], high energy above-threshold ionization (HATI) [2], non-sequential ionization (NSDI) [3], high-harmonic generation (HHG) [4] and, most recently, frustrated tunnel ionization (FTI) [5]. The underlying physics of these phenomena can be intuitively understood within both the semi-classical model (SCM) of strong-field interactions [11] [12] and its quantum mechanical counterpart [16]. Both are based on the sub-cycle electron dynamics in the laser field. The SCM divides the strong-field interaction of atoms in three-steps, which take place within one optical cycle, see Figure 1.1 a) for an illustration. In the first step at a time when laser field is strong, tunnel ionization of the atom in the continuous wave linearly polarized laser field, see e.g. [17] for a recent review, facilitates electron ejection at some starting time with respect to the laser. For the second the step, one neglects the influence of the atomic binding potential and calculates the electron trajectory using classical mechanics of an electron in the external laser field. Depending on the starting time and the time-dependent shape of the field, there are so-called direct trajectories, which leave the vicinity of the ion directly, and trajectories, which lead to a return of the field-accelerated electron to the parent ion at some later at the time of return. The return represents the third

step of the model. Different electron-ion interactions are responsible for the characteristic strong-field phenomena. Elastic electron-ion scattering is responsible HATI [2]. The effect of an inelastic scattering process between electron and ion can lead to electronic excitation including excitation to a second and higher order ionization state of the ion, which is summarized by NSDI [3]. More recently, the creation of Rydberg states due to electron recapture at the return has been observed and named FTI [5]. Radiative recombination between electron and ion is the origin of the emission of high-energy photons, which is known as HHG [4].

Having summarized the rich sub-cycle electron dynamics of atoms in strong fields, we turn now to strong-field dynamics of diatomic molecules. The existence of the rotational and vibrational degree of freedom lead to several phenomena [18] that are related to strong-field-driven electron-nuclear dynamics. These occur in addition to the molecular versions of the electron dynamics of ATI, HATI, NSDI, FTI and HHG, which were discussed along the SCM in the previous paragraph. The complexity of molecular strong-field interactions have led to a large number of publications on this topic in which keeping the common track of all effects and aspects is not trivial. Figure 1.1 b) tries to illustrate important phenomena in a compact way. Among them are:

Alignment of the molecule, i.e. the angle between the molecular axis and the linearly polarized laser is relevant from several aspects [19] [20] [21]. Already comparatively weak femtosecond laser fields induce a dipole moment that leads to a torque that rotates the molecular axis with respect to the linear polarization, i.e. a rotational wave packet is excited. The laser-field-free evolution of this wave packet leads to periodic alignment/anti-alignment of the molecular ensemble in the target on the picosecond time scale, which is regularly exploited to investigate strong-field interaction with aligned molecules in pump-probe schemes. For an initially unaligned ensemble of the target molecules, the orientation dependence of transition dipole moments and ionization rates selects portions of the angular distribution that preferably dissociate or ionize. This alignment dependence can often be used determine the underlying dynamics taking place, e.g. the kinetic energy resolved angular distributions of the fragments can be used to determine and distinguish different ionization and dissociation pathways [15] [16] [14].

The effects of *strong-field dissociation, multi-photon dissociation / above-threshold dissociation (ATD)* [22], *two and zero photon dissociation (TPD and ZPD)* [23], *bond-softening (BS)* [24] and *bond hardening (BH)* [25] are related to dissociation of the molecules by strong laser fields, e.g. the reaction $H_2^+ \rightarrow H^+ + H$ for the hydrogen molecular ion. Several perspectives can be used to understand and explain various aspects and observations of strong-field dissociation. Within the vertical transition picture, it is explained in such a way that the molecule is excited to a dissociative electronic state by absorbing energy from one or a few photons of the laser field. Due to repelling forces among the nuclei that occur in the dissociative electronic state, the nuclei gain kinetic energy by rolling down the dissociative potential energy curve, see Figure 1.1 b), such that corresponding kinetic energy release (KER) distributions for dissociation develop as depicted in the right part of Figure 1.1 b). Emission of one photon on the way out, gives the possibility to jump back to the binding potential energy curve such that the already accelerated and now out-going nuclei are decelerated. This effect can explain the observation of net two and even zero photon dissociation. All the mentioned effects can be considered such that the strength of the external field is taken into account and can explain intensity dependent effects that alter the shape of the KER distribution.

Coulomb explosion (CE) / Dissociative Ionization (DI) / Charge Resonance Enhanced Ionization (CREI) [26] [27], are names for strong-field ionization of the molecule, i.e. for the reaction $H_2^+ \rightarrow H^+ + H^+ + e^-$. For this reaction, the external field ionizes the molecule and creates two protons and an electron. The protons repel each other on the $1/R$ Coulomb potential and the electron moves in the combined potential of the protons and the strong field such that complex and rich dynamics occur. Similar to dissociation, the nuclei role down the potential and the corresponding kinetic energy release (KER) spectra are observed, see Figure 1.1 b). DI points out that the strong-field might excite the dissociative electronic state prior to ionization such that ionization can occur from there and thus from a wider range of internuclear distances, R, which leads to changes in the observed KER distribution of ionization. So-called CREI addresses the aspect that ionization of, e.g. H_2^+, in a quasi-static field is enhanced or suppressed depending on R due to the nuclear geometry [26] [28].

Molecular frustrated tunnel ionization [29] denotes, similar to atomic FTI, an electron recapture process. However, in contrast to atomic FTI, where the laser field drives the electron exactly back to the ion for a recapture, the nuclei that repel each after ionization while the electron is driven by the field can lead to the effect that one of the nuclei recaptures the electron. In this way, $H^+ + H$ pairs with high KER of Coulomb explosion ionization can be generated with the charge of dissociation.

Primary due to technological limitations, the vast majority of measurements on strong-field phenomena of atoms and diatomic molecules has been performed at laser wavelength below 1.0 μm. Only recent developments in femtosecond laser technology enable the investigation of strong-field interactions at longer wavelength experimentally [8]. Thereby, experimental and theoretical considerations on the wavelength scaling of strong-field interactions [8] have shown that longer laser wavelength is interesting from several perspectives and will be the primary focus of this thesis.

From a more application oriented perspective, increasing the laser wavelength increases the energy of the liberated electron during the strong-field interaction. This can be beneficial e.g. for the development of table-top extreme-ultraviolet (XUV) and soft-x-ray sources as it increases the energy of the emitted photons in the HHG process [30] [31]. At the same time, it has potential for the generation of shorter XUV attosecond pulses. Both can then be used in secondary measurements for the investigation of ultrafast dynamics. For the example of molecular HATI, higher electron energy is particularly attractive for laser-induced electron diffraction (LIED) [32]. In this scheme, the photoelectron signal from elastic scattering between the returning electron and the ion, i.e. the high-energy part of the photoelectron momentum distribution, is used as laser-driven electron diffraction signal to probe the molecular structure in a time-dependent manner. A recent example demonstrated the possibility of following bond breaking dynamics in small molecules based on LIED [33].

From a fundamental perspective, increasing the laser wavelength increases the parameter space of experimental investigations and, therefore, represents an experimental testbed for models on strong-field interactions. For example, the experimental investigation of strong-field photoionization revealed an unexpected large photoelectron yield at low photoelectron energies [9] [34], the so-called low-energy structures (LES). It is particularly pronounced if ionization is facilitated by long-wavelength driving fields. More recently, features at very low [35] and even around zero energy [36] received attention. The LES structure, its off-axis extension, its sensitivity to the pulse duration [10], and how it can be understood within the semi-classical model [37] are topics of this thesis in chapter 4. In view of fundamental aspects for strong-field photoionization of diatomic molecules, it might be imagined that

interesting coupled electron-nuclear dynamics occur as the strong laser field forces the motion of the electron to the time scale of the optical cycle. For the combination of a very light molecule, such as the hydrogen molecular ion, H_2^+, and a long wavelength field where the duration of the optical cycle is comparable to the time scale during which significant nuclear motion can take place [38] [39]. Another aspect is that the longer wavelength leads to a slower changing strength of the laser field and thus the assumption of static field ionization as the initial ionization mechanism in the SCM is better justified. Potentially, then the effect of CREI, i.e. that the ionization rate is sensitive to the internuclear distance, is more pronounced and can be better observed as in comparable measurements at wavelength below 1.0 μm, where a clear observation of CREI has been disputed [40] or only possible under specifically tailored experimental conditions so far [41].

1.2 Document Structure

The document is structured as follows. Chapter 2 "Generation of Intense Few-Cycle Laser Pulses at Short-Wave Infrared Wavelength" is about the generation of intense few-cycle laser pulses at short-wave infrared wavelength (SWIR) in the range between 1 to 2.5 μm. The source of intense femtosecond laser pulses at SWIR wavelength is put to operation and is characterized. Further, techniques to characterize this laser source are presented, namely, characterization of the focal spot, characterization of the pulse duration including the spectral phase and a post compression technique to generate SWIR few-cycle pulses with up to 1 mJ energy and a pulse duration below 12 fs at a center wavelength round 1.8 μm.

Before we turn to the investigation of strong-field ionization of atoms and diatomic molecules, relevant fundamentals of "Momentum Spectroscopy of Laser-Induced Fragmentation Processes" are shortly summarized and reviewed in chapter 3. Thereby, the measurement setups, i.e. the velocity map imaging (VMI) setup for the measurement of photoelectron momentum distributions (PMDs) and the Jena setup for Ion Target Recoil Ion Momentum Spectroscopy (ITRIMS), are introduced. They are used to investigate strong-field photoionization chapters 4 and 5.

In chapter 4 "Off-Axis Low-Energy Structures in Strong-Field Photoionization" (SFI) of atoms is investigated using Xenon as target. Measurement of the PMDs enables the observation of features at low electron energies, which are typical for SFI of atoms by SWIR fields. An eye catching fork-like feature perpendicular to the laser polarization is observed and investigated in greater detail. Comparing PMDs from ionization by long laser pulses, which are several optical cycles in duration, with PMDs from ionization by few-cycle fields, illustrates that all details of the observed features are susceptible to the time-dependent shape of the field. Comparison of the measurements to theoretical results that are obtained by a version of semi-classical model (SCM) of SFI, which takes electron trajectories that are substantially longer than one optical cycle as well as details of the electron-ion scattering cross-section into account, shows that low-energy features including the newly investigated fork-like feature can be traced to field-driven rescattering between electron and ion.

In chapter 5 "Probing Strong-Field Photoionization of a Beam of $\boldsymbol{H_2^+}$ at Short-Wave Infrared ", we turn to the investigation of diatomic molecules by measuring intensity-dependent vector momentum distributions from laser-induced fragmentation of an ion beam of H_2^+ molecules. The discussion of details of the measurement documents that the Jena ITRIMS setup can be used to perform kinematic complete measurements of SFI of H_2^+ ($H_2^+ \rightarrow H^+ +$

$H^+ + e^-$) where not only the momenta of the two protons, but also the momentum of the electron is accessible. Further, the investigation considers the intensity dependent of KER spectra and by making use of the electron momentum measurement, the so-called joint electron-ion energy distributions are investigated in detail. In order to gain insight into the SFI dynamics of diatomic molecules, the measurement results are compared to a one-dimensional two-level model of SFI of H_2^+. The comparison with the measurement demonstrates qualitative agreement, which seems to be reasonable given the simplicity of the model as it neglects e.g. rotations.

In chapter 6 Conclusion and Outlook the results of the thesis are concluded and possible future directions are mentioned.

2 Generation of Intense Few-Cycle Laser Pulses at Short-Wave Infrared Wavelength

2.1 Introduction and Outline
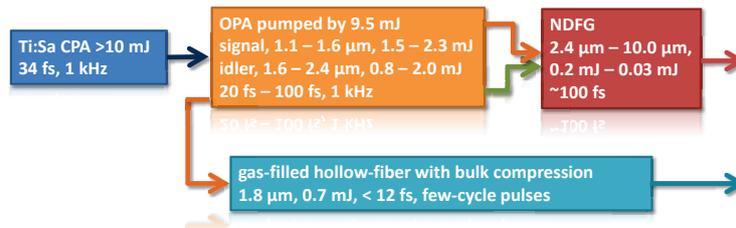
Figure 2.1: Schematic setup for the generation of intense femtosecond pulses in the infrared

A Titanium-Sapphire (Ti:Sapphire) based femtosecond chirped pulse amplification (CPA) system produces laser pulses with a wavelength around 0.8 μm. These pulses are used to pump a tunable optic parametric amplifier (OPA) where a fraction of the pulse energy is converted to the signal and the idler that have center wavelengths of 1.1 - 1.6 μm and 1.6 μm - 2.6 μm respectively. The pulse duration of both remains on the order of the pulse duration of the pump, i.e. in the regime of a few 10s of femtoseconds. An additional stage for non-collinear difference frequency generation (NDFG) can be used to further increase the wavelength. Both, the OPA output and the NDFG output can be used directly for strong-field experiments. In order to generate few-cycle pulses in the mid-infrared, the idler of the OPA can be spectrally broadened in a gas-filled hollow-fiber. Subsequent bulk compression yields few-cycle pulses with a center wavelength of 1.8 μm.

Since the discovery of strong-field interactions in atoms and molecules [1] and high energy above-threshold ionization (HATI) [2], non-sequential ionization (NSDI) [3], high-harmonic generation (HHG) [4], the vast majority of measurements and theoretical considerations has been done for laser wavelengths below 1.0 μm. Only recent advances in femtosecond optical parametric amplification (OPA) and optical parametric chirped amplification (OPCPA) technology enable the investigation of strong-field laser-matter interaction at substantially longer wavelength in the short-wavelength infrared (SWIR) range between 1.0 and 4.0 μm.

Increasing the driving laser wavelength in strong-field laser physics is interesting from several perspectives [8]. As mentioned, from a fundamental point of view, it opens an experimentally largely unexplored parameter range [9] where interesting dynamics for atoms and molecules can be expected. From a more practical viewpoint, it is, e.g., beneficial for the development of table-top extreme ultra-violet (XUV) sources as HHG with long wavelength driving lasers gives access to higher photon energies, see e.g. [30]. Simultaneously, longer driving laser wavelength increases the bandwidth in the XUV such that it holds potential for the generation of shorter attosecond pulses. For new methods for time-resolved imaging of ultrafast dynamics such as laser-induced electron diffraction [32] [33] and high-harmonic spectroscopy [42], longer driving lasers are beneficial.

A popular approach for increasing the driving laser wavelength is the use of traveling-wave OPA technology. A schematic of a typical setup is shown in Figure 2.1. The output of a high-energy standard femtosecond Titanium-

Sapphire (Ti:Sapphire) based chirped pulsed amplification (CPA) system is used as pump laser for an OPA. The OPA transfers a part of the available pulse energy around 0.8 μm to the signal and the idler wave with wavelengths between 1.0 and 1.6 μm and between 1.6 and 2.4 μm respectively, employing the non-linear optical process of difference frequency generation (DFG). The wavelength range between 2.4 and 10 μm becomes accessible with the use of an additional stage for non-collinear difference frequency generation (NDFG). The pulse duration remains in the femtosecond regime during these wavelength conversions such that both outputs, i.e. DFG-output and NDFG-output of the OPA, are intense enough to perform strong-field experiments. Few-cycle pulses with a center wavelength around 1.8 μm can be generated in an easy way by spectrally broadening the idler from the DFG by non-linear propagation in a gas-filled hollow fiber [43] in combination with bulk compression [44].

In the following section 2.2, the basic concepts of CPA are shortly mentioned and specific features of a CPA system that has been used in this thesis are concluded. Principles of OPA operation and results from the implementation and characterization of the commercially available OPA system "HE-TOPAS-C" from LIGHT CONVERSION™ are given in chapter 2.3. Also, the suitability of this source for strong-field ionization experiments is demonstrated. In chapter 2.4, few-cycle pulses with a center wavelength around 1.8 μm are generated and characterized. A simple approach to control the intensity of few-cycle pulses is demonstrated in appendix A1.

Note that much of the work on the generation of few-cycle pulse has been done in close collaboration with Frank Meyer during his master thesis [45]. First ionization experiments with the output of the NDFG stage at a center wavelength of 3.4 μm were achieved during the bachelor thesis of Hoang Le. Further we thank, Dr. Bruno E. Schmidt as he has been available for advice in construction and operation.

2.2 Chirped Pulse Amplification Laser System

Ti:Sapphire-based laser femtosecond laser technology has seen rapid progress for more than two decades now and the generation of intense femtosecond laser pulses with a center wavelength around 0.8 μm has become routine. Appropriate laser systems are commercially available from a number of producers. Most recent product leaflets advertise average powers up to 100 W. Thereby, these laser are capable of delivering CEP-controlled pulses with pulse durations down to 20 fs and pulse energies up to 30 mJ with repetition rates between 1 kHz and a few 10s of kHz. The key concepts of such systems are the generation of femtosecond pulses in Kerr-lens mode-mocked Ti:Sapphire lasers [46] which are then amplified by chirped-pulse amplification (CPA) and recompressed [47] close to the initial duration in the fs regime.

The CPA system at the Non-linear optics laboratory of the Friedrich-Schiller-University Jena, consists of a commercially available FEMTOPOWER™ Compact™ Pro HP/HR CEP front end [48]. Initially, it starts with a CEP stable Kerr-Lens-Mode-Locked Ti:Sa laser that delivers CEP-controlled [49] sub-10-fs pulses with an energy of a few nJ at a repetition rate of about 80 MHz. These pulses are stretched to about 60 ps using a bulk stretcher before they are amplified in cryogenically cooled multi-pass amplifier. After 4 passes in the amplifier, a Pockels cell is used to reduce the repetition rate to 4 kHz. The rest of the 80-MHz pulse train is dumped. After the Pockels cell, transmission through an acousto-optic programmable dispersive filter [50] (Dazzler, FASTLITE), allows controlling the amplitude and spectral phase of the laser pulses. It is typically used to control and correct high-order dispersion such that the shortest possible pulse duration is reached after compression at the output of the front-end. After the

Dazzler, another 5 passes in the amplifier boosts the energy from μJ-level to about 1.1 mJ. Pulse compression is done in a transmission-grating based compressor. Altogether, the "FEMTOPOWER" front end delivers CEP-controlled 1-mJ, 24-fs pulses at a repetition rate of 4 kHz. Typically, 90 % of this CPA's output is used for strong-field experiments directly while 10 % is sent to a secondary CPA that has been manufactured by THALES.

The "THALES" is an independent CPA by itself, i.e. it has a stretcher and a compressor and two more multi-pass amplification stages. Both, stretcher and compressor use reflective gratings. After the stretcher, the repetition rate is lowered to 1 kHz using a Pockels Cell. The first amplification stage of the "THALES" has been originally designed as a water-cooled two-pass amplifier and the second stage is a cryogenically cooled three-pass amplifier. After compression, 10-mJ, 34-fs pulses at a repetition rate of 1 kHz is easily reached in daily operation.

Installation of an acoustic optical modulator (AOM, Dazzler) and modifying the water-cooled 2 pass amplifier such that it becomes a 4 pass amplifier recently, enables more flexibility over the spectral phase and bandwidth of the "THALES" output pulses without loss in pulse energy. If the available energy from the pump laser would be fully used, even higher energy can be expected. For pulses with very clean spectral phase an increase of the conversion efficiency in the HE-TOPAS-C System by a few percent has been observed. Note that the numbers, which are given in the next chapter, have been measured without this recent modification of the system.

2.3 An Optical Parametric Amplifier for Frequency Down Conversion

In this section, we introduce details of commercially available HE-TOPAS-C System from the manufacturer LIGHT CONVERSION from Vilnius, Lithuania. In 2.3.1 we introduce the three-stage OPA with non-collinear difference frequency generation stage (NDFG). Later, in 2.3.2, the output of the "TOPAS" at typical daily operation is characterized.

2.3.1 White-light Seeded Three-Stage OPA with NDFG Stage - The HE-TOPAS-C System

The commercially available high-energy traveling-wave optical parametric amplification of white-light continuum system (HE-TOPAS-C) is based on optical parametric amplification (OPA). In this non-linear optical process, laser beams with three different frequencies are involved. They fulfill energy conservation, i.e. $\hbar\omega_P = \hbar\omega_I + \hbar\omega_S$. Here, ω_P is the angular frequency of the pump, ω_I is the angular frequency of the idler and ω_S is the angular frequency of the signal. They are related to their respective wavelength, λ_P, λ_I and λ_S. In the case here, $\lambda_P \approx 0.8$ μm. Thus, with the OPA process only smaller frequencies or longer wavelengths are accessible with this device. In order to reach high efficiency for the energy transfer from the pump beam to the signal and the idler beam, it is necessary to achieve momentum conservation or phase matching, i.e. $\vec{k}_P = \vec{k}_I + \vec{k}_S$. Thereby, $\vec{k}$ with the subscripts denote the k-vector of pump, signal and idler beam again. The HE-TOPAS-C that is used in this thesis, has been modified such that type II phase matching ($e_P \rightarrow o_S + e_I$) in the birefringent non-linear Beta Barium Borate crystals (BBO, $\theta = 28°$) is achieved in close-to collinear geometry for all amplification stages. Close-to collinear geometry minimizes spatio-temporal distortions in the amplification.
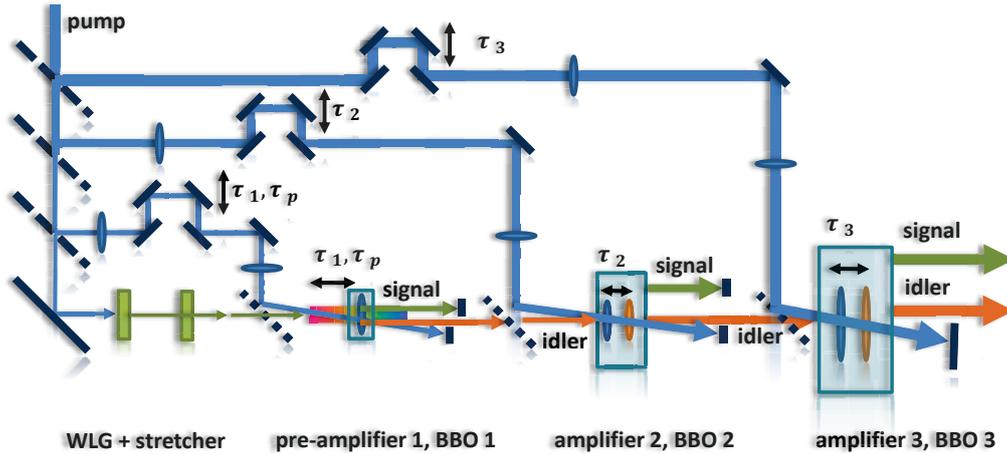
Figure 2.2: Schematic of the HE-TOPAS-C

The incoming pump beam is split into three pump arms. Each of them is equipped with a delay stage, τ_1, τ_2, τ_3 that can be adjusted with stepper motors. These delays are used to control the temporal overlap in the amplifier stages. In the bottom left region, white-light continuum generation is used to generate a seed for the subsequent amplification stages (WLG+stretcher). The white-light continuum is then stretched in time. Controlling the advent of the pump pulse via τ_1 on a coarse time scale in the pre-amplifier 1 allows to tune the wavelength of the OPA (pre-amplifier 1, BBO 1). The additional fine delay, τ_p, in the pre-amplifier allows one to control the CEP of the generated idler from the pre-amplifier via passive CEP stabilization. Using the idler beam as the seed in all subsequent amplification stages, amplifier 2 (amplifier 2, BBO 2) and amplifier 3 (amplifier 3, BBO 3) allows, in principle, the generation of an intense CEP-stable idler at the output of the OPA. The signal beam from the previous stages is not used for subsequent amplification. However, the signal beam from the last amplifier 3 (amplifier 3, BBO 3) is available for experiments and for further difference frequency generation between signal and idler in the NDFG stage. The HE-TOPAS-C, is fully software controlled such that the adjustment of delays and crystal angles is done fully automatically and changing the output wavelength requires pressing a button only. The NDFG stage is not shown here.

A sketch of the HE-TOPAS-C is shown in Figure 2.2. It consist of a white-light generation stage (WLG+stretcher) and three OPA stages (pre-amplifier 1, BBO 1; amplifier 2, BBO 2; amplifier 3, BBO 3). The white-light (WL) generation stage enables tune ability of the generated signal and the idler beam at the output of the TOPAS. At this stage, WL generation in a sapphire plate is used to generate a seed that takes the role of the signal beam in the first amplification stage. Propagating the WL through a material with high dispersion before amplification stretches it in time and generates a seed where the wavelength changes as a function of time. Thus, changing the relative timing, τ_1, between the short pump pulse and the stretched WL on a coarse time scale allows tuning the center wavelength of the idler from this OPA stage. Amplification of the idler in all subsequent stages increases the energy of the idler, but doesn't change the wavelength. In order to keep the conversion efficiency in all amplification stages high, the BBO crystals are rotated such that the phase matching is achieved for the selected wavelength and the relative timings, τ_2 and τ_3, are adjusted such that best temporal overlap is achieved. In the HE-TOPAS-C system, the coordinated adjustment of delays and crystal angles is software controlled and fully automated such that changing the output wavelength requires pressing a button only.
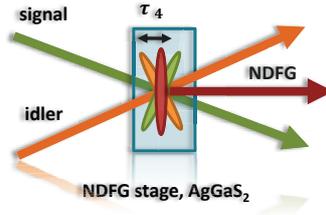
Figure 2.3: Schematic of the non-collinear difference frequency generation option in HE-TOPAS-C
The incoming pump signal and idler beam from the OPA stages are crossed at an angle in a Silver Thiogallate (AgGaS2) crystal. Again, a stepper motor is used to control the delay, τ_4, between the two pulses. It is adjusted such that output signal is maximized. Simultaneously, the angle of the AgGaS2 is adjusted such that phase matching is achieved.

In contrast to the standard HE-TOPAS-C setup, the HE-TOPAS-C that is used in this thesis, has been modified such that the idler beam from the pre-amplifier 1 stage is amplified in subsequent stages instead of amplifying the signal from the first stage. This has the advantage that the idler beam at the output of the HE-TOPAS-C is in principle passively CEP stable [51]. Passive CEP stability means that although, the 0.8 µm pump laser has a statistically fluctuating CEP, the CEP of the idler from the HE-TOPAS-C is constant while the CEP of the signal fluctuates as the pump. The origin of this mechanism lies in the phase relation of the OPA process [51], which is $\phi_P = \phi_I + \phi_S + \pi/2$ and yields $\phi_I = \phi_P - \phi_S - \pi/2$. As the pump and the signal in the first amplification stage are generated from the same laser pulse (i.e. they are separated by a beam splitter only), both have the same CEP fluctuations. Thus, they cancel each other yielding a constant phase for the idler. Further, the idler has a constant CEP at the output of the HE-TOPAS-C, which is controlled by the exact timing between pump and signal on a fine scale, i.e. on a sub-cycle scale. In order to achieve CEP control at the output of the HE-TOPAS-C, one of the mirrors in the WL beam path has been mounted on a piezo actuator. It can move by up to 9.6 µm, which is more than sufficient to change the CEP over 2π. The quality of the passive CEP stability of the idler is directly related to the interferometric stability of the beam path in the HE-TOPAS-C, which is more than two meters.

A sketch of the NDFG stage is shown in Figure 2.3. After the three OPA stages, the generated signal and idler beam are crossed at a small angle in a Silver Thiogallate (AgGaS$_2$) crystal where the difference frequency is generated. Phase matching in the DFG process is achieved via type I ($e_S + o_I \rightarrow o_{DFG}$) in the birefringent non-linear crystal. The wavelength of the NDFG output depends on the wavelength of the signal and the idler beam from the OPA. High conversion efficiency is ensured by adjusting the angle of incidence on the AgGaS$_2$ crystal for optimal phase matching as well as the delay, τ_4, between the signal and the idler beam. Again, all these necessary alignment steps are motorized and software controlled. The previously mentioned feature of the passive CEP stable idler from the OPA is gone in this stage as the CEP stable idler is mixed again with the signal which has CEP fluctuations. Thus, the NDFG output is not CEP stable.

2.3.2 Characterization of the HE-TOPAS-C – Output

Knowing the essential interaction parameters in an experiment is crucial for qualitative and quantitative comparisons between experimental and theoretical results in strong-field laser physics. To first order, these

parameters are the center wavelength, λ, the pulse duration, τ, and the peak intensity, I_0, in the strong-field experiment. In modern measurements, more precise characterization of laser pulse properties such as the precise temporal profile or spatio-temporal characteristics are needed. While some of the necessary measurements for the determination of interaction parameters are trivial and can most easily done using commercially available devices, others require more complex apparatuses that are not commercially available and thus, have to be developed and implemented. Here, we present the implementation of pulse characterization used to determine the interaction parameters for strong-field interaction experiments at SWIR wavelength in subsequent chapters. Thus, an impression of the output of the HE-TOPAS-C in pulse energy, spectrum, focal spot and pulse duration is given primarily for the idler range.

Wavelength Dependent Pulse Energy
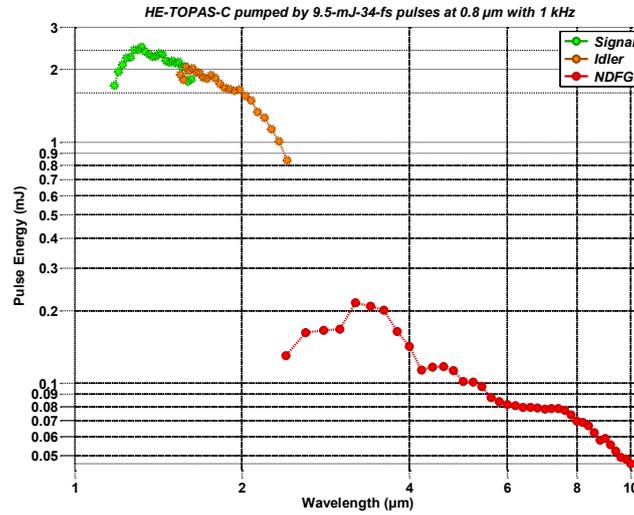
Figure 2.4: Pulse energy at the output of the HE-TOPAS-C as function of wavelength

The efficiency of the energy transfer from the pump beam to the sum of the signal and the idler beam reaches more than 40% (depending on the wavelength) for wavelengths in the signal and idler range between 1 and 2.5 μm. For the NDFG output, energy is converted from the pump to the NDFG beam with up to 2% efficiency.

Figure 2.4 shows the pulse energy as function of wavelength at the output of the used HE-TOPAS-C after installation. It is pumped by 9.5 mJ, 34-fs pulse at 1 kHz from the THALES. The energy of the THALES is set to 9.5 mJ by adjusting the pump power in the last cryogenic amplification stage. The demonstrated performance can be reached in daily operation if the in-coupling into the HE-TOPAS-C is optimized. The efficiency, i.e. $\eta_{OPA} = (\epsilon_S + \epsilon_I)/\epsilon_P$, of the energy transfer from the pump beam to the signal and the idler beam is wavelength dependent and reaches up to 43%. Similarly, $\eta_{DFG} = \epsilon_{NDFG}/\epsilon_P$, the energy transfer from the pump to the NDFG beam reaches an efficiency of up to 2%. The energy stability of the HE-TOPAS-C output is on the order of 3%.

Focal Spot Size
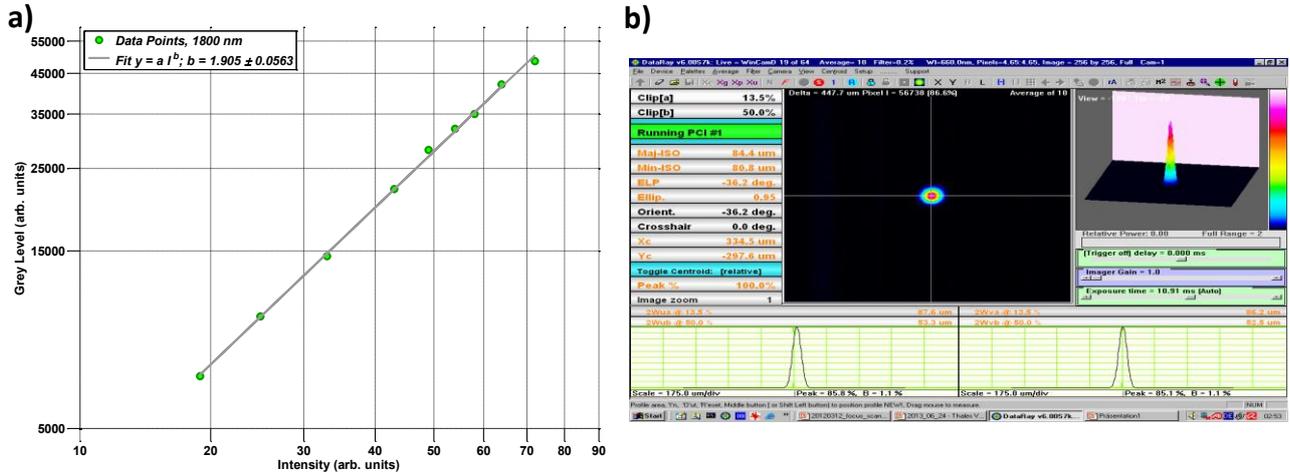
Figure 2.5: Focal Spot Characterization at IR wavelength based on a two-photon

a) Measurement of the Grey-Level of a standard CCD camera (WinCamD) as a function of incident intensity on a loglog-plot. The fit result, which is shown in the top left corner, indicates close to a two-photon process. b) shows a screenshot of the WinCamD's software. The values that are given for w_{meas} from the program need to be multiplied by $\sqrt{b}$ in order to account for the two-photon response of the detector.

At visible wavelength, characterization of the focal spot can simply be done using a camera. For infrared wavelength above 1.1 µm however, the sensitivity of typically Silicon-based CCD sensors drops dramatically. The reason for this is that the photon energy at long wavelength drops below the band gap energy of Silicon, which is about 1.12 eV (or ~1.1 µm in wavelength) at room temperature. Instead of using Silicon-based CCDs, other detector materials such as Indium-Gallium-Arsenid (InGaAs, up to 2.6 µm) or Indium-Antimonid (InSb, 1.0 µm up to 5.5 µm) might be used to characterize the focal spot. However, such detectors / cameras are rather expensive and typically have large pixel size.

Alternatively to an expensive detector, a two-photon process on a Silicon-based CCD can be used for the characterization of the focal spot. Figure 2.4 b) shows a screenshot of the signal at the focal spot for a center wavelength of 1.8 µm on the Silicon-based CCD sensor of a standard WinCamD camera. The spot shape is Gaussian. In case of a two-photon process, the peak of the grey level distribution on the camera is expected to follow a power law, $y = aI^b$. In order to verify this relation and to determine b for the given CCD sensor, the intensity of the attenuated beam has been changed without changing the geometry of the focus in Figure 2.5 a). To this end, the technique presented in appendix A1 has been used. As expected, the grey level, y, follows a line with a slope of $b \approx 1.90 \pm 0.06$ on a log-log plot indicating close to a two-photon process. Thus, for a Gaussian laser spot that has the waist size, w_0 and the intensity distribution, $I(r) = I_0 \exp(-2r^2/w_0{}^2)$, the grey level distribution on the CCD of the Silicon-based camera is, $y \sim [I(r)]^b$. It is now easy to show that, $w_0 = \sqrt{b}w_{meas} \approx 1.38 \cdot w_{meas}$. For the example in b), the WinCamD states, $w_{vertical\,meas} \approx w_{horizontal\,meas} \approx 43.45\ \mu m \rightarrow w_0 = 59.96\ \mu m$. Although, not shown here, it has been tested that b does not change significantly if the center wavelength is changed in the idler (1.6 µm $< \lambda <$ 2.4 µm) range of the TOPAS. For the signal range (1.1 µm $< \lambda <$ 1.6 µm) however, b is expected to become wavelength dependent such that it might be necessary to be determine b for a few center wavelengths.

Temporal Characterization using Frequency-Resolved Optical Gating
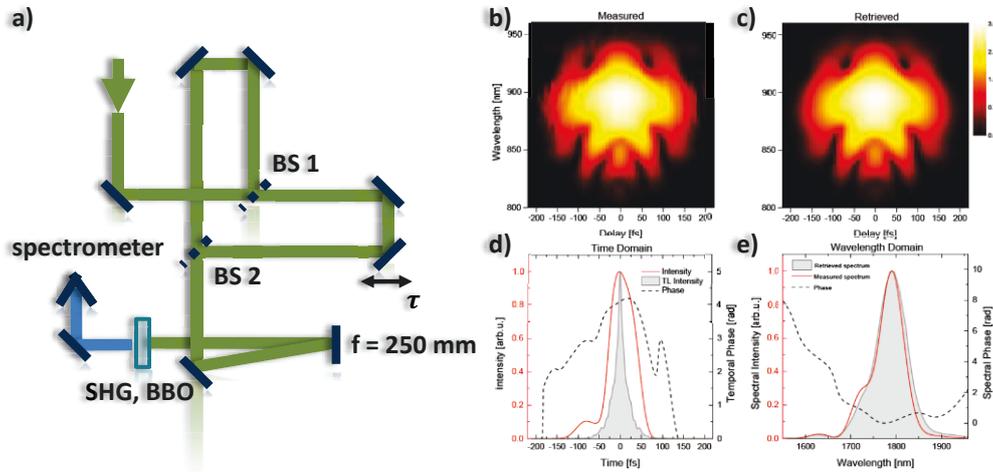
Figure 2.6: Setup for dispersion minimized frequency resolved optical gating (SHG-FROG) [45]

In a), the optical setup of the SHG FROG is shown. The laser pulses are sent into an interferometer that uses d-shaped mirrors as beam splitters. After the interferometer, the pulses are focused and overlapped spatially and temporally in a SHG crystal. The SHG signal is recorded as a function of the delay, τ, using a spectrometer yielding a so-called FROG-trace that is shown in b). In order to reconstruct the spectral phase and therefore, the temporal pulse profile, a commercial retrieval algorithm is used. As a consistency check, the FROG trace from the reconstruction is shown in c). The temporal intensity profile of the pulse is shown together with its Fourier transform limit (TL) in d). In e), the reconstructed spectrum and spectral phase is shown together with an independently measured spectrum as consistency check.

A second-harmonic generation frequency resolved optical gating (SHG-FROG) apparatus [52] has been implemented for temporal pulse characterization of the laser pulses in the signal and idler range of the HE-TOPAS-C [45]. A schematic is shown in Figure 2.6. Attenuated laser pulses come from the top and are sent in to an interferometer where the beam is split and combined using d-shaped mirror (BS 1 and BS 2). The delay, τ, is used to introduce a delay between both pulse copies. After combination, both pulses are focused and overlapped spatially and temporally at a very small angle in a BBO crystal for second harmonic generation (SHG). The BBO has a thickness of 50 μm and is cut for type I phase matching at the angle, $\theta = 21°$ and $\varphi = 90°$. Anti-reflection coatings for the wavelength range 1.0 μm and 2.4 μm for the fundamental as well as 0.5 μm to 1.0 μm for the second harmonic minimize losses. The small thickness of the crystal ensures large phase matching bandwidth such that very short pulses in the few-cycle regime can be characterized. After the BBO, the SHG light is sent to a spectrometer where the SHG spectrum is recorded stepwise as function of the delay, τ. From this so-called FROG trace, the spectral phase and thus, the complete time-dependent structure can be reconstructed using a phase retrieval algorithm which is done by a commercially available software (SWAMP OPTICS). However, due the use of SHG-FROG, an ambiguity in the sign of the spectral phase remains. This ambiguity can be solved by comparing the spectral phases of two FROG measurements where one has been taken with an additional piece of glass with known dispersion before the FROG apparatus. Such an analysis yielded an estimate for the GDD ≈ -630 fs^2 and a TOD $\approx +1000$ fs^3 at a pulse duration

of $\tau_p \approx 70$ fs (intensity full-width half-maximum) for the idler beam around 1800 nm behind the TOPAS. The fourier-limited duration (FTL) in this measurement was $\tau_{pFTL} \approx 20$ fs. Compared to τ_{pFTL} of the pulse, the measured GDD and TOD correspond to propagation through roughly 10 mm of fused silica. Assuming that a close-to FTL is generated by the optic parametric amplification in the last stage of the TOPAS, the measured GDD and TOD behind the TOPAS can be attributed to a large extend to the transmission of the idler through dichroic beam splitters, which are used to separate signal and idler.

One might deduce that using reflective beam splitter for the idler could yield a shorter idler pulse directly behind the TOPAS. At the same time, transmitting the signal would not stretch much as the signal wavelength is close to the zero GDD point of many materials. Alternatively, the dispersion might be compensated using chirped mirrors or propagation through materials that introduce positive GDD, e.g. noble gases. However, this approach is typically accompanied by the acquisition of higher order phase distortions and particularly positive TOD for typical materials in the range of the idler of the TOPAS. A third option might be to change the interaction in the last amplification stage of the TOPAS from collinear to slightly non-collinear. In this way, signal and idler can be separated spatially behind the crystal. However some pulse-front tilt is introduced onto the beams.

2.4 Hollow-Fiber Compression at Short-Wave Infrared Wavelength

Hollow-Fiber compression has become a standard technique for the generation of few-cycle pulses with up to mJ pulse energy at center wavelength around 0.8 μm. Here, Hollow-Fiber compression for a center wavelength around 1.8 μm is implemented and characterized as in [53].

2.4.1 Pulse Compression by Non-Linear Propagation in Gas-Filled Hollow Fibers

Due to bandwidth-limitations in the amplification process of ultrashort pulses such as gain narrowing, typical Ti:Sapphire based CPA laser systems deliver pulse durations around 25 fs only. However, compared to the optical period of 2.7 fs for 0.8 μm, the intensity full-width half-maximum duration (FWHM), τ, is thus, on the order of 10 optical cycles. In order to reach the few-cycle regime between 1 and 5 optical cycles various schemes that exploit various non-linear effects such as, self-phase modulation, self-steepening, four-wave mixing, plasma blue-shifting and filamentation have been investigated with the goal to increase the spectral bandwidth [54]. Around 0.8 μm, so-called hollow-fiber compression [55] [56] is presently the most powerful technique and has become a standard setup for the generation of few-cycle pulses [57]. Typically, 0.8 μm-25-fs-pulses with about 1 mJ in energy are focused into a roughly 1 m long glass capillary with an inner diameter of about 200 μm. Placing this capillary into a chamber where the pressure can be changed from a few mbars up to a few bars and filling it with a noble gas, allows one to achieve non-linear pulse propagation inside the gas-filled capillary, which yields significant spectral broadening. Collimating the pulses with a spherical mirror after the exit of the hollow-fiber and compensating the spectral phase using chirped mirrors [58] in combination with glass-wedges yields few-cycle pulses with a center wavelength around 0.8 μm and a few mJ in energy [59].

More recently, hollow-fiber compression is used for post-compression of the idler beam from the HE-TOPAS-C [53]. Similarly to the standard technique around 0.8 µm, the idler from HE-TOPAS-C is spectrally broadened by non-linear propagation in an Argon-filled hollow fiber and collimated afterwards. Due to the opposite signs of the second order dispersion of self-phase modulation and typical glasses at this wavelength, linear propagation in a bulk material after spectral broadening [44] yields sub-2cycle pulses with pulse energies on the mJ level.

In the next chapter, the implementation of a setup for hollow-fiber compression at 1.8 µm is implemented and bulk compression in fused-silica glass is characterized and optimized using the previously introduced SHG-FROG setup.

2.4.2 Generation of Sub-2-cycle Pulses at a Wavelength around 1.8 µm
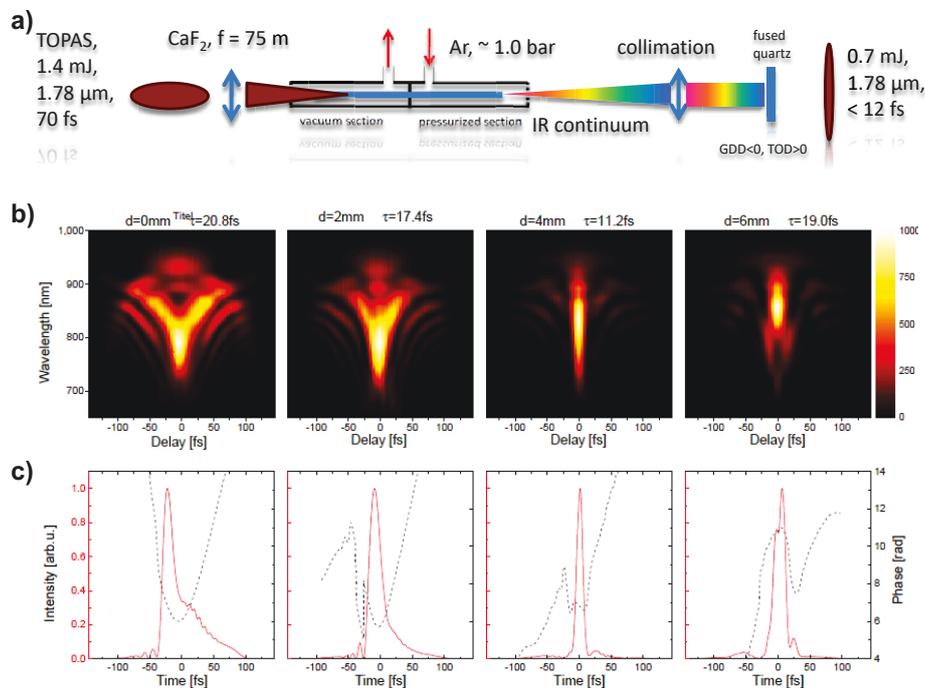
Figure 2.7: Hollow-fiber compression at a center wavelength of 1.8 µm [45].

a) A sketch of the setup. The top row, b), shows the recorded SHG-FROG traces while the thickness of fused quartz is increased from 0 mm to 6 mm in steps of 2 mm. Below, in c) the time-dependent intensity distribution and phase are shown. Best compression to close-to Fourier-transform limited 2-cycle pulses yields about 4 mm of fused silica.

A sketch of the scheme that is used for hollow-fiber compression at a center wavelength of 1.8 µm is shown in Figure 2.7. Laser pulses in the idler range of the HE-TOPAS-C with a duration of roughly 70 fs and a center wavelength of 1.78 µm are focused into a differentially pump setup for hollow-fiber compression [60] using an f=75 cm CaF2 lens. The inner diameter of the fiber is 400 µm. Behind the fiber, collimation is done using a spherical silver coated mirror with focal length f=1m. Applying about 1.1 Bar of Argon on the pressurized side of the setup yields sufficient spectral broadening to achieve sub-12-fs pulses around 1.78 µm with an energy of 0.7 mJ. The spectral

phase is characterized using the FROG technique presented previously. Compensation of the spectral phase is achieved if thickness of the fused silica plates is adjusted to about 4 mm after collimation.

2.5 Conclusion and Outlook

In summary, a commercially available 1-kHz-10-mJ-35-fs Ti:Sapphire-based multi-pass chirped pulse amplification system ("Thales") is used to pump a high pulse energy traveling wave optic parametric amplifier ("TOPAS") to generate energetic femtosecond laser pulses with tunable wavelength in the short-wave infrared and infrared spectral range. Further, hollow-fiber compression can be used to generate few-cycle pulses around 1.78 μm with an energy of 0.7 mJ. The output of the presented setups has been characterized and is regularly operated to study strong-field laser-matter interaction in this thesis. The setup presented is similar to many setups that are used to investigate strong-field laser-matter interaction around the world.

Presently developing and maturing technologies, which are expected to become relevant for strong-field laser-matter interaction in the future, are high average-power fiber lasers with wavelength in the near infrared and short-wave infrared spectral range as well as high average-power optic-parametric chirped pulse amplification. Also the combination of both is expected to play a vital role. Both technologies have the potential to shift the average-power from several ten Watts (for Ti:Sapphire-based lasers) to hundreds of Watts, which will enable investigation and application of strong-field laser-matter interaction at higher repetition rate.

3 Momentum Spectroscopy of Laser-Induced Fragmentation Processes

3.1 Introduction and Outline

Recent experimental and theoretical progress in understanding of atomic and molecular reactions would not have been possible without the availability of instrumentation for their analysis. Very significant advances in this field date back to the 1980's when the group around Prof. Horst Schmidt-Böcking at the University Frankfurt started the development of Cold-Target Recoil Ion Momentum Spectroscopy (COLTRIMS) [61] [62]. In COLTRIMS, the simultaneous measurement of full three-dimensional vector momenta of not only one, but ideally all fragments, i.e. electrons, ions, and in an ideal world even neutrals, that result from the interaction between a projectile or laser beam and a target jet, allows for the experimental analysis of complex reaction kinematics. The measurement principle relies on the use of static electric and magnetic fields to guide the charged fragments from the interaction zone to position- and time-sensitive detectors [63] [64]. As neutrals do not react to electric and magnetic fields, typically only charged fragments can be measured. Together with knowledge of the fragment mass, fragment charge and calibrated spectrometer fields; the measurement of impact time and impact position at the detectors is the basis for calculating fragment vector momenta, $\boldsymbol{p}'_i$, of each fragment. Repeating this many times (many initial particles of the same initial state), yields momentum differential cross-sections or rates, which can be used to infer reaction dynamics.

The COLTRIMS principle is so flexible that it has become a technique that has spread out over many fields in physics and chemistry. Many variants and/or simplifications of it, i.e. COLTRIMS-like fragment momentum spectrometers, are presently operated to measure momentum differential cross-sections of various kind of reactions around the world. As targets, cold jets of atoms, molecules, ions, clusters and nanoparticles are used. For the projectile, beams of electrons, ions, and photons of all kinds are applied. In view of this thesis, Xe atoms and H_2^+ ions are targets and photons in the form of intense femtosecond laser fields are the chosen projectiles to investigate ionization dynamics in intense laser fields with short-wave infrared wavelength.

The measurements in this work have been done using two variants of COLTRIMS-like fragment momentum spectrometers. A Velocity-Map Imaging Spectrometer (VMI) [65] [66] is applied to measure photoelectron momentum distributions (PMD) after strong-field photoionization of Xenon, see chapter 3.5. Details of the apparatus are shortly introduced in subsections 3.3 and 4.2. An Ion Target Recoil Ion Momentum Spectroscopy (ITRIMS) setup is used for the analysis of strong-field photoionization of H_2^+, in chapter 5. Both setups have been implemented, are regularly operated and are continuously improved at Friedrich-Schiller University and Helmholtz-Institute Jena. For further details, one might consult references, [67] [68] [45] for the VMIS and [14] [21] [69] [70] for the ITRIMS.

3.2 Kinematics in Setups for Momentum Spectroscopy of Laser-Induced Fragmentation Processes

Before we turn to details of the used VMI and ITRIMS setups, kinematics of the laser-induced fragmentation processes are summarized in this section. We begin by recalling the standard interpretation of measurement data in 3.2.1 and the semi-classical picture on laser-matter interaction in 3.2.2. Finally classical mechanics of laser-induced fragmentation is summarized in order to recall conservation laws that are relevant for the employed experimental setups.

3.2.1 Determination of Fragment Momenta – Micr
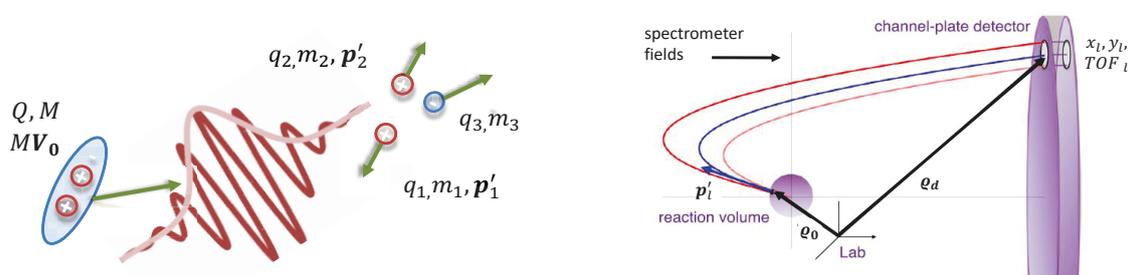
Figure 3.1: Determination of Fragment Momenta

a) Illustrates the microscopic time domain from a few tens of femtosecond before until few tens of femtoseconds after the laser-induced fragmentation process. The fragmentation creates l fragments that have the fragment momenta $\boldsymbol{p}'_l$. In the macroscopic domain, b), fragments emerge from the reaction volume (focal volume) with some momentum $\boldsymbol{p}'_l$. Electric and magnetic spectrometer fields guide them to the detector where measurement of impact position and time-of-flight (TOF) is the basis to calculate $\boldsymbol{p}'_l$. Both domains are connected due to momentum conservation. b) is an adaption from [71]

Independent of the details of the used experimental apparatus (COLTRIMS, ITRIMS, VMIS, etc.), momentum spectroscopy of laser-induced fragmentation processes relies on measurement of impact position and time of ideally all fragments. Thereby, the times and positions measured are macroscopically later and larger (nano- and microseconds; centimeters and meters) than the times and positions that are relevant for the quantum mechanical dynamics of the fragmentation (atto- and femtoseconds; pico- and nanometers). Using such a scenario to infer information on the microscopic quantum mechanical dynamics relies on dividing the full interaction, i.e. laser field and spectrometer fields, into a microscopic time domain of the laser-induced fragmentation and a macroscopic time domain during which the fragments are guided by external electric and magnetic spectrometer fields until they hit a detector, see Figure 3.1 [72] [73] [71].

The microscopic domain ranges from a few femtoseconds before until a few tens of femtoseconds after the laser field has passed. During this time, external spectrometer fields are typically neglected as they are much weaker than the typical strength of the reaction forces, e.g. the laser field or Coulomb fields among the fragments. Motions that occur during microscopic time domain are negligibly small (atto- and femtoseconds; pico- and nanometers)

compared to the relevant position and time scales in the macroscopic time domain e.g. size of the reaction volume (laser focus, micrometers) or the dimension of the spectrometer (centimeters and meters). Thus, the microscopic times and positions can be neglected for the dynamics on the scale of the macroscopic time domain during which the fragments travel e.g. from the reaction volume until they hit a detector after some time-of-flight (TOF). Both domains are connected as momenta gained in the one or the other domain are conserved and are not negligible from the one or the other perspective.

This connection uses the picture that the lth fragment with fragment mass m_l and fragment charge q_l emerges from the reaction volume with some fragment momentum

$$\boldsymbol{p}'_l = \boldsymbol{p}_l + \boldsymbol{p}_{0l} = \boldsymbol{p}_l + \boldsymbol{V}_0 m_l. \tag{3.1}$$

, see Figure 3.1. The contribution, $\boldsymbol{p}_{0l} = \boldsymbol{V}_0 m_l$, is the lth momentum fraction of the initial momentum of the target particle $\boldsymbol{P}_0 = M\boldsymbol{V}_0$. The mass of the initial particle is $M = \sum_l m_l$. The exact trajectory to the detector during TOF from the position of the fragmentation $\boldsymbol{\varrho}_0$ (in the interaction volume) depends on the type of the experimental apparatus. It is sensitive to $q_l, m_l, \boldsymbol{V}_0$ and of course, to the shape and size of electric and magnetic spectrometer fields. In order to determine $\boldsymbol{p}'_l$ from measured macroscopic impact times and positions, x_l, y_l and TOF_l, one uses classical mechanics of charged particles in the spectrometer fields. For each spectrometer, VMI, ITRIMS, COLTRIMS, etc., appropriate calibration techniques as well as coincidence filtering techniques are used in order to ensure precise and reliable determination of $\boldsymbol{p}'_l$. Combining this measurement of $\boldsymbol{p}'_l$ with precise knowledge, control or well justified assumptions on the distribution of initial velocities $\boldsymbol{V}_0$ respectively on $\boldsymbol{V}_0 m_l$ in the target, allows to separate the momentum gained due laser-induced fragmentation $\boldsymbol{p}_l$ from the measured sum $\boldsymbol{p}'_l = \boldsymbol{p}_l + \boldsymbol{V}_0 m_l$. Typically, the motion due to $\boldsymbol{V}_0 m_l$ can be transformed away and fragment momenta $\boldsymbol{p}_l$ due to laser-induced breakup respectively their distributions are then given within the center of momentum frame of the initial particle which has the momentum, $\boldsymbol{P}_0 = M\boldsymbol{V}_0$.

Typical measurement results that are then compared to models on the fragmentation process are momentum differential cross-sections or rates for fragmentation channels of interest. In other words, the measurements provide distributions or spectra, i.e. number of events as function of final fragment momenta $\boldsymbol{p}_l$ or quantities that can be calculated from it. Examples are photoelectron momentum distributions (PMDs) or kinetic energy release spectra (KER spectra). In most cases, modeling of the laser-induced fragmentation processes is typically concerned with the microscopic domain only. In order to compare to experimental results, theoretical results should be given as function of asymptotic momenta, i.e. when $t \to \infty$.

3.2.2 Semi-Classical Picture on Light-Matter Interaction and Definition of the Laser Field

It is well known that a rigorous description of light-matter interaction requires quantum electro dynamics. For the wavelength/photon energy range (0.5 - 2.5 μm; 2.5 - 0.5 eV; 0.092 - 0.018 a.u.) that are relevant here however, the photon densities are comparatively high already at low intensities. Thus, it is reasonable and common to use the semi-classical picture of the light matter interaction where the light field is treated classically based on Maxwell's equation and the atoms and molecules of the target are treated quantum mechanically [74]. A

consequence of this approximation is that there are - strictly speaking - no photons involved in the interaction as the classical description of the light field doesn't support this concept. Further, as the typical gas phase targets contain only a few particles, the effects of the target on the light field respectively on its propagation, i.e. absorption, dispersion, and so on are neglected.

Within the semi-classical picture of light matter interaction, the laser field is governed by Maxwell's equation and can be expressed as $\boldsymbol{E}(\boldsymbol{\varrho}, t) = -\nabla \varphi(\boldsymbol{\varrho}, t) - \partial_t \boldsymbol{A}(\boldsymbol{\varrho}, t)$ and $\boldsymbol{B}(\boldsymbol{\varrho}, t) = \nabla \times \boldsymbol{A}(\boldsymbol{\varrho}, t)$, using the scalar $\varphi(\boldsymbol{\varrho}, t)$ and the vector potential $\boldsymbol{A}(\boldsymbol{\varrho}, t)$ [74]. Atomic units are used unless stated otherwise. In the Coulomb gauge, $\nabla \boldsymbol{A}(\boldsymbol{\varrho}, t) = 0$, one sets $\varphi(\boldsymbol{\varrho}, t) = 0$, such that $\boldsymbol{A}(\boldsymbol{\varrho}, t)$ full-fills the wave equation, i.e. $\nabla^2 \boldsymbol{A}(\boldsymbol{\varrho}, t) - \partial^2 \boldsymbol{A}(\boldsymbol{\varrho}, t)/c^2 \partial t^2 = 0$. The solution can be expressed as $\boldsymbol{A}(\boldsymbol{\varrho}, t) = -A_0(\boldsymbol{\varrho}, t)\boldsymbol{\varepsilon}\sin(\boldsymbol{k}\boldsymbol{\varrho} - \omega t + \xi(t))$ using the amplitude $A_0(t)$, and the vector, $\boldsymbol{\varepsilon}$, of the linear polarization. The wave vector is $\boldsymbol{k} = \omega \boldsymbol{e}_z/c$, where ω denotes the angular frequency, and $\xi(t)$ an in general time-dependent phase that is related to the time-dependent evolution of the phase of the pulse such as e.g. chirp. The polarization vector and the wave vector satisfy, $\boldsymbol{k}\boldsymbol{\varepsilon} = 0$, for transversal waves. For $\xi(t) = \text{const}$, the corresponding electric field is $\boldsymbol{E}(\boldsymbol{\varrho}, t) = E_0(\boldsymbol{\varrho}, t)\boldsymbol{\varepsilon}\cos(\boldsymbol{k}\boldsymbol{\varrho} - \omega t)$. It has an amplitude of $E_0(\boldsymbol{\varrho}, t) = \omega A_0(\boldsymbol{\varrho}, t)$, which is approximately $|\boldsymbol{k}| = \omega/c$ times larger than the related magnetic field, $\boldsymbol{B}(\boldsymbol{\varrho}, t) = E_0(\boldsymbol{\varrho}, t)\omega^{-1}(\boldsymbol{k} \times \boldsymbol{\varepsilon})\cos(\boldsymbol{k}\boldsymbol{\varrho} - \omega t)$. $\boldsymbol{B}(\boldsymbol{\varrho}, t)$ is approximately hundred times smaller due to scaling of it's amplitude with $1/c$ and thus, only $\boldsymbol{E}(\boldsymbol{\varrho}, t)$ is taken into account.

Independent of the exact temporal evolution of $\boldsymbol{E}(\boldsymbol{\varrho}, t)$, a short laser pulse must be a traveling wave that has no direct-current components, i.e. no components with zero frequency. Thus, it fulfills $\int_{-\infty}^{\infty} \boldsymbol{E}(\boldsymbol{\varrho}, t')dt' = 0$ and hence, the vector potential satisfies, $-\boldsymbol{A}(\boldsymbol{\varrho}, t = \infty) + \boldsymbol{A}(\boldsymbol{\varrho}, t = \infty) = \text{const}$, which is consistent with choosing, const $\equiv 0$. As typical target particles (atoms, ions, molecules) are a lot smaller than the wavelength of the laser, the spatial dependence of the vector potential is dropped, which leads to $\boldsymbol{A}(\boldsymbol{\varrho}, t) = \boldsymbol{A}(t)$, and similarly $\boldsymbol{E}(\boldsymbol{\varrho}, t) = \boldsymbol{E}(t)$. The time-independent, real amplitudes are approximately related by $A_0 \cong -E_0/\omega$.

3.2.3 Classical Mechanics of a Two-Particle Breakup in a Laser Field

As one shall see later, the field of strong-field laser-matter interaction uses classical mechanics of charged particles in external electromagnetic fields to a large extend for interpretation and also for modeling and simulation of the fragmentation dynamics with the goal to maximize insight and to develop simple and intuitive models about the interaction [11] [12]. Here, we use classical mechanics to illustrate and summarize relevant conservation laws and approximations that are employed in experimental setups for momentum spectroscopy of laser-induced fragmentation processes. The illustrative consideration is done for a two particle breakup in an external field. More complex breakups, e.g. three or multiple particle breakups might be considered as a series of two-body breakups and could be discussed on a similar basis. Clearly this makes the problem more complex. Here we focus on the example of a two-body fragmentation. Atomic units are used unless stated otherwise.

The Lagrangian, $L = T - U$ of two particles of masses, m_1, m_2, and charges q_1, q_2, that interact via the potential, U, in the time-dependent external laser field $\boldsymbol{E}(t)$ with the vector potential $\boldsymbol{A}(t)$ is

$$L(\boldsymbol{r}_1, \boldsymbol{r}_2, \dot{\boldsymbol{r}}_1, \dot{\boldsymbol{r}}_2, t) = \frac{1}{2}m_1\dot{r}_1^2 + \frac{1}{2}m_2\dot{r}_2^2 + q_1\dot{\boldsymbol{r}}_1\boldsymbol{A}(t) + q_2\dot{\boldsymbol{r}}_2\boldsymbol{A}(t) - U(t, |\boldsymbol{r}_1 - \boldsymbol{r}_2|). \tag{3.2}$$

The positions and velocities of the two particles are $\boldsymbol{r}_1, \boldsymbol{r}_2, \dot{\boldsymbol{r}}_1, \dot{\boldsymbol{r}}_2$, T is the kinetic energy, the expression $q_1\dot{\boldsymbol{r}}_1\boldsymbol{A}(t) + q_2\dot{\boldsymbol{r}}_2\boldsymbol{A}(t)$ is the potential energy of the charged particles in the laser field and $U(t, |\boldsymbol{r}_1 - \boldsymbol{r}_2|)$ is the potential of forces, which act among the fragments. The potential, $U(t, |\boldsymbol{r}_1 - \boldsymbol{r}_2|)$, has been made explicitly time dependent in order to emphasize that for the classical description used here, the internal forces might start to act among the fragments starting from a certain breakup time, $t > t_b$, while they might be neglected before $t < t_b$, i.e. $U(t < t_b, |\boldsymbol{r}_1 - \boldsymbol{r}_2|) \approx 0$, during the time when the particles are considered as a single particle. As one shall see later, calculation of time-dependent probabilities for this transition together with probabilities for initial conditions at t_b are subject to quantum mechanical models of the fragmentation process, e.g. tunnel ionization. Further, U is assumed to depend on the distance between both particles, $r = |\boldsymbol{r}| = |\boldsymbol{r}_1 - \boldsymbol{r}_2|$, only. The field is modeled as a classical field as discussed in the previous section.

Introducing the relative coordinate, $\boldsymbol{r} = \boldsymbol{r}_1 - \boldsymbol{r}_2$, and center-of-mass coordinate $\boldsymbol{X}_{cm} = (m_1\boldsymbol{r}_1 + m_2\boldsymbol{r}_2)/(m_1 + m_2)$ together with the total mass $M = m_1 + m_2$ leads to the back transformations, $\boldsymbol{r}_1 = \boldsymbol{X}_{cm} + \boldsymbol{r}m_2/M$ and $\boldsymbol{r}_2 = \boldsymbol{X}_{cm} - \boldsymbol{r}m_1/M$ with the corresponding velocities, $\dot{\boldsymbol{r}}_1 = \dot{\boldsymbol{X}}_{cm} + \dot{\boldsymbol{r}}m_2/M$ and $\dot{\boldsymbol{r}}_2 = \dot{\boldsymbol{X}}_{cm} - \dot{\boldsymbol{r}}m_1/M$. Plugging those into (3.2) and introducing the reduced mass, $\mu = m_1m_2/M = m_1m_2/(m_1 + m_2)$, as well as the total charge $Q = q_1 + q_2$ yields

$$L(\boldsymbol{r}, \boldsymbol{R}, \dot{\boldsymbol{r}}, \dot{\boldsymbol{R}}, t) = \frac{1}{2}M\dot{\boldsymbol{X}}_{cm}^2{}^2 + Q\dot{\boldsymbol{X}}_{cm}\boldsymbol{A}(t) + \frac{1}{2}\mu\dot{r}^2 + \left(q_1\frac{\mu}{m_1} - q_2\frac{\mu}{m_2}\right)\dot{\boldsymbol{r}}\boldsymbol{A}(t) - U(t, |\boldsymbol{r}|). \tag{3.3}$$

In (3.2), the relative motion, i.e. the motion along $\boldsymbol{r}$ is separated from the center of mass motion along $\dot{\boldsymbol{X}}_{cm}$.

By application of the Euler-Lagrange equation, i.e. $d(\partial L/\partial \dot{\boldsymbol{q}}_j)/dt - (\partial L/\partial \boldsymbol{q}_j) = 0$, of the second kind together with $-d\boldsymbol{A}(t)/dt = \boldsymbol{E}(t)$ one arrives at the equation of motion,

$$\frac{d}{dt}\frac{\partial L}{\partial \dot{\boldsymbol{X}}_{cm}} - \frac{\partial L}{\partial \dot{\boldsymbol{X}}_{cm}} = \frac{d}{dt}\left(M\dot{\boldsymbol{X}}_{cm} + Q\boldsymbol{A}(t)\right) = 0 \rightarrow M\ddot{\boldsymbol{X}}_{cm} = -Q\frac{d}{dt}\boldsymbol{A}(t) = Q\boldsymbol{E}(t), \tag{3.4}$$

for the center-of-mass coordinate $\boldsymbol{X}_{cm}$. It reveals that the canonical momentum $\boldsymbol{C}(t) = M\dot{\boldsymbol{X}}_{cm} + Q\boldsymbol{A}(t)$ is conserved for all times.

Integrating (3.4) over the time interval between t_1 and t_2 yields $M\dot{\boldsymbol{X}}_{cm} = Q[\boldsymbol{A}(t_2) - \boldsymbol{A}(t_1)]$. Choosing $t_1 = -\infty$ and $t_2 = +\infty$ and combining this with the fact that the electric field is a traveling wave, i.e. the field fulfills $\int_{-\infty}^{\infty}\boldsymbol{E}(t')dt' = 0$ which leads to $\boldsymbol{A}(\infty) - \boldsymbol{A}(-\infty) = $ const, illustrates that the laser field doesn't change the initial momentum of the center-of-mass motion, i.e. $\boldsymbol{P}_0 = M\dot{\boldsymbol{X}}_{cm}(t = -\infty) = M\dot{\boldsymbol{X}}_{cm}(t = \infty) = M\boldsymbol{V}_0$ is a constant. Consequently, a kinematic complete measurement, i.e. a measurement where the momenta of all l fragments are measured fulfills the condition,

$$\sum \boldsymbol{p}_l' = \boldsymbol{V}_0 \sum m_l = M\boldsymbol{V}_0. \tag{3.5}$$

As examples for a kinematic complete measurements, we mention single ionization of atomic hydrogen or any other atom, i.e. $H \rightarrow H^+ + e^-$ where the momenta $\boldsymbol{p}'_{H^+}$ and $\boldsymbol{p}'_{e^-}$ are measured, or dissociation of H_2^+, i.e. $H_2^+ \rightarrow H^+ + H$ where $\boldsymbol{p}'_{H^+}$ and $\boldsymbol{p}'_H$ are measured.

As indicated, the property (3.5) of the laser-induced fragmentation is not limited to two-body fragmentation but is also valid for multiple particle fragmentation. It is regularly exploited in measurements in several ways.

i) A kinematic complete measurement can be used to characterize the distribution of initial velocities $\boldsymbol{V}_0$ respectively initial momenta $M\boldsymbol{V}_0$ in the target. The idea is realized in section 5.2.1 where a kinematic complete measurement of dissociation of H_2^+ is used to determine the initial momentum spread of the ion beam target in the ITRIMS setup.

ii) The second aspect is relevant if the initial momentum spread in the target is well controlled and known, i.e. if $M\boldsymbol{V}_0 \approx 0$ or $M\boldsymbol{V}_0 \approx$ const are justified approximations. This is the case for a cold target which is, e.g., produced using supersonic gas expansion techniques in a typical COLTRIMS apparatus. For an ITRIMS setup this is only possible if the velocity and the collimation of the ion beam target is very well controlled [14] [21] [15] [75].

    a) One can use the knowledge of $M\boldsymbol{V}_0 =$ const or $M\boldsymbol{V}_0 \approx 0$ as condition for coincidence filtering in kinematic complete measurements. This approach is able to reduce false coincidences [14] [21] [15] [75] and is used to increase the signal to noise ratio in measurements dramatically.

    b) Further, if $M\boldsymbol{V}_0 =$ const is well known and combined with a kinematic complete experiment, the achieved momentum resolution is limited by the precision of the measurement of impact time and impact position together with the spectrometer geometry only. It is then not or only weakly blurred by the fact that the measured momentum distributions are a convolution between the distribution of $\boldsymbol{p}_l$ (the momentum gained during laser-induced fragmentation) and the distribution of initial momenta in the target $\boldsymbol{p}_{0l} = \boldsymbol{V}_0 m_l$, remember $\boldsymbol{p}'_l = \boldsymbol{p}_l + \boldsymbol{p}_{0l} = \boldsymbol{p}_l + \boldsymbol{V}_0 m_l$, i.e. equation (3.1).

    c) One can use ii) to reduce the number of measured fragments as writing (3.5) for a two-body fragmentation illustrates. Consider, $\boldsymbol{p}'_1 + \boldsymbol{p}'_2 = \boldsymbol{p}_1 + m_1 \boldsymbol{V}_0 + \boldsymbol{p}_2 + m_2 \boldsymbol{V}_0 = (m_1 + m_2)\boldsymbol{V}_0 = M\boldsymbol{V}_0$ if $M\boldsymbol{V}_0$ is known, e.g. $M\boldsymbol{V}_0 \approx 0$, one can write, $\boldsymbol{p}_1 = -\boldsymbol{p}_2$. Thus, measuring $\boldsymbol{p}_{H^+}$ for e.g. the reaction $H \rightarrow H^+ + e^-$ is sufficient and $\boldsymbol{p}_{e^-}$ can be inferred. Measuring the heavy fragment, i.e. the so-called recoil ion (remember the name Cold Target Recoil Ion Momentum Spectroscopy), instead of the electron is beneficial for the achieved momentum resolution as its smaller velocity leads to larger TOF on the order of microseconds instead of nanoseconds for the electron. In addition, it is simpler to distinguish desired signals from signals that stem from ionization of the background gas because the produced target ion has typically a specific q/m ratio in contrast to electrons which cannot be distinguished. Another example are COLTRIMS measurements where neutral fragments that are typically not detected are involved, e.g. $H_2 \rightarrow H^+ + H$. The momentum of H^+ is measured and the momentum of H is inferred. The scheme can also be applied to more complex situations, e.g. ionization of $H_2^+ \rightarrow H^+ + H^+ + e^-$ where one measures the momenta of the two protons, $\boldsymbol{p}_1$ and $\boldsymbol{p}_2$ and uses $\boldsymbol{p}_1 + \boldsymbol{p}_2 = -\boldsymbol{p}_e$ to infer the momentum of the electron $\boldsymbol{p}_e$. This idea is used in section 5.2.1.

After this discussion on consequences of the conservation law (3.5) and their relevance for typical experimental setups, we turn to the equation of motion for the relative coordinate r next. Application of the Euler-Lagrange equation for this coordinate yields,

$$\frac{d}{dt}\frac{\partial L}{\partial \dot{r}} - \frac{\partial L}{\partial r} = \frac{d}{dt}\left(\mu\dot{r} + \left(q_1\frac{\mu}{m_1} - q_2\frac{\mu}{m_2}\right)A(t)\right) = -\frac{\partial}{\partial r}U(t,|r|)$$

$$\rightarrow \mu\ddot{r} = -\frac{\partial}{\partial r}U(t,|r|) - \left(q_1\frac{\mu}{m_1} - q_2\frac{\mu}{m_2}\right)\frac{d}{dt}A(t) \tag{3.6}$$

$$\rightarrow \mu\ddot{r} = -\frac{\partial}{\partial r}U(t,|r|) + \left(q_1\frac{\mu}{m_1} - q_2\frac{\mu}{m_2}\right)E(t).$$

The first line in (3.6) illustrates that the quantity $\left(\mu\dot{r} + (q_1\mu/m_1 - q_2\mu/m_2)A(t)\right)$ is affected by internal forces such as Coulomb forces or dissociative forces that occur among the fragments. They are represented by the term $-\partial U(t,|r|)/\partial r$. However, if these forces are small for the relevant values of $|r|$, e.g. for large distances, they can be neglected, $-\partial U(|r|)/\partial r \approx 0$. In this case, $c(t) = \left(\mu\dot{r} + (q_1\mu/m_1 - q_2\mu/m_2)A(t)\right)$ is conserved.

Next one can integrate between two times t_1 and t_2 and finds $\mu\dot{r} = (q_1\mu/m_1 - q_2\mu/m_2)[A(t_2) - A(t_1)] + \mu\dot{r}_0$. $\mu\dot{r}_0 = \mu(\dot{r}_{10} - \dot{r}_{20})$ is the initial relative momentum at the time t_1. Identifying t_1 with the time of the breakup $t_1 = t_b$ in the laser field and $t_2 = +\infty$ with the time of the measurement at the detector when $A(\infty) = 0$ yields an approximation (because $-\partial U(t,|r|)/\partial r \approx 0$ is used) for the relative momentum that is measured $\mu\dot{r} = -(q_1\mu/m_1 - q_2\mu/m_2)A(t_b) + \mu\dot{r}_0$. If one uses the back transformations $\dot{r} = (\dot{r}_1 - \dot{X}_{cm})M/m_2$ and $(-\dot{r}_2 + \dot{X}_{cm})M/m_1 = \dot{r}$ approximate expressions for the asymptotic momenta of the two fragments are found,

$$m_1\dot{r}_1(\infty) = -A(t_b)\left(q_1\frac{m_2}{M} - q_2\frac{m_1}{M}\right) + \frac{m_1 m_2}{M}\dot{r}_0 + m_1\dot{X}_{cm}(\infty)$$

$$m_2\dot{r}_2(\infty) = +A(t_b)\left(q_1\frac{m_2}{M} - q_2\frac{m_1}{M}\right) - \frac{m_1 m_2}{M}\dot{r}_0 + m_2\dot{X}_{cm}(\infty). \tag{3.7}$$

Performing a short consistency check by summing $m_1\dot{r}_1(\infty) + m_2\dot{r}_2(\infty) = m_1\dot{X}_{cm}(\infty) + m_2\dot{X}_{cm}(\infty) = M\dot{X}_{cm}(\infty) = MV_0$ illustrates again that the laser field doesn't change initial momentum.

Let us investigate (3.6) and (3.7) for a few examples in detail next.

i) For ionization of atomic Hydrogen, i.e. $H \rightarrow H^+ + e^-$ ($M = 1837, Q = 0, m_{H^+} = 1836$, $q_{H^+} = +1$, $q_{e^-} = -1$, $m_{e^-} = 1$) with the assumption, $\dot{r}_0 \approx 0$. One finds, $p_{H^+} = m_1\dot{r}_1(\infty) = -A(t_b) + 1836\dot{X}_{cm}(\infty)$ and $p_e = m_2\dot{r}_2(\infty) = A(t_b) + 1\dot{R}(\infty)$. Comparing the corresponding kinetic energies for a cold target, i.e. $\dot{X}_{cm}(\infty) = V_0 \approx 0$ and typical values for the field strength, $E_0 \approx 0.1$ ($I \approx 3.5\ 10^{14}$ W/cm^2), respectively the vector potential $A_0 \cong -E_0/\omega \approx 1.75$ at a center wavelength of $\lambda = 800$ nm $\rightarrow \omega = 0.057$ gives $T_{H^+} = A_0^2/2m_H \cong E_0^2/2m_H\omega^2 = (0.1/0.057)^2/2 \cdot 1836 \approx 10^{-3}$ a.u. ≈ 0.01 eV and $T_e = A_0^2/2 \cong E_0^2/2\omega^2 = (0.1/0.057)^2/2 \approx 1.54$ a.u. ≈ 41 eV. Comparing the numbers shows that the kinetic energy of the ion is approximately $1/m_H \approx 1/2000$ smaller. It reflects that the electron has an a lot smaller TOF until it hits the detector.

ii) Considering dissociation of H_2^+, i.e. $H_2^+ \rightarrow H^+ + H$ ($M = 3673, Q = 1, m_{H^+} = 1836$, $q_{H^+} = +1$, $q_H = 0$, $m_H = 1837$) using the same scheme reveals an interesting aspect, for $\dot{X}_{cm}(\infty) = V_0 \approx 0$ respectively after transformation to the center-of-momentum frame, it gives $p_{H^+} = -A(t_b)(1836/3673) \approx -A(t_b)/2$ and $p_H = +A(t_b)(1836/3673) \approx +A(t_b)/2$. This momentum kick occurs in addition to the momentum kick from the

internal dissociative forces. Compared to them, it is small for 800 nm but it is expected to become relevant if dissociation takes place in a very long wavelength field.

iii) As it is relevant in chapter 5, ionization of H_2^+, i.e. $H_2^+ \rightarrow H^+ + H^+ + e^-$ ($M = 3673, Q = 1, m_{H^+1} = m_{H^+2} = 1836$, $q_{H^+1} = q_{H^+2} = +1$, $q_e = -1$, $m_e = 1$) is studied as second example. It is the prototype of multiple breakup and the effect of internal potential can be studied. Again, $\dot{\boldsymbol{R}}(\infty) = \boldsymbol{V}_0 = 0$ is used. First, separation of the electron from the two protons gives, $\boldsymbol{p}_e = -\boldsymbol{A}(t_b)(-3672/3673 - 2 \cdot 1/3673) \approx +\boldsymbol{A}(t_b)$ and $\boldsymbol{p}_2 = +\boldsymbol{A}(t_b)(-3672/3673 - 2 \cdot 1/3673) \approx -\boldsymbol{A}(t_b)$. For this breakup, $\boldsymbol{p}_e$ can be inferred $\boldsymbol{p}_e = -(\boldsymbol{p}_1 + \boldsymbol{p}_2)$ from the two proton momenta, $\boldsymbol{p}_1$ and $\boldsymbol{p}_2$. Because of the sudden removal of the electron, the two protons start to separate at the same time. It can again be analyzed within the frame of (3.6). Both particles have the same charge, $q_1 = q_2 = +1$ and mass $m_1 = m_2 = 1836$ and the total mass is $M = 3672$. Consequently, the factor in front of $dA(t_b)/dt$ is zero, i.e. $(q_1\mu/m_1 - q_2\mu/m_2) = 0$ ($\mu = m_{H^+}/2$, now). Thus, no momentum kick from the field occurs for the breakup of the protons. The situation would be different if both heavy fragments, would not have the same mass e.g. for HD^+. Among the protons, only the term $-\partial U(t, |\boldsymbol{r}|)/\partial \boldsymbol{r} \approx -1/|\boldsymbol{r}|$ occurs in the equation of motion in (3.6). With $\boldsymbol{r}$ being the distance of the two protons one has the equation of motion, $\mu\ddot{\boldsymbol{r}} = -1/|\boldsymbol{r}|^2$, now. The energy W is conserved such that, $W(t_b) = T(t_b) + U(t_b) = T(\infty) + U(\infty) = W(\infty)$ can be used to calculate the asymptotic relative momentum at the detector when $\boldsymbol{r}(\infty) \rightarrow \infty$. It is $W(t_b) = \mu\dot{\boldsymbol{r}}^2/2 + 1/|\boldsymbol{r}| \rightarrow \dot{\boldsymbol{r}}(\infty) = \pm\sqrt{2W(t_b)/\mu}$ from which follows $\mu\dot{\boldsymbol{r}}(\infty)^2/2 = W(t_b)$. An estimate for the total energy at t_b is $W(t_b) = \mu\dot{\boldsymbol{r}}_0^2/2 + 1/|\boldsymbol{r}(t_b)|$. Assuming $\mu\dot{\boldsymbol{r}}_0^2/2 \approx 0$, one can estimate the distance, $|\boldsymbol{r}(t_b)|$, based on the measured momenta of both protons $\boldsymbol{p}_1$ and $\boldsymbol{p}_2$ by equating, $(\boldsymbol{p}_1 - \boldsymbol{p}_2)^2/2m_{H^+} = m_{H^+}\dot{\boldsymbol{r}}(\infty)^2/2 = \mu\dot{\boldsymbol{r}}(\infty)^2/2 \approx 1/|\boldsymbol{r}(t_b)|$. The initial condition for the angular momentum has been assumed to be zero.

iv) Expressions (3.7) further reveal that the effect of the initial momentum on the measured momentum depends on the fragment mass, i.e. $m_1\dot{\boldsymbol{r}}_1(\infty) \sim m_1\dot{\boldsymbol{X}}_{cm}(\infty) = m_1\boldsymbol{V}_0$ and $m_2\dot{\boldsymbol{r}}_2(\infty) \sim m_2\dot{\boldsymbol{X}}_{cm}(\infty) = m_2\boldsymbol{V}_0$. This connection allows to estimate the effect of an initial momentum spread, e.g. due to the target temperature, on the final momentum resolution in dependence of the fragment mass. Modeling the initial momentum/velocity distribution in the target as an ideal gas by assuming a Maxwell-Boltzmann distribution yields a spread of $\sigma = \sqrt{k_B\tau/M}$ for initial velocities in the target. For e.g. Xenon (Xe) atoms with a mass $M \approx 131 \cdot 1.660\,10^{-27}$ kg $= 2.38\,10^5$ a.u. and initial charge $Q = 0$ at room temperature $\tau = 300\,K$ this is $|v_\sigma| = \sqrt{1.38 \cdot 10^{-23} \cdot 300/(131 \cdot 1.660 \cdot 10^{-27})} \approx 138$ m/s $\approx 10^{-4}$ a.u.. Thus, Xe^+ ions after the breakup would have a final momentum of $\boldsymbol{p}_{Xe^+} \approx \boldsymbol{A}(t_b) + M|v_\sigma|\boldsymbol{e}_r \approx \boldsymbol{A}(t_b) + 15\boldsymbol{e}_r$. Thereby, $15\boldsymbol{e}_r$ points into every direction and follow the Maxwell-Boltzmann distribution. The electrons however, would have $\boldsymbol{p}_{e^-} \approx -\boldsymbol{A}(t_b) + 10^{-4}\,\boldsymbol{e}_r$. Comparing the initial momentum to the momentum kick from field for the mentioned typical values of $E_0 = 0.1$ and $|\boldsymbol{A}(t_b)| \approx 1.75$ at 800 nm shows that the effect of the initial velocity is small for the electron but dominant for the ion. In other words, the momentum kick from the laser field is a small change of the momentum of the ion on top of the wide initial momentum distribution. But for the electron, it is a big change on a narrow initial distribution. Consequently, measuring the ion requires cooling or a kinematic complete experiment while the electron momentum distribution can be measured with high precision without such efforts. This is the reason why a VMIS can be operated without cold target if photoelectron momentum distributions are measured.

Equation (3.7) also establishes a connection between the measured fragment momenta and the vector potential at the time of the breakup in the field. Thus, measured momentum distributions contain within some approximation information on the time-dependent shape of the electric field. This aspect is regularly used in COLTRIMS-like momentum spectrometer to characterize or estimate properties of the electric field, see e.g. the [76] [77] [78].

The detailed discussion of classical mechanics of a two-particle breakup dynamics inside a laser field revealed and illustrated several aspects that are regularly employed in measurements on momentum spectroscopy of laser-induced fragmentation processes. Next, central points which are relevant for this thesis are summarized.

3.2.4 Conclusion of Kinematics in Laser-Induced Fragmentation Setups

The review of classical mechanics of a two-particle breakup in a laser field in detail revealed several aspects which are exploited in the later chapters. This list summarizes the most relevant ones.

- A measurement where the momenta of all fragments are measured (kinematic complete measurement) can be used to characterize the momentum spread or temperature of the target. An example for this is the reaction $H_2^+ \rightarrow H^+ + H$ where $\boldsymbol{p}_{H^+}$ and $\boldsymbol{p}_H$ are measured. Momentum conservation states that $\boldsymbol{p}_H + \boldsymbol{p}_{H^+} = (m_H + m_{H^+})\boldsymbol{V}_0$ with $\boldsymbol{V}_0$ being the initial velocity of the target particle before fragmentation. This aspect is exploited in 5.2.1 to determine the momentum spread of the ion beam target.

- If the momentum spread of the target is well characterized, then this information can be used to infer the momentum of a fragment which is actually not detected, e.g. for $H_2^+ \rightarrow H^+ + H^+ + e^-$ one can measure $\boldsymbol{p}_1, \boldsymbol{p}_2$ and infer $\boldsymbol{p}_e$ exploiting momentum conservation $\boldsymbol{p}_1 + \boldsymbol{p}_2 = -\boldsymbol{p}_e$. This is used in section 5.2.1.

- For a breakup with one heavy, e.g. a proton, and one light fragment, e.g. an electron, the light fragment takes most of the energy from the kick of the laser.

- The measured fragment momenta contain information about the interaction potential, $U(t, |\boldsymbol{r}|)$, which is present among the fragments. If the interaction potential is known, information on fragmentation coordinates can be extracted.

- For the measurement of photoelectron momenta, the initial momentum spread due to e.g. the target temperature is negligibly small compared to the energy which is gained from the laser-induced breakup.

Having summarized, we turn to the details of the fragment momentum spectrometers which are used for our measurements. In the next subsections, details of the Velocity-Map Imaging Spectrometer (VMIS) which has been used to measure photoelectron momentum distributions (PMDs) after strong-field ionization of Xenon are summarized. Afterwards, we turn to a short introduction on the setup for Ion Target Recoil Ion Momentum Spectroscopy (ITRIMS).

3.3   Velocity-Map-Imaging Spectrometer

The Velocity-Map-Imaging (VMI) spectrometer setup which is used in this thesis, is introduced by comparing it to recent trends in the field VMI spectrometer development. Details of the measurement procedures which are used acquire photoelectron momentum distributions (PMDs) are given later together with experimental results in chapter 3.5 where the off-axis low-energy structure in strong-field photoionization is investigated experimentally and theoretically.
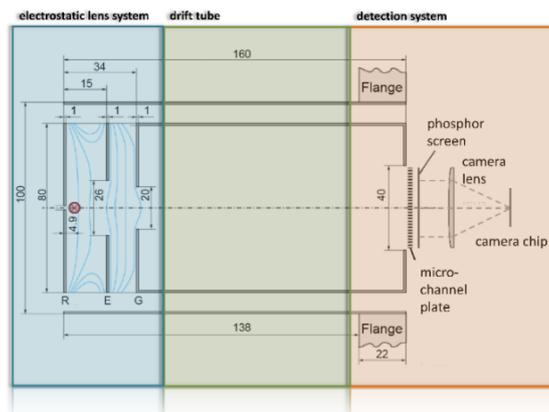
Figure 3.2: Sketch of the used velocity map imaging (VMI) spectrometer (VMIs)

Chief components are coded in color. Distances are given in mm. The chief components, electrostatic lens system, drift tube and detections of a VMI spectrometer are marked by the colors, i.e. electrostatic lens system (blue), drift tube (green) and detection system (orange). The electrostatic lens system consists of three electrodes, repeller (R), extractor (E) and ground (G) here and is used to accelerate charged particles from the red-marked interaction volume towards the detector. Thereby, particles with the same velocity are focused such that they reach the detector at the same time-of light and position. The whole apparatus is part of a vacuum chamber which the laser beam enters and exits through windows. Typically, the apparatus is implemented as a rotational symmetric object with the dotted horizontal line being the axis of rotational symmetry. The laser propagates into the drawing plane. The illustration is similar to [67] [45].

Velocity-Map-Imaging spectrometers (VMIs) are a very flexible method to measure three-dimensional momentum distributions (differential fragmentation rates) of photoions and photoelectrons [65] [66]. The spectrometer relies on using an electrostatic lens system to project charged particles that emerge from an interaction region onto the same position on a two-dimensional detector, if they have the same momentum. Afterwards an Abel inversion is applied in order to retrieve the three-dimensional momentum distribution from the measured two-dimensional projection. Due to the necessity of Abel inversion rotational symmetry is required for the applicability of the method. Thus, it has been limited to linear polarization in its original version due to the lack measurement or discrimination of the TOF. Combination with position- and time-sensitive detectors as well as high-voltage switching technology enable TOF measurement. Thus, modern VMIs have matured to coincidence momentum spectroscopy machines very similar to COLTRIMS, [79] [80]. Without time-sensitive detector, it is possible to extend VMI to light with arbitrary polarization state using tomographic reconstruction methods [81] [82].

A sketch of the used VMIs is shown in Figure 3.2 [45] [67]. The design is pretty simple and very similar to the original design [65]. An electrostatic lens system accelerates charged particles from the red-marked interaction volume towards the detector where a combination of a micro-channel plate and phosphor screen assembly converts the electron signal to fluorescence light whose intensity distribution is then observed by a camera. The intensity of the fluorescence is proportional to the number of charged particles that impact on the detector. The ionizing laser is linearly polarized with its axis aligned such that it lies in the plane of the paper and parallel to the detector surface. Rotational symmetry is fulfilled around this axis. Thus, algorithms for Abel inversion, e.g. [66], can be used to retrieve three-dimensional photoelectron momentum distributions (PMDs) from the measured projections. Cooling of the gas target is not necessary as the initial electron momentum is negligibly small compare to the momenta gained from the laser-induced breakup, see section 3.2.3.

In order to ensure detection of fluorescence signal with low noise and high-dynamic range, the images are recorded using a (12-bit) camera from "QImaging" which is equipped with a proper lens system that images the phosphor screen onto the camera chip. Depending on the sign of the repeller voltage, projections of the momentum distribution of photoelectrons or photo ions can be measured. Measurements are taken in the way that the laser is continuously producing, e.g. electrons, in the interaction volume at the repetition rate of the laser while the camera is recording the intensity profile with an exposure time that is very long compared to the repetition rate of the laser, i.e. several seconds up to half an hour. Combination of several acquisitions with different exposure times to a high-dynamic range image is used to increase the dynamic range in the measurement. In this way, even faint structures such as rescattered electrons can be detected. Details of the procedure can be found here [68] [45].

Under optimal imaging conditions for photoelectrons, energies up to 80 eV are detectable at the energy resolution, which is better than $\approx 1\%$ over the entire energy range. This is achieved for a repeller voltage of $V_R = 10$ kV and a ratio of 0.805 for the ration between repeller and extractor, $V_E/V_R = 0.805$, while V_G is set to $V_G = 0$. The highest detectable electron energy is limited by the size of the detector of 40 mm in diameter and the maximum applicable repeller voltage. Applying a lower V_R and scaling the extractor voltage accordingly allows to observe a smaller energy range with improved energy resolution much like zooming into the PMD.

The spectrometer function, $E = a \cdot V_R \cdot r^2 \cdot$ (eV/kV mm^2), connects the electron energy with the position of the detector. Thereby, $r = \sqrt{x_d{}^2 + y_d{}^2}$, is measured from the center of the phosphor screen. The energy calibration factor, a, has been found to be $a_{th} = 0.02068$ from theoretical simulation of the electron trajectories [67]. However, an experimental determination of a which uses the equal spacing of the energy position of above-threshold ionization peaks generated by 400 nm laser pulses yields $a_{exp} = 0.01713$. This calibration of the energy has to be repeated if another repeller voltage is used. The experimentally determined factor is used to convert the detector positions into velocity and momentum or electron energy respectively.

Several examples for the measured PMDs using described mentioned VMIS can be found in chapter 5 where an off-axis low-energy structures in above-threshold photoionization are investigated experimentally and theoretically.

## 3.4   Ion Target Recoil Ion Momentum Spectroscopy (ITRIMS)

Next, the Ion Target Recoil Ion Momentum Spectroscopy (ITRIMS) setup, which is used to investigate strong-field photoionization of H_2^+ in chapter 5 is introduced by comparing it to a standard COLTRIMS setup first in section 3.4.1. Properties of the ITRIMS, which is operated in Jena, are summarized as an overview in 3.4.2. Details of measurement procedures and relevant experimental effects are detailed in chapter 5 where experimental and theoretical results of strong-field photoionization of H_2^+ by strong infrared laser fields are presented.

3.4.1 Cold Target Recoil Ion Momentum Spectroscopy (COLTRIMS) and Ion Target Recoil Ion Momentum Spectroscopy (ITRIMS)
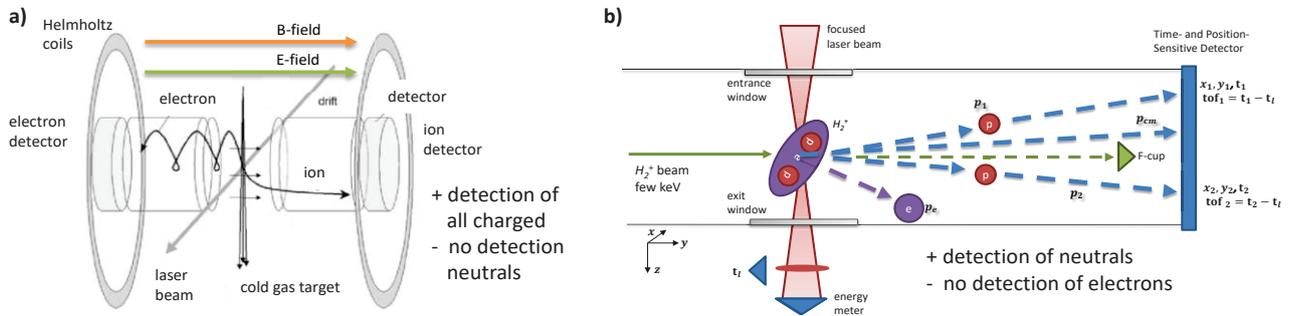
Figure 3.3: Comparison of a setup for standard "COLd Target Recoil Ion Momentum Spectroscopy (COLTRIMS)" [62] with the setup for "Ion Target Recoil Ion Momentum Spectroscopy (ITRIMS)" used here.

A comparison between a standard COLTRIMS setup and the Ion Target Recoil Ion Momentum Spectrometer (ITRIMS) used in the measurement in this work is shown Figure 3.3. In COLTRIMS, a neutral gas-phase target with small initial momentum spread (cold) is placed inside a spectrometer where electric and magnetic fields are used to steer charged fragments from the interaction with the laser towards position- and time-sensitive detectors, typically so-called delay-line detectors (DLD-detectors). Measuring the fragment's impact time and position at the DLD-detectors, together with knowing the spectrometer properties (geometry, distances) and the spectrometer settings (field strengths), allows back calculation of the vector momenta at a time shortly after the interaction with the laser pulse when the fragment is located in the focal region of the laser. Thereby, the small initial momentum spread of the target is very beneficial as it allows one to use the assumption of zero initial momentum in many cases. As neutral fragments don't react to electric and magnetic fields only the momenta of the charged fragments are measured in most cases.

The ITRIMS setup uses the same principle as COLTRIMS. However, a beam atomic or molecular ions with an initial kinetic energy of several keV, $E_{beam} = p_{beam}^2/2m$, is used as the target. Having an energetic ion beam instead of cold neutrals changes a few aspects of the setup. (i) The high initial beam velocity enables detection of neutral fragments, which can typically not be detected in COLTRIMS. (ii) The ion beam density is on the order of 10^4 to 10^6 less dense than a typical cold gas target, which makes measurements with good statistics challenging. (iii) A

combination of (i) and (ii) causes significant issues for the detection of electrons in coincidence with the heavy fragments, i.e. ions and neutrals. (iv) As compared to the COLTRIMS cold jet, the initial velocity of the ion beam target of the ITRIMS, typically leads to a larger initial momentum spread. It leads to a blurring of experimental results, if the momentum of one of the fragments is inferred based on momentum conservation.

Presently a few implementations of ITRIMS world-wide combine the ultra-fast intense laser pulse technology with recoil ion momentum spectroscopy. An overview over existing experimental techniques and setups is given in [21] [70]. Besides contributions from the group of Gerhard G. Paulus from Jena, main groups contributing in this field recently are from Kansas State University around Itzik Ben-Itzhak and from Frankfurt around Reinhard Dörner. Particularly, noteworthy is the setup used in the Dörner group recently [83]. In this setup, also the momentum of the electron after strong-field ionization of a beam of H_2^+ molecules has been detected in coincidence with the two proton fragments.

3.4.2 Ion Target Recoil Ion Momentum Spectroscopy (ITRIMS) in Jena

A sketch of the ITRIMS setup is shown Figure 3.4. The grey cylindrical tube in the center of the figure which contains several colored elements with labels as small letters (a-o) represents the ultra-high ($P < 10^{-9}$ mbar) vacuum chamber. Starting from the ion source, (a) to (m) label components that are responsible for creating a well collimated beam of atomic or molecular ions, which crosses the laser beam at angle of 90 degrees in the interaction region between the blue plates with the labels (m) and (n). The microchannel-plate delay-line detection system can be found further to the right at the label (o). Elements outside the tube with (1) to (7) illustrate the optical components of the setup.

Creation of atomic or molecular ions is done using electron impact ionization in an electric discharge within a Duoplasmatron ion source (a). This source facilitates creation, extraction and acceleration to kinetic energy of several keV. Afterwards an Einzel lens (b) (arrangement of static electric fields) and a deflector (c) collimate and steer the ion beam through the chamber. The differential pumping stage (d) separates the section for ion generation with higher pressure from the region with lower pressure in the rest of the apparatus. Another set of a deflectors (e) and an Einel lenses (f) guide the beam through a Wien filter (g). It enables the selection of a desired q/m-ratio such that measurements with different isotopologues, e.g. H_2^+ and D_2^+, are possible. At the same time, the Wien filter acts as a filter for the velocity of the ion beam. Afterwards, the Einzel lens (h) and deflectors (i)-(k) steer the beam through apertures with an adjustable size, (l) and (m), which are used to limit the initial momentum spread of the beam along its transversal direction, and are thus, important for the achieved momentum resolution. The interaction region lies inside an ion spectrometer (n). Together with an additional transversal static electric fields, it ensures separation fragments with different charge and mass in time and space on the position and time- sensitive detector (o). A faraday cup shortly before the detector prevents the detector from being illuminated by the ion beam directly, see Figure 3.4 b) also.

The optical setup facilitates controlling of the intensity using a motorized half-wave plate (1) (appendix A1), a germanium plate that acts as reflective polarizer (2) and a high-contrast transmittive polarizer (3). The high-contrast polarizer ensures that the direction of the linear polarization in the target remains constant while rotating the half-wave plate controls the intensity. The laser beam enters the chamber through a vacuum window after

focusing with an off-axis parabola, (4), and exits it through a second vacuum window and after the interaction with the ion beam. At the exit, beam splitter (5) sends one fraction to a photo diode (7), which provides the trigger for detecting of the time-of-flight signals, that the basis for reconstruction of the fragment the. The other fraction of the laser beam hits the head of a every single-shot energy meter (6). It delivers a value for the energy of every single laser shot, L, which is save together with all other measured data. Together with characterization of the focal spot and pulse duration the values is used to tag the pulse energy respectively the peak intensity for every single laser shot.

The measurement principle for determination of fragment momenta is illustrated in Figure 3.4 b). Strong-field fragmentation of H_2^+ is used as an example but also other target species can be used in a similar manner. The ion has an initial velocity parallel to the z-axis of the coordinate system and travels from the left to the right. The focused laser beam comes from the top and goes to the bottom. It crosses the ion beam at the position where the purple ellipse with the two red circles are drawn. The purple ellipse with the two red circles is representative for the constituents of the H_2^+ molecule, i.e. one electron, (e) (purple ellipse) which is shared by two protons (p) (red circles). Depending on whether the laser ionizes or dissociates it, the molecule breaks up into an electron and two protons, $H_2^+ \rightarrow e^- + H^+ + H^+$, with the momenta, $\boldsymbol{p}_e$, $\boldsymbol{p}_1$ and $\boldsymbol{p}_2$ or into a hydrogen atom and a proton, $H_2^+ \rightarrow H + H^+$ with momenta, $\boldsymbol{p}_H$, _p. Due to the intensity distribution in the volume, both reactions occur simultaneously during the experiment and thus, the particles and momenta of both reaction channels are detected.
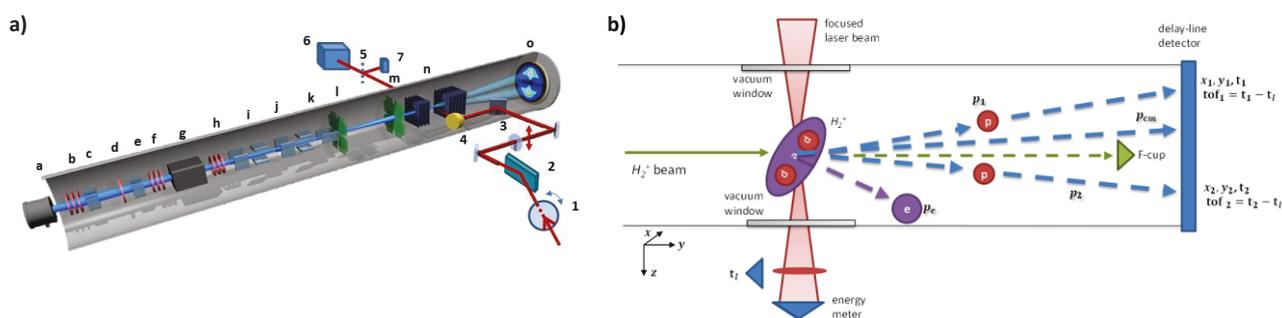
Figure 3.4: ITRIMS setup and illustration of momentum detection scheme for the case of ionization

a) ITRIMS setup. Letters label elements of the ion beam apparatus while numbers label the optical components of the setup, see text for the details. a - Duoplasmatron ion source, b – Einzel lens I, c- deflectors I, d – differential pumping stage, e - deflectors II, f –Einzel lens II, g – Wien filter, h - Einzel lens III, i to k - deflectors III, l - aperture I, m – aperture II, n – ion spectrometer, o – detector, p –trigger-diode, 1 - $\lambda/2$-plate, 2- Ge-plate, 3-High-contrast polarizer, 4-Off-axis parabola f=15 cm, 5 – beam splitter,6 – energy meter b) Detection scheme. The ion beam comes from the left an crosses the laser beam at an angle of 90 degrees. Due to the initial velocity of the ion beam, the fragments form the laser-ion interaction continue to fly towards the position and time-sensitive delay-line detector. Created photo electrons, however are too fast which is related to large deflections angles. Thus, they are not detected. (e) – electron, (p) – protons, F-cup – faraday cup to block direct exposure of the detector by the ion beam.

Figure 3.4 b) is drawn for the example of ionization. The protons hit the detector at the positions, x_1, y_1 and x_2, y_2 after the time-of-flights, tof_1 and tof_2, after the laser has triggered the measurement by arriving at the trigger diode at the time t_t. Measurement of the corresponding quantities for dissociation is done analogues. The measured

quantities, x_1, y_1 and x_2, y_2 as well as tof_1 and tof_2, are the basis for the backcalculation of the momenta at the end of the laser pulse, [21] [70] [69]. In contrast to the heavy fragments such as protons, atoms or ions, free electrons with the momentum, p_e, which result from the interaction between ion beam and the strong laser are too fast to hit the detector and cannot be detected in this setup. In addition, it is challenging to distinguish electrons from ionization of the background gas from ionization of the ion target due to the low density of the ion beam, see [83].

Data acquisition uses an 8-bit analog to digital converters (ADC) from "RoentDek", Frankfurt which is read out and controlled by a personal computer using the software "Cobold" ("RoentDek"). The whole MCP-DLD system including fast ADC electronics achieves a spatial resolution of better than 100 µm and a temporal resolution of better than 100 ps for the measurement of impact position and TOF (RoentDek). "Cobold" is used during the measurement for optimization as well as for saving the raw data after some preliminary filtering. Calculation of the three-dimensional momenta from the measurement of positions TOFs as well as the application of coincidence conditions to filter the data from noise or for specific events is done using "MATLAB" after exporting the raw data from "Cobold", see [21] [70] [69].

The final result of the measurement are two lists of triples, $\{p_1, p_2, L\}_i$, of i identified valid ionization and k dissociation events, $\{p_{H^+}, p_H, L\}_k$. Each of the triples contains momenta of the two protons, p_1, p_2 for ionization respectively of a H-atom and a proton, p_{H^+}, p_H, for dissociation as well as the corresponding value of the peak intensity, L, which got calculated using the tagged laser energy together with characterization of the focal spot and pulse duration. All momenta are given within the center of momentum frame of all dissociation events. The linearly polarized laser is aligned parallel to the x-axis of the coordinate system. Calculation of one or more dimensional distributions and spectra using MATLAB enable the analysis of differential ionization or dissociation rates.

An example of projected two-dimensional distribution of ionization and dissociation events is shown in Figure 3.5. In the plot, a histogram of ionization and dissociation events is shown together as a projection in the plane of the linear polarization.
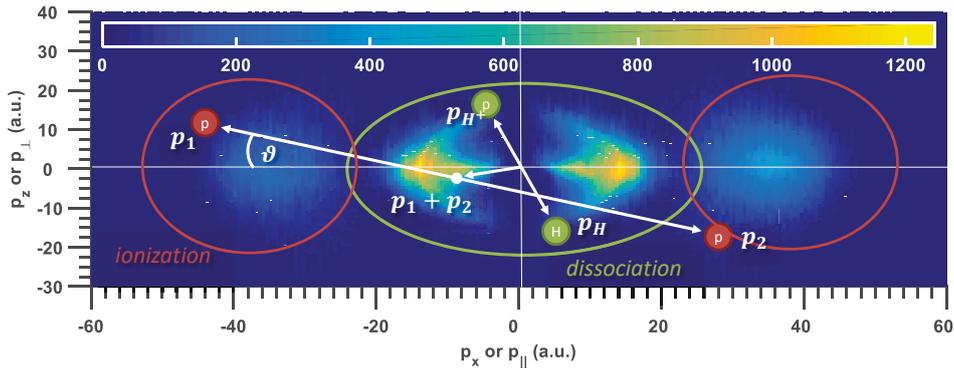
Figure 3.5: Illustration of typical measurement result for fragmentation of H_2^+ by a strong laser field

The figure shows a two-dimensional histogram of events after strong-field fragmentation of a H_2^+ ion beam target. A projection into the $p_x - p_z$-plane, i.e. in the plane of the linear polarization of the laser, is shown. The polarization of the laser is parallel to p_x. Ionization events have large momenta, i.e. larger kinetic energy realease (KER) than dissociation events. Thus, they are found in the outer region of this plot while dissociation events are found in the inner region.

To summarize, COLTRIMS allows to perform momentum spectroscopy of charge fragments (neutrals are not detected) including electron and ions which result from laser-induced fragmentation processes starting from cold neutral gas jet targets with high density. The ITRIMS setup enables investigation of strong-field laser-matter interaction starting from ion targets. Due to the initial velocity of the ion beam, detecting electrons in coincidence with ions is challenging and typically not done. However, the initial velocity of the ion beam enables detection of the neutral fragments, which is typically not the case in COLTRIMS setups. Both measurement setups, ITRIMS and COLTRIMS, are complementary techniques.

3.5   Conclusion and Outlook

In this chapter, we have discussed momentum spectroscopy of laser-induced fragmentation processes by reviewing classical kinematics in setups for momentum spectroscopy of laser-induced fragmentation processes first. The consideration could reveal several aspects which are relevant for the experimental setups of the Velocity-Map-Imaging (VMI) spectrometer and for the Ion Target Recoil Ion Momentum Spectroscopy (ITRIMS). Both setups are used to investigate strong-field photoionization atoms and ion in the following chapters.

For future work on the VMI and the ITRIMS setups in Jena, presently a VMI spectrometer which enables the measurement of higher photoelectron energies is under construction. The ITRIMS setups is routinely operated with atomic or molecular ions as targets, some approaches for, e.g. reduction of the measurement time in section 5.2.3 of chapter 5.

4   Off-Axis Low-Energy Structures in Strong-Field Photoionization

4.1   Introduction and Outline

Since the observation that an atom exposed to intense fields can absorb more energy than necessary for ionization above the single photon threshold [1], i.e. so-called above-threshold ionization (ATI) in 1979, experimental and theoretical work has revealed several remarkable features of strong-field photoionization (SFI) of atoms. Without the aspiration of giving a complete list, early examples are the observation of ponderomotive effects [84] and the discovery of the plateau at high photoelectron energies [2]. More recent examples are frustrated tunneling ionization [5], carpet-like patterns in the photoelectron momentum distribution (PMD) close to right angle to the polarization [85]. For comparatively long wavelength, the so-called low-energy structures (LES) [9] [34] and spiderlike interference features, which are interpreted as holograms [86] [87] [88], as well as features at very low [89] and even practically at zero kinetic photoelectron energy [35] caught the attention of researchers. Also, applications of SFI have matured over the past almost 40 years, e.g. a stereographic analysis of the PMD at high photoelectron energy emitted in narrow cone around the polarization axis of the linearly polarized laser is regularly used for single-shot measurement of carrier-envelope phase (CEP) and pulse duration of few-cycle laser pulses. If SFI is done using laser fields with short-wave infrared (SWIR) wavelength, the analysis of the PMDs at high photoelectron energies can be used to extract electron-ion scattering potentials for atoms [90] using so-called laser-induced electron diffraction (LIED) [32]. Application of LIED to SFI of small, aligned molecules recently demonstrated time-resolved imaging of bond-breaking dynamics in small molecules [33].

Here, we investigate SFI by SWIR fields into states with low electron momentum parallel to the linear polarization of the laser field. To this end, the velocity map imaging (VMI) technique is used to measure photoelectron momentum distributions (PMDs) from strong-field photoionization of Xenon by laser fields with durations of many and few optical cycles. The measurement setup and procedures are introduced in subsection 4.2. Typical features of the PMD and observations from the measurement are summarized in subsection 4.3. In subsection 4.4, we introduce the implementation of the semi-classical model of strong-field photoionization. The results of the simulation are compared to experimental observations qualitatively in subsection 4.5. Subsection 4.6 summarizes the results of the experimental and theoretical work of the chapter.

4.2   Measurement of Photoelectron Momentum Distributions

Figure 4.1 provides a sketch the experimental setup including the beam path for the laser and the vacuum apparatus, which contains the VMI spectrometer. Given peak intensities are based on the measurements of pulse duration, focal spot and on measurements of the pulse energy using an energy meter. The estimation accounts for additional losses that occur due to the transmission of the entrance window. For the FROG measurements, the amount of dispersion in the beam path to the FROG and the VMI are made equal.

Projections of the PMDs are measured and processed as detailed in [45]. In short, for each setting of laser parameters, a high-dynamic range image is recorded, background subtraction is done and the inversion algorithm [91] is applied. The inset, (a) to (d) in Figure 4.1, illustrate the data processing after recording of the high-dynamic range image. An example of a final measurement result is shown by the greyscale image in (d). It is a cut through the $p_z = 0$ plane of the three-dimensional PMD. The linear polarization of the laser is oriented as indicated in the inset. Typically, the logarithm of the PMD is shown.
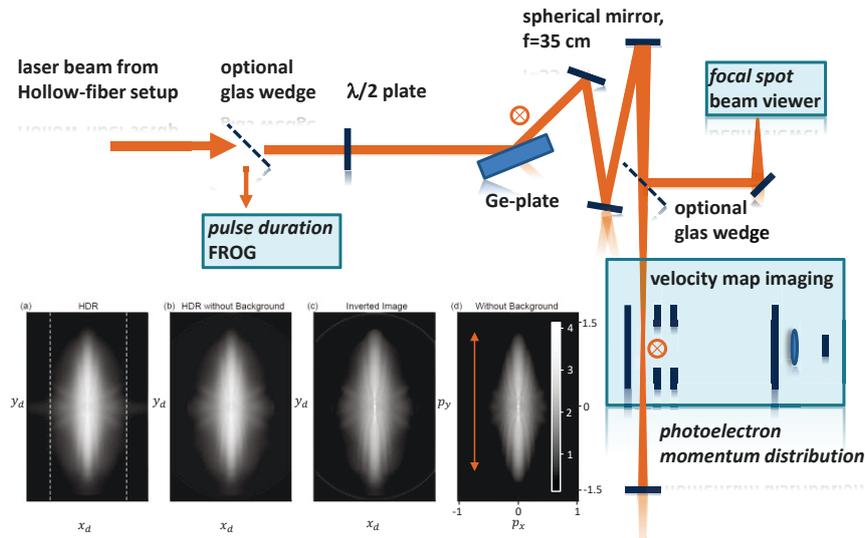
Figure 4.1: Sketch of the experimental setup which is used to measure PMDs

The laser beam comes from the hollow-fiber setup. The front-surface reflection from an optional wedge is used to attenuate the beam in order to allow pulse characterization using a home-built FROG setup. Controlling the pressure inside the hollow fiber and adjusting the dispersion by adding/removing glass plates from the beam path allows one to measure PMDs with different pulse duration. The $\lambda/2$- plate in combination with the Ge-plate (acts as polarizer) allows to change the peak intensity without changing the focal volume by changing the pulse energy in the target. Focusing with a focal length of $f = 35$ cm leads to peak intensities up to a few 10^{14} W/cm^2. The second optional wedge is used to characterize the focal spot using the Si-based CCD. The inset of images, (a)-(d), illustrate the data processing. The arrow in (d), which is an example of a final experimental result, indicates the orientation of the linear polarization. It represents a cut through the PMD [45].

4.3   Photoelectron Momentum Distributions from Strong-Field Ionization

4.3.1 Ty
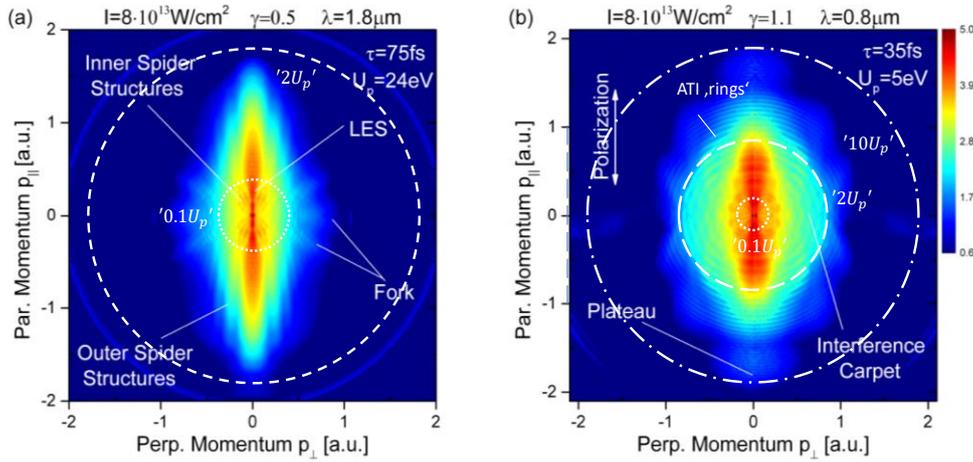
Figure 4.2: Comparison of PMDs from strong-field ionization of Xenon from long pulses of different wavelength The wavelength is 1.8 μm shown in (a) and 0.8 μm in (b) [45]. As typical, the logarithm of the photoelectron yield is shown. The distributions exhibit significant differences, particularly different spectral features are more or less pronounced depending on the laser parameters. The circles mark momenta of characteristic energies, i.e. the $p = \sqrt{2 \cdot 2U_p}$ (dashed circles) in (a) and $p = \sqrt{2 \cdot 10U_p}$ dot-dashed circle in (b) only. A short survey of the marked spectral features is given in text.

As Figure 4.2 illustrates, PMDs from strong-field ionization are very beautiful complex patterns, which contain a huge number of spectral features. Most of the features are sensitive to laser parameters, such as the pulse duration, intensity and wavelength and the target species [92] [93]. Figure 4.2 displays measured data at a wavelength of 0.8 μm and 1.8 μm. The target gas is Xenon, the peak intensity is $I \approx 8 \cdot 10^{13}$ W/cm^2, linear polarization has been used in both cases. Several characteristic spectral features are marked.

Such momentum distributions can be reproduced by direct numerical integration of the time-dependent Schrödinger equation (TDSE) within a single active electron approximation using modern computers, e.g. [92] [93]. However, this typically requires a meaningful single active electron potential and thus, naturally excludes multi-electron effects that might play a role. In addition, such calculations, particularly in all three spatial dimensions and potentially for laser fields with arbitrary polarization state, became possible only recently, and are computationally very demanding. Further, direct integration of TDSE delivers insight into the interaction mechanism only if meaningful observables are evaluated during the calculation and are analyzed later. In that sense, numerical integration of the TDSE can be viewed as a numerical experiment. Alternatively to the direct TDSE approach, several more analytical theories have been developed to describe strong-field ionization. Examples are the simple man's model [11], [94] [12] or its quantum mechanical version, the strong-field approximation [95] [96]. Although these models employ several approximations and might yield worse agreement than solving the TDSE, they have been invaluable particularly in the early days of the field. They are able to reproduce characteristic features and provide

detailed insight into the interaction as the ingredients are electron orbits, which have an intuitive interpretation. Based on these orbits, characteristic features in the PMDs can be identified and assigned to characteristic processes that take place during strong-field ionization. An overview of these spectral features is given next.

First, the rings in Figure 4.2 mark the classical cut-off of electrons with momenta of up to $p_{max\ direct} = \sqrt{2 \cdot 2U_p}$ (dashed line in a) and b)), $p_{max\ forwardscatter} = \sqrt{2 \cdot 0.09\ U_p}$ (dotted line in a) and b)) and $p_{max\ backscatter} = \sqrt{2 \cdot 10U_p}$ (dashed-dotted line in b) only). $p_{max\ backscatter}$ is marked in b) but not marked in a) as this momentum is too high to be measured with the used VMI apparatus for the longer wavelength. These features are connected to the highest electron energy of three different classes of electron trajectories: i) direct trajectories, ii) forward scattered trajectories and iii) backward scattered trajectories. Direct trajectories leave the vicinity of the ion without being driven close to it at some time later in the field. As is shown later, according to the classical model, they can reach energies up to $2U_p$. The other two classes are driven close to the ion by the field and thus, scatter elastically with it. This changes the electron's direction of escape and allows a range of momenta from relatively low to very high, i.e. $p_{max\ forwardscatter} = \sqrt{2 \cdot 0.09\ U_p}$ and $p_{max\ backscatter} = \sqrt{2 \cdot 10U_p}$ depending on the scattering direction.

First evidence of elastic scattering effects in SFI have been observed at high energies [2], which is typically referred to the high-energy plateau. It appears parallel to the laser polarization and is marked in Figure 4.2 b). However, as recently found and discussed later, scattering does not only occur in backward direction but in principle in any direction. Thereby, forward scattering is a somewhat special case as it can lead to relatively low final electron energies and to peaked features in the PMD due to a bunching mechanism as will be shown later. These low-energy structures (LES) are marked in a) and b). They are particularly prominent if long laser wavelength is used. The LES effect has attracted a lot attention since the availability of long-wavelength laser sources [9] [34] [97] [98] [99]. An off-axis extension of these features is marked by "Fork" in (a) and will be discussed in detail below [10].

Second, there are these ring structures that are particularly prominent in Figure 4.2 (b). They are marked with "ATI-rings" and are a clear signature of quantum effects in strong-field ionization, which is one of the first features that was observed in strong-field ionization [1]. They are peaks in the photoelectron yield at energies that are separated by one photon energy. The structure is also present in a). However, it is washed out as the photon energy is almost smaller than the energy resolution of the VMI apparatus for this wavelength. Phenomenologically, these peaks could be viewed as the multi-photon version of Einstein's photoelectric effect where energy of the photo electron is simply, $E_{Ph} = I_p - n \cdot \omega\hbar$, with I_p being the ionization potential of the target, and n being the number of absorbed photons. From the perspective of quantum orbits/electron trajectories, the peaks occur due to the interference of electron trajectories which start at different times during the laser field. The feature, which is marked by the interference carpet [85], is closely linked to this explanation slightly modified for electron emission with zero longitudinal momentum.

Third, there are the spider structures in a), which are particularly prominent for long wavelength [100] [101]. Similar to the "ATI-rings" the explanation for these features lies in an interferences effect of electron bursts that are emitted at different times during the laser pulse and go along different electron orbits. Sometimes, they are interpreted as holograms between direct electron trajectories, which leave the vicinity of the ion without scattering, and rescattered electron trajectories, which come close to the ion and scatter before they reach the detector.

4.3.2 Momentum Distributions at a Few Wavelength from Xenon
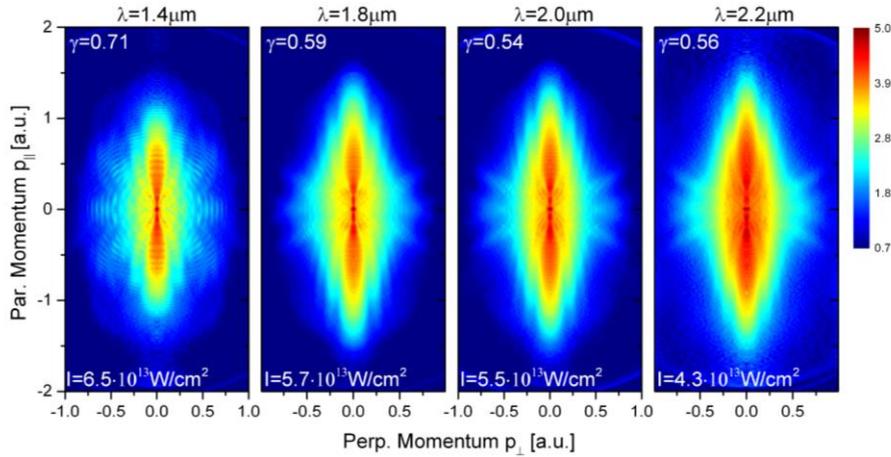
Figure 4.3: Logarithm of PMDs of Xenon from long pulses with different center wavelength.
Laser pulses from the signal and the idler beam of the TOPAS have been used [45]. The peak in each of the measurement is $I \approx 5 \cdot 10^{13}$ W/cm^2. Interesting is the fork-like structure which occurs close to right angle to the polarization axis. It becomes more prominent the longer the laser wavelength.

Figure 4.3 shows PMDs from SFI of Xenon in the signal and idler range of the TOPAS for intensities around $I \approx 5 \cdot 10^{13}$ W/cm^2 and linear polarization. As the detection range of VMI is limited to energies below 80 eV, only the energy region of direct electrons is observed. Increasing the wavelength leads to higher photoelectron energies and thus to a wider PMD. This is expected from the scaling of the $2U_p$ cut-off with wavelength, $U_p \sim I\lambda^2$. In addition, the longer the wavelength, the worse the visibility of ATI peaks becomes. The observation can be attributed to the fact that the separation of ATI peaks is proportional to the laser frequency. Thus, the visibility of ATI peaks decreases for increasing wavelength until they are completely washed out by the limited momentum resolution of the VMI spectrometer. An eye catching feature are these prominent prongs of a fork-like structure, which appear close to right angle to the laser polarization axis of the laser. They are the more pronounced, the longer the wavelength becomes and even contain interesting interference features if the momentum resolution of the spectrometer is sufficient to resolve them, see e.g. the 1.8µm or the 2.0 µm measurement. These features are similar to the ATI peaks less visible the longer the wavelength.

Similar fork-like structures have has also been observed in an experiment where meta stable Xenon ($I_P = 3.8$) is ionized by a 7µm-laser pulses from an infrared free-electron laser [100] at significantly lower intensity of $I \approx 5 \cdot 10^{11}$ W/cm^2. The major experimental and theoretical results of this work are summarized in Figure 4.4. The overall shape is found to be very similar to the observations, which were made in the PMDs from the table-top experiment in Figure 4.3 where the intensity is high enough to allow the use of Xenon atoms in the ground state ($I_P = 12.13$) as the target. The performed TDSE and coulomb-corrected strong-field approximation [102] [103] simulations also shown in Figure 4.4 reproduce the measurement including the off-axis features.

Altogether, Figure 4.3 and Figure 4.4 brought an interesting off-axis fork-like structure to our attention, which exists over a wide range of parameters in SFI by SWIR fields and is reproduced by direct integration of the TDSE and the coulomb-corrected strong-field approximation.
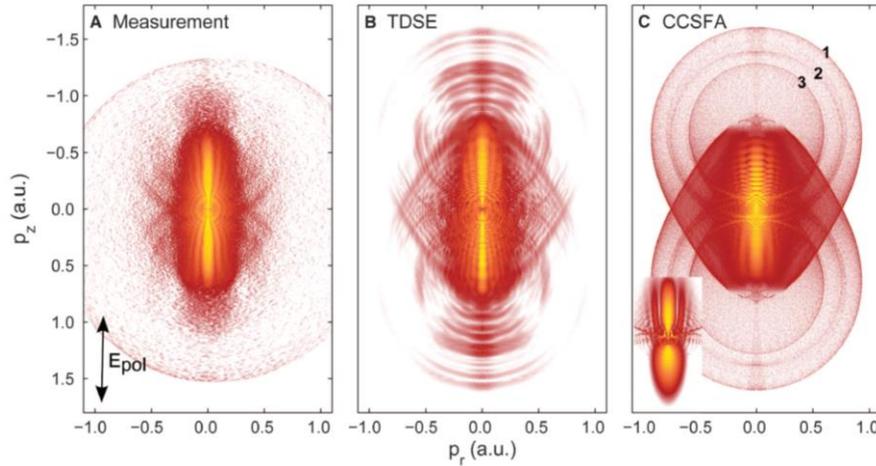
Figure 4.4: PMDs from metastable Xenon ionized by 7 μm laser at a peak intensity of $I \approx 5 \cdot 10^{11}$ W/cm²

This figure is taken from the original publication by [100]. The experimental and theoretical results in this work revealed a very similar structure close to right angle to the polarization axis. However, in this experiment laser pulses from an infrared free-electron have been used. These lasers can have very long wavelength but typically have a lot longer pulse duration than the table-top measurements presented here.

4.3.3 Momentum Distributions from a Long Pulse and Few-Cycle Pulse from Xenon

Here we compare PMDs from SFI of Xenon produced by a laser field with many-cycle duration with the PMD produced by a few-cycle pulse.

Figure 4.5 shows the logarithm of the PMD from strong-field ionization for Xenon generated by a 75-fs pulse and a 12-fs pulse at a center wavelength of 1.8 μm. The peak intensity is $I \approx 8 \cdot 10^{13}$ W/cm² for both cases. Previously discussed features that are particularly prominent are labeled in a) again. The color bar is clipped on the high-yield side in b) and d) in order to emphasize the three pronged structure that appears at close to a right angle to the polarization axis. Almost all features of the PMD are washed out if ionization is caused by the few-cycle pulse, reminiscent of the ATI peaks, the spider structure is a lot less pronounced and the fork changes from a prong to a to a smooth distribution. Thus, the fork-like structure is almost certainly due to rescattering electron orbits that travel for long times in the laser field and which are naturally not supported by a few-cycle laser pulse.

Figure 4.6 e) and f) shows simulations of strong-field photoionization of the experiment by Dejan Milosevic [10] for parameters that are representative for the experimental conditions. These simulations use the so-called improved strong-field approximation (iSFA) [104]. It is the quantum mechanical formulation of SCM of strong-field ionization. In contrast to standard strong-field approximation (SFA), not only direct quantum obits are taken into account but also scattered quantum orbits are used. Figure 4.5 e) is calculated for an infinitely extended monochromatic plane wave (CW) while Figure 4.5 f) is for a finite pulse of five optical cycles total duration (11 fsFWHM) with a cos² envelope and averaged over the carrier-envelope phase. Focal averaging is taken into account in the simulation. The fork feature is qualitatively clearly reproduced for the cw pulse and reducing the pulse duration washes it out as observed in the measurement.
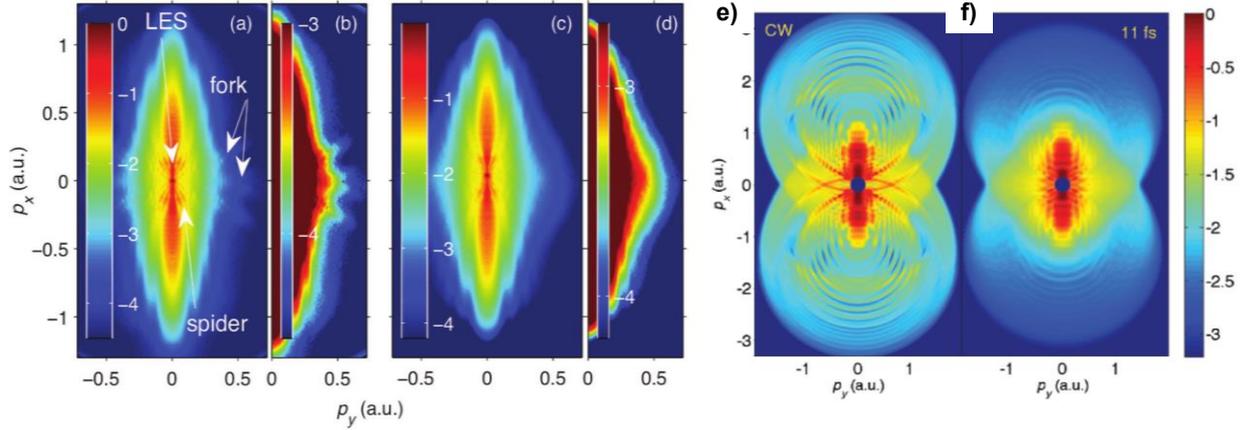
Figure 4.5: Measured and simulated logarithm of PMDs from strong-field ionization of Xenon

For the long pulse a)-b), e) and the short pulse c)-d), f). The center wavelength is 1.8 μm. In a), several feature which are characteristic for long wavelength are marked. The color bar in (b) is clipped on the high-count rate side in order to emphasize the fork-like structure close to right angle to the laser polarization. This structure is strongly smeared out in c) and d), where the short pulse is used. Peak intensity in the experiment a)-d) is $I \approx 8 \cdot 10^{13}$ W/cm^2 compared to $\approx 5 \cdot 10^{13}$ W/cm^2 for the simulations in e) and f). The simulation is volume averaged and uses the improved strong-field approximations theory (iSFA) with both direct and rescattered electrons. As in the experiment, the fork structure is washed out [10].

A more detailed investigation of the influence of the pulse duration based on the experimental data is shown Figure 4.6 where the photoelectron spectrum for an emission direction of $\pm 1°$ around the laser polarization axis and electron energies up to 50 eV (roughly $2U_p$, $U_p = 24$ eV) is compared for ionization by a long and a short pulse in Figure 4.6 a). The spectrum has been generated from the measured PMDs. The vertical shift is artificially in order to improve visibility. For both cases, long pulse and short pulse, the LES peaks at energies below roughly $0.09\, U_p$ (2.16 eV) are visible. For the few-cycle pulse, the first-order LES peak moves towards smaller energy, which is consistent with a recently published experimental and theoretical study of the pulse duration dependence of the LES [99]. In addition, the height of the peak at very low energy (<1 eV) is suppressed. Figure 4.6 b) compares the electron yield as function of emission angle for a fixed electron momentum of $p = 0.75$ au. The polarization axis of the laser is points towards 180° here. While a regular modulation of the electron yield as function of the emission angle is observed for the long pulse, this modulation is suppressed for the case of the few-cycle pulse.
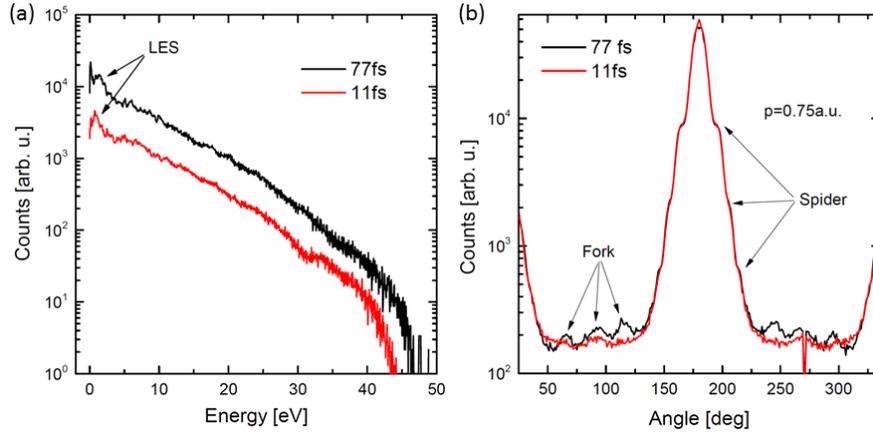
Figure 4.6: Details of the comparison between PMDs from ionization with a long pulse and few-cycle pulse
a) Photoelectron spectrum parallel to the laser polarization axis [45]. b) Angular distribution of photoelectrons with an energy of $p = 0.75$ [45].

4.4   Semi-classical Model of Strong-Field Ionization

Altogether, the previous chapter on measurements of PMDs from SFI by an SWIR and IR laser fields revealed an off-axis low-energy structure that is more pronounced the longer the wavelength. Similar features have been previously observed in ionization experiments with even longer driving lasers from an IR free-electron laser. For this experimental parameters, the feature has been reproduced by direct integration of the TDSE and coulomb corrected SFA theory. For the experimental parameters here, simulations based on improved SFA theory qualitatively reproduced the off-axis LES as well it's previously unobserved sensitivity to the pulse duration of the used laser pulse. Particularly, it was found that off-axis LES structure is supported by improved SFA (iSFA) theory, which takes into account direct and rescattered electron trajectories. Motivated by the fact that the iSFA is basically the quantum mechanical version of the semi-classical model (SCM) on strong-field ionization, here we aim to trace the origin of the off-axis LES and its sensitivity to the pulse duration to rescattered electron trajectories within SCM. To this end, the SCM will be augmented by rescattering at multiple returns. Further, details of the elastic scattering cross-section are taken into account. As demonstrated, the improved SCM supports on- and off-axis low energy as well as on- and off-axis high energy features in the PMD including their susceptibility to the pulse duration. Further, it allows to trace the common origin of the features to rescattering dynamics between the field-driven photoelectron and the parent ion.

4.4.1 Overview

The semi-classical model (SCM) [11] [12] has been extremely influential and become one of the backbones in the field strong-field interactions and attosecond science. It described SFI as three step process: (i) tunneling ionization in quasi-static field; (ii) propagation and thereby acceleration of classical electron trajectories in the laser field; (iii) an electron-ion interaction if trajectories lead back into the range of the potential. The most prominent options for

the interaction at (iii) are: a) recombination to the ground state, which leads to the emission of high harmonics (HHG); b) an inelastic collision between electron an ion that causes a knock-out of a second or several electrons known as non-sequential ionization (NSDI); c) elastic scattering between electron and ion that is responsible for the generation of low- and high-energy on- and off- axis electron momenta as will be demonstrated.

Here, we construct the PMD, $W(\boldsymbol{p})$, i.e. the probability for finding an electron with momentum, $\boldsymbol{p}$, after ionization of an atom by the field, $\boldsymbol{E}(t)$, along the lines of the SCM. The approach that we use for this purpose is similar to what has been done in refs. [13] [105]. However, the model here goes in slightly different direction, particularly in the method of how a weight is put onto the contribution of rescattered trajectories, which have a long travel time. Specifically, the PMD, $W(\boldsymbol{p})$, is composed of the weighted contributions from direct and scattered trajectories that lead to the final momentum $\boldsymbol{p}$, i.e. $W(\boldsymbol{p}) = W_{dir}(\boldsymbol{p}) + W_{sc}(\boldsymbol{p})$. Each of the contributions, is the sum of ionization weights, $W_{ion}(t_s^k)$, from k starting times, t_s^k, in the laser field that lead to the same final momentum, $\boldsymbol{p}$. For the direct contribution, i.e. for the contribution of trajectories that do not rescatter, this means $W_{dir}(\boldsymbol{p}) = \sum_k W_{ion}^k(t_s^k, \boldsymbol{p})$. The procedure is slightly more complex for scattered contribution, $W_{sc}(\boldsymbol{p})$. Each trajectory with the starting time, t_s^i, has the possibility to return at j return times, t_r^j. Thus, one has to sum the contributions from each combinations of starting times, t_s^i, and return times, t_r^j, which lead to the final momentum, $\boldsymbol{p}$, i.e. $W_{sc}(\boldsymbol{p}) = \sum_{ij} W_{ion}^{ij}(t_s^i, t_r^j, \boldsymbol{p})$. As it is shown below, each of the contributions, $W_{ion}^k(t_s^k, \boldsymbol{p})$, and $W_{ion}^{ij}(t_s^i, t_r^j, \boldsymbol{p})$ are thereby modeled in the form of a product where each factor represents an aspect of the interaction.

A central aspect of our construction of the PMD is to establish the connecting between the ionization time, t_s, and the final momentum $\boldsymbol{p}$. For the direct contributions, this can be approximately done by neglecting the influence of the binding potential and finding the trajectory by integrating Newton's equation of a free electron in the laser field. For scattered trajectories, the influence of the binding potential is taken into account by deflecting the potential-free trajectories into an angle, θ, upon return at some time after t_s with the return velocity v_r. Details of the potential, e.g. its shape, are then incorporated using a scattering cross-sections that weights the deflection angle, θ, independence of, v_r. Thereby, we account for proper normalization of the relative weights of earlier and later returns.

In order to provide and discuss the details of the model, we start by direct and scattered electron trajectories in section 4.4.2. The contribution of direct trajectories to the PMD, $W_{dir}(\boldsymbol{p})$, is constructed in section 4.4.3. The construction of the contribution from rescattering, $W_{sc}(\boldsymbol{p})$, is detailed in 4.4.4. The results of the model calculations are illustrated and analyzed in section 4.4.5. A comparison between the model and the measurement is presented in section 4.5. The results of the chapter are summarized in section 4.6.

4.4.2 Direct and Rescattered Trajectories in the Laser Field

Newton's equation of motion for a classical electron, in a linearly polarized field, $\boldsymbol{E}(t) = E(t)\boldsymbol{e_z}$, with the vector potential, $\boldsymbol{A}(t) = A(t)\boldsymbol{e_z} = -\int_{-\infty}^{t} E(t')dt' \, \boldsymbol{e_z}$, is $\ddot{\boldsymbol{r}}(t) = -\boldsymbol{E}(t)$. Atomic units are used unless stated otherwise. Integrating it from the starting time, t_s, until t, yields

$$\dot{\boldsymbol{r}}(t, t_s) = \boldsymbol{v}(t, t_s, v_\perp) = \boldsymbol{A}(t) - \boldsymbol{A}(t_s) + \boldsymbol{v}_0 = \boldsymbol{A}(t) - \boldsymbol{A}(t_s) + \boldsymbol{v}_\perp. \tag{4.1}$$

The initial velocity, $\boldsymbol{v}_0$, is decomposed into components parallel and perpendicular to the linear polarization of the ionizing laser field, $\boldsymbol{v}_0 = v_\parallel \boldsymbol{e}_\parallel + v_\perp \boldsymbol{e}_\perp$. As it is typical for tunneling, $v_\parallel = 0$, is used in (4.1). A second integration leads to the position

$$\boldsymbol{r}(t, t_s) = \boldsymbol{\alpha}(t) - \boldsymbol{\alpha}(t_s) + (t - t_s)(\boldsymbol{v}_\perp - \boldsymbol{A}(t_s)). \tag{4.2}$$

Thereby, it is assumed that the trajectory starts at the position of the ion that is placed at the origin, $\boldsymbol{r}_0 = 0$. The influence of the ionic potential has been ignored completely. Also, the motion of the ion in the field is neglected as it is small, see equation (3.7). The quantity, $\boldsymbol{\alpha}(t)$, denotes the integral over the vector potential, $\boldsymbol{\alpha}(t) = \int_{-\infty}^{t} \boldsymbol{A}(t')dt'$ [106].

Scattering is included if equation (4.2) leads back close the potential of the ion at some return time, $t_r^j > t_s$. For such a return, the trajectory has to fulfill the condition of return,

$$\boldsymbol{r}\left(t_r^j, t_s, \boldsymbol{v}_\perp = 0\right) \approx 0. \tag{4.3}$$

For linear polarization, $\boldsymbol{v}_\perp = 0$ has to be used as this is the only possibility to fulfill (4.3) strictly a linearly polarized field. A graphical solution of (4.3) can be formulated by the condition, $\boldsymbol{\alpha}\left(t_r^j\right) = \boldsymbol{\alpha}(t_s) + \left(t_r^j - t_s\right)\boldsymbol{A}(t_s) = \boldsymbol{\alpha}(t_s) + \left(t_r^j - t_s\right)\partial\boldsymbol{\alpha}/\partial t|_{t_s}$, [107] [108]. This formulation reflects that a return can be found by searching for times where the tangent on $\boldsymbol{\alpha}(t_s)$ intersects with $\boldsymbol{\alpha}\left(t_r^j\right)$ itself. As $\boldsymbol{\alpha}(t) \sim \boldsymbol{E}(t)$ for a plane wave field, the graphical procedure can be applied to $\boldsymbol{E}(t)$ directly. Due to the periodicity of a typical laser field, it is possible to find several return times, t_r^j, for a given starting time, t_s. Therefore, the index j is used to indicate the order of the return.

Upon return, the trajectories have spent the travel time, $t_t^j = t_r^j - t_s$, in the field and got accelerated to the return velocity

$$\boldsymbol{v}_r\left(t_r^j, t_s\right) = \boldsymbol{A}\left(t_r^j\right) - \boldsymbol{A}(t_s). \tag{4.4}$$

At this time, the interaction with the ion is included in the form of elastic electron-ion scattering by assuming a deflection into the angle theta, θ, while the $\left|\boldsymbol{v}_r\left(t_r^j, t_s\right)\right|$ is assumed to be unchanged. Thus, the velocity after scattering can be found by modifying the initial condition in (4.1),

$$\boldsymbol{v}_{sc}\left(t, \theta, t_r^j, t_s\right) = \boldsymbol{A}(t) - \boldsymbol{A}\left(t_r^j\right) + \boldsymbol{v}_r\left(t_r^j, t_s\right)\left[\cos(\theta)\,\boldsymbol{e}_z + \sin(\theta)\,\boldsymbol{e}_y\right]. \tag{4.5}$$

Using equation (4.5) means assuming an instantaneous deflection into the scattering angle, θ. The scattering is limited to the plane of the linearly polarized laser field, which is appropriate as the measured PMDs from the VMI spectrometer represent a cut through the three-dimensional PMD.

The asymptotic velocity of a trajectory, $\boldsymbol{v}_{sc}^f\left(\theta, v_r\left(t_r^j, t_s\right), t_r^j, t_s\right)$, that started at t_s, returned at t_r^j with the velocity, $v_r\left(t_r^j, t_s\right)$ and scattered into the angle θ is

$$\boldsymbol{v}_{sc}^{f}\big(\theta, v_{r}(t_{r}^{j}, t_{s}), t_{r}^{j}, t_{s}\big) = \boldsymbol{v}_{sc}^{f}\big(\theta, t_{r}^{j}, t_{s}\big) = -\boldsymbol{A}(t_{r}^{j}) + \boldsymbol{v}_{r}(t_{r}^{j}, t_{s})\big[\cos(\theta)\,\boldsymbol{e}_{z} + \sin(\theta)\,\boldsymbol{e}_{y}\big]. \tag{4.6}$$

It can be found from equation (4.5) by letting t go to infinity, $t \to \infty$. In this limit, the property of a traveling wave $\int_{-\infty}^{\infty} \boldsymbol{E}(t')\,dt' = 0$ (it has no direct current component) is used by applying $\boldsymbol{A}(t \to \infty) = 0$. Inspecting equation (4.6) shortly reveals that each scattered trajectory is a circle, which is shifted by the vector potential at the time of return in the PMD, see e.g. [105]. Trajectories that do not fulfill the condition of return, i.e. equation (4.3), do not come close to the ion and thus, do not scatter. These trajectories are classified as direct trajectories and have the asymptotic velocity,

$$\boldsymbol{v}_{dir}^{f}(t_{s}, \boldsymbol{v}_{\perp}) = -\boldsymbol{A}(t_{s}) + \boldsymbol{v}_{\perp}. \tag{4.7}$$

(4.7) follows from applying, $\boldsymbol{A}(t \to \infty) = 0$, to (4.1), i.e. $\boldsymbol{v}(t \to \infty, t_{s}, \boldsymbol{v}_{\perp}) = \boldsymbol{v}_{dir}^{f}(t_{s}, \boldsymbol{v}_{\perp})$.

Equations (4.1) to (4.7) establish a connection between an electron trajectory that is released at the time t_{s} and it's asymptotic velocity the detector, $\boldsymbol{v}^{f}$, for a given field, $\boldsymbol{E}(t)$. Depending on whether, t_{s}, leads to fulfillment of the condition of return, i.e. (4.3), for some return times, $t_{r}^{j} > t_{s}$, of the order j, $\boldsymbol{v}^{f}$ is either calculated using the method for a direct trajectory, $\boldsymbol{v}_{dir}^{f}(t_{s}, \boldsymbol{v}_{\perp})$ in (4.7) or a scattered trajectory, $\boldsymbol{v}_{sc}^{f}\big(\theta, v_{r}(t_{r}^{j}, t_{s}), t_{r}^{j}, t_{s}\big)$ in (4.6). For direct trajectories, this is a simple relation that depends on the vector potential at the starting time, $\boldsymbol{A}(t_{s})$, and an initial perpendicular velocity, $\boldsymbol{v}_{\perp}$. For scattered trajectories, the relation is more complex. A single starting time, t_{s}, can lead to j return times, t_{r}^{j}, where scattering into an angle, θ, takes place with the return velocity, $\boldsymbol{v}_{r}(t_{r}^{j}, t_{s})$. Scattering causes an instantaneous deflection such that the asymptotic velocity is affected by the vector potential at t_{s} and t_{r}^{j}. It is therefore extremely sensitive to the time-dependent shape of the field on time-scale below one optical period. The previous analysis of classical electron trajectories in the laser field does not predict the photoelectron momentum distribution, $W(\boldsymbol{p})$ respectively $W(\boldsymbol{v})$, so far. Equations (4.1) to (4.7) only establish the connection between the starting times, t_{s}, and the asymptotic velocity, $\boldsymbol{v}^{f}$, either on a direct path, $\boldsymbol{v}_{dir}^{f}$, or on a scattered path, $\boldsymbol{v}_{sc}^{f}$.

Next, probabilities for each of the paths are constructed along the lines of the previous discussion. Both constructions are finally used to calculate PMDs as the sum, $W(\boldsymbol{v}) = W_{dir}(\boldsymbol{v}) + W_{sc}(\boldsymbol{v})$, which is compared to experimental data on a qualitative level later.

4.4.3 Construction of the PMD Contribution from Direct Trajectories

The final velocity of a direct trajectory, $\boldsymbol{v}_{dir}^{f}(t_{s}, v_{\perp})$, depends on the starting time, t_{s}, via the vector potential, $\boldsymbol{A}(t_{s})$, and on the initial perpendicular velocity, $\boldsymbol{v}_{\perp}$. Thus, the weight of the direct contribution at the final velocity, $W_{dir}(\boldsymbol{v})$, is found by summing over the ionization probabilities from all combinations of starting times, t_{s}^{k}, and initial perpendicular velocities $v_{\perp}^{k}$, which lead to the same final velocity according to (4.7),

$$W_{dir}(\boldsymbol{v}) = \sum_{k} W_{ion}(t_{s}^{k}, \boldsymbol{v} = -\boldsymbol{A}(t_{s}^{k}) + v_{\perp}^{k}) = \sum_{k} W_{ion}(t_{s}^{k}, v_{\perp}^{k}) = \sum_{k} W_{ion}(t_{s}^{k}) W_{ion}(v_{\perp}^{k}). \tag{4.8}$$

The ionization probability, $W_{ion}(t_s^k)$, is modeled using typical formulas for tunnel ionization rates, $\Gamma\big(E(t_s^k)\big)$, in a quasi-static strong electric field, $E(t_s^k)$. A common expression is,

$$\Gamma(|E(t_s^k)|) = \Gamma(t_s^k)$$

$$= \frac{|C_{nl}|^2 Q(l,m)^2}{(2\kappa)^{|m|}|m|!} \left(\frac{2\kappa^2}{|E(t_s^k)|}\right)^{\frac{2B}{\kappa}-|m|-1} \exp\left(-\frac{2\kappa^3}{3|E(t_s^k)|}\right) \exp\left(-\beta\frac{2B}{\kappa^2}\frac{|E(t_s^k)|}{\kappa^3}\right). \tag{4.9}$$

The constants, C_{nl}, $Q(l,m)$, $|m|$, B and $\kappa = \sqrt{2|I_P|}$ in equation (4.9) are specific for the atomic target and can be found in Table 4.1. For example, I_P denotes the ionization potential of the target atom. The first three factors come from the well-known Ammosov-Delone-Krainov (ADK) formula [109] and the fourth factor accounts for an empirically obtained correction to this ionization rate. It is used if the quasi-static field strength, $E(t_s^k) = |E(t_s^k)|$, is close to the over-barrier field strength, $F_C = \kappa^4/8|2Z - \kappa(m+1)|$ [110] [111] and is specific for the atomic target, too. To calculate $W_{ion}(t_s^k)$ based on equation (4.9) depletion of the ground state,

$$W_{ion}(t_s^k) = \Gamma(t_s^k) \exp\left(-\int_{-\infty}^{t_s^k}\Gamma(t')dt'\right), \tag{4.10}$$

is taken into account. It reflects that the probability or population to find the electron in the bound ground state decreases with the rate $\Gamma(t_s^k)$. Thereby, the total probability of the bound part, $P(t)$, and the ionized part, $C(t)$, is one, i.e. $C(t) + P(t) = 1$. Equation (4.10) follows from solving the rate equation, $dP(t)/dt = -\Gamma(t)P(t)$.

Further, there is a chance for tunneling out with an initial perpendicular velocity, i.e. $W_{ion}(v_\perp^k)$, in (4.8). It is modeled using the expression,

$$W_{ion}(v_\perp^k) = \frac{4\pi\kappa}{|E(t_s^k)|} \exp\left(-\frac{\kappa[v_\perp^k]^2}{|E(t_s^k)|}\right). \tag{4.11}$$

Such Gaussian shaped extension of the weight with chance for tunneling with an initial perpendicular velocity is well known [109] and has been proven to yield reasonable agreement with experimental data [112][113] [114] [115].

Equations (4.8) to (4.11) allow to calculate the PMD from direct ionization, $W_{dir}(v)$, for a given field $E(t)$. An illustrative example for starting times from a single half-cycle in an infinitely long laser field (plane wave) is discussed in subsection 4.4.5. A formalism to calculate the PMD from scattered trajectories is discussed next.

4.4.4 Construction of the PMD Contribution from Scattered Trajectories

The final contribution of scattered trajectories is the sum of all trajectories with the starting time, t_s^i, and the return time, t_r^j, which scatter with the return velocity, $v_r\big(t_r^j, t_s^i\big) = v_r^{ji}$, into the angle, θ, and lead to the final velocity, v, at the detector calculated according to equation (4.6),

$$W_{sc}(v) = \sum_{ij} W_{ij\theta}\big(\theta, v_r^{ij}, t_r^j, t_s^i, v_{sc}^f\big) = \sum_{ljk} W_{ion}(t_s^i)W_{travel}(t_r^j, t_s^i)\sigma(v_r^{ij}, \theta). \tag{4.12}$$

Next, the probability of the individual summands is constructed as a product along the lines of the trajectories which were discussed in section 4.4.2.

The first factor in equation (4.12), $W_{ion}(t_s^i)$, is the probability for tunnel ionization in a quasi-static field. It is the same as for direct trajectories, i.e. equation (4.9), but used with the initial velocity set to $v_\perp = 0$ as this is a prerequisite for a scattered trajectory in a linearly polarized field. The electron would miss the ion otherwise. The second factor,

$$W_{tr}(t_r^j, t_s^i) = (t_r^j - t_s^i)^{-\xi} = (t_r^j - t_s^i)^{-3/2},\tag{4.13}$$

lowers the contribution of returns with longer travel time, $t_t^j = t_r^j - t_s^i$. This is motivated by the idea that ionization from each t_s^i creates a spatially confined three-dimensional electron wave packet in the continuum, which is subsequently steered by the field. As an electron wave packet in the continuum spreads in space, this causes a lowered electron density and thus, a lower probability for returns that have a longer traveling time, t_t^j. Choosing $\xi = 3/2$ mimics the combination of two-aspects: (i) three-dimensional spreading of the released electron wave-packet (this would yield $\xi = 3$) while it travels from t_s^i to t_r^j in the continuum and (ii) Coulomb-focusing that contracts the wave-packet in due to the attraction of the nearby ion [116].

Last but not least, there is the differential cross-section for elastic scattering, $\sigma(v_r^{ij}, \theta)$, of the scattering potential in equation (4.12). To model the scattering of a noble gas ion, a screened potential of the form, $V(r) = -Ze^{-\mu r}/r$, with the cross-section,

$$\sigma(\theta, v_r^{ij}) = (2Z)^2 / \left[\mu^2 + 4\left[v_r^{ij}\right]^2 \sin^2(\theta/2)\right]^2,\tag{4.14}$$

is used here. Choosing this form is mainly motivated by the desire to be able to have an analytical expression. The parameters, Z and μ, are specific to the noble gas and are given in Table 4.1. They have been found by fitting $V(r)$ to more complex model potentials [110]. Instead of using this type of the potential, one might use numerically calculated scattering cross-sections, which are expected to give a lot better agreement between theory and experiment. It has been shown that high-energy part of the PMDs from strong-field ionization can be used to extract elastic differential scattering cross-section of the target ion from the measured PMD, see e.g. [117]. This so-called laser-induced electron diffraction (LIED) scheme has been used to probe several structures and dynamics of rare gas atoms [118], and molecules [32] [105] [119] [120]. Very recently, following even bond breaking dynamics in small molecules has been demonstrated [33].

An important aspect of the construction, (4.12), in the context here is the weight between scattering contributions that belong to the same starting time, t_s^i, but have several return orders t_r^j. Here, the normalization, $W_{ion}(t_s^i) = \int_\theta \int_j W_{ij\theta}\, dj d\theta$, is used in order to ensure appropriate weight for returns of different orders. It accounts for the fact that a later return with lower return velocity (high cross-section but lower return probability due to wave packet spreading) might be preferred, compared to an earlier return with high return velocity (low cross-section but higher return probability due to wave packet spreading). This schmes seems to be appropriate to weight the probability of different return orders in a reasonable way, but it might underestimates the direct contribution

compared to the scattered contribution as the mentioned wave packet spreading would lead to direct contribution from $W_{ion}(t_s^i)$ even if t_s^i leads to a return.

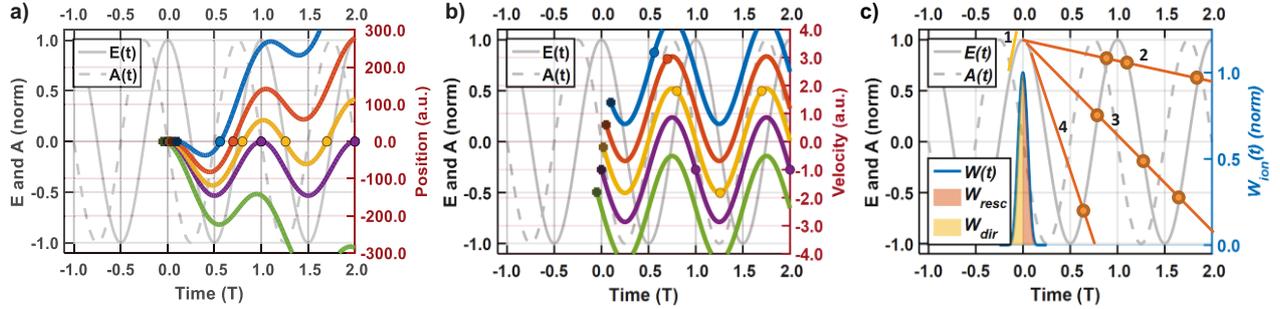### 4.4.5 Illustration of the Model - PMDs from a Single Half-Cycle

Figure 4.7: Classical trajectories in the laser field and ionization probability.

a) shows the position, $r(t, t_s)$, of five trajectories with starting times before and after the peak of the field around $t \approx 0$. The wavelength of the driving field in the example is $\lambda = 1780$ nm ($\omega = 0.026$ a.u.) and has an intensity of $I_0 = 8 \times 10^{13}$ W/cm^2 ($E_0 = 0.048$ a. u.). The green trajectory starts before the peak. It thus, never returns to the position of the ion at $r \approx 0$ and yields a direct trajectory. All others (purple, yellow, orange and blue) belong to scattered trajectories with one or multiple returns at the return times as indicated by the dots. b) shows the time-dependent velocities of the example in a). All trajectories start with zero velocity but have been shifted vertically for better visibility. The return velocities, i.e. v_r, at the return times are indicated by the dots. c) shows the ionization probability, $W_{ion}(t)$ for Xenon as the target. Only the half-cycle that peaks around $t \approx 0$ is considered. The area under the curve indicates which starting times lead to direct and scattered trajectories. The numbered lines (1-4, yellow and orange) illustrate the graphical method for finding the return times. They are the tangent on $\alpha(t_s) \propto E(t_s)$ that intersect $\alpha(t_r) \propto E(t_r)$ at the return time indicated by the dots.

 Having explained the constructions of the direct and the rescattered contribution to the PMD in sections 4.4.3 and 4.4.4, we turn to illustrate the model using example calculations here. To this end, the results of the model are illustrated by considering the ionization from a single laser half-cycle in an infinitely long pulse. The analysis is similar to what has been done in references [16] [108] [121]. Considering ionization from a single laser half-cycle in an infinitely long pulse allows to perform some of the necessary numerical analysis analytically. Thus, scaling laws with experimental parameters of notable features in the PMDs can be given. Thereby, the major interest lies on the formation of on- and off-axis low-energy structures that have been investigated in recent experimental [9] [122] [10] [99] and theoretical work [98] [123] [124] [108]. It will be shown that these features can be well reproduced and understood by the constructions of the PMD that follows from the SCM as presented in section 4.4.2, 4.4.3 and 4.4.4. The analysis demonstrates that rescattering is the origin of the features and puts them on the same basis as the high-energy plateau [2] [16].

 The field is chosen as an infinitely long plane wave with linear polarization along the z-axis of the laboratory frame. Thus, the PMD is calculated in the plane of the linear polarization, i.e. the zy-plane. The field has the amplitude E_0, the frequency, ω, and the optical period, $T = 2\pi/\omega$ and reads,

$$E(t) = E_0 \cos(\omega t). \tag{4.15}$$

Integrating two times yields, the vector potential is $A(t) = -E_0/\omega \sin(\omega t) = -A_0\sin(\omega t)$ and it's integral $\alpha(t) = E_0/\omega^2 \cos(\omega t) = \alpha_0\cos(\omega t)$. Using (4.1) and (4.2), one finds the position, $r(t, t_s)$, and the velocity, $v(t, t_s)$, for a given starting time, t_s, and for initial perpendicular velocity $v_\perp = 0$,

$$r(t, t_s) = \frac{E_0}{\omega^2}\cos(\omega t) - \frac{E_0}{\omega^2}\cos(\omega t_s) + (t - t_s)\frac{E_0}{\omega}\sin(\omega t_s)$$

$$\tag{4.16}$$

$$v(t, t_s) = -\frac{E_0}{\omega}\sin(\omega t) + \frac{E_0}{\omega}\sin(\omega t_s) = v_{osc}(t) + v_{drift}(t_s).$$

Equations (4.16) are illustrated in Figure 4.7 for a few examples with starting times close to the peak of the laser field around $t \approx 0$. Inspection of (4.16) and Figure 4.7 reveals that the electron follows the oscillation of the field overlapped with a linear drift motion at constant speed, i.e. $v(t, t_s) = v_{osc}(t) + v_{drift}(t_s)$. The constant speed is sensitive to the starting time, t_s, in its magnitude and direction.

The position and the velocity terms scale with the field strength and the frequency of the driving laser. The amplitude of the velocity is, $A_0 = E_0/\omega$, and the excursion of the trajectory is $\alpha_0 = E_0/\omega^2$. For the chosen example of $\lambda = 1780$ nm ($\omega = 0.026$ a.u.) and an intensity of $I_0 = 8 \times 10^{13}$ W/cm² ($E_0 = 0.048$ a.u.) this yields, $A_0 = 1.86$ a.u. and $\alpha_0 = 72.87$. Comparing these numbers to typical values for the energy and the position of valence electrons in a noble gas atom of $I_p \approx 0.5$ a.u. and $a_0 \approx 1$ a.u (the Bohr radius) illustrates that the kinetic energy in the field, $T_{osc} = 0.5A_0^2 \approx 1.74$ is of comparable size to the binding energy while the distance is a lot larger than the typical size of an atom, i.e. $\alpha_0 \gg a_0$. Both aspects, (i) large distance between electron and ion with (ii) high kinetic energy give arguments for neglecting the influence of binding potential on the trajectory for most of the time at least in a first order model. However, the trajectories shown in Figure 4.7 also reveal situations, i.e. the returns, where the electron trajectory approaches the ion with some velocity that can reach a whole range, $v_r = 0 \dots v_{max}$ of velocities.

4.4.5.1 Direct Contribution to the Photoelectron Momentum Distribution

The ionization probability, $W_{ion}(t)$, for trajectories with starting times from a single optical half-cycle around $t \approx 0$ is shown in Figure 4.7 c). Only starting times before the peak of the field lead to direct trajectories, which have final velocities in negative z-direction, $\boldsymbol{v}_{dir}^f < 0$. It reflects that for the SCM only times, $t_s < 0$, with asymptotic velocities, $\boldsymbol{v}_{dir}^f \propto -\boldsymbol{A}(t_s)$ are classified as direct trajectories and thus, contribute to the PMD while trajectories from $t_s > 0$ always lead to scattered trajectories and are consequently omitted in the discussion of the direct ones. The region, $\boldsymbol{v}_{dir}^f > 0$ in Figure 4.8 would be filled if trajectories from the next half-cycle are allowed. Including them would lead to a distribution that is simply symmetric around the $\boldsymbol{v}_z^f = 0$ axis as is obvious from specifying equation (4.7) for the field in (4.15),

$$\boldsymbol{v}_{dir}^{f}(t_s, \boldsymbol{v}_\perp) = +\frac{E_0}{\omega}\sin(\omega t_s)\boldsymbol{e_z} + \boldsymbol{v}_\perp. \tag{4.17}$$
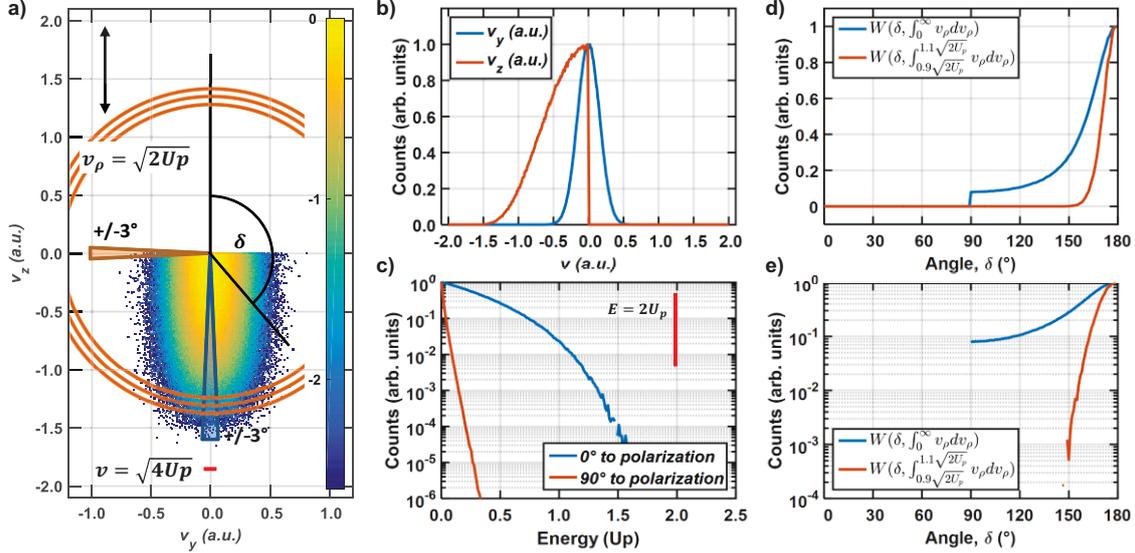

Figure 4.8: Illustration of the direct contribution to the PMD for starting times from a single half-cycle.

The logarithm of the photoelectron yield, $W_{dir}(\boldsymbol{v})$, is shown in a) as function of the final velocities parallel (z-direction, v_z) and perpendicular (y-direction, v_y) to the field in a colored 2D plot. The black arrow top left indicates the direction of the linear polarization. The short red line at the bottom marks the position of $v_\rho = \sqrt{2 \cdot 2U_p}$ which is the highest velocity that a direct trajectory could reach. Also shown are wedges (orange and blue) that illustrate the cuts through the PMD for electron emission within a certain solid angle. The three rings (orange) indicate a velocity region around $v_\rho = \sqrt{2U_p}$. Projections of the PMD along the axis of the coordinate system are shown in b). Energy spectra for electron emission along the cuts as indicated by the wedges in a) are given in c). Angular distributions, i.e. the probability for electron emission with the velocity, $v_\rho = \sqrt{v_y^2 + v_z^2}$ into the angle, δ, are shown on a linear scale in d) and a log scale in e). The blue line in d) and e) shows $W(\delta, \int_0^\infty dv_\rho)$, i.e. the velocity integrated angular distribution and the orange line shows the same but for a velocity range around $v_\rho = \sqrt{2U_p}$, that is indicated in a), see the legend in the figure. The region with positive velocities, $v_z > 0$, is empty as starting times from a single half-cycle of the laser field are considered only. It would be filled if direct trajectories from a full optical are allowed.

Introducing the ponderomotive potential next,

$$U_p = \frac{1}{T}\int_0^T \frac{1}{2}\left[\frac{E_0}{\omega}\sin(\omega t')\right]^2 dt' = \frac{1}{2}\frac{E_0^2}{\omega^2}\left[\frac{T}{2} - \frac{\sin(\omega T)}{4\omega}\right] = \frac{1}{4}\frac{E_0^2}{\omega^2}, \tag{4.18}$$

as a scaling quantity, yields the maximum kinetic energy of direct trajectories $\max(T_{dir}) = 2U_p$. However, the probability at these high energies is very small (strictly speaking zero) according to (4.10). This is a consequence of the SCM. Trajectories with the highest energy occur for starting times, $t_s \approx \pi/2$, i.e. for ionization times where $E(t) = 0$ and thus $W_{ion}(t) = 0$ is zero. Consequently, one does not expect to observe direct trajectories at these energies if one strictly follows the semi-classical model. However, quantum mechanical considerations allow these

trajectories such that one can mitigate the previous statement by expecting only a small contribution to the PMD from these trajectories.

The projection of the PMD perpendicular to the direction of the ionizing laser field, $W(v_{dir}^f)$, resembles a Gaussian distribution. This is expected as each t_s with the field strength, $E(t_s)$, contributes with a Gaussian probability to the final, i.e. $W_{ion}(v_\perp^k) \propto \exp(-[v_\perp^k]^2/\sigma^2)$. Thereby, the width of the Gaussian scales with the field strength at the ionization times, i.e. $\sigma^2 \propto |E(t_s^k)|$. Thus, ionization times close to the peak of the field yield a wider distribution into the direction of the perpendicular velocity. However, these trajectories have lower velocity parallel to the field such that the width decreases with higher, v_z, see Figure 4.8.

4.4.5.2 Scattered Contribution to the Photoelectron Momentum Distribution

Now we turn to the PMD of scattered trajectories. First, one has to find return times, t_r^j, by solving the condition of return, (4.3), for the chosen field (4.15), i.e. solutions of

$$z(t_r^j, t_s) = \frac{E_0}{\omega^2}\cos(\omega t_r^j) - \frac{E_0}{\omega^2}\cos(\omega t_s) + \frac{E_0}{\omega^2}\omega(t_r^j - t_s)\sin(\omega t) = 0$$

$$\to [\cos(\omega t_r^j) - \cos(\omega t_s) + \omega(t_r^j - t_s)\sin(\omega t_s)] = 0 \tag{4.19}$$

need to be found. Introducing, the travel time, $t_t^j = t_r^j - t_s$ [108], with the corresponding travel phase, $\tau_t^j = \omega(t_r^j - t_s)$, and expressing, $t_r^j = \omega t_r^j = \tau_t^j + \omega t_s$, yields

$$\cos(\tau_t^j + \omega t_s) - \cos(\omega t_s) + \tau_t^j \sin(\omega t_s) = 0. \tag{4.20}$$

Rewriting, using trigonometric functions, $\cos(a + b) = \cos(a)\cos(b) - \sin(a)\sin(b)$, [45] one has

$$\cos(\tau_t^j)\cos(\omega t_s) - \sin(\tau_t^j)\sin(\omega t_s) - \cos(\omega t_s) + \tau_t^j \sin(\omega t_s) = 0. \tag{4.21}$$

Dividing by $\cos(\omega t_s)$ yields after rearrangement,

$$\cos(\tau_t^j)\cos(\omega t_s) - \cos(\omega t_s) - \sin(\tau_t^j)\sin(\omega t_s) + \tau_t^j \sin(\omega t_s) = 0$$

$$\to \tan(\omega t_s) = \frac{\cos(\tau_t^j) - 1}{(\sin(\tau_t^j) - \tau_t^j)} \to t_s = \frac{1}{\omega}\arctan\left[\frac{\cos(\tau_t^j) - 1}{(\sin(\tau_t^j) - \tau_t^j)}\right]. \tag{4.22}$$

This expression gives the starting time for a given travel time. The relation is shown in Figure 4.9 a) for return times, i.e. $t_r^j = t_t^j + t_s$, between a quarter of an optical cycle 0.25 T up to 3 T. The smaller the starting time is, the later the return times can be and the more return orders, i.e. js, exist.
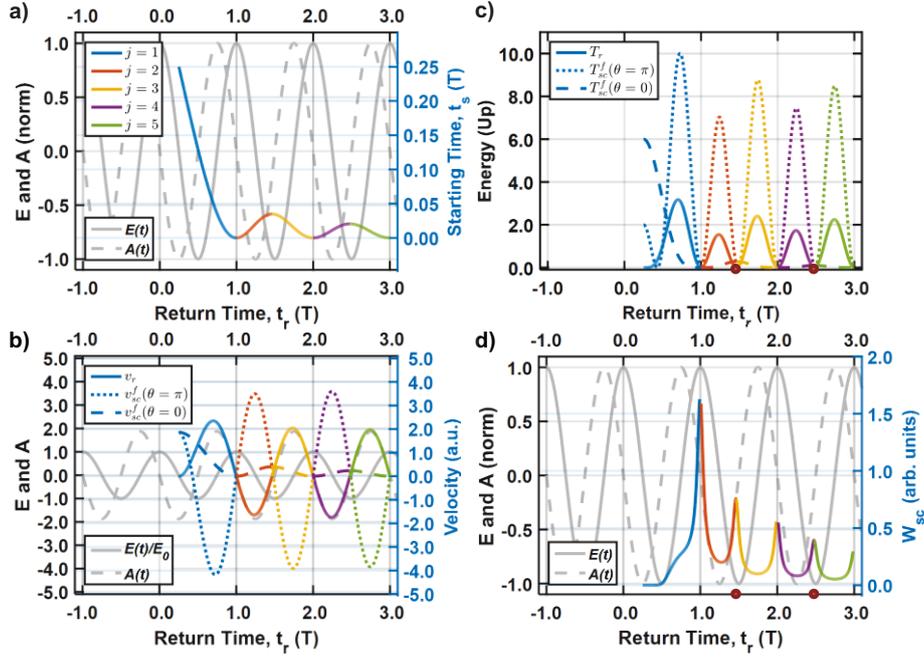
Figure 4.9: Illustration of rescattering dynamics in a plane-wave field for starting times from a single half-cycle.

a) shows the relation between the return time, t_r^j, and the starting time, t_s, for return times in the interval, $t_r^j = 0.25\,T \dots 3T$. This leads to starting times in the range $t_s = 0 \dots 025\,T$. Different return orders i.e. first return $j = 1, \dots j = 5$, are indicated by the colors (blue, orange, yellow, purple, green). The color code is used in all plots a)-d). If t_s is close to the peak of the field, i.e. $t_s \approx 0$, several return orders exist. b) shows return velocity, v_r, (solid colored line) and final velocities for backward, $v_{sc}^f(\theta = \pi)$, (dotted colored lines) and forward scattering, $v_{sc}^f(\theta = 0)$ (dashed colored lines). The corresponding energies are shown in units of the ponderomotive potential, U_P. Forward scattering energies, $E_{fs}(\theta = 0)$, have been multiplied by three for better visibility of the curve. d) shows the angle integrated scattering probability, i.e. $W_{sc}(t_r^j) = \int W_{sc}(\theta, t_r^j) d\theta$, as function of return order. The field and the vector potential are shown for reference as indicated in the legend of each of the panels.

Having established the connection between t_s and t_r equations (4.4) and (4.5) can be used to calculate the return velocity, $\boldsymbol{v}_r(t_r^j, t_s)$, and the velocity after scattering into an angle, $\boldsymbol{v}_{sc}^f(\theta, t_r^j, t_s)$, see Figure 4.9 b). Therefrom, one can give the corresponding energies, $T_r(t_r^j, t_s)$, and $T_{sc}(\theta, t_r^j, t_s)$ that are shown in Figure 4.9 c). It is possible to do further analytical analysis [108] however, the expressions become rather lengthy such that this is not repeated here.

We continue numerically and focus on some aspects. Depending on the return time (and thus starting time), the trajectory approaches the parent ion with high velocity from both sides, i.e. in positive or negative z-direction see Figure 4.9 b). In dependence of the deflection angle, θ, in the scattering process different final velocities are reached. For example, backscattering, $\theta = \pi$, reverses the sign of $\boldsymbol{v}_r$ and creates a situation where the field driven motion after scattering leads to an acceleration as the reversed $\boldsymbol{v}_r$ (i.e. the velocity after scattering) and the vector potential $-\boldsymbol{A}(t_r^j)$ point into the same direction. In the consequence, backscattering trajectories of a given set of t_r^j and t_s can reach final velocities in the full range between $\boldsymbol{v}_{sc}^f(\theta = \pi, t_r^j, t_s) \approx -4 \dots 3.5$ a. u. in the example, see Figure 4.9 b). Forward scattering, $\theta = 0$, however, does not change the sign of the incoming velocity which leads to a deceleration by the subsequent field-driven motion as $-\boldsymbol{A}(t_r^j)$ points into the opposite direction. Thus, final velocities in a

smaller range between $\boldsymbol{v}_{sc}^f(\theta = 0, t_r^j, t_s) \approx 0 \dots 2$ a. u. are reached only. In this sense, low energy for forward scattering trajectories as well as high energy for backscattering are a result of the mapping between t_s and t_r^j with the corresponding vector potentials at both times. Consequently, scattering is governed and can be controlled by the sub-cycle shape of field. Thereby, it is clear that the model used here, neglects the influence of the binding potential on the trajectory. It takes it only into account via deflection into the angle θ which might be questionable particularly for low energy returns. Naturally, the acceleration and deceleration mechanism for forward- and backscattering is reflected in the energies shown Figure 4.9 c). The return energy has a maximum at $\max(T_r(t_r^1, t_s)) = 3.17\, U_p$ and is reached for $t_s \approx 0.05\, T$ with the first order return at $t_r^1 \approx 0.7T$. Returns with higher order have lower highest energy that oscillates in dependence of the order of the return. Zero energy occurs for travel times $t_t = nT$ and once between full cycles if the return order is larger than one. The last of these trajectories are marked by the red dots on the t_r-axis in Figure 4.9 c) and Figure 4.9 b). They are responsible for the soft recollisions that are discussed in greater detail in section 4.4.5.3.

The backscattering energy follows roughly the curve of the $T_r(t_r^j, t_s)$ but at higher energies with a maximum around $T(\theta = \pi, t_r^j, t_s) = 10.0\, U_p$ followed by the maxima of the higher return orders which lie in the region between $6\, U_p$ and $9\, U_p$. The combination of all the high-order back scattering returns leads to the formation of smooth cut-offs in this momentum region of the PMD. Thereby, the whole energy range between 0 and $10.0\, U_p$ is accessed. Forward scattering reaches a smaller energy range between $T(\theta = 0, t_r^j, t_s) \approx 0 \dots 2.0\, U_p$. Note that the curve in Figure 4.9 c) has been multiplied by three in order to improve the visibility. Particularly, high order returns lead to rather small energies around $\approx 0.1\, U_p$ and below. These energies are well in the energy range which can be addressed by the contribution from direct trajectories, too.

To impart an impression on the probability for each of the t_r^j and t_s^i, an analysis of the integrated scattering probability $W_{sc}(t_r^j) = \int W_{ion}(t_s^i) W_{travel}(t_r^j, t_s^i) \sigma(v_r^{ij}, \theta) d\theta$ as a function of t_r^j is shown in Figure 4.9 d). The combination of the ionization probability for a starting time, $W_{ion}(t_s^i) \sim \exp(-1/3|\boldsymbol{E}(t_s^k)|)$, the punishment for longer travel times, $W_{travel}(t_r^j, t_s^i) \sim (t_r^j - t_s^i)^{-\xi}$, and particularly the velocity dependence of the elastic scattering cross-section, $\sigma(\theta, v_r^{ij}) \sim [\mu^2 + 4v_r^2 \sin^2(\theta/2)]^{-2}$, leads to a strongly peaked shape of $W_{sc}(t_r^j)$. Interestingly, the probability of returns with longer travel time can clearly compete and even exceed the probability for some of the earlier returns. The origin of the effect is two-fold, on the one hand, the ionization probability, $W_{ion}(t_s^i)$, for trajectories with longer travel time is higher as these start close to the peak of the field. Additionally, and more importantly, $\sigma(\theta, v_r^{ij})$, becomes very large for, $v_r^{ij} \approx 0$, such that combination of both can beat the punishment for a longer travel time $W_{travel}(t_r^j, t_s^i)$.

The scattered contribution to the PMD from a single laser cycle is shown in Figure 4.10. Contributions from different return orders as well as the highest velocities, i.e. the angular cut-offs, from different orders of the returns are investigated. Each return order contributes a velocity distribution that is reminiscent of a droplet, see Figure 4.10 d)-h) for the individual contributions. Figure 4.10 a) shows the total result over the full momentum region while Figure 4.10 b) is zoomed into the low momentum region. The returns of odd order ($j = 1,3,5$) yield wide distributions that have momenta at positive $v_z > 0$ as well as negative $v_z < 0$. For these trajectories, a final velocity of $v_z > 0$ is related to close-to forward scattering. The deceleration by the field after scattering causes these

trajectories to bunch in the final velocity such that they yield a velocity region with comparatively high yield at low velocities, see Figure 4.10 d), f) and h). Increasing scattering angle has decreasing scattering cross-section, $\sigma(\theta, v_r^{ij}) \sim [\mu^2 + 4v_r^2 \sin^2(\theta/2)]^{-2}$, thus these trajectories have lower yield. In addition, the stronger the acceleration after scattering is, i.e. the closer the trajectories come to backscattering, the more spread out are the final velocities in the region $v_z < 0$ and the lower is the yield. The PMDs from returns of even order ($j = 2,4$) have similar shape but access the region $v_z > 0$ only. The magnitude of the return velocity for close-to forward scattering of these trajectories are not higher than the corresponding deceleration by the field after scattering. Thus, forward scattering cannot reach the $v_z < 0$ region. Close-to backscattering from returns of even order returns yields similar contributions as back scattering from odd returns.
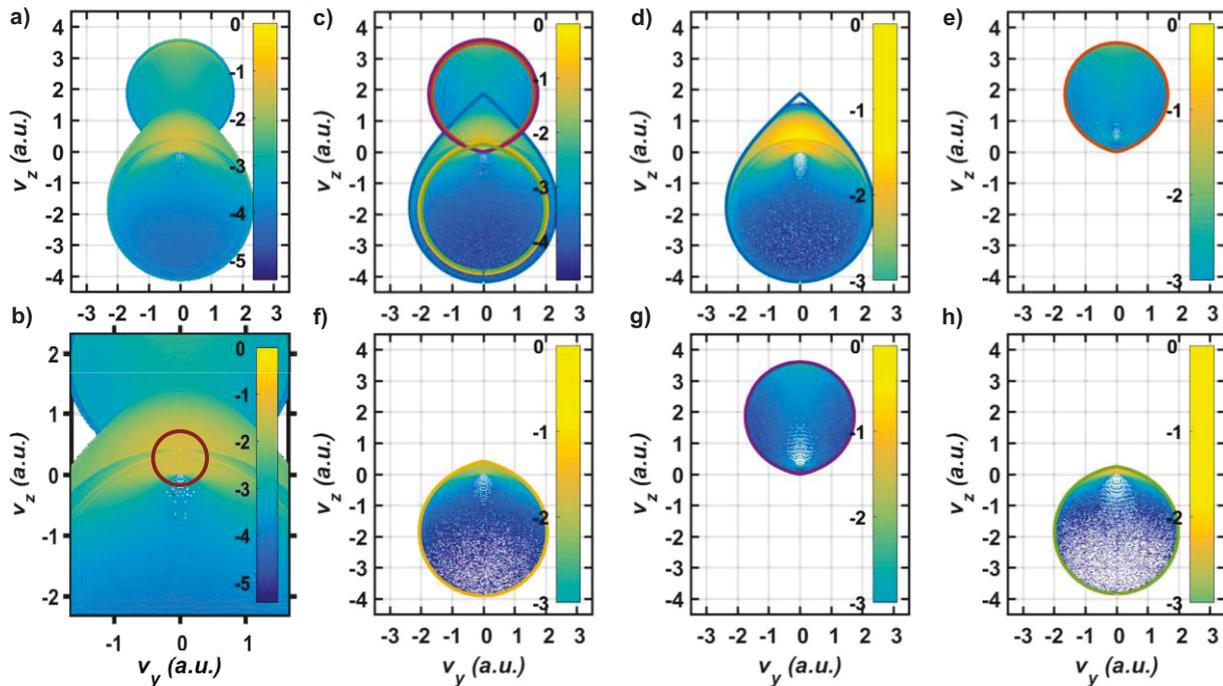
Figure 4.10: Scattered contribution to the PMD from a single half-cycle resolved for each return order

a) shows the logarithm of the photoelectron yield, $W_{sc}(\mathbf{v})$, of all return orders. b) is a section of a) with smaller velocity. c) is the same as a) but with colored solid lines (blue $j = 1$, orange $j = 2$, yellow $j = 3$, purple $j = 4$, green $j = 5$) that mark the highest velocities, i.e. the cut-offs, that can be reached by the corresponding order. These lines are given in b), too. In d)-h), the contribution of each order with the corresponding cut-offs is illustrated in a different plot.

For both even and odd return orders, returns with close to zero return velocity lead to distinct features. First, these trajectories have high probability as the scattering cross-section is large. Second, the final velocity is mostly independent of the scattering angle such that the yield from these trajectories is strongly bunched in the final PMD and causes confined velocity regions with particularly high yield, see Figure 4.10 a) and b) where the confined regions are encircled in read. The peaks in $v_z > 0$ stem from the odd return orders and the peak at even lower velocity exactly at zero comes from the even return orders. These velocity regions with particularly high yield are known as the low-energy structure which have observed experimentally [9] [122] with their off-axis extension [10] and have been investigated theoretically [98] [123] [124] [108]. Within the semi-classical model used here, they

can be understood by two aspects: (i) a very high cross-section for trajectories that return with low velocity and by (ii) the deceleration due to the field driven motion after scattering of forward scattering trajectories which leads to a bunching in the final PMD. Along the lines of the SCM, the structures occur already if the trajectories are calculated taking into account the laser field only and by incorporating the influence of the binding potential via deflection at the scattering event. Thus, the low energy features can be understood and explained on the same footing as high energy features in the PMD such as e.g. the plateau [2]. Due to the strong link to the field, it is expected the low-energy trajectories are at least similarly sensitive to the sub-cycle shape of the laser field and can thus, be controlled by it [123] similarly to e.g. [125].

Besides the low-energy features, the angular cut-offs of each of the returns can be clearly identified in the calculated final PMD from rescattering, Figure 4.10 a), b) and c). The cut-offs manifest as sharp jumps of the probability, see Figure 4.10 a) and b) in combination with Figure 4.10 c) where the angular cut-offs are overlapped with the PMD from Figure 4.10 a). In addition to these jumps, inspecting the contributions from individual return orders, Figure 4.10 d)-h), shows very similar structures that cannot be related to the angular cut-offs directly. These features are not removed if the contributions from individual returns are combined to the full contribution from rescattering, see Figure 4.10 a), b) and c) where they are present, too. They are a result of the normalization, i.e. $W_{ion}(t_s^i) = \iint W_{ij\theta} dj d\theta$, that adjusts the weight of the different returns. It reflects that a trajectory that has several return orders distributes it's probability among all possible returns. Thus, the probability which is shifted to one of the next returns, causes a lowered yield at velocities which could have been reached if scattering would have happened at the previous return. This redistribution of probability among multiple returns leads to the sharp features that are very pronounced in Figure 4.10 d).

Similarly to the PMD from direct electrons, the PMD of the scattered contribution is further analyzed in Figure 4.11. Projections of the scattered contribution to the PMD parallel and perpendicular to the polarization axis of the laser are shown in Figure 4.11 b). In both projections, the position of the classical cut-offs as well as the discussed low-energy structures can be identified as sharp peaks. The angle dependent yield in Figure 4.11 c) integrated for all velocities drops for increasing angle dramatically and has a sharp jump in the direction close to right angle to the polarization axis of the laser field. If only the angular distribution in a certain velocity range is considered, several peaks occur in the region close to right angle to the polarization axis. These are related to the position of the angular cut-offs of the different return orders as well as to additional cut-offs which occur due to the normalization which is used to weight the probabilities with returns of different order.

Energy spectra for emission into different solid angles are shown in a semi logarithmic plot in Figure 4.11 d). Emission into $v_z > 0$ as well as $v_z < 0$ shows sharp peak in the yield at the position of the cut-offs of the different return orders. In the spectrum that is emitted perpendicular to the polarization axis, the angular cut-offs as well as the additional cut-offs lead to a modulation of the energy-dependent yield. Considering the spectrum at smaller energies only, as in Figure 4.11 e), allows to identify the sharp low-energy peaks in the spectrum that is emitted into the $v_z > 0$ direction.
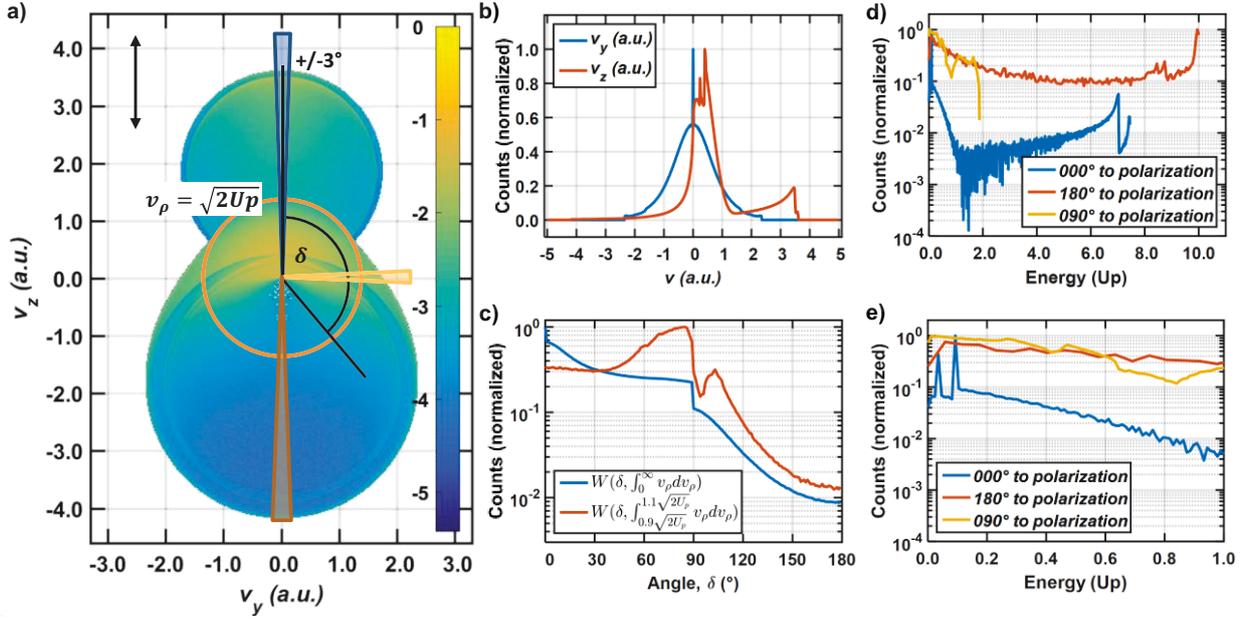
Figure 4.11: Analysis of the scattered contribution to the PMD from a single half-cycle

a) shows the logarithm of the photoelectron yield, $W_{sc}(\boldsymbol{v})$, as function of the final velocity components parallel, v_z, and perpendicular, v_y, to the direction of the polarization of the laser field, which is indicated by the black arrow top left. The intensity in the calculations has been 8×10^{13} W/cm^2. In b), the projections of the PMD on each of the axis are given. c) illustrates the angular distribution as function of emission angle, δ, once integrated over the full momentum range (blue solid line) and integrated over a certain momentum region around $v_\rho = \sqrt{2U_P}$ as given in the legend. Both, the angle δ (black solid lines) and the momentum region of interest, $v_\rho = \sqrt{2U_P}$, (orange ring that is centered around zero velocity) are indicated in a). The wedges with different colors in a) show the angle regions for that the energy spectra are shown in d) in a wide range from zero energy up to 11 U_P and e) in a narrow energy range below U_P.

The previous analysis and discussion of the calculated scattered contribution PMD illustrates that the semi-classical model supports high-energy as well as on- and off-axis low energy features rescattering features. These low-energy features have been observed in on-axis photoelectron spectra [9] [122] [99] and off-axis PMDs [10] as well as in theoretical work [98] [123] [124] [108]. The presented semi-classical results do not allow for the inference between different electron trajectories. Thus, the interference structures between direct and scattered contributions to the PMD, which that are termed Spider in Figure 4.2, are not supported by the SCM used here. Next, we turn to a detailed analytical investigation of the soft-recollisions and the corresponding low-energy features.

4.4.5.3 Soft-Recollision and Low-Energy Structure

Here, the cut-off positions of the soft-recollision trajectories, which are responsible for the on-axis low-energy structure, are derived for the plane-wave field (4.15). Our consideration further confirms that the low-energy structures are supported by the SCM. The analysis is done along the lines of [108].
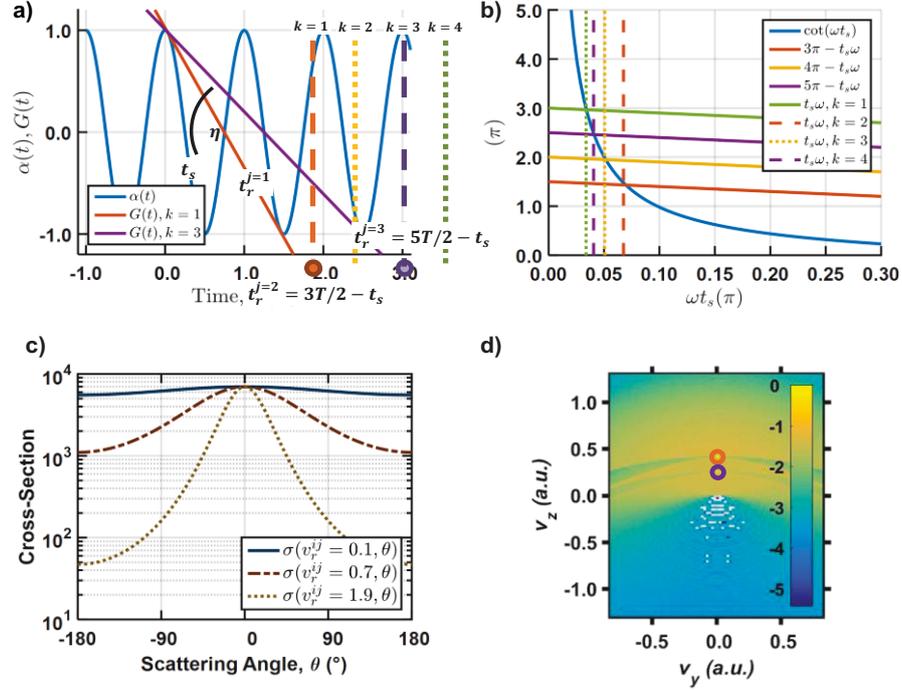
Figure 4.12: Illustration of the graphical method to solve the condition of return for soft-recollisions

a) shows the graphical method which is used to identify soft-recollision returns. Soft-recollisions as described by equations (4.23) to (4.29) are found when the tangent on $\alpha(t_s)$ crosses with $\alpha(t_r^j)$ in such a way that also the slopes are the same at both points, $\partial\alpha/\partial t|_{t_r^j} = \partial\alpha/\partial t|_{t_s}$, see the lines, $G(t)$ for two examples. The angle η is used to read-off this condition in a suitable way from the figure. Vertical lines indicate the resulting t_r for the approximate solutions in equation (4.27). Dashed lines belong to odd k and deliver the soft-recollisions. Dotted lines belong to even k and are unwanted. b) Illustrates (4.27) with the corresponding solutions. Dashed and dotted lines are used as in a). c) shows the scattering cross-section as function of scattering angle for three different momenta. For small scattering momenta, the cross-section becomes more and more isotropic. d) shows the PMD from Figure 4.11 in small velocity range. The low-energy peeks are the encircled very narrow regions with very high yield.

We start by considering the graphical solution of the condition of return that reads for the cosine-field in (4.15),

$$\alpha(t_r^j) = \alpha(t_s) + (t_r^j - t_s)\frac{\partial\alpha}{\partial t}\bigg|_{t_s} = G(t_r^j). \tag{4.23}$$

A soft-recollision is found if the return velocity is zero in addition, i.e.

$$v\left(t_r^j, t_s\right) = -\frac{E_0}{\omega}\sin\left(\omega t_r^j\right) + \frac{E_0}{\omega}\sin(\omega t_s) = 0 \rightarrow -\sin\left(\omega t_r^j\right) + \sin(\omega t_s) = 0, \quad (4.24)$$

which transfers to

$$\left.\frac{\partial\alpha}{\partial t}\right|_{t_r^j} = \left.\frac{\partial\alpha}{\partial t}\right|_{t_s}, \quad (4.25)$$

for the graphical method. This is illustrated in the sketch Figure 4.12. Equation (4.25) can be used in (4.23) in order to obtain a second version of (4.23) that takes the condition of zero return velocity, i.e. (4.24), into account. All together one has,

$$\alpha\left(t_r^j\right) = \alpha(t_s) + \left(t_r^j - t_s\right)\left.\frac{\partial\alpha}{\partial t}\right|_{t_s}$$

$$\alpha(t_s) = \alpha\left(t_r^j\right) - \left(t_r^j - t_s\right)\left.\frac{\partial\alpha}{\partial t}\right|_{t_r^j}. \quad (4.26)$$

Graphically, this means that a soft-recollision is found if the tangent on $\alpha(t_s)$, i.e. $\left(t_r^j - t_s\right)\partial\alpha/\partial t|_{t_s}$, intersects $\alpha(t)$ at a point t_r^j where $\alpha\left(t_r^j\right)$ has the same slope. Or in other words, following the tangent on $\alpha(t_s)$ and going forward in time must yield the same line as starting at $\alpha\left(t_r^j\right)$ and following the tangent backward in time. Due to symmetry reasons, this is achieved for return times, $t_r^j = (1 + k/2)T - t_s$ with $n = 1,2, \ldots$ being a natural number. Thereby, t_s has been limited to the interval, $t_s = 0 \ldots 0.25\ T$, see Figure 4.12 a). Higher order soft-recollision, i.e. higher n, shift the corresponding t_s closer to 0 where the peak of the field is located.

From the inspection of Figure 4.12 a) one can introduce the angle η in order to find an alternative formulation of equation (4.26),

$$\tan(\eta) = \frac{2\alpha(t_s)}{\left(1 + \frac{n}{2}\right)T - 2t_s} = \left|\left.\frac{\partial\alpha}{\partial t}\right|_{t_s}\right| \rightarrow \frac{2\frac{E_0}{\omega^2}\cos(\omega t)}{\left(1 + \frac{n}{2}\right)T - 2t_s} = -\frac{E_0}{\omega}\sin(\omega t)$$

$$\rightarrow \frac{\cos(\omega t)}{\left(1 + \frac{n}{2}\right)\pi - \omega t_s} = \sin(\omega t) \rightarrow |\cot(\omega t_s)| = \left(1 + \frac{k}{2}\right)\pi - t_s\omega. \quad (4.27)$$

Using the approximation for small angles, $|\cot(\omega t_s)| \approx 1/\omega t_s$, in equation (4.27) one reads $0 = (1 + k/2)\pi\omega t_s - (t_s\omega)^2$. It can be solved using a Taylor expansion in first order, $0 = -1 + (1 + k/2)\pi\omega t_s$, the solutions are

$$t_s\omega = \frac{1}{(1 + k/2)\pi} = \frac{2}{(2 + k)\pi} \quad (4.28)$$

with the corresponding the return times, $t_r^j = (2 + k)\pi/\omega - 2/\pi(2 + k)\omega$. The found solutions, Figure 4.12 a) and b) show that equation (4.28) does not only include the soft-recollsions (odd k) but also yields the points where the slope has the same value but different sign between two soft-recollisions (even k). Thus, one can give the approximate combinations of starting phase, ωt_s, that lead to a soft-recollsion by taking only odd $k = 2m + 1$ into account,

$$\delta_m = \frac{2}{(2m + 3)\pi}, m = 0,1,2, \ldots, \quad (4.29)$$

with corresponding return times, $t_r^j = (3 + 2m)\pi/\omega - 2/\pi(3 + 2m)\omega$, and starting times, $t_s = 2/\pi(2m + 3)\omega$.

Using equation (4.6) yields the final velocities, $v^f = E_0 \sin(\omega t_s)/\omega \approx 2E_0/\pi(2m + 3)\omega$ (small angle approximation) which lead to the corresponding energies,

$$T_m = \frac{1}{2}\frac{E_0^2}{\omega^2}\frac{4}{\pi^2(2m+3)^2} = \frac{8U_p}{\pi^2(2m+3)^2}, m = 0,1,2,\dots, \tag{4.30}$$

, which are $T_m \approx 0.090\,U_p, 0.032\,U_p, 0.017\,U_p, \dots$ or not using (4.30) and solving (4.27) numerically, $T_m = 0.0944\,U_p, 0.0330\,U_p, 0.0167\,U_p$. This result coincides with [37] as well as with [98] [123].

The effect of the soft-recollision in the PMD are momentum regions around momenta of $p_z \approx 2E_0/\pi(2m + 3)\omega$ parallel to the polarization of the laser field that are narrow in the velocity perpendicular to the field. The regions for $m = 0$ and $m = 2$ are encircled Figure 4.12 d). Clearly, very narrow low-energy peaks at the expected positions are found. It is expected that the soft-recollision effect will be smeared out if pulsed laser fields and averaging over the in the focus is applied to the model. These low-energy narrow regions can be very well understood by considering the angular dependence of the scattering cross-section for different velocities as shown in Figure 4.12 c). For small return velocity, v_r^{ij}, as it is the case for soft-recollision, scattering is more and more isotropic which leads to the low-energy peaks in the PMD. The shift of the peaks away from zero momentum parallel to the laser field is a consequence of the fact that the motion after scattering adds a small kick as $\boldsymbol{A}(t_r^j)$ is not zero.

The previous discussion illustrates that the SCM supports low-energy scattering features in the PMD [37] on the same footing as high-energy features [2] [16]. Both phenomena are strongly field-driven dynamics that and are governed by time-dependent evolution of the electric field on the time-scale of a few optical cycles and below. Thus, both features in the PMD are expected to be sensitive to reduction of the pulse duration to a few optical cycles and to tailoring the sub-cycle shape of the field using .e.g the carrier-envelope phase or multi-color fields. For high-energy features, the CEP sensitivity is well explored [126] and applied for the characterization of few-cycle pulses [77] with center wavelengths around 800 nm. For low-energy features similar opportunities are presently under investigation [10] [127].

4.5   Comparison between Semi-classical Model and Experimental Data

4.5.1 Details of the Numerical Implementation and an Example

After the discussion of the SCM in section 4.4, we turn to details of the numerical simulations that are compared to experimental observations later in section 4.5. The simulations use a linearly polarized field, account for the depletion of the ground state and are averaged over the three-dimensional intensity distribution in the focal volume as discussed in appendix A1.2.

The field has the frequency, ω, peak field strength, E_0, and is expressed as product of the envelope, $f(t)$, and a carrier wave,

$$\boldsymbol{E}(t) = E_0 f(t) \cos(\omega t + \phi)\,\boldsymbol{e_z}. \tag{4.31}$$

Thereby, t, denotes the time and ϕ is the carrier-envelope phase. A typical envelope of the laser pulse, $f(t)$, would, e.g., be a Fourier-transform-limited Gaussian, i.e. $f(t) = \exp(-2\ln2 t^2/\tau^2)$, where τ denotes the full-width half-maximum pulse duration of the intensity, $I(t) = f(t)^2 = \exp(-4\ln2 t^2/\tau^2)$. However, this envelope is not very convenient for numerical calculations as ensuring $\int_{-\infty}^{\infty} F(t)\, dt \approx 0$ with sufficient accuracy requires to calculate over a long time interval. Instead, it is common to use a $\sin^2$-shape envelope although it does not represent a physical field of a traveling wave. A convenient form is [106],

$$f(t) = \begin{cases} \sin^2(\omega t/4n - \pi/2) & \text{if} & t \geq -nT \text{ and } t < 0 \\ 1 & \text{if} & t < NT \\ \sin^2(-\omega t/4n + \omega TN/4n + \omega T/4) & \text{if} & t \geq NT \text{ and } t < (N+n)T \end{cases}. \tag{4.32}$$

Here, n and N are natural numbers that influence the field as illustrated Figure 4.13. One should notice, that, $f(t) = 0$, except on the interval, $t = [-nT; (n+N)T]$. This limits the necessity of the calculation the interval where the field is defined. Subsequently, conservation laws are used to calculate the asymptotic limit, $t \to \infty$. Figure 4.13 illustrates $E(t)$ which starts with a turn-on ramp of length, nT, is followed by a flat part of length, NT, until a turn-off with $\sin^2$-ramp goes back to zero. Although, this seems to be a very artificial and arbitrarily chosen shape of the field, it is useful to investigate the interaction in the long pulse limit as a number of optical cycles have the same amplitude. Also, varying, N, allows to study effects which stem from subsequent cycles [106].
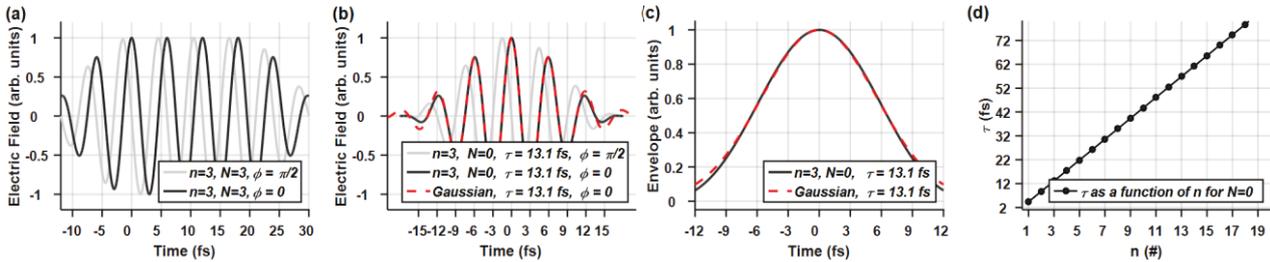
Figure 4.13: The laser field which is used to model strong-field ionization
For the illustrative example, a wavelength of $\lambda = 2\pi c/\omega = 1800$ nm for the carrier wave is shown. Choosing $N > 0$ allows investigating of the long pulse limit at reduced time interval for the numerical integration, see (a). (b) Choosing, $N = 0$, yields a field that is very similar to that of a Gaussian envelope with appropriate pulse duration. Also, the influence of the carrier-envelope phase is reproduced correctly. (c) is a comparison of the envelopes and (d) shows the relation between the intensity FWHM pulse duration of a Gaussian and the parameter, n.

Further, setting, $N = 0$, and choosing ,$n \geq 1$, yields a field and intensity profile which is very similar to a Gaussian envelope as the comparison performed in Figure 4.13 (c) shows. Thereby, the integer number, n, is used to match the intensity FWHM duration τ of the Gaussian envelope as shown in $\tau(n)$, Figure 4.13 (d). The pulse duration can be changed in steps of, n, i.e. in steps of the period of the carrier-wave. The constants that are used to model the Xenon target properties are given in Table 4.1. Adjusting the constants allows to investigate the influence of the target gas on the final PMD on a qualitative level.

Atom	$|I_P|$ (eV)	B	l	C_{nl}	m	β	r_c (a.u.)	Z	μ	ξ
Xe	12.13	1	1	2.72	± 1	*9.0*	2.46	54	3.604	3/2

$$Q(l,m) = (-1)^{(|m|-m)/2} \sqrt{\frac{(2l+1)(l+|m|)!}{2(l-|m|)!}}$$

Table 4.1 Parameters for the tunnel ionization rate of Xenon in the semi-classical model. [128][110][129][130][131][132][133]. Values that are given in italic, are reasonable estimates.

The simulations account for the three-dimensional intensity distribution in the focus as given in appendix A1.2. Therefore, the yield, $Y(I)$, at the end of the laser pulse, $Y = C(t = t_{end})$, as function of intensity, $Y(I)$, is first calculated by integrating (4.10) for different intensities. Multiplying $Y(I)$ with the frequency of intensities as they are present in the focal volume, $F(I)$, a curve that measures the fraction which a single intensity contributes to the intensity averaged result $H(I) = Y(I) F(I)$.
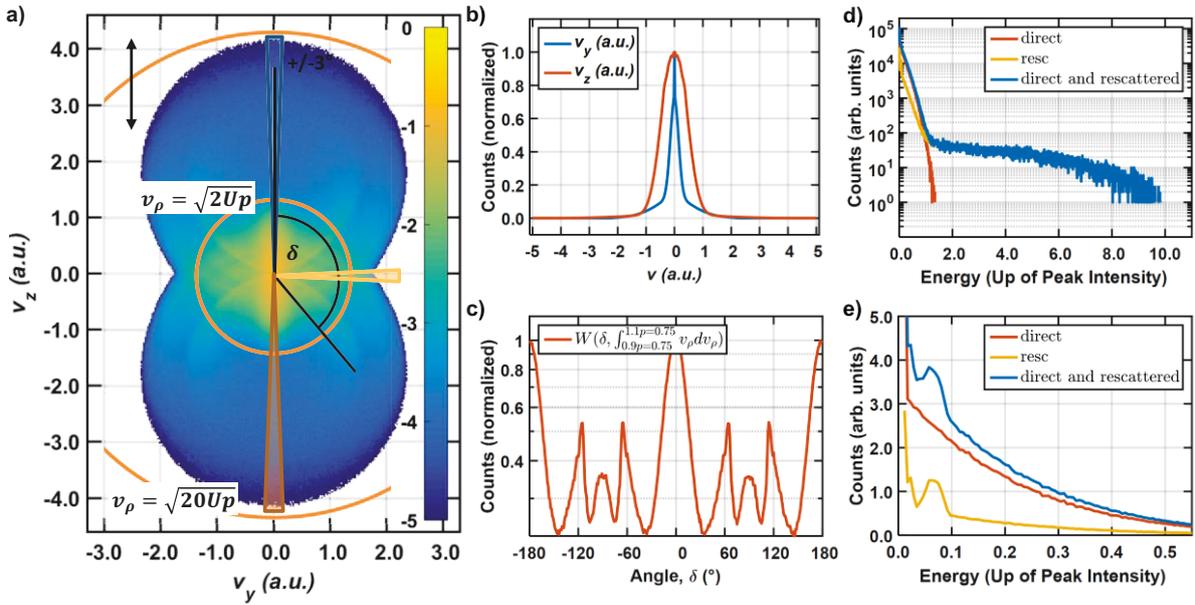
Figure 4.14: Example of a simulated PMD

a) shows the simulated PMD for a peak intensity, $I_0 = 8 \times 10^{13}$ W/cm^2, and an $n = 18$-cycle pulse with a center wavelength of $\lambda = 1780$ nm. The calculation is averaged over the intensity distribution in the focal volume as well as over the CEP. In b), the projection on each of the coordinate axis are given and c) shows the angular dependence of the photoelectron yield for a certain momentum range in a semi-logarithmic plot. d) and e) are photoelectron spectra that were extracted from a) for electron emission around a narrow angle parallel to the polarization of the laser. d) shows the spectrum over the entire energy range using semi-logarithmic plot. e) is a zoom into the low energy region but a linear scale is used. High-energy rescattering forms the characteristic plateau in d) and low-energy rescattering is responsible for the pronounced low-energy peaks in e). At intermediate momenta, the angular dependence, c), is structured due the scattering from multiple return orders with intermediate energies.

Figure 4.14 illustrates a typical results of the simulation. The figure is organized very similarly to Figure 4.10 and Figure 4.9. The characteristic features discussed in the previous section survive averaging over the intensity distribution in the focal volume and can clearly be identified. These are direct ionization with quickly decaying yield for increasing energy in the region, $|v| < \sqrt{4U_p}$ (discussed in 4.4.5.1) and a rescattered contribution (discussed in 4.4.5.2) that is spread over a larger momentum range with a broader angular distribution and has thus lower probability. The rescattered contribution exhibits several characteristic features. (i) At low energy, the peaks, seen in Figure 4.14 e) slightly below $\sim 0.1 U_p$ are the low-energy structure [9] [34]. (ii) At intermediate energies a particularly pronounced angular dependence [10] [108], named "Fork" is observed, see Figure 4.14 c). (iii) The plateau in above-threshold ionization, [2] [16] is found in the high-energy range. Besides demonstrating that the characteristic features survive averaging over the intensity distribution in the focus, Figure 4.14 illustrates that intensity averaging shifts the energy position of the features to lower energies if the energy is measured in units of the pondermotive potential calculated for the peak intensity in the focal volume. It reflects that that the peak intensity contributes with very small volume only. In addition, averaging over the intensity distribution in the focus smoothes the appearance of the features (i)-(iii).

4.5.2 Influence of the Pulse Duration on the PMD

The influence of the pulse duration in experiment and theory is compared in Figure 4.15. The used parameters, peak intensity, pulse duration, three-dimensional focal spot in the calculation match the experimental conditions within the error bars of their experimental determination. A visual comparison shows a reasonable match, i.e. the overall shape with a cigar-like region with high yield at momenta below $|p_y| < 0.3$ is reproduced. Outside this region, one finds a quickly dropping yield with a wider angular spread in both theory and experiment. For the long pulse measurement and simulation, Figure 4.15 a)-d), the scattered contribution yields a Fork-like structure (labeled with fork in Figure 4.15 a) and c)) at small momenta, $|p_x|$ (parallel to the laser polarization). Also, the low-energy structure can be found in both theory and simulation. Reducing the pulse duration in Figure 4.15 e)-f) changes the measured PMD and the simulated PMD similarly on a qualitative level, the fork structure is washed out and the low-energy peaks move to smaller momenta. For both cases, i.e. long pulse and short pulse, the simulation is not reproducing the spider-like (Figure 4.15 a)) features as the interference between electrons from different trajectories is neglected by the SCM.
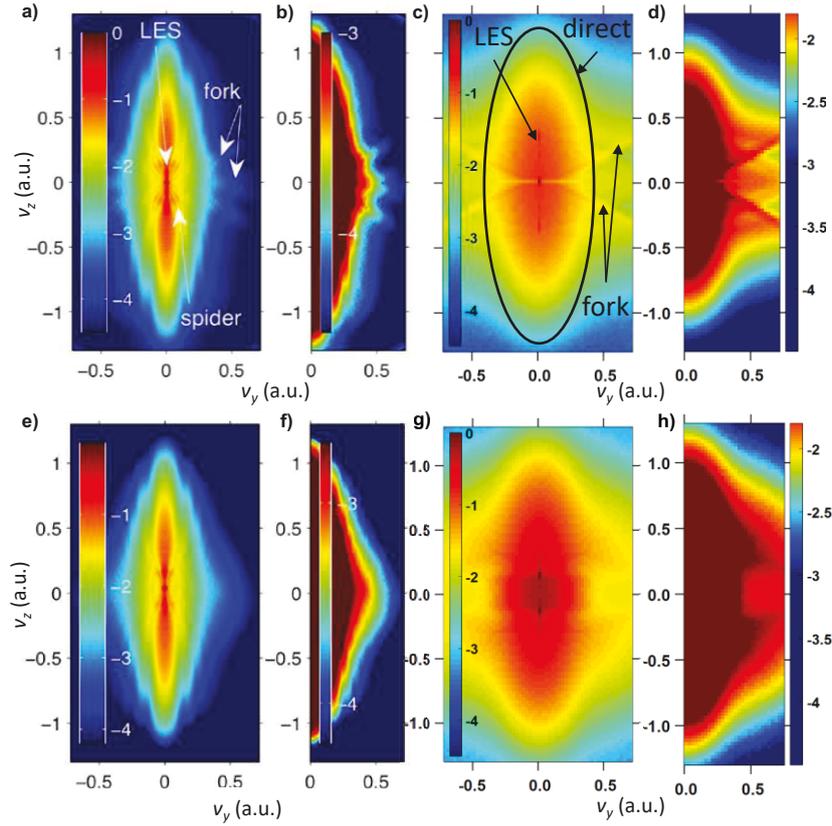
Figure 4.15: Comparison between measured and modeled PMD

a) - d) show the measured, a) and b), and calculated, c) and d), logarithm of the PMD from ionization with the long laser pulse for a peak intensity of, $I_0 = 8 \times 10^{13}$ W/cm^2, with a center wavelength of $\lambda = 1780$ nm. Previously mentioned features are labeled, i.e. LES, fork and spider in a). The pulse duration in the experiment has been 75 fs (intensity full-width half-maximum) such that $n = 18$ is used in the calculation. The color scale in b) and d) is clipped in order to emphasize the fork-like structure marked in a). Measured, e)-f), and simulated, g)-h), logarithm of the PMD for ionization by a few-cycle pulse with a duration of 11 fs (intensity full-width half-maximum) for the same center wavelength and peak intensity are shown. $n = 2$ has been used in the calculation, which yields slightly shorter pulse duration of 9 fs (intensity full-width half-maximum) in the simulation. In addition to the characteristic features that are labeled a), the momentum region where direct electrons are found is encircled in c). The spider-structures are absent in the simulations as the SCM is not able to explain them. They are not of interest for the focus here.

A conspicuous difference between the measurement and the simulation is the width of the cigar-like region with high yield in the center of the PMD in Figure 4.15 c), d), g) and h). In this region, ionization of the direct contribution is dominant and gives obviously a too wide distribution along the p_y axis. It is clear that this can be cured by adjusting the pre factor, $\kappa = \sqrt{2I_p} \rightarrow \kappa' = \eta\sqrt{2I_p}$ in equation (4.11) as it has been done in [13]. Choosing e.g. $\eta = 3.5$ would give a narrower spread of the direct ionization along the p_y-axis in Figure 4.15 that fits the experimental data better. A starting point to justify this ad-hoc adjustment is given by considering the fact that the SCM neglects the influence of the Coulomb potential on the electron wave packet for direct electrons. The Coulomb potential would contract the wave packet of direct electrons to a narrower distribution while it is accelerated away by the laser field causing so-called Coulomb focusing [134].

A more detailed comparison of the angular dependence of the photoelectron yield for a momentum of $v = 0.75$ is done in Figure 4.16. Changing the pulse duration influences the angular distribution at this momentum, i.e. the three-pronged fork-structure for the long pulse is washed out for the short pulse in measurement and simulation, see the figure caption for details.
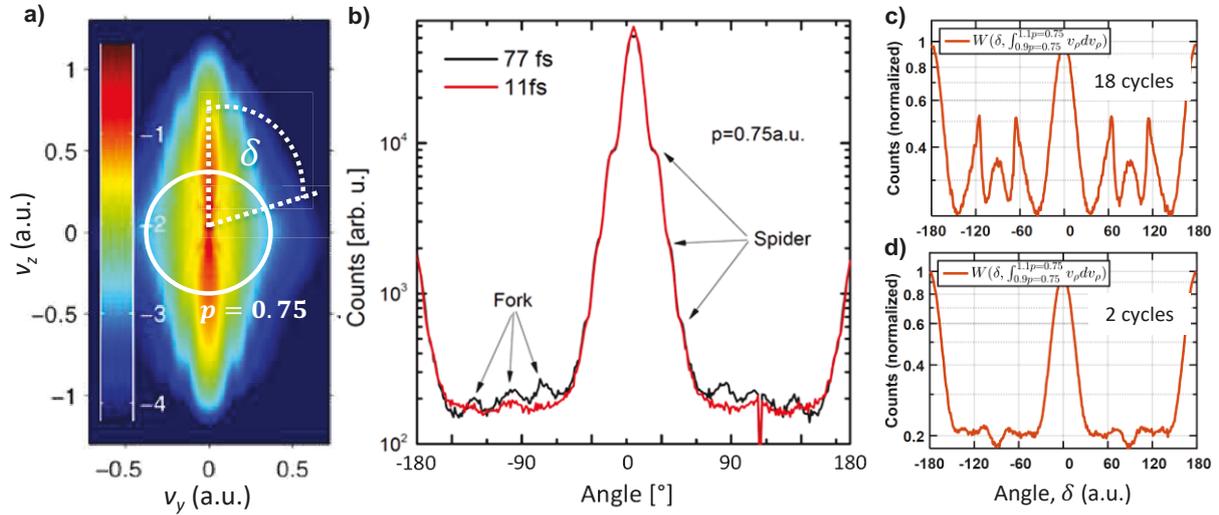
Figure 4.16: Comparison of the Fork between measurement and simulation

a) illustrates the angle δ and the momentum $p = 0.75$ at which the angular dependence of the photoelectron yields is compared in b) for measurement, long pulse (black) and short pulse measurement (red), and simulation in c) and d) as indicated. The fork is more pronounced for the long pulse in both measurement and simulation. Shortening the pulse to few-cycle duration, affects the angular distribution, i.e. the pronounced peaks are washed out.

In Figure 4.17, the influence of the pulse duration on the position of the LES peak in the photoelectron spectra parallel to the polarization axis is illustrated. It has been found experimentally that the position shifts to lower energy if the pulse duration is reduced to a few optical cycles [45], Figure 4.17 a). This could be confirmed by the simulations based on the SCM as implemented here, see Figure 4.17 b) and c). A detailed experimental and theoretical investigation of this effects has been done by others in [99] where Figure 4.17 d) is taken from. As the definition of the laser field used in [127] differs from the definition of the field used here, i.e. in (4. 31) / (4.32), the pulse duration of the data from [127] has been converted such that it matches the field definition in equation (4. 31) / (4.32). The position of the LES peak position as function of pulse duration after conversion is shown in Figure 4.17 e). Error bars from the experimental results in Figure 4.17 d) have been omitted. Also, theoretical results from [127] that were obtained based on the soft-recollision model have been converted. Thus, the dependence in Figure 4.17 e) contains measured data and simulated data from two models. Thereby, the pulse duration is given in units of n that matches the definition in equations (4. 31) and (4.32) with $N = 0$. Figure 4.13 d) can be used to convert to the intensity full-width half-maximum pulse duration.

Figure 4.17 e) shows a very good match between the theoretical results obtained with the SCM as implemented here. Given the fact that theoretical results from soft-recollision model in [127] were "shifted down by 15% to match the experiment", the agreement achieved with the SCM here is even superior. The origin of this mismatch between

experimental data and the soft-recollision model in [127] can have several reasons. It is part of the discussion in [127].
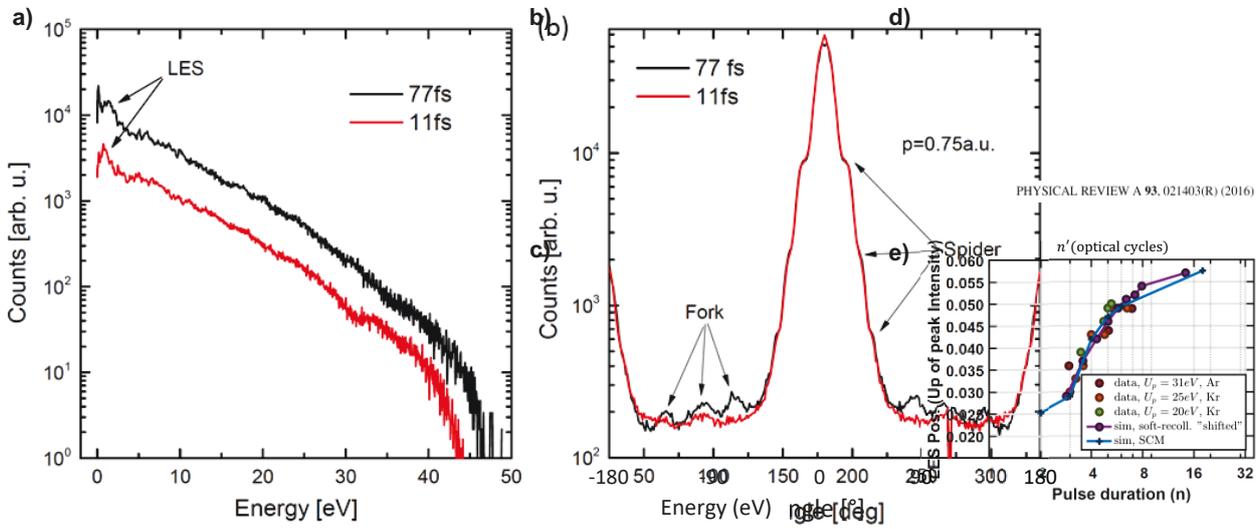
Figure 4.17: Comparison of the low-energy peak position as function of pulse duration

In a), measured photoelectron spectra parallel to the polarization of the laser field for the long and the short pulse are shown. These experimental results were obtained in Xenon for $U_p = 24$ eV at the peak of the field. The curves have been separated along the y-axis in order to improve visibility. The rescattered high-energy photoelectrons above 50 eV are missing as they were not detected in the measurement. The position of the LES peak (marked by LES) changes if the pulse is shortened. b) and c) show the results of the simulation that is averaged over the focal volume and the CEP. d) is taken from [99] where the position of the LES peak as function of the pulse duration has been investigated in detail. Dots with error bars are experimental results obtained in Krypton for $U_p = 20$ eV (green) and $U_p = 25$ eV (orange) and Argon for $U_p = 31$ eV (red circles). Black triangles are the results of the classical simulation [123]. The lines are results from an analytical model based on the soft-recollision [99]. e) shows the data from [99] and simulated data from SCM model as implemented here. Thereby, the pulse duration of data from [99] has been converted to match the definition of the field here.

The agreement between experimental data and the SCM simulations, which is confirmed in Figure 4.15, Figure 4.16 and Figure 4.17, supports the statement that SCM reproduces low-energy features on a qualitative level reasonably well. In addition, it shows that the low-energy features are strongly governed by the laser field. The LES peak position is independent of the atomic target and if measured in units of the pondermotive potential U_p independent of the used wavelength and intensity of the used laser. With that, we continue to trace the observed changes in the PMD to the field-governed trajectories.

4.5.3 Tracing the Influence of the Pulse Duration to the Trajectory

The previous chapter illustrates the qualitative agreement between experimental data and the SCM. Major features of the PMD, e.g. the LES peaks, the high-energy plateau and the "Fork" are reproduced and behave as one would expect from the SCM if the pulse duration is reduced. At the same time, it is obvious that the SCM oversimplifies some aspects. E.g. the experimentally observed "Spider" structure is absent in the theory due the neglected interferences between different electron orbits. Further, the direct contribution to the PMD yields a too wide distribution in the direction perpendicular to the polarization of the linearly polarized field which might be due to neglecting the influence of the binding potential on the direct trajectories. Despite these mismatches, the SCM is well suited for gaining insight into the interaction as its basis on classical trajectories in the field allows an easy and straightforward interpretation.
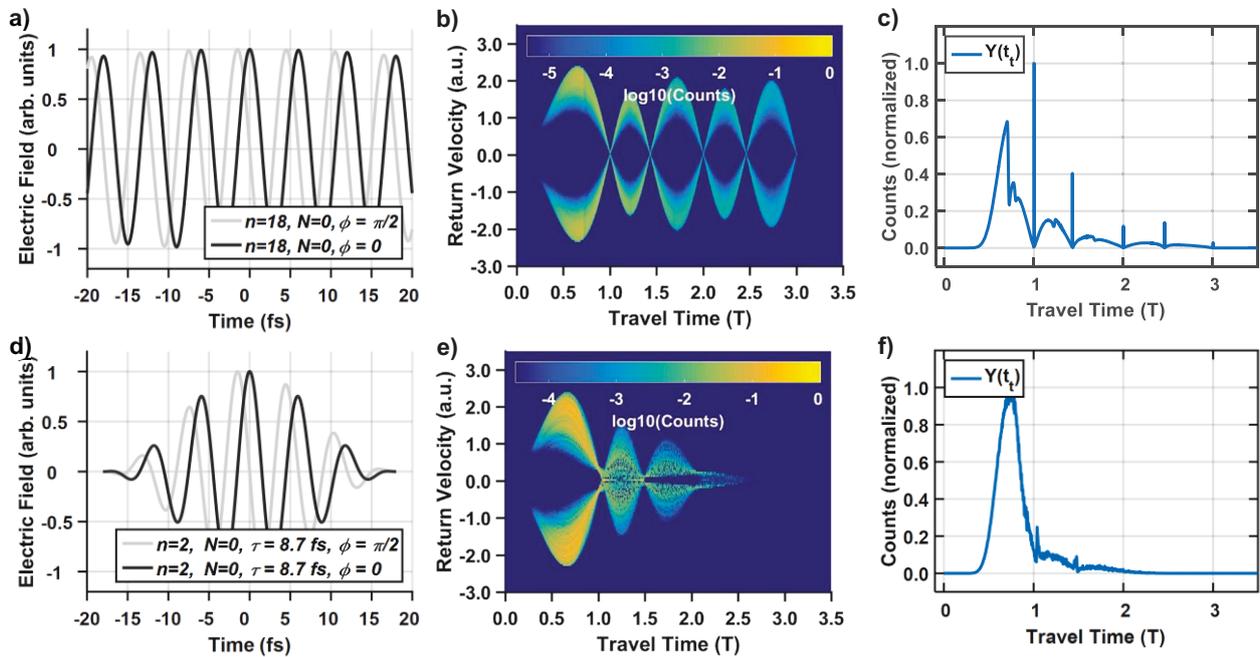
Figure 4.18: Tracing the influence of the pulse duration to the trajectories

a) and d) show the field around the peak of the envelope of the long pulse and the short pulse for two different CEPs. b) (long pulse) and c) (short pulse) are two-dimensional histograms of the return velocity and travel time. While the long pulse allows high-order returns, i.e. long travel times, to significantly contribute to rescattered contribution of the PMD, this is naturally not supported by the short pulse. Thus, the two-dimensional histogram in e) exhibits a higher yield for short travel times and lowered yield at longer travel time. The argument is further supported by e) and f) where the histogram of the travel time is shown. For the long pulse in c), also long travel times contribute while only short travel times contribute in f).

In Figure 4.18, the SCM simulations are used to trace the changes in the PMD to the time-dependent shape of the laser field. Therefore, the fields for the long pulse and the short pulse are compared in Figure 4.18 a) and d). Two-dimensional histogram of the travel time and the return velocity are shown in b) and c) for the long pulse and the short pulse, respectively. They reflect that the long pulse naturally supports longer travel times while for the short pulse only short travel times contribute to rescattering, see c) and f) also. In addition, the shape of the field alters

the timing and thus influences the momentum distribution of the rescattered contribution directly as the vector potential at two times is relevant for the final momentum, i.e. $\boldsymbol{A}(t_s)$ and $\boldsymbol{A}(t_r^j)$ as, $\boldsymbol{v}_{sc}^f(\theta, t_r^j, t_s) = -\boldsymbol{A}(t_r^j) + [\boldsymbol{A}(t_r^j) - \boldsymbol{A}(t_s)][\cos(\theta)\,\boldsymbol{e}_z + \sin(\theta)\,\boldsymbol{e}_y]$, is involved for these trajectories. Reducing the duration of the laser field to a few optical cycles, changes the combinations of $\boldsymbol{A}(t_s)$ and $\boldsymbol{A}(t_r^j)$ that contribute. The sharp peaks in Figure 4.18 c) are related to the soft recollisions where the return velocities is very low such that the model pics these rescattered trajectories with high probability. Comparing to Figure 4.18 f) for the few-cycle field, these trajectories are heavily suppressed as the few-cycle does not support these trajectories. Again, the reason lies in the accessible combination of starting and return times which are governed by the shape of the field.

Particularly, Figure 4.18 b) and e) are interesting from another point of view. The presented histograms illustrate the probability for returning with some return velocity at some travel time after the starting time. From this, regions with high $|\boldsymbol{v}_r| = |\boldsymbol{A}(t_r^j) - \boldsymbol{A}(t_s)|$ are limited to a short time interval around $t_t^j \sim 0.6T$. Employing so-called laser-induced electron diffraction (LIED), in a few-cycle field with controlled, carrier-envelope phase, it is imaginable that reading of the photoelectron yield at different final energies can gives access to the scattering cross-section over a time-span which is longer than one optical cycle. Further, one might envision pump-probe measurements where a short pump pulse starts some molecular stretching dynamics and LIED in CEP controlled few-cycle probe pules is used to follow the stretching dynamics over an extended range of pump-probe delays.

4.6   Conclusion and Outlook

In conclusion, the velocity-map imaging (VMI) technique has been used to compare three-dimensional photoelectron momentum distributions (PMDs) from strong-field photoionization of Xenon by short-wavelength infrared (SWIR) laser fields. Besides enabling the experimental observation of several features in the PMDs that are characteristic for this wavelength range e.g. spider-like holograms and low-energy structures, the measurements motivated the experimental and theoretical investigation of a pronounced fork-like structure, the so-called off-axis low-energy structure (off-axis LES). It appears close to right angle to the field's linear polarization. Comparing measurements with many- and few-cycle fields, demonstrated strong susceptibility of the fork and other features to the pulse duration of the ionizing laser pulse.

The performed semi-classical simulations show that on- and off-axis LES features are supported by the semi-classical model of strong-field ionization (SCM) and that they can be traced to electron trajectories which scatter off the atom before they reach the electron detector. To this end, the SCM got augmented by: (i) Rescattering trajectories which are substantially longer than one optical cycle. (ii) A scattering cross-section that depends on the scattering angle as well as on the scattering velocity and (iii) by a proper method to normalize the weight between returns of different optical cycles (return order) which takes the angle- and velocity dependence of the scattering cross-section into account.

During the analysis, it has been pointed out that the velocity- and angle-dependence of the scattering cross-section leads to the situation that trajectories with long travel times and low return velocity (i.e. the "soft-recollisions") can have higher yield than trajectories with shorter travel time but higher return velocity (i.e. the "hard recollsions"). The contributions from electron trajectories of this kind lead to on- and off-axis low-energy features in the PMD that

are particularly prominent for strong-field photoionization by infrared fields. Simulations for the few-cycle field could show that the experimentally observed changes in the PMD occur as the few-cycle field does naturally not support the these trajectories with long travel times. Altogether, these findings put the low-energy features in above-threshold ionization onto the same footing as e.g. high-energy features such as the plateau.

For future work, it might be interesting to control the shape of the laser field with sub-cycle resolution by e.g. using the CEP in few-cycle pulses. Besides more detailed insight into low-energy scattering phenomena, investigation of the CEP dependence might lead to approaches for CEP measurement of few-cycle short-wavelength infrared (SWIR) fields similar to as it is done based on with high-energy rescattered electrons at shorter wavelength of the ionizing laser [135] [7]. Working towards sub-cycle control of the laser field can also be beneficial for laser-induced electron diffraction where it can be used to tailor the time-dependent velocity distribution of the returning electrons in such a way that laser-induced electron diffraction signals over an extended or tailored time window could be measured. Further, one might envision the use of laser-induced electron diffraction in CEP-controlled few-cycle fields to follow molecular dynamics over an extended time interval using pump-probe schemes.

5 Probing Strong-Field Photoionization of a Beam of H_2^+ at Short-Wave Infrared Wavelength

5.1 Introduction and Outline

The interest in strong-field photofragmentation of small diatomic molecules has been stimulated by the discovery of new phenomena in strong-field ionization of atoms such as above-threshold ionization (ATI) [1] in 1979. Due to the additional rotational and vibrational degrees of freedom, photo fragmentation of diatomic molecules leads to several additional phenomena [136] [18] [137], for which the hydrogen molecular ion, H_2^+, and it's isotopologues, D_2^+, as the simplest diatomic molecule serve as the benchmark systems.

The interaction of H_2^+ with a strong laser field can lead to multiphoton/strong-field dissociation ($H_2^+ \rightarrow H + H^+$) and ionization ($H_2^+ \rightarrow H^+ + H^+ + e^-$). For each fragmentation channel, several phenomena have been observed and are investigated using steadily improving measurement techniques as well as the expanding range of accessible experimental parameters in laser intensity, wavelength and pulse duration. To name a few examples for each of the channels, without having the aspiration of giving a complete list, dissociation is related to the phenomena of bond-softening [24], bond-hardening/vibrational trapping [138], zero-photon dissociation [139], laser-induced alignment [140] and above threshold detachment [141] [21]. For ionization, enhanced ionization, Coulomb explosion [142] and frustrated tunnel ionization are of relevance. More recently, coupling between electronic and nuclear dynamics particularly for ionization is catching the interest of investigations [143] [75] [39] [144], as well studies where the sub-cycle shape of the laser field is used to control the fragmentation exploiting, e.g. the carrier-envelope phase [145] [15] or the relative phase between two-color fields [146].

As mentioned, measurement techniques on strong-field fragmentation of H_2^+ have become more differential and "cleaner" over time. In order to structure them, the method of H_2^+ preparation can be used. In the early days, , strong-field photoionization of H_2 has been used to create H_2^+ as a transient species during the same laser pulse that probes the dynamics in H_2^+. Typical measurement quantities have been photoelectron or ion energy spectra. It is clear that this method of H_2^+ preparation and variants of it (e.g. pump-probe schemes), require some modeling on the creation of H_2^+ from H_2 in order to have a hand on initial conditions for the interaction between H_2^+ and the field. However, this is typically not trivial as strong-field photoionization (SFI) of H_2^+ from H_2 creates a coherent vibrational wave packet in the H_2^+ ion, which will not have dephased when the interaction between the field and H_2^+ starts only atto- and femtoseconds later. Therefore, interpretation of experimental results that use this scheme can be difficult.

Nowadays, modern Ion Target Recoil Ion Momentum Spectroscopy (ITRIMS) setups [14] [15] [83], see chapter 3.4.1, use coincidence imaging techniques to measure three-dimensional vector momenta of all fragments from strong-field fragmentation of an ion beam of H_2^+ molecules. This means, for dissociation $H_2^+ \rightarrow H + H^+$, the momenta of the proton, $\boldsymbol{p}_{H^+}$, and the hydrogen atom, $\boldsymbol{p}_H$, are measured. For ionization $H_2^+ \rightarrow H^+ + H^+ + e^-$, the proton momenta, $\boldsymbol{p}_1$ and $\boldsymbol{p}_2$, and the electron momentum, $\boldsymbol{p}_e$, can be measured [83]. In these ITRIMS setups, H_2^+ is typically created by electron impact ionization of H_2 in an ion source. Afterwards, it travels for several microseconds from the ion source to the region where it interacts with the laser. Thus, the initial distribution of vibrational states can well be approximated by an incoherent sum where the population follows a Franck-Condon distribution of an

electronic transition from H_2 to H_2^+. This removes the necessity of modeling the initial step of H_2^+ creation by the laser, but it is on cost of experimental complexity as handling of a low density ion beam is necessary.

Independent whether an ion beam has been used or not, the vast majority of existing experimental studies have been done at laser wavelength in the visible and near-infrared spectral range below 1 μm. With recent advances in laser technology, measurements at infrared wavelength are now possible. Despite curiosity and experimental availability, investigating fragmentation dynamics of H_2^+ using strong infrared fields is motivated by the idea that a strong external laser field forces the motion of the electron to the optical cycle. If the optical period is long enough such that the nuclei can significantly move during one cycle, interesting phenomena of coupled electron nuclear dynamics might be expected for dissociation and ionization.

Here, the Jena ITRIMS setup is used together with the output of the optic parametric amplifier to study intensity-dependent strong-field fragmentation of an H_2^+ ion beam target by a laser field with short-wave infrared wavelength. The measurement contains intensity tagged vector momentum data of events of the two fragmentation channels, dissociation $H_2^+ \rightarrow H + H^+$, and ionization, $H_2^+ \rightarrow H^+ + H^+ + e^-$. However, the discussion of data analysis as well as modeling of the interaction focuses on the ionization channel.

In section 5.2, details on the measurement setup are shortly reviewed together with improvements, which have been realized during this thesis. Specifically noteworthy is section 5.2.1 where the possibility to extract the momentum of the photoelectron $\boldsymbol{p}_e$ from the measurement of the two proton momenta, $\boldsymbol{p}_1$ and $\boldsymbol{p}_2$, using momentum conservation is demonstrated. It opens the opportunity to gain insight into correlated electron nuclear dynamics by investigation of $\boldsymbol{p}_e$ in dependence of the correlated proton momenta. With the aim of keeping the modeling simple while the fundamental dynamics are captured, a one-dimensional two-level model on strong-field photoionization of H_2^+ is proposed in section 5.3. It considers the nuclear dynamics by coupling of two electronic levels in the time-dependent external field and takes ionization into account using sets of quasi-static ionization rates, which are sensitive to the internuclear distance, R, and the instantaneous field strength, $|E|$. As natural for a one-dimensional model, rotations are neglected. Two versions of the model, which use different sets of ionization rates, are compared to the measurement results in section 5.4. The results of the investigation are concluded in 5.5.

5.2 Intensity Dependent Ionization of a Beam of H_2^+ at Short-Wave Infrared Wavelength

The measurement combines the output of the femtosecond OPA, see section 2.3, with the ITRIMS setup that has been presented in chapter 3.4. More details on the ITRIMS are documented in [21] [70] [69]. The next chapters focus on implemented improvements and measurement procedures which have been realized here. Further, some experimental effects that are relevant for interpretation of the measured data are addressed.

In order to remind the reader, Figure 5.1 shows a combination of two previous figures from section 3.4. A sketch of the ITRIMS setup is shown in Figure 5.1 a) and an example of the measurement result on strong-field fragmentation of H_2^+ can be found in Figure 5.1 b). As mentioned, the result of the measurement are two lists of triples, $\{\boldsymbol{p}_1, \boldsymbol{p}_2, I_0\}_i$, of i identified valid ionization and k dissociation events, $\{\boldsymbol{p}_{H^+}, \boldsymbol{p}_H, I_0\}_k$. Each contains the momenta of the two heavy fragments, i.e. protons, $\boldsymbol{p}_1, \boldsymbol{p}_2$ for ionization, and $\boldsymbol{p}_{H^+}, \boldsymbol{p}_H$, for dissociation and corresponding value of the peak intensity of the laser, I_0. The opportunity of automated scanning and tagging of the

peak intensity has been added to the ITRIMS setup during this thesis. Details of the realization are presented in 5.2.2.
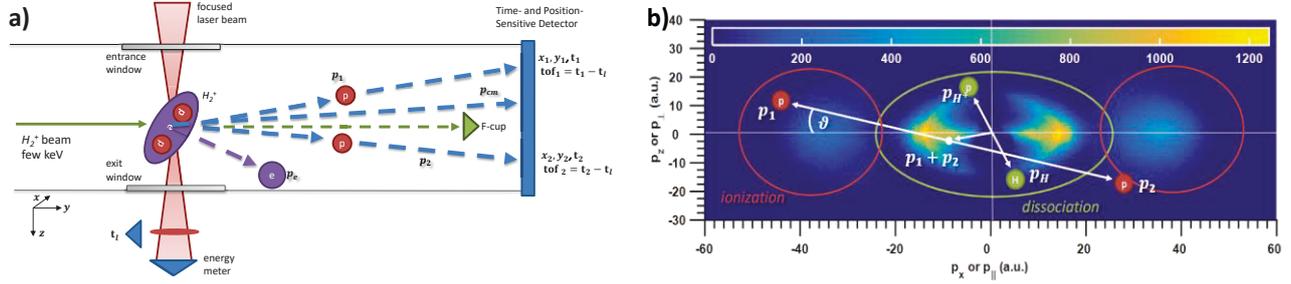

Figure 5.1: Reminder of ITRIMS principle and the typical measurement results

a) shows fragment detection scheme in the ITRIMS. The ion beam comes from the left and crosses the laser beam at an angle of 90°. Due to the initial velocity of the ion beam, the fragments continue to fly towards the position and time-sensitive delay-line detector where the measurement of impact time and position is the basis for determination of the fragment momenta. Longitudinal and transversal static electric fields that are not drawn, separate the fragments in space and time on the detector. Created photoelectrons are not detected. The symbols illustrate fragments, (e) – electron, (p) – protons and parts of the ITRIMS setup. b) illustrates experimental results of strong-field fragmentation of a beam of H_2^+ ions. A two-dimensional histogram projected into the plane of the linear polarization of the laser is shown. The polarization of the laser is parallel to p_x. Ionization events have larger proton momenta than dissociation events and are found in the outer region of this plot while dissociation events are found in the inner region.

Binning of the individual events to one or more dimensional distributions and spectra using MATLAB enables the analysis of differential rates on fragmentation channels (here ionization or dissociation) of interest. An example for such a result is given in Figure 5.1 b). A two-dimensional momentum distribution after strong-field fragmentation of H_2^+ projected into the plane of the linear laser polarization is shown. The plot contains data on dissociation (encircled green, lower momenta) and ionization (encircled red, larger momenta). Events from all peak intensities are taken into account or in other words, it is integrated over the distribution of peak intensities which have been present over the time of the measurement. The linearly polarized laser is aligned parallel to the x-axis of the coordinate system.

The fact that dissociation events are found at lower momenta reflects that their kinetic energy release (KER) is smaller compared to the KER of ionization. The KER distribution of ionization, i.e. the yield as function of $E_{KER} = (p_1 - p_2)^2/2m_{H^+}$ following the derivation in 3.2.3 is analyzed in detail and compared to simulations in section 5.4. The angle, ϑ, in Figure 5.1 denotes the angle between the orientation of the linear polarization of the laser and the vector $p_1 - p_2$ (for ionization) respectively, $p_{H^+} - p_H$ (for dissociation).

The overlaid arrows and symbols in Figure 5.1 b) are exemplary for one specific dissociation and one specific ionization event within the histogram. They illustrate that all events are given within the center of momentum frame of all dissociation events, i.e. all momenta are given relative to $\sum_k (p_{H^+} + p_H)_k = \sum_k p_{0_k} = P_0 = MV_0 \equiv 0$ with $M = m_{H^+} + m_{H^+} + m_{e^-}$ using the notation of chapter 3.2.3. Using this reference, leads to the fact that the sum momentum $p_1 + p_2$ of an individual ionization event is shifted with respect to P_0 as it is indicated by the white arrows. This shift can be used to infer the corresponding electron momentum as momentum conservation yields,

$\boldsymbol{p}_1 + \boldsymbol{p}_2 = -\boldsymbol{p}_e$, as discussed in 3.2.3. However, the precision of this method depends on the initial momentum spread of the incoming H_2^+ molecules of the ion beam target. This spread can be characterized using the dissociation data of H_2^+. To that end, one employs that laser-induced fragmentation does not change the total momentum if the momenta of all fragments are measured, i.e. $\boldsymbol{p}_0 = \boldsymbol{p}_{H^+} + \boldsymbol{p}_H$ where $\boldsymbol{p}_0$ is the initial momentum of an individual H_2^+ molecule. Thus, analysis of the measured distribution of $\boldsymbol{p}_0 = \boldsymbol{p}_{H^+} + \boldsymbol{p}_H$ can be used to characterize the initial momentum spread of the ion beam target. Details of the procedure are given in section 5.2.1.

In section 5.2.3 several experimental effects, i.e. the event rate, focal volume effects and the saturation intensity, chirp, carrier-envelope phase, and the distribution of initial vibrational states, which are relevant for interpretation and analysis of the experimental results are addressed.

5.2.1 Measuring the Electron Momentum without Detecting It

Kinematic complete measurements, i.e. measurements where the momenta of all fragments are measured in coincidence, yield deep insight into laser-induced fragmentation dynamics and are thus highly desirable. While such measurements are regularly done for laser-induced fragmentation of neutral targets using COLTRIMS (measuring the electron and the corresponding recoil ion), they are less common for laser-induced fragmentation of ion targets in ITRIMS setups. For the case of the prototype reaction of SFI of a beam of H_2^+ ions i.e. for $H_2^+ \rightarrow H^+ + H^+ + e^-$ (measurement of the two proton momenta, $\boldsymbol{p}_1, \boldsymbol{p}_2$ and the electron momentum, $\boldsymbol{p}_e$), only one realization of a kinematic complete measurement [75] [83] exists. Major reasons for this limited number of realizations are the necessity of detecting a three-particle coincidence, experimental complexity (ion beam handling, electron detector, ion detector), low density of the ion target (signal to noise for the electron measurement) and the initial momentum spread of the ion beam target (high temperature) which is comparable to the typical size of the momentum kick that is acquired by the electron for the typical laser wavelength of 800 nm [83].

Here we demonstrate an experimental method to measure the electron momentum without detecting it. To that end, we use momentum conservation, $\boldsymbol{p}_1 + \boldsymbol{p}_2 = -\boldsymbol{p}_e$, to infer $\boldsymbol{p}_e$ from the measurement of $\boldsymbol{p}_1 + \boldsymbol{p}_2$. Not detecting the electron significantly reduces experimental complexity, but is at the cost of resolution for the electron momentum as $\boldsymbol{p}_e$ obtained by this method is blurred by the initial momentum distribution of the target. Therefore, the method becomes particularly successful if laser fields with infrared wavelength are used as is demonstrated.

As said, inferring $\boldsymbol{p}_e$ from the measured $\boldsymbol{p}_1 + \boldsymbol{p}_2$ is blurred by the initial momentum distribution of the target beam. In order to characterize the effect of this blurring, we employ that laser-induced dissociation of H_2^+ fulfills momentum conservation $\boldsymbol{p}_0 = \boldsymbol{p}_H + \boldsymbol{p}_{H^+}$ as discussed in chapter 3.2.3. It means that the measured sum momentum of the two dissociation fragments is equal to the initial momentum of the H_2^+ molecule before the interaction with the laser. Making histograms of the measured $\boldsymbol{p}_0$ along each coordinate axis, $D_x(\boldsymbol{p}_{0x}), D_y(\boldsymbol{p}_{0y}), D_z(\boldsymbol{p}_{0z})$, in the laser frame of reference (linear polarization along the x-axis) yields the plot in Figure 5.2 a). Fitting normal distributions to each gives an estimate for width as the standard deviation along each direction. They are, $\Delta p_x = \sigma_x \approx 0.53$ a. u. , $\Delta p_y = \sigma_y \approx 0.43$ a. u., and $\Delta p_z = \sigma_z \approx 0.43$ a. u.. Altogether, $\Delta p_r = \left(\sigma_x^2 + \sigma_y^2 + \sigma_z^2\right)^{1/2} \approx 0.79$ a. u. is the spread in an arbitrary direction. The related energy uncertainty is $\Delta p_r^2 / 2 \approx 0.31$ a. u. $= 8.2$ eV. This experimentally determined spread of $\boldsymbol{p}_0$ compares well to estimates that are based on the velocity of the ion beam and on the size of collimating apertures together with the size of the laser spot, see [21] [70] [69]. Typical values for the initial spread in

COLTRIMS under ideal conditions are on the order $\Delta p \approx 0.01$ a. u. to $\Delta p \approx 0.1$ a. u. depending on the target atom and the orientation of the supersonic gas expansion.
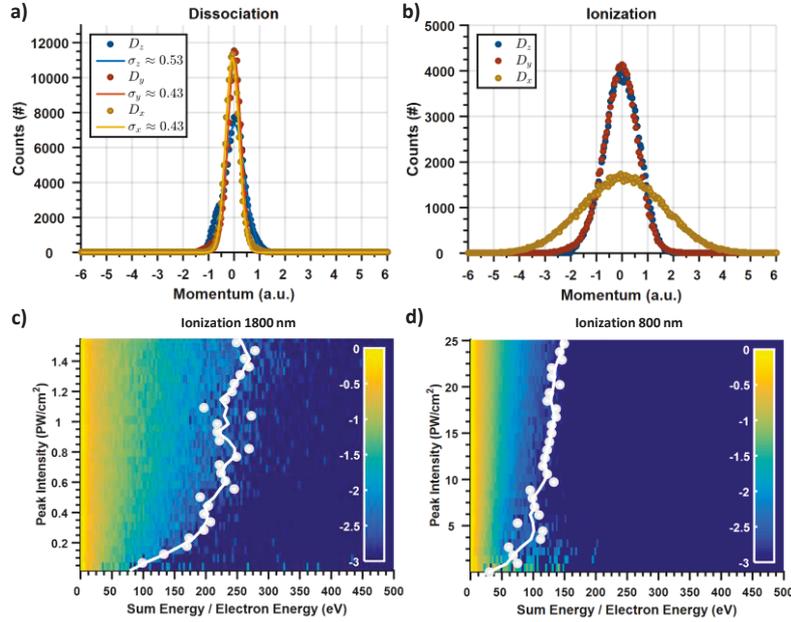

Figure 5.2: Measuring the momentum of the electron without detecting it

a) shows the distribution of the sum momentum of dissociation events projected along different directions within the laser frame of reference. The direction of the linearly polarized laser is along the x-axis here. b) shows the same as in a) but for ionization events of this measurement. c) and d) show the intensity dependence of the photo electron spectra within a narrow cone around the polarization axis of the of two different measurements, c) for a 1.8μm-50-fs laser and d) for 0.8μm-35-fs laser. The color bar is the logarithm of the normalized spectrum for each intensity. White dots are the energy at which the normalized spectra drop below 10^{-3}. The white line is a smoothing of these points based on a moving average. For c), this line increases with intensity for low intensities until it saturates starting around the saturation intensity 0.35 PW/cm^2. For d), the interpretation of the data is not as clear as due to the shorter wavelength, the energy due to the kick from the laser is not much larger than initial momentum spread of the ion beam. However, it seems as saturation is still visible.

Comparing the determined Δp_r to expectations on the magnitude of the electron momentum in SFI, $|\boldsymbol{p}_e|$, for typical field strength of $E_0 \approx 0.1$ a. u. shows that the measurement is strongly blurred by the initial distribution if ionization by a 800 nm laser is considered. For this case, one has $|\boldsymbol{p}_e| \approx |+\boldsymbol{A}(t_b)| = |E_0/\omega| = |0.1/0.057| = 1.75$ a. u. for a direct electron. The situation becomes better if 1800 nm are used i.e. $|\boldsymbol{p}_e| \approx |0.1/0.0253| = 3.95$ a. u.. The behavior is illustrated by the distribution of ionization events for a measurement at 1800 nm in Figure 5.2 b) where the momentum distribution parallel to polarization reaches approximately this width. The corresponding intensity dependence of the inferred electron energy spectra based on this method are shown for 1800 nm in Figure 5.2 c) and for 800 nm in Figure 5.2 d). The 1800 nm data shows the expected behavior of increasing width of the electron energy spectrum for increasing intensity. The interpretation of the intensity-dependent electron spectra of the 800 nm measurement is less clear, see the figure caption for details.

Altogether, if the ionizing laser has a sufficiently long wavelength, i.e. if the transferred momentum kick to the electron is large enough, measuring the sum momentum of both protons yields access to momentum of the

photoelectron without detecting it. The photoelectron momentum distribution, which is obtained in this way, is blurred with the initial momentum spread of the ion beam, which decreases the momentum resolution for the electron momentum.

5.2.2 Automated Scanning and Tagging of the Pulse Energy during the Measurement
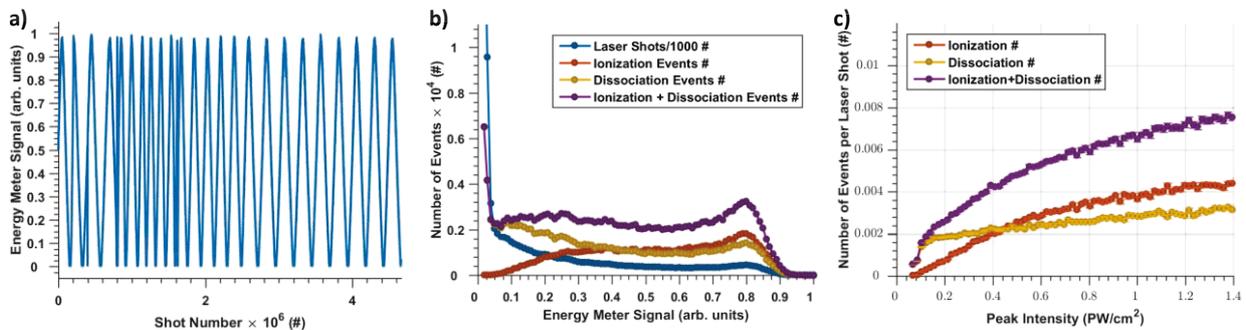

Figure 5.3: Illustration of pulse energy control and pulse energy tagging

a) Temporal evolution of the measured signal from the energy meter while the pulse energy is looped and tagged. b) Example of the histogram of pulse energies at the end of a measurement. All laser shots (blue curve); Shots with ionization events (red curve) and dissociation events (yellow curve), sum of ionization and dissociation events (purple curve). Note that the curve for all laser shots is divided by 1000 in order to show all curves on the same scale. c) Events per laser shot for ionization, dissociation and the sum of both. Experimental parameters in the shown example are wavelength, $\lambda = 1800$ nm, pulse duration $\tau = 48$ fs.

The measurement setup has been augmented by tagging and automated scanning of the pulse energy. To this end, the method of controlling the pulse energy without changing the focal spot or pulse duration as presented in attachment A1 is used .The pulse energy of every single laser shot is saved together with other measurement signals which enables subsequent binning and filtering of the measurement results according to the peak intensity of the laser pulse using the measured properties of the focal spot and pulse duration. Here we turn to the details of the implementation.

Tagging of the pulse energy is achieved by digitization of the output voltage of an every-single laser shot pulse energy meter. A calibration measurement connects the digitized voltage signal with the pulse energy in the target, see section 3.4, respectively Figure 5.3 a) for the optical setup. Scanning of the peak intensity is realized using a motorized and computer controlled mount to rotate a half wave plate in front of a combination of reflective and transmissive polarizers. Motor control over the time of the measurement is done using a MATLAB software in which a list of motor positions together with a resting time for the corresponding position is defined. During the measurement, the motor loops over this list sequentially and thus, the peak intensity changes continuously while it is tagged and recorded automated.

The scheme described here has two advantages. i) Continuously looping over the full range of available intensities at a frequency of several minutes while the full measurement time is on the order of hours and days ensures that the measured data contains the full range of peak intensities independent whether the measurement is stopped in case of a failure. ii) In addition, drifts, e.g. of the ion beam current or the energy of the laser, which would affect one

part of the measurement more significant than others if a single intensity sweep is done are avoided by repeatedly sweeping intensity. Further, having the option to adjust the resting time at some intensities, gives the opportunity to achieve a more homogenous distribution of counts over the full intensity range by spending more measurement time at lower intensities where the yield is lower. In this way, the measured differential rates that are obtained at different intensities can be compared with similar statistics.

However, following an arbitrary path with the peak intensity over the measurement time, yields an inhomogeneous distribution of laser shots at the end of the measurement, see Figure 5.3 b). In order to have access to the number of events per laser shot (event rate) as shown in Figure 5.3 c), it is necessary to renormalize the number of events within an intensity bin by dividing it through the number of laser shots that have been taken at this intensity position. The resulting event rate of ionization and dissociation increase with increasing peak intensity. While the event rate of dissociation is very steep and then increases slowly, ionization has a high slope over a large intensity range. It can even overtake the dissociation rate. In the region of highest intensity, both curves have almost equal slope. The observed intensity dependence of the event rate is not only governed by the intrinsic intensity dependence of the probability for ionization or dissociation of H_2^+, but it is also influenced by effects that originate from the fact that the experiment averages of the intensity distribution within the focal volume [147]. This focal volume effect will be analyzed in detail in the next section.

Altogether, a method for automated scanning and tagging of the peak intensity in the measurement has been demonstrated. It is used to investigate the intensity dependence of strong-field photoionization of H_2^+ at infrared laser wavelength.

5.2.3 Relevant Experimental Effects in Detail

The typical parameters to characterize the laser field in strong-field laser-matter interactions are the peak intensity, I_0, the intensity full-width half-maximum pulse duration, τ, and it's central wavelength, λ. However, it is well known that measurements are affected by several second order effects such as the focal volume , saturation intensity, chirp of the laser pulse, it's carrier-envelope phase and the distribution of initially populated vibrational states see, e.g. [21]. Here, some important effects and experimental limits are addressed as these are relevant for analysis and interpretation of the measurements.

Event Rate

The event rate, ϵ, is the number of detected coincidence events per unit of measurement time. Due to limits in measurement time, it sets limits on the available statistics of the measurement. Here its dependencies on several variables is investigated. Thereby, the goal is to identify the most limiting variable and to provide approaches for increasing the event rate for future work. Thereby, theoretical expectations are compared to observations made during the measurements.

ϵ is proportional to the number of particles that overlap with the laser beam per laser shot, N_{shot}, to the laser's repetition rate, f_{rep}, to the intrinsic probability of the investigated process, $P_{Prozess}$, and to the detection probability, D. $P_{Prozess}$ is related to the cross-section of the investigated process and depends on the experimental conditions such as the laser's peak intensity, wavelength or pulse duration. N_{shot} can be decomposed into two more factors,

which are the focal volume, V_{foc}, that overlaps with the ion beam, and ρ, which is the homogenous density of the ion beam. Thus, altogether, the event rate is proportional to, $\epsilon \propto \rho \cdot V_{foc} \cdot D \cdot P_{Prozess} \cdot f_{rep}$.

A major limit for ITRIMS measurements comes from ρ of the target. An analysis of limits can be found in [21]. Here we estimate it for typical conditions in the measurement using $\rho = C\sqrt{m_{ion}}/A_B q\sqrt{2B_{kin}}$. Assuming an ion current of $C = 10$ nA, a cross-sectional area of $A_B = 0.1$ mm^2 and an ion beam energy of $B_{kin} = 9$ keV and for H_2^+ with $q = e$ (e, being the elementary charge) and m_{ion} being the mass of H_2^+, one finds, $\rho = 6 \cdot 10^4$ particles/cm^3. Increasing this number is primarily limited by the current, which is available from the ion source. Other effects such as space charge issues, which would influence the measured momentum due to the repelling Coulomb forces between different particles play a minor role and are not a limit at ion densities below $\rho < 10^7$ particles/cm^3. A density on the order of $\rho < 10^5$ particles/cm^3 in the Jena ITRIMS setup is several orders of magnitude smaller than densities that are available for neutral targets such as gas cells ($\rho \approx 10^{17}$ particles/cm^3 and more), or cold supersonic gas jets $\rho < 10^{11}$ particles/cm^3 as in a COLTRIMS. Thus, ITRIMS experiment are hard to realize and are very time consuming compared to e.g. COLTRIMS or VMI measurements.

The influence of V_{foc} on the event rate is estimated next [147]. The volume within a Gaussian laser focus of spot size, w_F, peak intensity, I_0, and Rayleigh range, $z_{rF} = \pi w_F^2/\lambda$, which overlaps with a cuboid of edge length, z_{rF}, is approximately $V_2(I_0, I_{sat}) \approx \pi w_F^2 z_{rF} \ln(I_0/I)$. The ion beam crosses the laser beam perpendicular to the laser's propagation direction and is assumed to have a cuboid shape. Using the volume function, $V_2(I_0, I_{sat})$, one can calculate the volume within the focus where the intensity is higher than a certain saturation intensity, I_{sat}, below the peak intensity, I_0. For typical conditions, which are sufficient to reach $I_0 \approx 10^{15}$ W/cm^2 using the present setup, i.e. $w_F = 0.024$ mm, $z_{rF} = 1$ mm, $\lambda = 1800$ nm, this gives $V_2(I_0/I_{sat} = 100) \approx 4.2 \cdot 10^{-6}$ cm^3. Together with the ion beam density, one finds that $N_{shot} = V_{foc} \cdot \rho = 4.2 \cdot 10^{-6}$ cm$^3 \cdot 6 \cdot 10^4$ cm$^{-3} \approx 0.2$ particles are hit by the laser beam per laser shot at an intensity higher than $I_{sat} \approx 10^{13}$ W/cm^2. Lowering I_0 by a factor of 10 lowers N_{shot} roughly by a factor of 2, i.e. $N_{shot} \approx 0.1$.

Next, we have the coincidence detection probability, D. The probability for detecting a single particle with a typical microchannel-plate (MCP) delay-line detector is on the order of 0.3 due to the limited open area ratio of the MCP. Thus, for a two-particle coincidence D is $D = 0.3^2 = 0.09$. In order to keep the estimate simple, it is assumed that $P_{Prozess}(I > I_{sat}) \approx 1$. Altogether, one finds $\epsilon \sim 0.018 \cdot P_{Prozess}$ per laser shot which leads to $\epsilon \approx 18$ Hz at a repetition rate of 1 kHz if an ion beam current of $C = 10$ nA is achieved in the target area. In many cases, $C = 1$ nA is more realistic, thus $\epsilon \approx 2$ Hz or $\epsilon \sim 0.002 P_{Prozess}$ per laser shot is feasible. Thus, if 10^5 coincidence events are desired, a typical measurement time is on the order of several hours up to days.

The estimation of the event rate compares well to the experimentally observed values shown in Figure 5.3 c). This low number for the event rate illustrates that ITRIMS measurements using current kHz laser technology with good statistics is more challenging compared to typical COLTRIMS or VMI measurements. The measurement times become very long and are on the order of hours and days up to weeks depending on the requirements of the statistics. During this time, stable operation of the laser and the ion beam is required. Further, the processes, which can be investigated are required to have an intrinsic probability, which is close to one, $P_{Prozess} \approx 1$, as lowering this factor, would lengthen the measurement times even further. This fact sets limits on the parameter range that can be investigated within a reasonable amount of time as, for example, lowering the intensity or shortening the pulse duration can dramatically reduce $P_{Prozess}$.

Obvious approaches to improve this situation are: (i) Increasing the ion beam density, (ii) increasing the volume where the laser overlaps with the ion beam (on both side, ion beam and laser beam) or (iii) increasing the average power of the laser (higher repetition rate at the same pulse energy). (i) Might be achieved by using an ion source that delivers higher current or by the use of a source that delivers ion bunches that are synchronized with the repetition rate of the laser. (ii) Is a more gentle, less elaborate approach but is on cost of peak intensity if the average power of the laser is not increased. Still, it might be employed for intensity scans by shifting the focal position with respect to the position of ion beam, using the so-called z-scan method, [147]. (iii) Requires progress in femtosecond laser technology, which are currently underway.

Focal Volume Effect and Saturation Intensities

It is well known that measurements of strong-field processes are affected by the intensity distribution in the focus of the laser beam. Thereby, the so-called saturation intensity, I_{sat}, which is the intensity above which the probability for a certain strong-field process is 1, plays a central role. Here, the intensity dependence of an ITRIMS measurement is used to determine I_{sat} for ionization and dissociation of H_2^+ by $\lambda = 1800$ nm, $\tau = 48$ fs pulses. Thereby, we illustrate the focal volume effect.

We start by considering the time- and space-dependent intensity distribution, $I(x, y, z, t) = I_0 f(t) g(x, y, z)$. Here, I_0 is the peak intensity, $f(t)$, the time-dependent electric field, $g(x, y, z)$ is the spatial intensity distribution in the focal spot. Modeling $f(t)$ by a temporal Gaussian and further modeling $g(x, y, z)$ using the approximation of an ideal Gaussian laser spot, one can give the peak intensity, $I_0 = 1.88\varepsilon/\pi\tau w_F^2$ as function of the pulse energy, ε, the pulse duration, τ, and the waist, w_F, of the focal spot, see attachment A1. Last but not least, the Rayleigh range, $z_{rF} = \pi w_F^2/\lambda$, is needed to determine $g(x, y, z)$ precisely. Using the radial coordinate, $r = \sqrt{x^2 + y^2}$, the three-dimensional Gaussian intensity distribution in the focus is, $g(r, z) = I_0[w_F/w(z)]^2 \exp(-2r^2/w_F^2)$ with $w(z) = w_F\sqrt{1 + (z/z_{rF})^2}$. This spatial distribution is crossed with the volume of the ion beam, $b(x, y, z)$, which we assume to be a cuboid of homogenous density as in the previous consideration on the event rate. The cuboid is infinitely long along the direction of the ion beam, i.e. the y-axis, and of limited size for the other two directions, $d_z \approx d_x \approx 450$ μm. Experimentally, the extension along the x- and the z-direction is controlled by the opening of the adjustable apertures labeled with (m) in Figure 3.4.

Having defined a geometry of the ion beam, one can now use a Monte-Carlo method to calculate the volume, $V_{I>I_{sat}}(I_0, I_{sat})$, which overlaps with the laser beam, $g(r, z)$, and has an intensity, I, which is higher than I_{sat} for a given peak intensity I_0. Scanning I_0 in the Monte-Carlo calculation yields the dots in Figure 5.4. Comparing the Monte-Carlo result to an analytical expression for volume functions [147] shows that the intensity dependence of the Monte-Carlo result fits extremely well to the analytical expression for a thin target that has a thickness of $d_z \approx 0$, is located at $z = 0$, and is not limited along the other dimensions,

$$V_{I>I_{sat}}(I_0, I_{sat}) = \frac{1}{2}\pi w_F^2 \log\left(\frac{I_0}{I_{sat}}\right) \rightarrow f(I_0) = a \log\left(\frac{I_0}{I_{sat}}\right), \tag{5.1}$$

see Figure 5.4 a). Therefore, it is justified to use equation (5.1) as analytical expression for the target volume with an intensity which is higher than I_{sat}. Recalling the ratio between the waist of the spot, $d_x/w_F \approx 19$, this might not be surprising. However, it was worth to in view of the fact that the ratio between the experimental Rayleigh range, $z_{rF} \approx 1$ mm, and the size of the target is $d_z/z_{rF} \approx 0.46$ only.
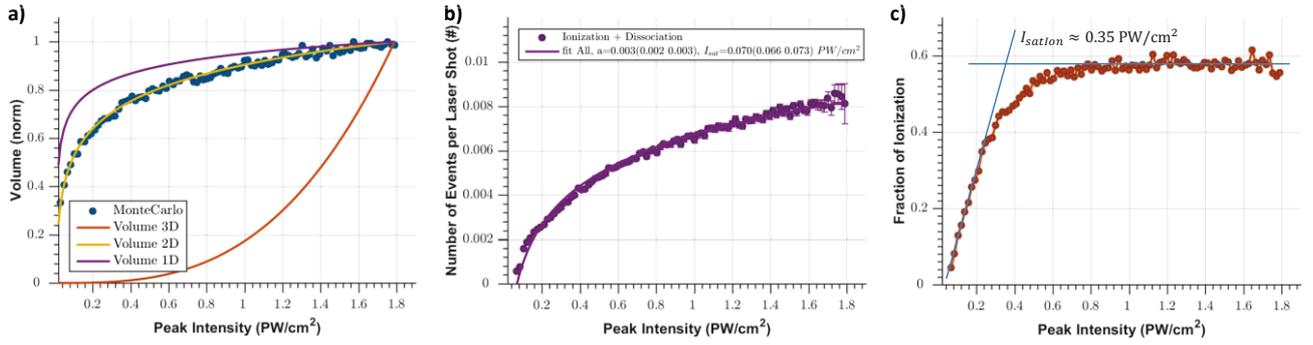
Figure 5.4: Intensity Dependence of the Event Rate due to Volume Effect

a) shows a comparison between volume functions within different approximation of the target geometry from [147] in comparison to a Monte Carlo simulation, see text for details. b) illustrates the fit of (5.1) to the measured sum of ionization and dissociation events per laser shot. c) Fraction of ionization events per laser shot as function of intensity.

The observation of a very flat intensity dependence for the event rate of dissociation almost over the whole intensity range suggests that even the lowest peak intensity in the measurement, Figure 5.3 c), might be close to or even higher than the saturation intensity for dissociation, $I_{satDiss}$. Further assuming that $I_{satDiss} < I_{satIon}$ allows one to fit a function with the form of equation (5.1) to the measured intensity dependence of the sum of ionization and dissociation events per laser shot. Taking the sum of ionization and dissociation events is justified by the idea that dissociation saturates before ionization and thus, the ionization volume must only be added to the dissociation volume. The result of the fit is shown in Figure 5.4 b) together with the experimental data. The determined value based on the fit is $I_{satDiss} \approx 7 \times 10^{13}$ W/cm^2 for the data in the example measurement ($\lambda = 1800$ nm, pulse duration $\tau = 48$ fs).

The saturation intensity of the ionization process, I_{satIon}, can be estimated using the observation that ionization overtakes dissociation until both event rates grow with very similar slope in Figure 5.1 c). Plotting the fraction of ionization, i.e. the ionization yield curve divided by the sum of the dissociation and the ionization in Figure 5.4 c), shows an almost constant ionization fraction for high peak intensity while at low peak intensity a steep increase of the ionization faction is observed. The behavior can be understood by considering that the volume of ionization and dissociation grow evenly, once the peak intensity is higher than the saturation intensity of both processes. This statement can be checked by calculating the derivative of (5.1), i.e. $\partial f(I_0)/\partial I_0 = a/I_0$, which is independent of I_{sat}. Identification of the crossing between the tangent of the steep increase of the ionization fraction and it's constant region gives an estimate for the saturation intensity $I_{satIon} \approx 3.5 \times 10^{14}$ W/cm^2.

I the peak intensity is higher than the saturation intensity, differential momentum distributions of ionization or dissociation are expected to be less sensitive to changes of peak intensity.

Chirp

The characterization of the idler beam from the TOPAS in chapter 2 shows that it exhibits a negative GDD of several hundreds of fs^2 and positive TOD of several hundreds of fs^3 depending on the exact wavelength. This is only partially compensated by the propagation through air and the beam path through the optical elements into the

interaction region of the ion beam apparatus. Thus, the measurements are done with slightly chirped pulses, which have a longer duration than their Fourier-transform limit. The given values for the pulse duration, τ (intensity full-width half-maximum), are the result of second-harmonic generation autocorrelation (SHG-AC) measurements performed at the same distance in air and with the same optical elements in the beam path as the laser takes to reach the interaction region of the ion beam. Thus, the given values for τ, include the effects of the residual GDD and TOD but the exact frequency dependent spectral phase of the pulse is not specified.

Later on, the measurements are compared to theoretical results which use a $\cos^2$-envelope. The duration of the $\cos^2$-envelope is adjusted such that the corresponding intensity full-width half-maximum duration matches the measured ones. Thus, theory accounts for the stretched envelope due to the chirp but not for the time-dependent frequency sweep during the pulse which is present in the experiment. The influence of the frequency sweep is expected to play a minor role for the comparison between measurements and theoretical results as well as for the interpretation.

Carrier-Envelope Phase

The measured data is not influenced by the carrier-envelope phase (CEP) of the laser pulses as laser pulses with random CEP have been used in the measurement.

Initial Population of Vibrational States

Alternatively to using an ion beam source, many measurements on strong-field interaction of H_2^+ have been done using COLTRIMS and starting from neutral H_2 in a supersonic gas jet. In such experiments, H_2^+ is created from H_2 by laser induced photoionization which is typically realized using an additional pump pulse to create H_2^+ from H_2. The pump comes shortly before the probe laser pulse and ionizes H_2 such that H_2^+ is available in the target at the time the main pulse arrives, see e.g. for a recent example [41].

A major difference to these schemes and the measurement data here is the initial preparation of the H_2^+ target. Creation of H_2^+ using laser-induced ionization of H_2 causes an electronic transition from H_2 to H_2^+ which yields a coherent sum of vibrational states, i.e. a vibrational wave packet that follows coherent dynamics on the Born-Oppenheimer (BO) potential energy curve of H_2^+. The exact details of the initial shape and the on-going dynamics are sensitive to the laser parameters of the pump pulse, e.g. wavelength, intensity, pulse duration. If now, the probe pulse is used for dissociation ($H_2^+ \rightarrow H^+ + H$) or ionization of H_2^+ ($H_2^+ \rightarrow H^+ + H^+ + e^-$), only very short times later, i.e. before the nuclear wave packet has dephased, the experimental result contains signatures related to the temporal delay between the creation of H_2^+ from H_2. Thus, comparison of experimental data to theoretical results relies on some modelling or assumptions of this first step including a modeling of the subsequent dynamics. It makes the interpretation of results more complex.

Complementary to this scheme, in the ITRIMS one starts with a beam of H_2^+ that is created by electron impact ionization in a discharge plasma. Due to the long time-of flight between ion source and the interaction with the laser of several micro-seconds, the H_2^+ molecules in the target will have a large spread in time-of flight compared to the vibrational period of the molecule. Thus, the initial population of vibrational states in the ion beam experiment can be treated as an *incoherent sum of vibrational states*, [21]. The initial population can well be described by a vertical transitions from the vibrational ground state of H_2 based on the Frank-Condon principle, see Figure 5.5 a) for illustration. The distribution along the internuclear distance, R, on the BO potential of H_2^+ is the result of the

incoherent sum of the Franck-Condon distribution. A measurement and comparison to theoretical results of the distribution of vibrational states after electron impact ionization has been done [148] and is shown in Figure 5.5 b). This distribution is used to average the theoretical results over the vibrational state in order to enable a comparison to the experimental data.
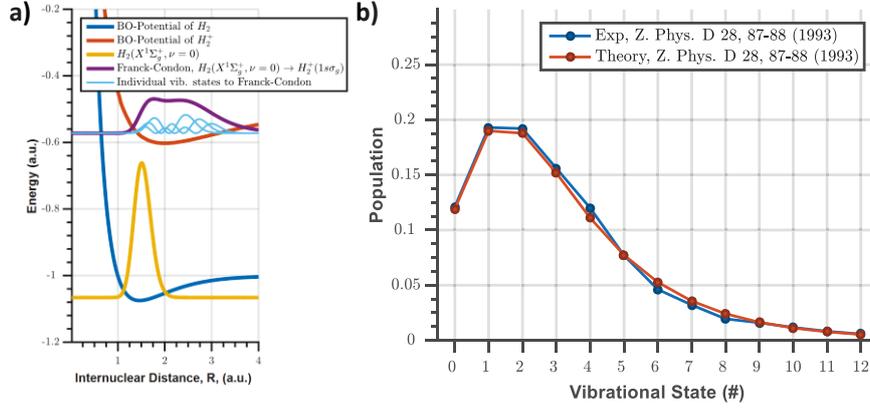

Figure 5.5: Distribution of initially populated vibrational states
a) illustrates how electron impact ionization in the ion source excites H_2 to H_2^+. Releasing an electron from the vibrational ground state (yellow curve) on the Born-Oppenheimer potential of H_2 (dark blue) excites H_2 to H_2^+. Thereby, an initial distribution of vibrational states, which is well approximated by a Franck-Condon distribution is formed. b) shows theoretical and experimental distributions of vibrational states after electron impact ionization taken from the given reference. The experimental curve is used to compare to theoretical results later on.

With the previous discussion of the event rate, focal volume and saturation intensity, chirp, carrier-envelope phase and the initial population of vibrational states important second-order experimental effects have been clarified. Particularly the information on chirp, pulse duration, and the intensity distribution in the focal volume as well as the initial population of vibrational states is relevant for the modeling of the strong-field interaction and should be taken into account by simulations.

5.3 A One-dimensional Two-Level Model on Strong-field Photoionization of H_2^+

With the aim of keeping the modeling simple while the fundamental dynamics are captured, we propose a one-dimensional two-level model on strong-field photoionization of H_2^+ here. The results of the simulations are compared to the experimental data in chapter 5.4 on a qualitative level. As the modeling has several steps and combines several ideas, we start by giving an overview on it using the structure chart in Figure 5.6. More detailed explanations can be found in the subsequent sections 5.3.1, 5.3.2 and 5.3.3.

The calculations of the model start from an Eigenstate, $\psi(\boldsymbol{r}, R, t) \approx \chi_g^\nu(R, t)\varphi_g$ with φ_g being the $1s\sigma_g$ electronic Eigenstate and $\chi_g^\nu(R, t)$ being the nuclear Eigenstate with quantum number ν. The symbols, R and t denote the time and the internuclear distance, see the top green box in the structure chart in Figure 5.6. As illustrated by the purple

box in Figure 5.6, from the initial Eigenstate, the dynamics of the bound electronic states due to the interaction with the external laser field, $E(t)$, with pulse duration, τ, and field strength, E_0, are modeled by solving the time-dependent Schrödinger equation (TDSE) numerically using the split-step method [149]. Thereby, see the cyan box in Figure 5.6, only the $1s\sigma_g$ and the $2p\sigma_u$ electronic Eigenstate, i.e. $\psi(\mathbf{r},R,t) \approx \chi_g(R,t)\varphi_g + \chi_u(R,t)\varphi_u$, are taken into account.

Ionization is incorporated by damping the bound wave function after each step, Δt, of the split-step algorithm, using quasi-static ionization rates, $\Gamma_{g,u}(R,|E(t)|)$ (one for each electronic state), see Figure 5.6. Applying absorbing boundaries after each Δt next, avoids reflections of the wave functions on the edges of the numerical grid along R. Accumulation of the damping (top orange box, Figure 5.6) due to ionization for every time step yields a R- and t-dependent population of the molecule's ionized state, $P_{ion}(R,t)$, while accumulation of the damping due to absorbing boundaries (lower orange box, Figure 5.6) is viewed as time-dependent dissociation probability, $P_{dis}(t)$.

Calculation of $W(R,t) = dP_{ion}(R,t)/dt$ represents an ionization rate which is characteristic for the laser parameters τ and E_0 as well as for the initial vibrational state, v. It is the basis for the Monte-Carlo methods which are used to calculate the corresponding KER spectra and joint electron-nuclear energy distributions (JEDs), see Figure 5.6 the green box at the bottom. This calculation is repeated for several initial vibrational states, and peak field strength, see the blue arrow in Figure 5.6. In order to be able to compare to the measurement later on, the calculation results from the different field strength and initial vibrational states are averaged over the distribution of field strength in the focal volume as well as over the distribution of the vibrational states taking into account the ionization probability at the end of the pulse, see Figure 5.6 red arrow and box.

The calculations of the model start from an Eigenstate, $\psi(\mathbf{r},R,t) \approx \chi_g^v(R,t)\varphi_g$ with φ_g being the $1s\sigma_g$ electronic Eigenstate and $\chi_g^v(R,t)$ being the nuclear Eigenstate with quantum number v. The symbols, R and t denote the time and the internuclear distance, see the top green box in the structure chart in Figure 5.6. As illustrated by purple box in Figure 5.6, from the initial Eigenstate, the dynamics of the bound electronic states due to the interaction with the external laser field, $E(t)$, with pulse duration, τ, and field strength, E_0, are modeled by solving the time-dependent Schrödinger equation (TDSE) numerically using the split-step method [149]. Thereby, see cyan box in Figure 5.6, only the $1s\sigma_g$ and the $2p\sigma_u$ electronic Eigenstate, i.e. $\psi(\mathbf{r},R,t) \approx \chi_g(R,t)\varphi_g + \chi_u(R,t)\varphi_u$, are taken into account. Ionization is incorporated by damping the bound wave function after each step, Δt, of the split-step algorithm, using quasi-static ionization rates, $\Gamma_{g,u}(R,|E(t)|)$ (one for each electronic state), see Figure 5.6. Applying absorbing boundaries after each Δt next, avoids reflections of the wave functions on the edges of the numerical grid along, R. Accumulation of the damping (top orange box, Figure 5.6) due to ionization for every time step yields a R- and t-dependent population of the molecule's ionized state, $P_{ion}(R,t)$ while accumulation of the damping due to absorbing boundaries (lower orange box, Figure 5.6) is viewed as time-dependent dissociation probability, $P_{dis}(t)$. Calculation of $W(R,t) = dP_{ion}(R,t)/dt$ represents an ionization rate which is characteristic for the laser parameters τ and E_0 as well as for the initial vibrational state, v. It is the basis for the Monte-Carlo methods which are used to calculate the corresponding KER spectra and joint electron-nuclear energy distributions (JEDs), see Figure 5.6 bottom green box. This calculation is repeated for several initial vibrational states, and peak field strength, see the blue arrow in Figure 5.6. In order to be able to compare to the measurement later on, the calculation results from the different field strength and initial vibrational states are averaged over the distribution of field

strength in the focal volume as well as over the distribution of the vibrational states taking into account the ionization probability at the end of the pulse, see Figure 5.6 red arrow and box.

With that overview we turn to more detailed explanations and illustrations of each step.
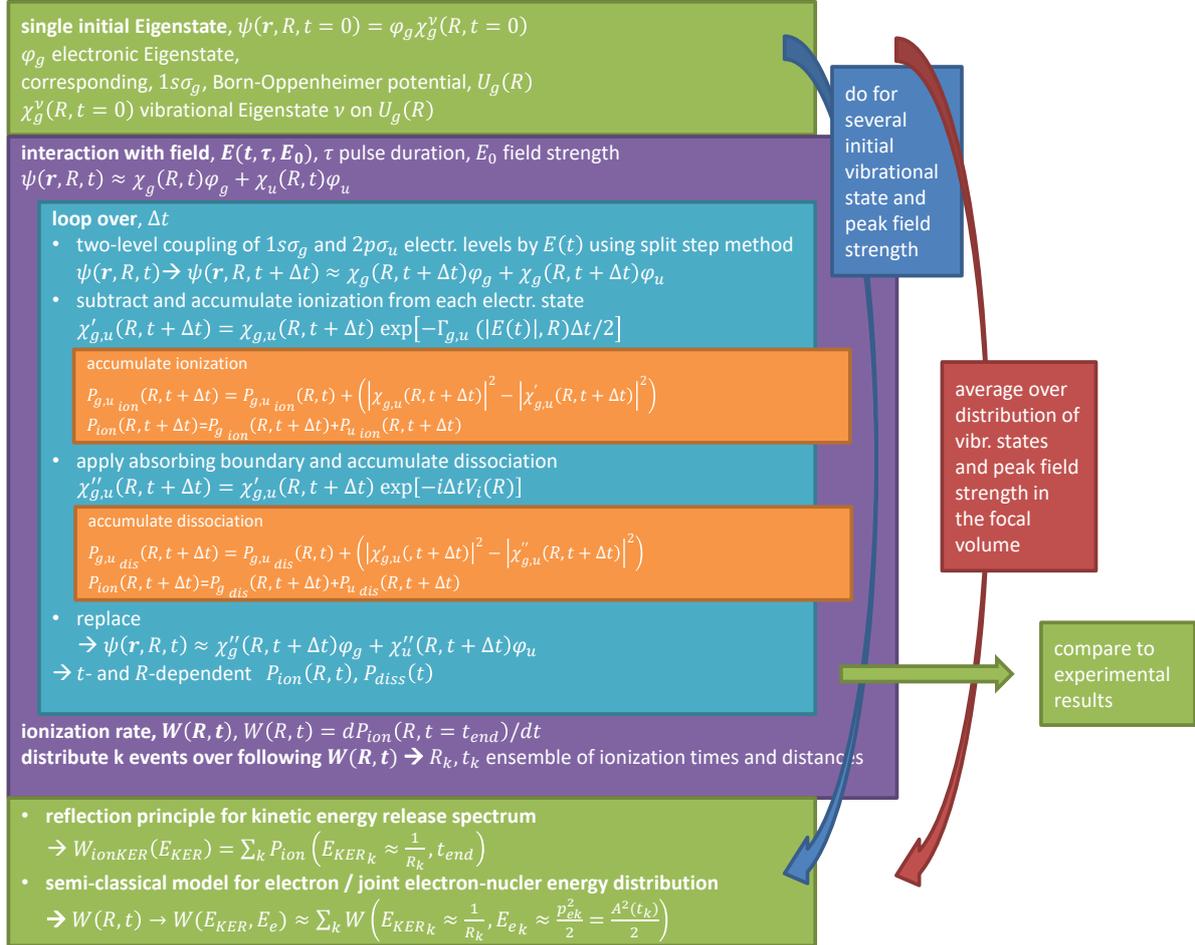
Figure 5.6: Structure chart of the one-dimensional two-level model on strong-field photoionization of H_2^+, see text for details.

5.3.1 Time-Dependent Coupling of Born-Oppenheimer Potentials in H_2^+ augmented for Ionization

The one-dimensional two-level model on H_2^+ strong-field photoionization of H_2^+ neglects rotations and uses the approximation of linearly polarized laser field that is parallel to the nuclear axis. The total wave function, $\psi(\boldsymbol{r}, R, t)$, is approximated using the $1s\sigma_g$ and the $2p\sigma_u$ electronic wave functions, $\varphi_g(R; \boldsymbol{r})$ and $\varphi_u(R; \boldsymbol{r})$, i.e. $\psi(\boldsymbol{r}, R, t) \approx \chi_g(R, t)\varphi_g + \chi_u(R, t)\varphi_u$. Having the electronic problem solved, one applies the BO approximation and arrives at the corresponding field-free BO potentials, $U_g(R)$ and $U_u(R)$, on which the nuclear wave functions, $\chi_g(R, t)$ and $\chi_u(R, t)$, evolve, see Figure 5.7 a) for an illustration. As demonstrated in attachment A4.2, the two potentials are coupled by the external field. The coupled two-level TDSE of H_2^+ in the external laser field, $E(t)$, reads,

$$i\frac{d}{dt}\begin{bmatrix} \chi_g(R,t) \\ \chi_u(R,t) \end{bmatrix} = \begin{bmatrix} T_N + U_g(R) & E(t)d_{gu}(R) \\ E(t)d_{gu}(R) & T_N + U_u(R) \end{bmatrix}\begin{bmatrix} \chi_g(R,t) \\ \chi_u(R,t) \end{bmatrix}. \tag{5.2}$$

$T_N = \partial^2/2\mu\,\partial R^2$ is the operator for the nuclear kinetic energy and $\mu = M_A M_B/(M_A + M_B) = m_p/2$ is the reduced mass for a diatomic molecule. $m_p \approx 1836$ is the proton mass and $d_{gu}(R)$ is the R-dependent dipole strength of $1s\sigma_g - 2p\sigma_u$ transition. In all simulations, tabulated values for $U_g(R)$ and $U_u(R)$ [150] as well as for $d_{gu}(R)$ [151] [152] are used.
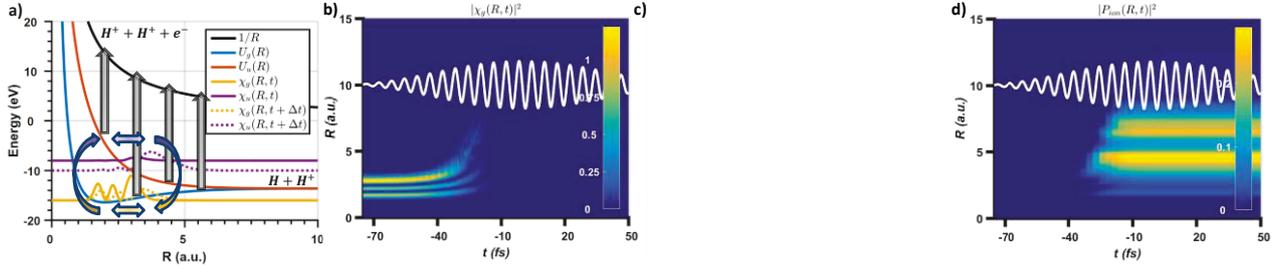

Figure 5.7: Time evolution on two coupled BO curves and ionization signal in external time-dependent field.

a) Illustrates the coupling of the BO curves and ionization based on a quasi-static rate in an external field. At each time step, a "copy" of the nuclear wave function from the other BO potential is added to the field free propagation on the corresponding BO potentials. The blue line is the BO potential of the $1s\sigma_g$ electronic state. The red line is the same but for the $2p\sigma_u$ potential. The black line is the $1/R$, potential, which is relevant when the molecule has been ionized, i.e. the electron is freed. The solid and dashed line in yellow respectively purple illustrate nuclear wave functions, $\left|\chi_g(R,t)\right|^2$ respectively $|\chi_u(R,t)|^2$ at an earlier (solid) and a later time (dashed). Coupling of the states where the electron is bound is illustrated by the yellow and the purple arrows. Ionization, i.e. the transition to the $1/R$ potential by the quasi-static rate is illustrated by the black arrows.

b) and c) show the time-dependent evolution of $\left|\chi_g(R,t)\right|^2$ respectively $|\chi_u(R,t)|^2$ in the external field in a two-dimensional plot. The field in the calculation, $E(t)$ in a.u. , is shown for reference. It got multiplied by 15 and shifted by 10 a. u. in order to allow for a convenient visibility in the plot. The shown example includes the effect of ionization using the method as explained in the next chapter. The quantity, $P_{ion}(R,t)$, which is representative for the R- and t- dependent population of the ionic state calculated within this method is shown in d).

Before we continue, we illustrate how the external field couples the two BO potential curves in a time-dependent manner by formally integrating (5.2),

$$\chi_g(R,t_1) = -i\int_{t_0}^{t_1}[T_N + U_1(R)]\chi_g(R,t')dt' - i\int_{t_0}^{t_1}E(t')d_{gu}(R)\chi_u(R,t')dt'$$

$$\chi_u(R,t_1) = -i\int_{t_0}^{t_1}[T_N + U_2(R)]\chi_u(R,t')dt' - i\int_{t_0}^{t_1}E(t')d_{gu}(R)\chi_g(R,t')dt'.$$

(5.3)

The nuclear wave function on each of the BO curves is written in form of two summands. The first is representative for the field-free time evolution on the respective BO potential. The second summand can be understood as kind of a "copy" of the nuclear wave function from the other BO curve which is "created". The strength of the generated "copy" is proportional to the strength of the electric field, $E(t)$, and the transition dipole matrix element, $d_{12}(R)$, as well as to the complex amplitude of the wave function on this curve. As the R-dependent wave function is complex valued, the contributions from the "copy" interfere with the part of the wave function which is already on the respective BO potential. Thus, the coupling can lead to an enhancement (constructive interference) or suppression (destructive interference) of the probabilities on each of the curves, $|\chi_u(R,t')|^2$ or $|\chi_u(R,t')|^2$. Figure 5.7 illustrates

the coupling scheme of the two bound electronic states. After this excursion to illustrate the coupling mechanism between the two electronic levels, we return to continuing with the details of the model.

Numerical integration of (5.2) using the split-step method [149] as presented in attachment A4 allows one to calculate time-dependent dynamics of H_2^+ on the $1s\sigma_g$ and the $2p\sigma_u$ electronic states. In each of these states, the electron is bound at both or one of the two protons. In order to incorporate ionization ($H_2^+ \rightarrow H^+ + H^+ + e^-$), which is a transition to the $1/R$-potential Figure 5.7 a), quasi-static field ionization rates, $\Gamma_g(R, |E|)$ and $\Gamma_u(R, |E|)$, for each of states are used. This is done in the following way. If $\chi_g(R, t + \Delta t)$ and $\chi_u(R, t + \Delta t)$ denote the wave functions on each BO potential after each round of the split-step method in A4 with the time-step Δt, then,

$$\chi'_g(R, t + \Delta t) = \chi_g(R, t + \Delta t)\exp(-\Delta t \Gamma_g(R, |E(t)|)/2)$$
$$\chi'_u(R, t + \Delta t) = \chi_u(R, t + \Delta t)\exp(-\Delta t \Gamma_u(R, |E(t)|)/2),$$

(5.4)

are calculated as the new wave functions which are then used in the subsequent time step of the split-step method. This is done before the absorbing boundaries are applied, see attachment A4 for further details.

The effect of this method for incorporating ionization is very similar to the use of the quasi-static field ionization rate for atoms that has been described in section 4.4.3. However, it is augmented for each R here. In section 4.4.3, the population of the ground state, $P(t)$, follows the differential equation, $dP(t)/dt = -\Gamma(|E(t)|)P(t)$. It's solution is analytically known, $P(t) = P_0\exp(-\int_{-\infty}^{t} \Gamma(|E(t')|)dt')$ with P_0 being the initial population. Comparing this to the effect of (5.4) on the R-dependent propabilities $P_g(R, t + \Delta t) = \left|\chi_g(R, t + \Delta t)\right|^2$ and on $P_u(R, t + \Delta t) = |\chi_u(R, t + \Delta t)|^2$ shows that (5.4) is equal to approximating the integral in the exponential of $P(t)$,

$$P'_{g,u}(R, t + \Delta t) = \left|\chi'_{g,u}(R, t + \Delta t)\right|^2 = \left|\chi_{g,i}(R, t + \Delta t)\right|^2 \exp\left(-\int_t^{t+\Delta t} \Gamma_{g,u}(R, |E(t)|)dt'\right)$$

$$P'_{g,u}(R, t + \Delta t) \approx \left|\chi_g(R, t + \Delta t)\right|^2 \exp\left(-\Delta t \Gamma_g(R, |E(t)|)\right).$$

(5.5)

This means that (5.4) introduces a loss of probability in the bound states to a quasi-static field ionization channel. Back coupling from ionization to bound states as among the g- and the u-state is not supported by this scheme. The fact that (5.4) is done only after (and not somehow in between) every loop of the normal split-step method is expected to introduce some numerical error, which is accepted for small enough Δt.

The time- and R-dependent population in the field ionization channel from the $P_{gion}(R, t)$ and $P_{uion}(R, t)$ from each BO potential is then accumulated by calculating

$$P_{gion}(R, t + \Delta t) = P_{gion}(R, t) + \left(\left|\chi_g(R, t + \Delta t)\right|^2 - \left|\chi'_g(R, t + \Delta t)\right|^2\right)$$
$$P_{uion}(R, t + \Delta t) = P_{uion}(R, t) + (|\chi_u(R, t + \Delta t)|^2 - |\chi'_u(R, t + \Delta t)|^2).$$

(5.6)

The second summand on the right hand side leads to summation of the lost probability from each of the bound states. It ensures numerical stability and conservation of the norms. The full population of the ionized state of H_2^+ is then the sum of the population from both channels

$$P_{ion}(R, t) = P_{gion}(R, t) + P_{uion}(R, t).$$

(5.7)

Figure 5.7 d) shows an example for the time-evolution of this quantity. It is clear that summation of the R-dependent probabilities in (5.7) does not support interference phenomena.

The recorded $P_{ion}(R, t)$ from this calculation can further be used to calculate a time- and R-dependent transition rate,

$$W_{ion}(R,t) = \frac{d}{dt} P_{ion}(R,t). \tag{5.8}$$

It gives the information at which time and at which R during the laser pulse the transition from one of the bound electronic states to the ionized state, i.e. to the $1/R$ potential of H_2^+, occurs.

With equations (5.2) to (5.8), one has a one-dimensional two-level model on strong-field photoionization of H_2^+. The model uses two BO potentials, which are time-dependently coupled by the external laser field to calculate the nuclear dynamics on the $1s\sigma_g$ and the $2p\sigma_u$ electronic state. Ionization, i.e. the transition of the nuclear wave packet to the $1/R$-potential, is incorporated at each time-step using R-resolved and field-strength dependent quasi-static field ionization rates, $\Gamma_g(R,|E(t)|)$ and $\Gamma_u(R,|E(t)|)$. The result of a single calculation where the molecule is initially in some vibration state, v, interacts with a laser field, $E(t)$, of peak field strength, E_0, pulse duration, τ, and center frequency ω, (see (4. 31) and (4.32)) are time- and R-dependent populations, $P_{ion}(R,t)$, of the ionized state of H_2^+. From $P_{ion}(R,t)$ a transition rate, $W_{ion}(R,t)$, can be calculated. It gives information on the question, at which time and R the transition from one of the bound electronic states to the ionized state of H_2^+ occurs. Next we use the reflection principle to connect the R-dependent dynamics with measured kinetic energy release distributions.

5.3.2 Connecting to Kinetic Energy Release using the Reflection Principle
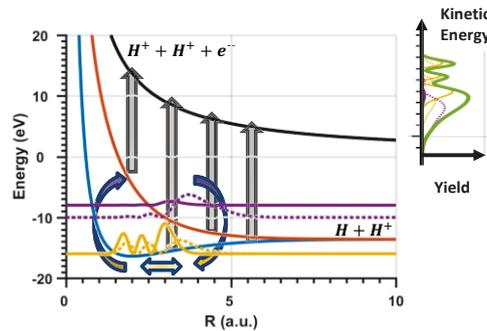
Figure 5.8: Reflection principle and one-dimensional two-level model

The two-level model is used to model the dynamics on the $1s\sigma_g$- and the $2p\sigma_u$ electronic states. Ionization based on the quasi-static ionization rates as explained in 5.3.1, yields R-dependent population of the ionized state. The reflection principle, $E_{KER} \approx 1/R$, can be used to convert from R to the measured kinetic energy release spectra.

The one-dimensional two-level model on strong-field photoionization of H_2^+ yields time- and R-dependent population, $P_{ion}(R,t)$, as well a corresponding transition rate, $W_{ion}(R,t) = dP_{ion}(R,t)/dt$, to the ionized state of the molecule ($1/R$-potential) for a given initial vibrational state, v, and laser parameters (peak field strength, E_0, pulse duration, τ, and center frequency ω).

Next, the reflection principle [153] is used to connect the R-dependent quantities to measured quantities such as kinetic energy release (KER) spectra and joint nuclear-electron energy distributions (JEDs). The reflection principle is illustrated in Figure 5.8. The idea behind it is that a sudden ionization, i.e. a transition from $1s\sigma_g$- or the $2p\sigma_u$-potential to the $1/R$-potential (or to any other dissociative potential) generates two protons which repel each other.

Due to the repulsion among the protons, the fragments gain kinetic energy which is measured as kinetic energy release (KER) at infinite distance $R \to \infty$, as illustrated in Figure 5.8.

In order to calculate KER spectra for a given set of initial vibrational states and laser parameters, we take the R-dependent population of the ionized state at the end of the simulation, i.e. $P_{ion}(R, t_{end})$, when the laser-field's amplitude is $E(t_{end}) = 0$, and use that the KER of a single transition to the ionized state ($1/R$ potential) at the position, R, is approximately,

$$E_{KER} \approx \frac{1}{R}.$$
(5.9)

The assumption of a vertical transitions means that one assumes that the nuclei don't move when the electron is ejected. The corresponding measured quantity is $E_{KER} = (\boldsymbol{p}_1 - \boldsymbol{p}_2)^2/2m_{H^+}$ where $\boldsymbol{p}_1$ and $\boldsymbol{p}_2$ are two measured proton momenta from strong-field ionization of H_2^+ in a ITRIMS.

A KER spectrum is then calculated from $P_{ion}(R, t_{end})$, using a Monte-Carlo approach, i.e. k events with ionization distances, R_k, are distributed such that their histogram follows $P_{ion}(R, t_{end})$. Using a Monte-Carlo approach from here on is convenient as it allows to bin and calculate the calculation results in various ways. Equation (5.9) allows to convert each R_k to E_{KER_k}. Binning them onto a KER-axis and yields the KER spectrum

$$W_{ionKER}(E_{KER}) = \sum_k W_{ion}\left(E_{KER_k} = \frac{1}{R_k}, t_{end}\right).$$
(5.10)

Using (5.9) to approximate the measured KER distribution means that ionization by a quasi-static field is assumed to create two protons which move on the $1/R$-potential in Figure 5.8. Thereby, zero initial momentum is assumed. The preceding dynamics on the bound states is only taken into account as it alters $|\chi_g(R, t)|^2$ and $|\chi_u(R, t)|^2$ as it was described in the previous section. An analysis of the momentum space representation of $\chi_g(R, t)$ and $\chi_u(R, t)$ wave functions during the calculations showed that this approximation is reasonable [154].

Now we turn to the method of calculating joint nuclear-electron energy distributions (JEDs) based on $W_{ion}(R, t)$. Under JED we understand, a two-dimensional distribution/count rate, i.e. $W_{ionJED}(E_{KER}, E_e)$. On the one axis, one has KER, E_{KER}, of the nuclei and on the other axis, one has the electron energy, E_e, while the count rate/the distribution is given as color code, see Figure 5.9 a) for an example. In order to connect, $W_{ion}(R, t)$ and $W_{ionJED}(E_{KER}, E_e)$, we assume that the transition to the $1/R$-potential by field ionization in a quasi-static field at the time, t_s, leads to a sudden creation of a pair of protons and a free electron. While the relative motion of the protons leads to the asymptotic KER in (5.9), the asymptotic electron velocity is approximately,

$$\boldsymbol{v}_{dir}(t_s) = -\boldsymbol{A}(t_s)$$
(5.11)

and thus, the sum momentum of the protons is $\boldsymbol{p}_1 + \boldsymbol{p}_2 = -\boldsymbol{p}_e = +\boldsymbol{A}(t_s)$, see chapter 3.2.

It is clear that using (5.11) for the asymptotic electron velocity means that we neglect the Coulomb interaction between the electron and the protons. Therefore, rescattering or recapture processes are not supported by this model. In order to generate the desired 2D distributions, a Monte-Carlo approach is used again. Therefore, k events are distributed with ionization times, t_{s_k}, and corresponding ionization distances, R_k, in such a way that their 2D histogram follows $W_{ion}(R, t)$. Calculation of E_{KER_k} and E_{e_k} based on (5.10) and (5.11) for each of the events and subsequent calculation of the yields the JED as,

$$W_{ionJED}(E_{KER}, E_e) = \sum_k W_{ion}\left(E_{KER_k} = \frac{1}{R_k}, E_{e_k} = \boldsymbol{v}_{dir}^2(t_{s_k})/2\right).$$
(5.12)

One can also use this distribution to generate the KER spectrum in (5.10) by integrating along the electron energy axis, i.e.

$$W_{ionKER}(E_{KER}) = \int W_{ionJED}(E_{KER}, E_e)\, dE_e. \tag{5.13}$$

Further, one can calculate the mean of the photoelectron energy for each bin along the KER axis, i.e.

$$M_{ionE_e}(E_{KER}) = \frac{\int E_e W_{ionJED}(E_{KER}, E_e) dE_e}{W_{ionKER}(E_{KER})}. \tag{5.14}$$

It is representative for the KER-dependent width of the electron energy spectrum. Also, one can analyze e.g. KER spectra for different electron energies.
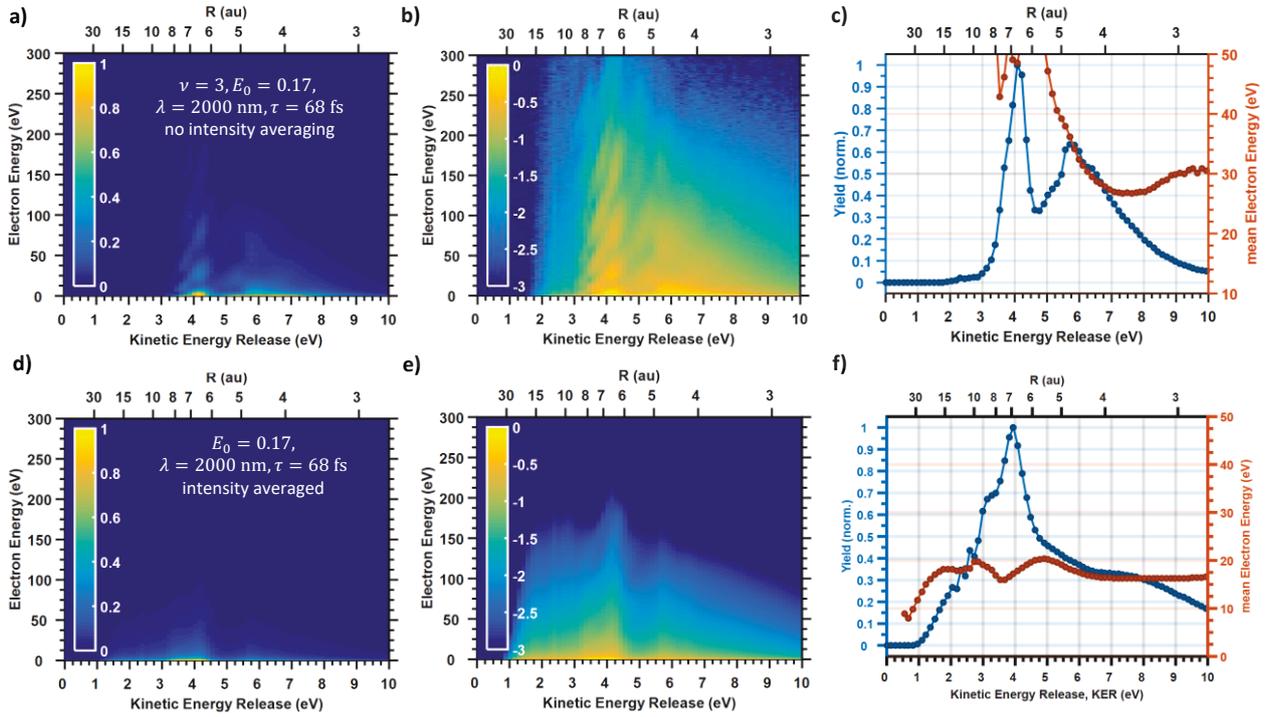

Figure 5.9: Illustration of simulated joint nuclear-electron energy distributions (JEDs)

a) Calculated JED based on the described model, $\nu = 3, E_0 = 0.17, \lambda = 2000$ nm, $\tau = 68$ fs. b) logarithm of the JED in a). c) KER spectrum and KER-dependent mean of the electron energy for the calculation shown in a) and b). d), e) and f) show the same plots as a), b) and c) but after averaging over the intensity distribution in the focal volume and the initial distribution of vibrational states.

Oben: not vib avg, nu3= wvl=2000nm, E0=0.17 (ca. 1e15), 68 fs
Unten v avg, Ipeak=1e15, wvl=2000nm, 68 fs

With (5.9) to (5.14) and the model from section 5.3.1, one has a method to calculate KER spectra and JED for a given set of initial vibrational state, ν, and laser parameters. Last but not least, the calculations must be averaged over the initial population of vibrational states and the distribution of field strengths, E_0, in the focal volume. The focal volume is characterized by the spatial peak intensity I_0, the Rayleigh range, z_R and the geometry of the ion beam target, see 5.2 and attachment A1. Therefore, the calculations for a pulse duration, τ, and center frequency, ω, are repeated for up to 400 E_0 on an equally spaced grid and for 13 vibrational states. Calculation of $P(E_0, \nu) = n_{ion}(t_{end}) = \int_0^{R_{max}} P_{E_0,\nu}(R, t_{end})\, dR$, is the probability with which the corresponding KER spectrum occurs. It is the basis for calculating focal volume averaged and vibrational state averaged KER spectra and JEDs for different spatial

peak intensities, I_0. Thereby, we follow the scheme in [147]. The analytical expression for a thin 2D target as characterized in 5.2.3 is the basis for the averaging the calculation over the distribution of peak field strength in the target, see also attachment A1.2. In Figure 5.9, we compare single-intensity single-vibrational state JED a) to c) with a calculation that is averaged over the focal volume as well as over the vibrational states d) to f), see the figure caption for details. An immediate observation is that the averaged results are more smeared out. Further, the contribution of the higher lying vibrational states, which ionize at lower field strength than $v = 3$, lead to a narrower JED and a shoulder at lower KER. The focal volume averaged calculations are compared to the experimental data in chapter 5.4.

5.3.3 Quasi-Static Ionization Rates

The previous sections introduced a one-dimensional two-level model for strong-field photoionization of H_2^+. The model combines the dissociative nuclear dynamics based on the coupling of the two-electronic levels ($1s\sigma_g$, $2p\sigma_u$) by an external laser field $E(t)$. Ionization is incorporated using quasi-static ionization rates, $\Gamma_g(R, |E(t)|)$ and $\Gamma_u(R, |E(t)|)$. Having the two aspects of dissociative nuclear dynamics and ionization separated in the model, one can test the influence of different sets of ionization rates on the result of the calculation and compare different versions to experimental data on a qualitative level later. Here, the two sets of ionization rates which are tested are illustrated.

Target	$|I_P|$ (eV)	B	l	C_{nl}	m	β
$H_2^+ - g$	$I_g(R) = U_g(R) - 1/R$	2	0	2.87	0	0
$H_2^+ - u$	$I_u(R) = U_u(R) - 1/R$	2	0	2.87	0	0

$$Q(l, m) = (-1)^{(|m|-m)/2} \sqrt{\frac{(2l+1)(l+|m|)!}{2(l-|m|)!}}$$

Table 5.1 Parameters used in the ADK-inspired R-dependent ionization rate of H_2^+.
R-dependent ionization rates for different electronic levels in H_2^+, are obtained by modifying the atomic ionization rate with an R-dependent ionization potential for each of the states.

The first set of rates is inspired by the atomic ionization rate (ADK rate) in (4.9). We repeat the expression here for completeness,

$$\Gamma(|E(t)|) = \frac{|C_{nl}|^2 Q(l,m)^2}{(2\kappa)^{|m|}|m|!} \left(\frac{2\kappa^2}{|E(t)|}\right)^{\frac{2B}{\kappa}-|m|-1} \exp\left(-\frac{2\kappa^3}{3|E(t)|}\right) \exp\left(-\beta \frac{2B}{\kappa^2} \frac{|E(t_s^k)|}{\kappa^3}\right). \tag{5.15}$$

The molecular character of H_2^+ is taken into account by making the electron's binding energy, I_P, which occurs in (5.15) via $\kappa = \sqrt{2|I_P|}$, sensitive to R, i.e. $\Gamma(|E(t)|) \to \Gamma(\kappa(I_P(R)), |E(t)|) \to \Gamma(R, |E(t)|)$. For this purpose, the R-dependent electronic binding energies, i.e. $I_g(R) = U_g(R) - 1/R$ and $I_u(R) = U_u(R) - 1/R$ are used for each of the states. In the end one has a set of two R-dependent ionization rates, $\Gamma_g^A(R, |E(t)|)$ and $\Gamma_u^A(R, |E(t)|)$, one for each

electronic state. For the other parameters in (5.15), the values in Table 5.1 are taken independent of R. This set of R- and $|E|$-dependent rates is abbreviated with atom-like ionization rates (A-rate) from here on.
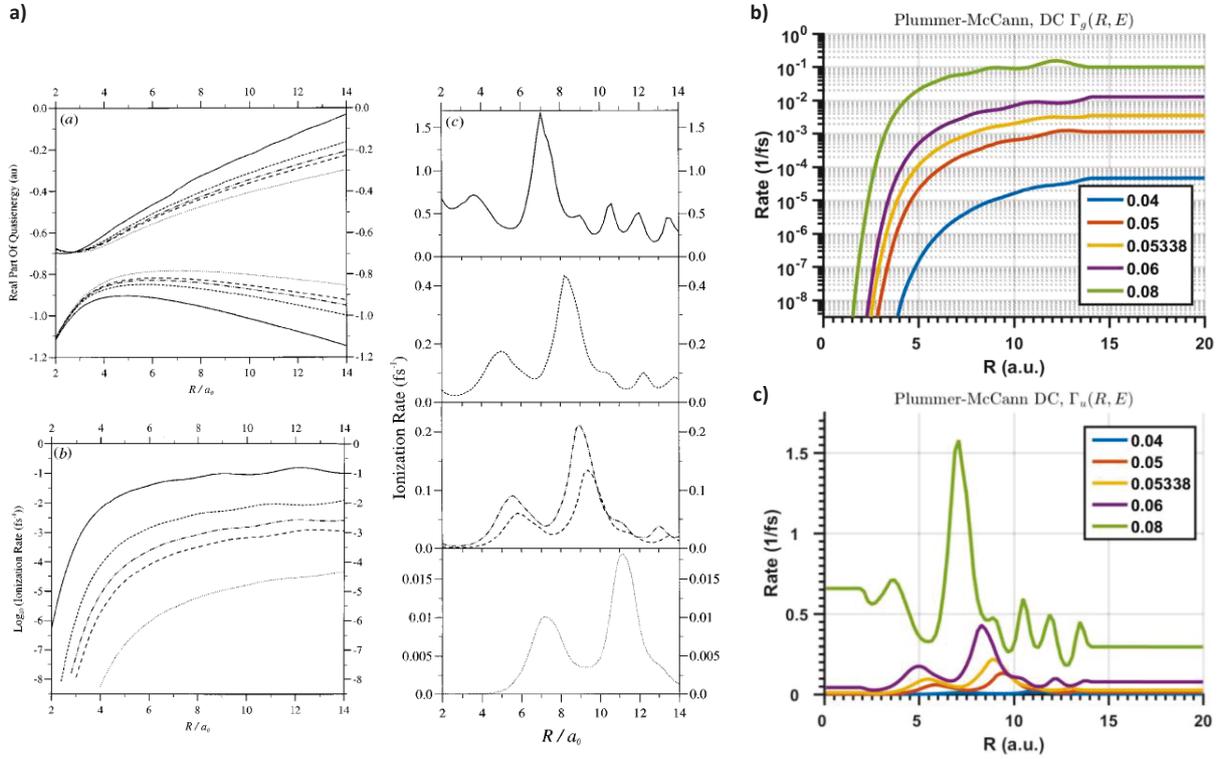

Figure 5.10: Illustration of the ionization rate of Plummer and McCann reproduced by a fit.
a) shows the central figure [28]. The subgraphs show the mentioned real part of the quasi-energy for different strength of the external field in a)(a) for the $1s\sigma_g$ (lower set) and the $2p\sigma_u$ (upper set). a)(b) and a)(c) show the corresponding imaginary parts which are the ionization rate, $\Gamma(R)$. b) and c) illustrate the fit which is used in the two-level calculations for the same field strength as in [28].

The second set of rates is based on an exact three-dimensional calculation of field ionization rates of H_2^+ in a static external field [155] [28] [156]. These calculations use complex energy eigenvalues (so-called quasi-energies), $W(R) = W_{real}(R) - i\Gamma(R)/2$, to define the state of H_2^+ in a static external field strength $|F|$ for various Rs. The real part, $W_{real}(R)$, of the quasi-energies is the energy of the bound part of the wave function. Its energetic position is shifted depending on $|E|$, see Figure 5.10 a)(a) for illustration. The imaginary part, $\Gamma(R)$, of the quasi-energy is the ionization rate of the system in a static field of strength $|E|$, see Figure 5.10 a)(b) for $1s\sigma_g$ and Figure 5.10 a)(c) for the $2p\sigma_u$ state. The corresponding Eigenfunctions are the electronic wave function of H_2^+ under the effect of the static external field. In order to have appropriate rates, $\Gamma_g^{PM}(R, |E|)$ and $\Gamma_u^{PM}(R, |E|)$, which are based on this exact calculations, a two-dimensional along R and $|E|$ inter- and extrapolation is done. Thereby, the values for the atomic- and separated atom limit from [156] are used for Rs that lie outside the available R-range in [28]. For field strengths, which lie outside the available range of $|F|$ values, an extrapolation of the rates is done. Figure 5.10 b) and c) demonstrate that the used fit matches the exact calculations at the available sample points. This set of R- and $|E|$-dependent ionization rates is abbreviated with Plummer-McCann ionization rates (PM-rate) from here on.

The atom-like rates and the PM-rates as function of R and $|E|$ are qualitatively compared based on 2D plots in Figure 5.11. The first observation is that the atom-like rate is a lot higher particularly for high field strength, see Figure 5.11 a) and c). But apart from that, it seems as the shape of the rates for ionization from $1s\sigma_g$ is rather similar. The major qualitative difference between both sets of rates is found in the modulation along the R-direction for ionization from the $2p\sigma_u$ state. While the atom-like rate, see Figure 5.11 b), is a rather smooth and flat surface as function of R and $|E|$, the corresponding PM-rate, see Figure 5.11 d), has several maxima and minima along the R for fixed field strength. The number of maxima and their position changes with the field strength.
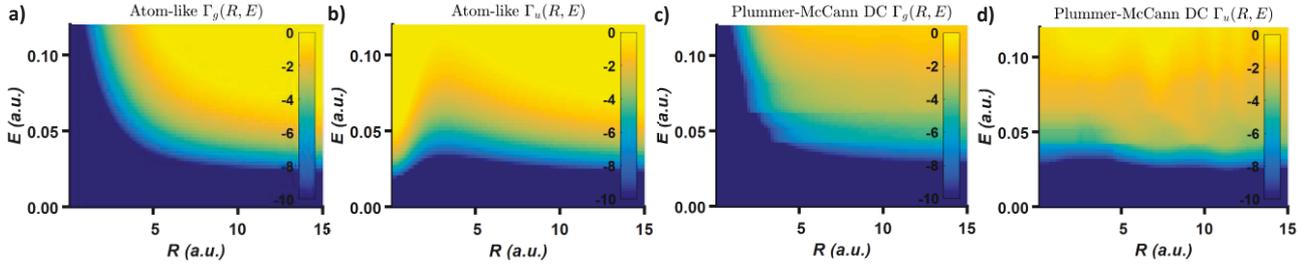

Figure 5.11: Comparison of the atom-like (atom-like rate) ionization rate with the exact ionization rate (PM-rate). a) shows the logarithm of the atom-like rate as function of R and $|E|$ for ionization from $1s\sigma_g$ electronic state. b) shows the same as a) but for ionization from the $2p\sigma_u$ electronic state. c) and d) show the same as a) and b) but for the PM-rate.

Altogether, we have illustrated two sets of R- and $|E|$-dependent ionization rates here. One, the so-called atom-like rate, is an *ad hoc* modification of the atomic ionization rate which takes into account the R-dependence of the electron's binding energy. The other, the so-called PM-rate, is based on an exact numerical calculation of the ionization rate of H_2^+ in a static external field of strength $|E|$, which has been an inter- and extrapolated to cover the needed range of values along R and $|E|$. The major qualitative difference between both sets of rates is that the PM-rate exhibits R-dependent modulations for ionization from $2p\sigma_u$ state which are not found in the atom-like -rate for ionization from the same state.

5.4   Comparison between Two-Level Model and Experimental Data

The previous section introduced a 1D two-level model on strong-field photoionization of H_2^+. It combines dissociative nuclear dynamics on the $1s\sigma_g$- and the $2p\sigma_u$-electronic levels with static ionization rates, $\Gamma_g(R, |E(t)|)$ and $\Gamma_u(R, |E(t)|)$, which are sensitive to the internuclear distance, R, and the strength of the electric field, $|E(t)|$. Thereby, two sets of different ionization rates can be tested in the model. The first set is an atom-like rate, $\Gamma_g^A(R, |E(t)|)$ and $\Gamma_u^A(R, |E(t)|)$ (atom-like rate). The second set of rates $\Gamma_g^{PM}(R, |E(t)|)$ and $\Gamma_u^{PM}(R, |E(t)|)$ (PM rates) is based on an exact calculation of the ionization rate of H_2^+ in a static external field. In this chapter, the results of the two versions of the 1D two-level model are compared to experimental data. All presented calculations are averaged over the initial distribution of vibrational states as well as over the intensity distribution in the focal volume as close as possible to the conditions in the measurement. For the whole comparison, measured data for ionization of H_2^+ by $\tau = 65$ fs, $\lambda = 2000$ nm with peak intensitites up to 1.3×10^{15} W/cm^2 is shown.

5.4.1 Intensity Dependence of Kinetic Energy Release Spectra

Here we compare the measured intensity dependence of the KER spectrum parallel to the polarization axis of the laser to results from the 1D two-level model calculations with the two different sets of ionization rates.

For the plot of the experimental data in Figure 5.12 a), ionization events where the angle between the polarization axis and the vector $\boldsymbol{p}_1 - \boldsymbol{p}_2$ is smaller than $\vartheta \pm 20°$ have been selected, see Figure 5.1 b) for an illustration of the geometry. Afterwards, the selected events are binned into a 2D histogram, $Y(E_{KER}, I_0)$, with $E_{KER} = (\boldsymbol{p}_1 - \boldsymbol{p}_2)^2/2m_{H^+}$, on the one axis and the tagged peak intensity, I_0, on the other axis. Removing the monotonous increase of the yield for increasing I_0 by normalizing the 2D histogram within each I_0 bin (along each row in Figure 5.12), reveals intensity-dependent shape of the KER spectrum as shown in Figure 5.12 a). Corresponding cuts of the normalized KER spectra are shown in Figure 5.12 b). Note that spectra for different I_0 are shifted along the y-axis by 0.5 in order to improve readability in this plot. Together with the data points, also a smooth of the measured data is shown. One can use the approximate conversion between internuclear distance, R, and KER, i.e. $R \approx 1/E_{KER}$, to investigate the measured distribution as function of R instead of as function of KER. The corresponding R-dependent distributions of the lines in Figure 5.12 b) for different I_0 are shown in Figure 5.12 c).

Inspection of Figure 5.12 a) and Figure 5.12 b) shows that the KER spectrum changes for increasing peak intensity. The overall trend is that higher peak intensity shifts the KER spectrum to larger KERs. At low intensities, $I_0 \approx 0.2 \times 10^{15}$ W/cm^2, the KER spectrum peaks around $E_{KER} \approx 3.5$ eV and has a shoulder around $E_{KER} \approx 5$ eV. Increasing to $I_0 \approx 0.4 \times 10^{15}$ W/cm^2, leads to two peaks of almost equal height at 3.5 and 5 eV. Further increasing I_0 allows the peak at 5 eV to take over the highest yield while the peak at 3.5 eV gradually develops into a shoulder with smaller yield.

Observing the R-dependent distributions shows that higher peak intensity leads to ionization at smaller distances. The peaks in the KER spectrum lead to the formation of corresponding peaks in the approximate ionization distances. For small $I_0 \approx 0.2 \times 10^{15}$ W/cm^2 ionization most likely occurs around $R \approx 10$ a. u.. Increasing I_0 leads to ionization at smaller Rs a and to formation of a double peak structure where ionization peaks around $R \approx 6$ and 8.

Comparing the measured data to calculated results from the two-level model in Figure 5.12 d)-i) reveals qualitative agreement with the measurement. Higher I_0 leads to ionization with higher KER, which corresponds to ionization at smaller distances. Investigation of Figure 5.12 d)-f) shows that use of the atom-like set of ionization rates does not lead to a peaked structure in the KER or the R distribution as observed in the experiment. However, the use of the PM-rates Figure 5.12 g)-i) support the observation of the peaks. Even the transition from a single peak at low KER to a double peak and to a single peak at high KER for increasing I_0 is reproduced by this calculation. However, the position of the maxima in Figure 5.12 g)-i) are at too small in KER too large in R, respectively. Despite this noticed discrepancies, the agreement between measured data and the simple 1D two-level model with PM rate is reasonable on a qualitative level particularly in view of the model's simplicity. The model reproduces the trends of the intensity dependence as well as the changes of the peaks in the KER spectra. Both are observed in the measurement.
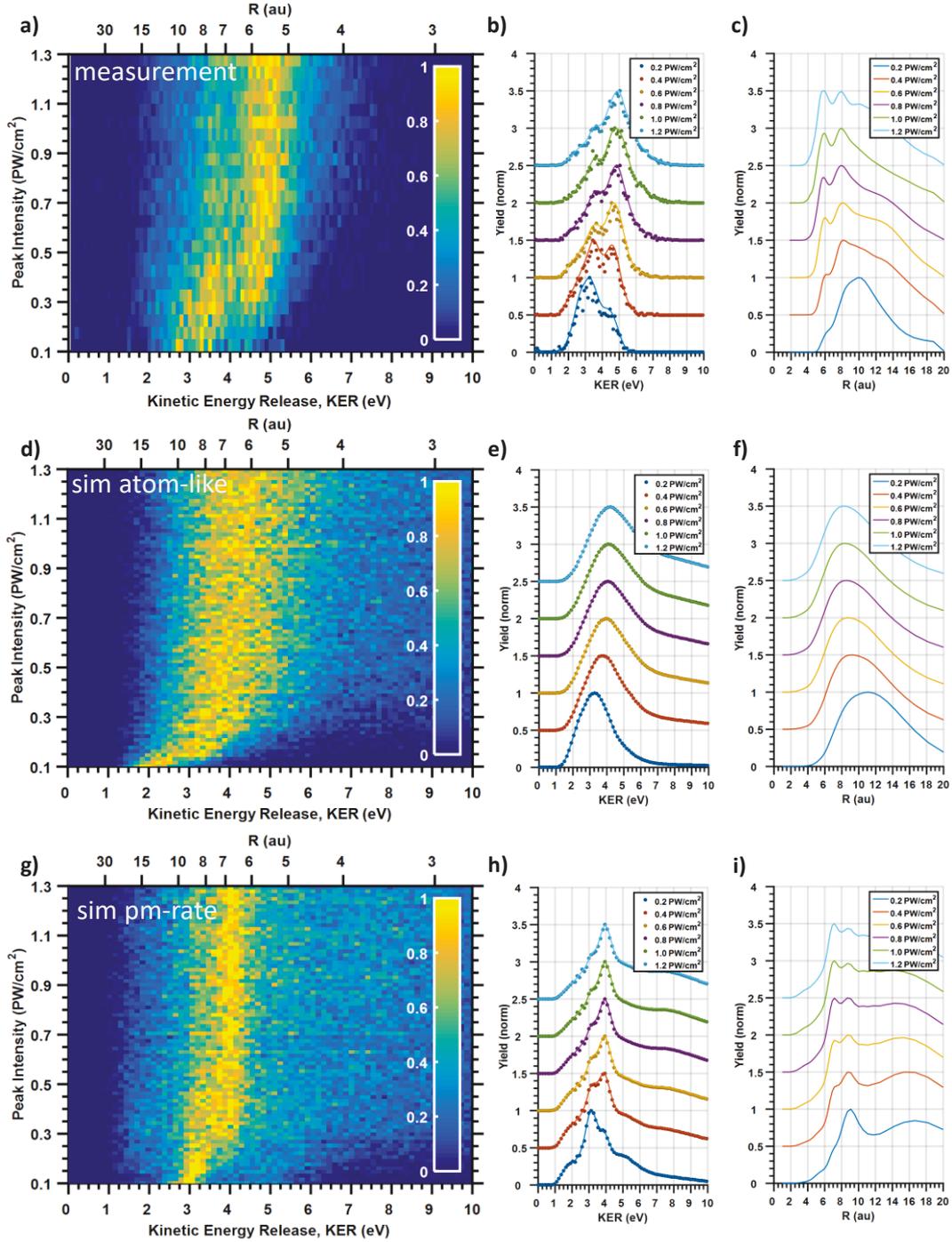
Figure 5.12: Intensity dependent KER spectra $\pm 20°$ for ionization of H_2^+ by an infrared laser pulse ($\tau = 65$ fs, $\lambda = 2000$ nm). a) - c) illustrate the measured KER spectrum as function of the peak intensity of the laser pulse. Note that the 2D histogram in a) has been normalized along each line with constant intensity in order to emphasize the shape of the KER spectrum. b) shows corresponding lineouts which are integrated within $\pm 0.1 \times 10^{15}$ W/cm^2 around the given values for I_0 in the inset. The dots are the data points while the line is a smooth of the data. An approximate conversion of the smooths from KER to R using $R \approx 1/E_{KER}$ and taking into account the Jacobian allows to investigate the distributions as function of R as is shown in c). d)-f) show the same as a)-c), but calculated within the two-level model using the atom-like ionization rate. g)-i) shows the same as d)-f) but the PM rates have been used in the calculation.

The reason for the mentioned discrepancies can be attributed to several simplifications and imperfections in the model : i) The set of PM-rates from [28] has only been published up to a field strength of $|E| \approx 0.08$ a. u. corresponding to $I \approx 0.2 \times 10^{15}$ W/cm^2. This is only a fifth of the intensity range that is covered by the measurement. The extrapolation used is likely to be erroneous for high field strength. In order to improve this situation one might try to calculate ionization rates at higher field strength based on [157]. ii) The two-level model neglects molecular rotations. Therewith, effects of dynamic alignment as well as the effects that stem from the orientation dependence of the coupling efficiency between $1s\sigma_g$- and the $2p\sigma_u$-electronic levels are neglected. Further, the dependence of the ionization rate on the angle between the molecular axis and the direction of the linear polarization, ϑ, [156] is completely neglected in the model while the measurement is integrated over some range of ϑ. iii) Limiting the model to two electronic states might oversimplify the nuclear dynamics before ionization. iv) Using the reflection principle in the model together with the assumption of zero initial velocity on the $1/R$-potential to connect between the R-dependent ionization and the final KER might cause discrepancies as well as neglecting the possibility of interferences between ionization from the different two electronic states.

Despite the discrepancies, the demonstrated qualitative agreement between the measurements allows for explanation and interpretation of the observations along the lines of the model 1D two-level model. We start with the observation that higher peak intensity leads to higher KERs. Increasing the intensity at constant pulse duration leads to a faster increase of the field strength during the pulse envelope. Due to the limited speed of the nuclear stretching dynamics, a rapidly increasing pulse envelope allows ionization at smaller Rs which leads to the observation of higher KERs. In turn, this means that ionization at large Rs is depleted and thus, the signal from low KER such that altogether, the high intensity KER spectrum is shifted to higher KERs compared to the low intensity KER spectrum. This behavior is supported by the measurement and by both versions of the model.

The peaked features in the KER spectra are reproduced by the model, only if the calculation uses an ionization rate that supports these peaks such as PM-rates. From this, one can conclude that the peaked features do not stem from the initial distribution of the vibrational states or nuclear dynamics before ionization. However, they are related to the intrinsic property of the field ionization rate of H_2^+ from the $2p\sigma_u$ electronic state, which is that it is enhanced for certain combinations of the external field strength $|E|$ and internuclear distance R. This has been shown by numerically exact calculations of the ionization rate of H_2^+ in a quasi-static field in ref. [28] which were also used for the model calculations presented here. However, as the simulations show [28], the exact positions and number of enhanced peaks in KER (or R) is not fixed, but is sensitive to the applied peak intensity as both theory and measurement demonstrate, see Figure 5.12 and Figure 5.10. Further, the positions, strength and width of the enhanced peaks is sensitive to the molecular alignment. Fundamentally, the peaks originate from the three-dimensional shape of the electron density and the corresponding outgoing electron density flux which adjusts in the combined potential of the protons and an the external field to complex shapes, see [28] for details.

Altogether, one can understand strong-field photoionization of H_2^+ at infrared wavelength along the lines of the 1D two-level model with PM-rates. In the beginning of the laser pulse, the external field couples, time-dependently, the $1s\sigma_g$ and the $2p\sigma_u$ electronic states. The coupling leads to stretching nuclear dynamics such that the wave function is spread over a wide range of Rs where the $1s\sigma_g$ and the $2p\sigma_u$ electronic state are populated. The shape of the stretched nuclear wave function is sensitive to the initial vibrational state, and the time-dependent shape of the external field which characterized by parameters such as the intensity, wavelength, pulse duration. After and

during the stretching, the molecule is ionized in the quasi-static, but oscillating, field predominantly from the $2p\sigma_u$ electronic state. For the protons, ionization means that they repel each other on the $1/R$-potential such that their relative motion leads to a gain in energy, which is then observed as the final KER. Observed peaks in the KER spectra originate from intrinsic property of the ionization rate of H_2^+ in a static external field. The observability and exact position in the KER spectrum is sensitive to the details of the stretching nuclear dynamics.

5.4.2 Observations in Joint Nuclear-Electron Energy Distributions

In order to gain further insight into the ionization dynamics the 1D two-level model is tested by comparing the measured and calculated joint nuclear-electronic energy distributions (JED) in Figure 5.13. As explained earlier in section 5.2.1, the electron energy of the experimental JED is based on the electron momentum, $\boldsymbol{p}_e$, which is inferred from the measured proton momenta employing momentum conservation, $\boldsymbol{p}_e = -(\boldsymbol{p}_1 + \boldsymbol{p}_2)$. Figure 5.13 a) shows a 2D histogram with electron energy, E_e, on one axis and the kinetic energy release, E_{KER}, on the other axis. The colorcode shows the logarithm with base 10 of the E_{KER}- and E_e-dependent yield, i.e. $\log_{10}(W_{ionJED}(E_{KER}, E_e))$.

For the plot, ionization events with a peak intensity in the range between 0.5 and 1×10^{15} W/cm^2, have been selected. The mean intensity of all shots is $\approx 0.76 \times 10^{15}$ W/cm^2. The distributions at lower and higher intensities are similar. For the electron energy, events from all electron emission angles are taken into account, while the calculation of electron energy uses the momentum component that is parallel to the linear polarization of the laser only, i.e. the z-axis such that $E_e = 0.5p_{e_z}{}^2$. The observed JED in Figure 5.13 a) is a smooth distribution with the highest yield at the lowest electron energies. The KER spectrum exhibits the double peak feature as discussed earlier and shown as blue line in Figure 5.13 b) for reference. Interesting is the observation that the yield of photoelectrons at high energies oscillates with the kinetic energy of the nuclei, see the JED in Figure 5.13 a). The energetic width of the photoelectron spectrum measured by the mean of the electron energy, $M_{ionE_e}(E_{KER})$, see equation (5.14), behaves similarly. This observation is emphasized by the orange curve in Figure 5.13 b) where $M_{ionE_e}(E_{KER})$, is plotted as function of E_{KER}. It clearly oscillates as function of E_{KER}. Thereby, the maxima of the KER spectrum are found very close to the position of the minima of the mean electron energy and vice versa.

Comparing the experimental plots to calculated JEDs for two different versions of the 1D two-level that are shown in Figure 5.13 c)-d) yields better qualitative agreement for the version that used the PM rates. While the atom-like rates neither reproduce the observed structures in the JED nor in M_{ionE_e}, see Figure 5.13 c) and d), the version with the PM rates shows faint features that can be related to experimental observations on a qualitative level. Particularly, $W_{ionJED}(E_{KER}, E_e)$ is structured and M_{ionE_e} shows modulations, whose minima are found near the positions of the maxima in the KER spectrum. In contrast, the atom-like version exhibits a smooth JED and the modulations in $M_{ionE_e}(E_{KER})$ are missing. Additional to this qualitative agreement, however, the JEDs of both versions are found to be too narrow in energy. For the version with the PM rate it is likely that the discrepancies originate from the non-perfect ionization rate, which was published only in a smaller parameter range than necessary for the model calculation. Further, the model calculations neglect rotation and also angular dependencies of the coupling strength between the electronic levels as well of the $|E|$ and R-dependent ionization rate.
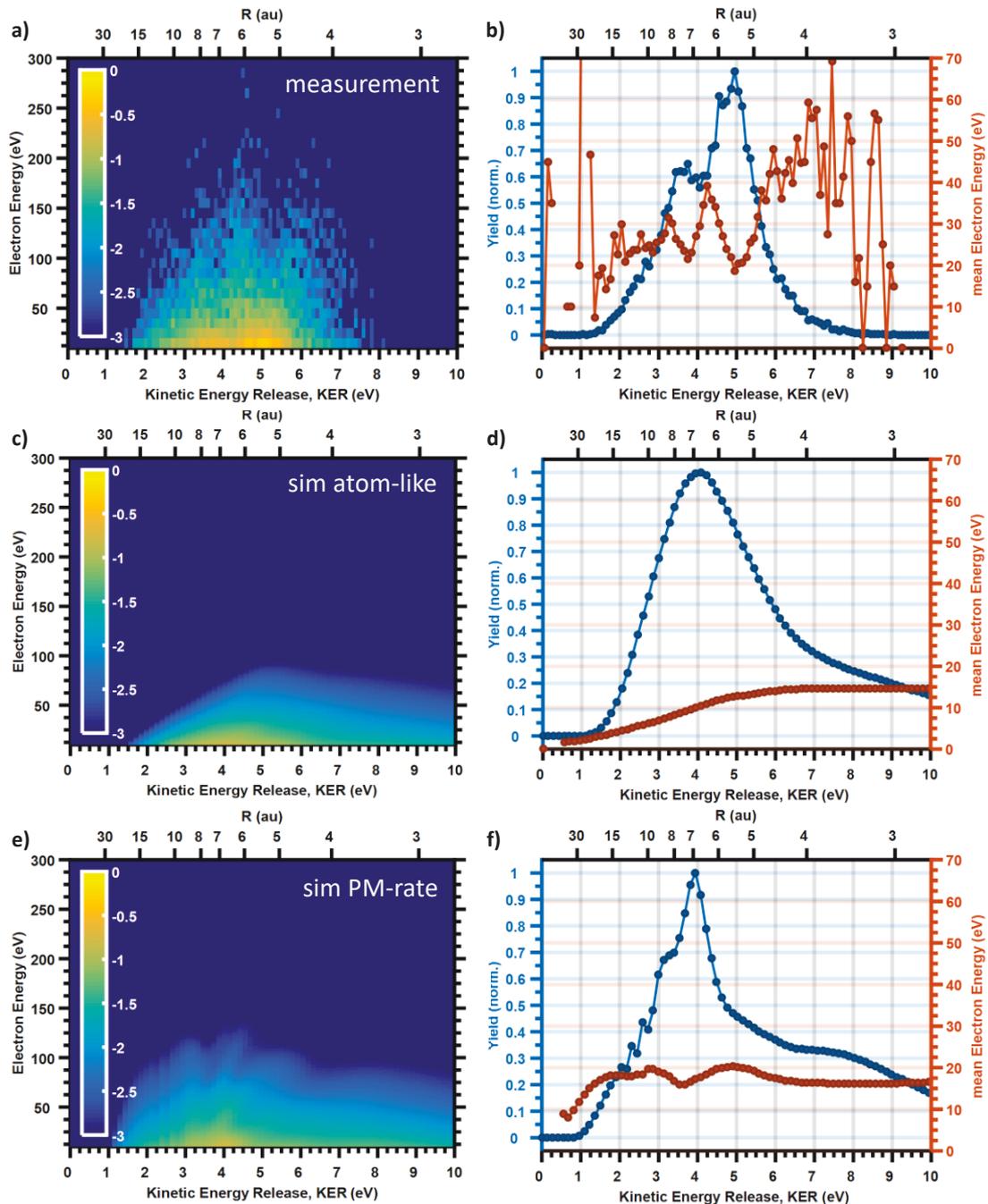
Figure 5.13 Joint nuclear-electron energy distrbution from ionization of H_2^+ by 65-fs-2000nm laser pulse.

a) shows the logarithm of the measured JED as a two-dimensional histogram. In b), the corresponding KER spectrum (blue) and the mean of the photoelectron energy spectrum is shown. This quantity is a measure for the width of the photoelectron energy spectrum. c) and d) show the corresponding plots of the simulation which uses the atom-like ionization rate. e) and f) shows the same as c) and d) but for the version of the model that uses PM rate.

An explanation for the observed modulations of the KER dependent photoelectron spectra can be given along the lines of the 1D two-level model with the PM rate where qualitative agreement between simulation and measurement has been demonstrated. As said, the leading edge of the pulse stretches the wave function along R, where it creates a wide distribution. Then ionization in the quasi-static field facilitates electron ejection. As the

ionization rate is enhanced for certain Rs, ionization at the Rs with enhancement takes place at effectively lower field strength. Thus, the photoelectrons that are ejected at these Rs reach lower energies as the photoelectron spectrum of direct electrons scales with $U_P = E_0{}^2/(4\omega^2 9$ where E_0 is the field strength of the laser at ionization and ω its frequency. All these arguments proceed from R to KER as discussed before such that finally, modulations in the JED and KER-dependent mean of the photoelectron energy occur as observed in Figure 5.13 a) and b) as well as in the 1D, two-level PM-rate model calculations in Figure 5.13 e) and f). Thereby, the minima of $M_{ionE_e}(E_{KER})$ coincide with maxima in the KER spectrum as a large ionization rate leads to high yield but lower electron energy as one would expect from this mechanism.

5.5   Conclusion and Outlook

In this chapter, strong-field photoionization of a beam of H_2^+ by an short-wave infrared laser field has been investigated. During the discussion of the measurement, it has been demonstrated that the initial momentum distribution of the ion beam target in the Jena ITRIMS setup is narrow enough to infer the electron momentum from the measurement of the proton momenta using momentum conservation. However, it should be noted that the initial momentum spread blurs the inferred electron momentum distribution approximately with a Gaussian function which has a width of $\Delta p_r \approx 0.79$. Further, equipping the Jena ITRIMS setup with the opportunity for automated scanning and tagging of the peak intensity enables detailed investigation of the intensity dependence of different processes. As an example for intensity tagging, the saturation intensity of dissociation and ionization of H_2^+ by 1800 nm-50-fs laser pulses have been determined to be $I_{satDiss} \approx 0.07 \times 10^{15}$ W/cm^2 and $I_{satIon} \approx 3.5 \times 10^{14}$ W/cm^2. Thereby, it has been demonstrated that the geometry of the ion target in the ITRIMS setup is well approximated by an ultrathin, two-dimensional target, that is infinitely extended perpendicular to the direction of laser polarization, but ultrathin along the propagation direction.

Next we have introduced a one-dimensional two-level model for strong-field photoionization of H_2^+. It aims on gaining intuitive insight into the relevant physics of the ionization dynamics. To this end, the $1s\sigma_g$- and the $2p\sigma_u$- electronic levels are coupled by the external field to describe the nuclear stretching dynamics. During the stretching, ionization is embedded in the model using quasi-static ionization rates, $\Gamma_g(R, |E(t)|)$ and $\Gamma_u(R, |E(t)|)$. The implemented ionization rates from both levels are sensitive to the internuclear distance, R, and the strength of the electric field, $|E(t)|$. Further, two different sets of ionization rates, i.e. an atom-like set of rates $\Gamma_g^A(R, |E(t)|)$ and $\Gamma_u^A(R, |E(t)|)$ (atom-like rate) and a fit to an exact calculation of static field ionization rates from H_2^+ $\Gamma_g^{PM}(R, |E(t)|)$ and $\Gamma_u^{PM}(R, |E(t)|)$ (PM rate), have been introduced. All calculations are averaged over the distribution of intensities in the focal volume and over the initial distribution of the vibrational states of the target.

Next, the measured intensity dependence of the kinetic energy release spectra (KER) for 2000 nm-65-fs pulses is compared with the two versions of the model. The comparison shows that both versions support the experimentally observed trend that higher intensity leads to KER spectra at higher energy which is related to ionization at smaller internuclear distance R. However, the experimentally observed peak structures in the measured KER spectra are qualitatively reproduced only if the exact ionization rate, i.e. the PM-rate with it's R-dependent enhancements, is used. This demonstrates that intrinsic properties of the static ionization rate can be seen in the measurement and

simulations if the nuclear dynamics before ionization leads to population of a wide range of internuclear distances. Continuing the comparison for joint nuclear-electronic energy distributions (JEDs) demonstrates that the simple model with PM-rate reproduces the observation of modulations of the mean of the electron energy whose minima approximately overlap with the maxima of the yield in the KER spectrum. Along the lines of the model one can understand this behavior in such a way that ionization with high yield effectively takes place at lower field strength which then leads to narrower electron energy distribution as ionization at lower field strengths causes less acceleration of the electron by the field.

The experimental and theoretical efforts lead to the following mechanism for strong-field photoionization of H_2^+ at infrared wavelength. In the beginning of the laser pulse, the external field time-dependently couples the $1s\sigma_g$ and the $2p\sigma_u$ electronic states. The coupling leads to stretching nuclear dynamics which populates a wide range of Rs. During the stretching, the molecule is ionized by the quasi-static but oscillating field predominantly from the $2p\sigma_u$ electronic state. Ionization creates two protons which repel each other on the $1/R$-potential and thus, gain kinetic energy that is then observed as the final KER distribution. Observed maxima in the KER spectra originate from modulations of the R-dependent ionization rate of H_2^+ in a static external field. These peaks in the ionization rate propagate from R to KER and lead to maxima in the observed KER spectrum. The maxima in the KER spectrum are correlated with a lower electron energy in the JED as ionization around the enhancements of the rate effectively takes place at lower field strength.

The present investigation is an example of coupled electron nuclear dynamics which are driven by strong infrared fields. The cycle duration of the external field forces the electron motion on a time-scale during which the light nuclei of the H_2^+ molecule can significantly adjust their positions. An interesting question to be addressed in the future might be whether the sub-cycle nuclear dynamics are relevant or whether the nuclear dynamics on the timescale of the envelope of the field are important. To this end, one might consider a measurement and theoretical investigation with different pulse durations. Possibly, ionization could be caused by intense infrared few-cycle fields at a wavelength around 1.8 μm ideally with control or tagging of the fields carrier-envelope phase. A first step towards such an investigation has been taken with the realization of the few-cycle laser source in chapter 2.

In view of coupled electron nuclear dynamics, it would also be interesting to push the measurement further towards even longer wavelength. As preliminary simulations based on the presented model for strong-field photoionization of H_2^+ show, this will give the nuclei even more time to move during the optical cycle such that interesting dynamics can be expected.

Regarding the relevance of the observed dynamics for other molecules, one should have in mind that H_2^+ is the simplest molecule but also the lightest and thus, the one with the fastest nuclear dynamics. In order to test whether the observed dynamics are relevant for heavier molecules, one might consider an investigation which compares ionization of H_2^+ and D_2^+, e.g. using similar experimental conditions as in the measurement here.

6   Conclusion and Outlook

This thesis describes the implementation and operation of a source of intense femtosecond laser pulses in the short-wave infrared (SWIR) spectral domain that has been used to investigate the interaction between atoms and diatomic molecules, specifically the strong-field photoionization (SFI) of Xe and of an ion beam of H_2^+ molecules. Both interactions have also been investigated using theoretical models that are both simple enough to allow intuitive understanding while fundamental underlying time-dependent mechanisms of the interaction are captured.

In chapter 2, a description of how the source has been put to operation and has been characterized. Implementation of frequency-resolved optical frequency resolved optical gating enabled the measurement of the pulse duration and characterization of spectral phase. The use of the hollow-fiber compression technique allowed the generation of passively carrier-envelope phase stable few-cycle pulses with a pulse duration close to two optical cycles and an energy of >0.7 mJ in short-wave infrared spectral domain around 1.8 μm at a repetition rate of 1 kHz. The source is suited to investigate strong-field laser-matter interaction directly as detailed in the thesis here or to be used as driver for applications of strong-field processes, such as the generation of femtosecond extreme ultraviolet radiation possibly into the water window via the high-harmonic generation process.

In chapter 4, SFI of Xe has been investigated [10]. To this end, the velocity-map imaging technique has been applied to measure three-dimensional photoelectron momentum distributions (PMDs) from SFI of Xe. Besides the observation of low-energy features that are typical for SFI of atoms by SWIR and IR fields, the measurements revealed an interesting prominent fork-like structure at close to a right angle to the polarization axis of the laser. Comparing measurements where ionization is caused by long pulses with measurements where ionization is caused by few-cycle pulses revealed a strong dependence on the pulse duration for the fork as well as other typical features of the PMD. The measurements were compared to theoretical expectations of an improved version of the semi-classical model (SCM) of atomic SFI, which models the ionization dynamics of atoms using quasi-static field ionization rates, electron trajectories in the laser field and elastic rescattering between electron and ion. It is shown that the SCM reproduces low-energy features including the fork and their observed susceptibility to pulse duration, if it is augmented by rescattering trajectories that are substantially longer than one optical cycle. Further, it has been shown here that the modeling of the elastic electron-ion rescattering must take the angle and energy dependence of the differential scattering cross-section into account in order to reproduce low energy features. This finding puts low energy features in SFI of atoms by SWIR fields on the same footing as, e.g. the high-energy plateau in the PMD. Further, it shows that, similar to high-energy features, low energy features in the PMD are governed by the time-dependent shape of the laser field.

In chapter 5, SFI of diatomic molecules by SWIR fields has been investigated, specifically ionization of an ion beam of H_2^+ molecules [158]. To this end, the Jena ion-target recoil-ion momentum spectroscopy setup (ITRIMS) for three-dimensional (3D) coincidence momentum imaging has been used together with the source of intense femtosecond SWIR fields to measure the intensity-dependent 3D vector-momentum distribution of both fragmentation channels of H_2^+, i.e. dissociation $(H_2^+ \rightarrow H^+ + H, \boldsymbol{p}_{H^+}, \boldsymbol{p}_H,)$ and ionization $(H_2^+ \rightarrow H^+ + H^+ + e^-, \boldsymbol{p}_1, \boldsymbol{p}_2, \boldsymbol{p}_e)$. For the data analysis, we have concentrated on the ionization channel. The measurement demonstrates that for ionization by

SWIR fields, the initial momentum spread of the ion beam target is narrow enough and the measurement resolution is high enough to infer the electron momentum, $\boldsymbol{p}_e$, although only the two protons with momenta, $\boldsymbol{p}_1, \boldsymbol{p}_2$, have been detected. To this end, one uses momentum conservation in laser-induced fragmentation, i.e. $-\boldsymbol{p}_e = \boldsymbol{p}_1 + \boldsymbol{p}_2$. The trick gives access to all fragment momenta, $\boldsymbol{p}_1, \boldsymbol{p}_2, \boldsymbol{p}_e$ and enables the analysis of joint electron-nuclear energy distributions (JEDs), which are of particular interest for the investigation of coupled electron nuclear dynamics.

Turning to the results of laser-induced fragmentation of the H_2^+ measurement, which have been analyzed in detail, the intensity dependence of the kinetic energy release spectra (KER) shows a peaked shaped, which moves for increasing intensity to higher KER. Using the approximate conversion from KER to the internuclear distance, R, of ionization, i.e. $E_{KER} \approx 1/R$, this observation means that ionization as function of R is peaked and that ionization at higher intensity leads to ionization at smaller distance R. The second observation is found in the JEDs. They show that the width of the photoelectron spectrum is modulated as function of KER. Thereby, higher yields in the KER spectrum are correlated with a narrower photoelectron spectrum.

The H_2^+ measurements were compared to expectation from a one-dimensional two-level model on the SFI of H_2^+. It uses time-dependent coupling of the $1s\sigma_g$ and $2p\sigma_u$ electronic states in H_2^+ by the external laser field to model the dissociative dynamics of the nuclei. Ionization from both states is incorporated using quasi-static field ionization rates that are sensitive to the inter-nuclear distance, R, and the instantaneous field strength, $|E|$. The electron momentum is inferred from the connection between ionization and the instantaneous vector potential at the time of ionization, i.e. $p_e(t_i) \approx +A(t_s)$. Comparing the measurement and the model based on the intensity dependence of the KER spectrum and the JEDs demonstrates reasonable qualitative agreement. Thus, one can conclude that SFI of diatomic molecules by SWIR fields proceeds by the following coupled nuclear electron dynamics: Coupling of electronic states in the beginning of the laser field induces a nuclear stretching motion, which leads to the population of a wide range of internuclear distances. From there, ionization by the quasi-static, but oscillating, field of increasing strength facilitates electron ejection which suddenly creates two protons who gain kinetic energy on their way to the detector as they repel each other. The simultaneously freed electron is driven away by the ionizing laser field. As the quasi-static ionization has the property of being enhanced / suppressed for some internuclear distances, signatures of these enhancements can be found as modulation in the kinetic energy release spectra. For the electron, an enhancement of the ionization rate leads to ionization at effectively lower field strength such that the photoelectron spectrum is narrower for regions where the ionization rate is enhanced. The observed dynamics are an example of coupled electronic and nuclear motions in a molecule which is driven by the external field.

For future directions, the development of single-shot carrier-envelope phase measurement based on strong-field ionization at short-wave infrared fields might enable the investigation of strong-field ionization of atoms and fragmentation dynamics of molecules in few-cycle, short-wave infrared fields as function of the carrier-envelope phase. Having this opportunity might be used to address the question of whether the discussed stretching dynamics of the nuclei before ionization of H_2^+ take place on the time scale of the envelope, i.e. a few tens of femtoseconds, or whether they are fast enough to be sensitive to the carrier-envelope phase and can, thus be controlled on a few fs time scale.

References

[1]   P. Agostini, F. Fabre, G. Mainfray, G. Petite, and N. K. Rahman, "Free-free transitions following six-photon ionization of xenon atoms," *Phys. Rev. Lett.*, vol. 42, no. 17, pp. 1127–1130, 1979.

[2]   G. G. Paulus, W. Nicklich, H. Xu, P. Lambropoulos, and H. Walther, "Plateau in above threshold ionization spectra," *Phys. Rev. Lett.*, vol. 72, no. 18, pp. 2851–2854, 1994.

[3]   C. L'Huillier, A., Lompre, L. A., Mainfray, G., Manus, "Multiply charged ions induced by multiphoton absorption in rare gases at 0.53 μm," *Phys. Rev. A*, vol. 27, no. 5, pp. 2503–2512, 1983.

[4]   M. Ferray, A. L'Huillier, X. F. Li, L. A. Lompre, G. Mainfray, C. Manus, H. Search, C. Journals, A. Contact, M. Iopscience, and I. P. Address, "Multiple-harmonic conversion of 1064 nm radiation in rare gases," *J. Phys. B At. Mol. Opt. Phys.*, vol. 31, p. L31, 1988.

[5]   T. Nubbemeyer, K. Gorling, a. Saenz, U. Eichmann, and W. Sandner, "Strong-Field Tunneling without Ionization," *Phys. Rev. Lett.*, vol. 101, no. 23, p. 233001, Dec. 2008.

[6]   G. G. Paulus, F. Lindner, H. Walther, a. Baltuška, E. Goulielmakis, M. Lezius, and F. Krausz, "Measurement of the Phase of Few-Cycle Laser Pulses," *Phys. Rev. Lett.*, vol. 91, no. 25, pp. 1–4, Dec. 2003.

[7]   T. Wittmann, B. Horvath, W. Helml, M. G. Schätzel, X. Gu, A. L. Cavalieri, G. G. Paulus, and R. Kienberger, "Single-shot carrier–envelope phase measurement of few-cycle laser pulses," *Nat. Phys.*, vol. 5, no. 5, pp. 357–362, Apr. 2009.

[8]   P. Colosimo, G. Doumy, C. I. Blaga, J. Wheeler, C. Hauri, F. Catoire, J. Tate, R. Chirla, a. M. March, G. G. Paulus, H. G. Muller, P. Agostini, and L. F. DiMauro, "Scaling strong-field interactions towards the classical limit," *Nat. Phys.*, vol. 4, no. 5, pp. 386–389, Mar. 2008.

[9]   C. I. Blaga, F. Catoire, P. Colosimo, G. G. Paulus, H. G. Muller, P. Agostini, and L. F. DiMauro, "Strong-field photoionization revisited," *Nat. Phys.*, vol. 5, no. 5, pp. 335–338, Mar. 2009.

[10]   M. Möller, F. Meyer, A. M. Sayler, G. G. Paulus, M. F. Kling, B. E. Schmidt, W. Becker, and D. B. Milošević, "Off-axis low-energy structures in above-threshold ionization," *Phys. Rev. A*, vol. 90, no. 2, p. 23412, Aug. 2014.

[11]   H. B. van Linden van den Heuvell and H. G. Muller, *Multiphoton Processes*. Cambridge, England: Cambridge University Press, 1988.

[12]   P. B. Corkum, "Plasma perspective on strong field multiphoton ionization," *Phys. Rev. Lett.*, vol. 71, no. 13, pp. 1994–1997, 1993.

[13]   S. Skruszewicz, J. Tiggesbäumker, K. H. Meiwes-Broer, M. Arbeiter, T. Fennel, and D. Bauer, "Two-Color Strong-Field Photoelectron Spectroscopy and the Phase of the Phase," *Phys. Rev. Lett.*, vol. 115, no. 4, pp. 1–6, 2015.

[14]   I. Ben-Itzhak, P. Q. Wang, J. F. Xia, A. M. Sayler, M. A. Smith, K. D. Carnes, and B. D. Esry, "Dissociation and Ionization of H_{2}^{+} by Ultrashort Intense Laser Pulses Probed by Coincidence 3D Momentum Imaging," *Phys. Rev. Lett.*, vol. 95, no. 7, pp. 1–4, 2005.

[15]   T. Rathje, A. M. Sayler, S. Zeng, P. Wustelt, H. Figger, B. D. Esry, and G. G. Paulus, "Coherent Control at Its Most Fundamental: Carrier-Envelope-Phase-Dependent Electron Localization in Photodissociation of a H_{2}^{+} Molecular Ion Beam Target," *Phys. Rev. Lett.*, vol. 111, no. 9, p. 93002, Aug. 2013.

[16]   W. Becker, F. Grasbon, R. Kopold, D. Milošević, G. G. Paulus, H. Walther, D. B. Milosevic, G. G. Paulus, and H. Walther, "Above-threshold ionization: From classical features to quantum effects," in *Advances in Atomic Molecular and Optical Physics*, vol. 48, no. 1979, 525 B STREET, SUITE 1900, SAN DIEGO, CA 92101-4495 USA: ACADEMIC PRESS INC, 2002, pp. 35–98.

[17]   S. V. Popruzhenko, "Keldysh theory of strong field ionization: history, applications, difficulties and perspectives," *J. Phys. B At. Mol. Opt. Phys.*, vol. 47, no. 20, p. 204001, 2014.

[18]   J. H. Posthumus, "The dynamics of small molecules in intense laser fields," *Reports Prog. Phys.*, vol. 67, no. 5, pp. 623–665, 2004.

References

[19]   J. H. Posthumus, J. Plumridge, M. K. Thomas, K. Codling, L. J. Frasinski, A. J. Langley, and P. F. Taday, "Dynamic and geometric laser-induced alignment of molecules in intense laser fields," *J. Phys. B At. Mol. Opt. Phys.*, vol. 31, pp. L553–L562, 1998.

[20]   W. A. Bryant, J. H. Sanderson, A. El-Zein, W. R. Newell, P. F. Taday, and A. J. Langley, "Laser-induced Coulomb explosion, geometry modification and reorientation of carbon dioxide," *J. Phys. B At. Mol. Opt. Phys.*, vol. 33, pp. 745–766, 2000.

[21]   A. M. Sayler, "Measurement of Ultrashort Intense Laser-Induced Fragmentation of Simple Molecular Ions," 2008.

[22]   A. Giusti-Suzor, X. He, O. Atabek, and F. H. Mies, "Above-Threshold Dissociation of H2+ in Intense Laser Fields," *Phys. Rev. Lett.*, vol. 64, no. 5, pp. 515–518, 1990.

[23]   J. . H. Posthumus, J. Plumridge, L. J. Frasinski, K. Codling, E. J. Divall, A. J. Langley, and P. F. Taday, "Slow protons as a signature of zero-photon dissociation of H2+," *J. Phys. B At. Mol. Opt. Phys.*, vol. 33, pp. 563–569, 2000.

[24]   P. H. Bucksbaum, A. Zavriyev, H. G. Muller, and D. W. Schumacher, "Softening of the H2+ Molecular Bond in Intense Laser Fields," *Phys. Rev. Lett.*, vol. 64, no. 16, pp. 1931–1934, 1990.

[25]   L. Frasinski, J. Posthumus, J. Plumridge, K. Codling, P. Taday, and a. Langley, "Manipulation of Bond Hardening in H2+ by Chirping of Intense Femtosecond Laser Pulses," *Phys. Rev. Lett.*, vol. 83, no. 18, pp. 3625–3628, 1999.

[26]   T. Zuo and A. D. Bandrauk, "Charge-resonance-enhanced ionization of diatomic molecular ions by intense lasers," *Phys. Rev. A*, vol. 52, no. 4, pp. 2511–2514, 1995.

[27]   J. H. Posthumus, A. J. Giles, M. R. Thompson, and K. Codling, "Field-ionization, Coulomb explosion of diatomic molecules in intense laser fields," *J. Phys. B At. Mol. Opt. Phys.*, vol. 29, no. 23, pp. 5811–5829, 1996.

[28]   M. Plummer and J. F. McCann, "Field-ionization rates of the hydrogen molecular ion," *J. Phys. B At. Mol. Opt. Phys.*, vol. 29, pp. 4625–4640, 1996.

[29]   B. Manschwetus, T. Nubbemeyer, K. Gorling, G. Steinmeyer, U. Eichmann, H. Rottke, and W. Sandner, "Strong laser field fragmentation of H2: Coulomb explosion without double ionization," *Phys. Rev. Lett.*, vol. 102, no. 11, pp. 1–4, 2009.

[30]   T. Popmintchev, M.-C. Chen, D. Popmintchev, P. Arpin, S. Brown, S. Alisauskas, G. Andriukaitis, T. Balciunas, O. D. Mücke, A. Pugzlys, A. Baltuska, B. Shim, S. E. Schrauth, A. Gaeta, C. Hernández-García, L. Plaja, A. Becker, A. Jaron-Becker, M. M. Murnane, and H. C. Kapteyn, "Bright coherent ultrahigh harmonics in the keV x-ray regime from mid-infrared femtosecond lasers.," *Science*, vol. 336, no. 6086, pp. 1287–91, Jun. 2012.

[31]   C. Ding, W. Xiong, T. Fan, D. D. Hickstein, T. Popmintchev, X. Zhang, M. Walls, M. M. Murnane, and H. C. Kapteyn, "High flux coherent super-continuum soft X-ray source driven by a single-stage, 10mJ, Ti:sapphire amplifier-pumped OPA." *Opt. Express*, vol. 22, no. 5, pp. 6194–202, Mar. 2014.

[32]   C. I. Blaga, J. Xu, A. D. DiChiara, E. Sistrunk, K. Zhang, P. Agostini, T. A. Miller, L. F. DiMauro, and C. D. Lin, "Imaging ultrafast molecular dynamics with laser-induced electron diffraction," *Nature*, vol. 483, no. 7388, pp. 194–197, 2012.

[33]   B. Wolter, M. G. Pullen, A.-T. Le, M. Baudisch, K. Doblhoff-Dier, A. Senftleben, M. Hemmer, C. D. Schroter, J. Ullrich, T. Pfeifer, R. Moshammer, S. Grafe, O. Vendrell, C. D. Lin, and J. Biegert, "Ultrafast electron diffraction imaging of bond breaking in di-ionized acetylene," *Science (80-.).*, vol. 354, no. 6310, pp. 308–312, 2016.

[34]   W. Quan, Z. Lin, M. Wu, H. Kang, H. Liu, X. Liu, J. Chen, J. Liu, X. He, S. Chen, H. Xiong, L. Guo, H. Xu, Y. Fu, Y. Cheng, and Z. Xu, "Classical Aspects in Above-Threshold Ionization with a Midinfrared Strong Laser Field," *Phys. Rev. Lett.*, vol. 103, no. 9, pp. 1–4, Aug. 2009.

[35]   B. Wolter, C. Lemell, M. Baudisch, M. G. Pullen, X. M. Tong, M. Hemmer, A. Senftleben, C. D. Schröter, J. Ullrich, R. Moshammer, J. Biegert, and J. Burgdörfer, "Formation of very-low-energy states crossing the ionization threshold of argon atoms in strong mid-infrared fields," *Phys. Rev. A*, vol. 90, no. 6, p. 63424, Dec. 2014.

[36]   Q. Z. Xia, D. F. Ye, L. B. Fu, X. Y. Han, and J. Liu, "Momentum Distribution of Near-Zero-Energy Photoelectrons in the Strong-Field Tunneling Ionization in the Long Wavelength Limit." *Sci. Rep.*, vol. 5, no. September 2014, p. 11473, 2015.

[37] W. Becker, S. P. Goreslavski, D. B. Milošević, and G. G. Paulus, "Low-energy electron rescattering in laser-induced ionization," *J. Phys. B At. Mol. Opt. Phys.*, vol. 47, no. 20, p. 204022, Oct. 2014.

[38] N. Takemoto and A. Becker, "Time-resolved view on charge-resonance-enhanced ionization," *Phys. Rev. A - At. Mol. Opt. Phys.*, vol. 84, no. 2, 2011.

[39] R. E. F. Silva, F. Catoire, P. Rivière, H. Bachau, and F. Martín, "Correlated Electron and Nuclear Dynamics in Strong Field Photoionization of H_{2}^{+}," *Phys. Rev. Lett.*, vol. 110, no. 11, p. 113001, Mar. 2013.

[40] I. Ben-Itzhak, P. Q. Wang, A. M. Sayler, K. D. Carnes, M. Leonard, B. D. Esry, A. S. Alnaser, B. Ulrich, X. M. Tong, I. V. Litvinyuk, C. M. Maharjan, P. Ranitovic, T. Osipov, S. Ghimire, Z. Chang, and C. L. Cocke, "Elusive enhanced ionization structure for H2+ in intense ultrashort laser pulses," *Phys. Rev. A - At. Mol. Opt. Phys.*, vol. 78, no. 6, pp. 1–7, 2008.

[41] H. Xu, F. He, D. Kielpinski, R. T. Sang, and I. . V. Litvinyuk, "Experimental observation of the elusive double- - - peak structure in R- - - dependent strong- - - field ionization rate of H 2 +," *Sci. Rep.*, vol. 1, no. August, pp. 1–7, 2015.

[42] P. M. Kraus, B. Mignolet, D. Baykusheva, A. Rupenyan, L. Horný, E. F. Penka, G. Grassi, O. I. Tolstikhin, J. Schneider, F. Jensen, L. B. Madsen, A. D. Bandrauk, F. Remacle, and H. J. Wörner, "Measurement and laser control of attosecond charge migration in ionized iodoacetylene.," *Science*, vol. 350, no. 6262, pp. 790–5, 2015.

[43] B. E. Schmidt, A. D. Shiner, P. Lassonde, J.-C. Kieffer, P. B. Corkum, D. M. Villeneuve, and F. Légaré, "CEP stable 1.6 cycle laser pulses at 1.8 μm.," *Opt. Express*, vol. 19, no. 7, pp. 6858–64, Mar. 2011.

[44] P. Béjot, B. Schmidt, J. Kasparian, J.-P. Wolf, and F. Legaré, "Mechanism of hollow-core-fiber infrared-supercontinuum compression with bulk material," *Phys. Rev. A*, vol. 81, no. 6, pp. 2–7, Jun. 2010.

[45] F. Meyer, "Generation and Application of Intense Few-Cycle Pulses at 1.8 μm," 2014.

[46] D. E. Spence, P. N. Kean, and W. Sibbett, "60-fsec pulse generation from a self-mode-locked Ti:sapphire laser.," *Opt. Lett.*, vol. 16, no. 1, pp. 42–44, 1991.

[47] P. Maine, D. Strickland, P. Bado, M. Pessot, and G. Mourou, "Generation of ultrahigh peak power pulses by chirped pulse amplification," *IEEE J. Quantum Electron.*, vol. 24, no. 2, pp. 398–403, 1988.

[48] Femtolasers, "USER MANUAL FEMTOPOWER ™," pp. 1–61, 2014.

[49] S. Cundiff and J. Ye, "Colloquium: Femtosecond optical frequency combs," *Rev. Mod. Phys.*, vol. 75, no. 1, pp. 325–342, 2003.

[50] F. Verluise, V. Laude, Z. Cheng, C. Spielmann, and P. Tournois, "Amplitude and phase control of ultrashort pulses by use of an acousto-optic programmable dispersive filter: pulse compression and shaping," *Opt. Lett.*, vol. 25, no. 8, p. 575, 2000.

[51] G. Cerullo, a. Baltuška, O. D. Mücke, and C. Vozzi, "Few-optical-cycle light pulses with passive carrier-envelope phase stabilization," *Laser Photon. Rev.*, vol. 5, no. 3, pp. 323–351, May 2011.

[52] R. Trebino, *Frequency-Resolved Optical Gating: The Measurement of Ultrashort Laser Pulses: The Measurement of Ultrashort Laser Pulses.* Springer Science & Business Media, 2000.

[53] B. E. Schmidt, A. D. Shiner, P. Lassonde, J. C. Kieffer, P. B. Corkum, D. M. Villeneuve, and F. Legare, "CEP stable 1.6 cycle laser pulses at 1.8 mu m," *Opt. Express*, vol. 19, no. 7, pp. 6858–6864, 2011.

[54] R. W. Boyd, *Nonlinear Optics*, 3rd ed. Elesevier, 2008.

[55] M. Nisoli, S. De Silvestri, and O. Svelto, "Generation of high energy 10 fs pulses by a new pulse compression technique," *Appl. Phys. Lett.*, vol. 68, no. 20, pp. 2793–2795, 1996.

[56] M. Nisoli, S. De Silvestri, O. Svelto, R. Szipöcs, K. Ferencz, C. Spielmann, S. Sartania, and F. Krausz, "Compression of high-energy laser pulses below 5 fs.," *Opt. Lett.*, vol. 22, no. 8, pp. 522–4, Apr. 1997.

[57] A. J. Verhoef, J. Seres, K. Schmid, Y. Nomura, G. Tempea, L. Veisz, and F. Krausz, "Compression of the pulses of a Ti:sapphire laser system to 5 femtoseconds at 0.2 terawatt level," *Appl. Phys. B Lasers Opt.*, vol. 82, no. 4, pp. 513–517, 2006.

[58] R. Szipocs, K. Ferencz, C. Spielmann, and F. Krausz, "Chirped multilayer coatings for broadband dispersion control in femtosecond lasers.," *Opt. Lett.*, vol. 19, no. 3, p. 201, 1994.

[59] S. Bohman, A. Suda, M. Kaku, M. Nurhuda, T. Kanai, S. Yamaguchi, and K. Midorikawa, "Generation of 5 fs, 0.5 TW pulses focusable to relativistic intensities at 1 kHz.," *Opt. Express*, vol. 16, no. 14, pp. 10684–9, Jul. 2008.

[60] J. Robinson, C. Haworth, H. Teng, R. Smith, J. Mangaros, and J. Tisch, "The generation of intense , transform-limited laser pulses with tunable duration from 6 to 30 fs in a differentially," *Appl. Phys. B*, vol. 85, pp. 525–529, 2006.

[61] R. Dörner, V. Mergel, O. Jagutzki, L. Spielberger, J. Ullrich, R. Moshammer, and H. Schmidt-Böcking, "Cold Target Recoil Ion Momentum Spectroscopy: a 'momentum microscope' to view atomic collision dynamics," *Phys. Rep.*, vol. 330, no. 2–3, pp. 95–192, 2000.

[62] J. Ullrich, R. Moshammer, A. Dorn, R. Dörner, L. P. H. Schmidt, R. Doerner, and H. Schmidt-Boecking, "Recoil-ion and electron momentum spectroscopy :," *Reports Prog. Phys.*, vol. 66, no. 9, pp. 1463–1545, 2003.

[63] M. Lampton, O. Siegmund, and R. Raffanti, "Delay line anodes for microchannel-plate spectrometers," *Rev. Sci. Instrum.*, vol. 58, no. 12, pp. 2298–2305, 1987.

[64] O. Jagutzki, V. Mergel, K. Ullmann-Pfleger, L. Spielberger, U. Spillmann, R. Dörner, and H. Schmidt-Böcking, "A broad-application microchannel-plate detector system for advanced particle or photon detection tasks: Large area imaging, precise multi-hit timing information and high detection rate," *Nucl. Instruments Methods Phys. Res. Sect. A Accel. Spectrometers, Detect. Assoc. Equip.*, vol. 477, no. 1–3, pp. 244–249, 2002.

[65] A. T. J. B. Eppink and D. H. Parker, "Velocity map imaging of ions and electrons using electrostatic lenses : Application in photoelectron and photofragment ion imaging of molecular oxygen Velocity map imaging of ions and electrons using electrostatic lenses : Application in photoelectron and," *Rev. Sci. Instrum.*, vol. 68, pp. 3477–3484, 1997.

[66] M. J. J. Vrakking, "An iterative procedure for the inversion of two-dimensional ion/photoelectron imaging experiments," *Rev. Sci. Instrum.*, vol. 72, no. 11, p. 4084, 2001.

[67] M. Kübel, "Photoionisation with Intense laser Fields," 2010.

[68] D. Würzler, "Untersuchung der Ionisationsdynamik nichtsequentieller Mehrfachionisation in Edelgasen im Sub-Femtosekundenbereich," 2013.

[69] P. Wustelt, "Ionisation atomarer Ionen in intensiven Inhaltsverzeichnis," 2013.

[70] T. Rathje, "Photodissoziation des Wasserstoffmolekülions durch Einzelzyklenlaserpulse," 2013.

[71] J. S. Briggs and J. M. Feagin, "Autonomous quantum to classical transitions and the generalized imaging theorem," *New J. Phys.*, vol. 18, no. 3, p. 33028, 2016.

[72] A. N. Pfeiffer, "Attosecond Electron Kinematics in Strond-field Single and Double Ionization," 2011.

[73] J. M. Feagin and J. S. Briggs, "Reaction imaging in uniform electric and magnetic fields," *J. Phys. B At. Mol. Opt. Phys.*, vol. 47, p. 115202, 2014.

[74] B. H. Bransden and C. J. Joachain, *Physics of Atoms and Molecules*. Pearson Education Limited, Harlow, England, 2003.

[75] M. Odenweller, N. Takemoto, A. Vredenborg, K. Cole, K. Pahl, J. Titze, L. P. H. Schmidt, T. Jahnke, R. Dörner, and A. Becker, "Strong field electron emission from fixed in space H2+ ions," *Phys. Rev. Lett.*, vol. 107, no. 14, pp. 1–4, 2011.

[76] T. Wittmann, B. Horvath, W. Helml, M. G. Schatzel, X. Gu, A. L. Cavalieri, G. G. Paulus, and R. Kienberger, "Single-shot carrier-envelope phase measurement of few-cycle laser pulses," *Nat. Phys.*, vol. 5, no. 5, pp. 357–362, 2009.

[77] T. Rathje, N. G. Johnson, M. Möller, F. Süßmann, D. Adolph, M. Kübel, R. Kienberger, M. F. Kling, G. G. Paulus, and a M. Sayler, "Review of attosecond resolved measurement and control via carrier–envelope phase tagging with above-threshold ionization," *J. Phys. B At. Mol. Opt. Phys.*, vol. 45, no. 7, p. 74003, 2012.

[78] C. Smeenk, J. Z. Salvail, L. Arissian, P. B. Corkum, C. T. Hebeisen, and A. Staudte, "Precise in-situ measurement of laser pulse intensity using strong field ionization.," *Opt. Express*, vol. 19, no. 10, pp. 9336–44, May 2011.

[79] A. Vredenborg, W. G. Roeterdink, and M. H. M. Janssen, "A photoelectron-photoion coincidence imaging apparatus for femtosecond time-resolved molecular dynamics with electron time-of-flight resolution of sigma=18 ps and energy resolution Delta E/E=3.5%.," *Rev. Sci. Instrum.*, vol. 79, no. 6, p. 63108, Jun. 2008.

[80] C. . S. Lehmann, N. B. Ram, and M. H. M. Janssen, "Velocity map photoelectron-photoion coincidence imaging on a single detector.," *Rev. Sci. Instrum.*, vol. 83, no. 9, p. 93103, Sep. 2012.

[81] C. Smeenk, L. Arissian, A. Staudte, D. M. Villeneuve, and P. B. Corkum, "Momentum space tomographic imaging of photoelectrons," *J. Phys. B At. Mol. Opt. Phys.*, vol. 42, no. 18, p. 185402 (5p, 2009.

[82] M. Wollenhaupt, M. Krug, J. Köhler, T. Bayer, C. Sarpe-Tudoran, and T. Baumert, "Three-dimensional tomographic reconstruction of ultrashort free electron wave packets," *Appl. Phys. B*, vol. 95, no. 4, pp. 647–651, Apr. 2009.

[83] M. Odenweller, J. Lower, K. Pahl, M. Schütt, J. Wu, K. Cole, A. Vredenborg, L. P. Schmidt, N. Neumann, J. Titze, T. Jahnke, M. Meckel, M. Kunitski, T. Havermeier, S. Voss, M. Schöffler, H. Sann, J. Voigtsberger, H. Schmidt-Böcking, and R. Dörner, "Electron emission from H2+ in strong laser fields," *Phys. Rev. A*, vol. 89, no. 1, p. 13424, 2014.

[84] P. Agostini, J. Kupersztych, and L. A. Lompré, "Direct evidence of ponderomotive effects via laser pulse duration in above-threshold ionization," *Phys. Rev. A*, vol. 36, no. 8, pp. 4111–4114, 1987.

[85] P. Korneev, S. Popruzhenko, S. Goreslavski, T.-M. Yan, D. Bauer, W. Becker, M. Kübel, M. Kling, C. Rödel, M. Wünsche, and G. Paulus, "Interference Carpets in Above-Threshold Ionization: From the Coulomb-Free to the Coulomb-Dominated Regime," *Phys. Rev. Lett.*, vol. 108, no. 22, pp. 1–5, May 2012.

[86] Y. Huismans, A. Rouzée, A. Gijsbertsen, J. H. Jungmann, A. S. Smolkowska, P. S. W. M. Logman, F. Lépine, C. Cauchy, S. Zamith, T. Marchenko, J. M. Bakker, G. Berden, B. Redlich, A. F. G. van der Meer, H. G. Muller, W. Vermin, K. J. Schafer, M. Spanner, M. Y. Ivanov, O. Smirnova, D. Bauer, S. V. Popruzhenko, and M. J. J. Vrakking, "Time-resolved holography with photoelectrons.," *Science*, vol. 331, no. 6013, pp. 61–64, 2011.

[87] X. B. Bian, Y. Huismans, O. Smirnova, K. J. Yuan, M. J. J. Vrakking, and A. Bandrauk, "Subcycle interference dynamics of time-resolved photoelectron holography with midinfrared laser pulses," *Phys. Rev. A*, vol. 84, no. 4, pp. 1–8, Oct. 2011.

[88] D. D. Hickstein, P. Ranitovic, S. Witte, X. M. Tong, Y. Huismans, P. Arpin, X. Zhou, K. E. Keister, C. W. Hogle, B. Zhang, C. Ding, P. Johnsson, N. Toshima, M. J. J. Vrakking, M. M. Murnane, and H. C. Kapteyn, "Direct Visualization of Laser-Driven Electron Multiple Scattering and Tunneling Distance in Strong-Field Ionization," *Phys. Rev. Lett.*, vol. 109, no. 7, p. 73004, Aug. 2012.

[89] C. Wu, Y. Yang, Y. Liu, Q. Gong, M. Wu, X. Liu, X. Hao, W. Li, X. He, and J. Chen, "Characteristic Spectrum of Very Low-Energy Photoelectron from Above-Threshold Ionization in the Tunneling Regime," *Phys. Rev. Lett.*, vol. 109, no. 4, pp. 1–5, Jul. 2012.

[90] C. D. Lin, A.-T. Le, Z. Chen, T. Morishita, and R. Lucchese, "Strong-field rescattering physics—self-imaging of a molecule by its own electrons," *J. Phys. B At. Mol. Opt. Phys.*, vol. 43, no. 12, p. 122001, 2010.

[91] M. J. J. Vrakking, "An iterative procedure for the inversion of two-dimensional ion / photoelectron imaging experiments An iterative procedure for the inversion of two-dimensional ion Õ photoelectron imaging experiments," vol. 4084, no. 2001, 2001.

[92] T. Marchenko, H. G. Muller, K. J. Schafer, and M. J. J. Vrakking, "Wavelength dependence of photoelectron spectra in above-threshold ionization," *J. Phys. B At. Mol. Opt. Phys.*, vol. 43, no. 18, p. 185001, Sep. 2010.

[93] T. Marchenko, Y. Huismans, K. J. Schafer, and M. J. J. Vrakking, "Criteria for the observation of strong-field photoelectron holography," *Phys. Rev. A*, vol. 84, no. 5, p. 53427, Nov. 2011.

[94] P. Corkum and N. Burnett, "Above-threshold ionization in the long-wavelength limit," *Phys. Rev. Lett.*, vol. 62, no. 11, pp. 1259–1262, 1989.

[95] M. Lewenstein, P. Balcou, M. Y. Ivanov, A. L'Huillier, and P. B. Corkum, "Theory of High-harmonic Generation By Low-frequency Laser Fields," *Phys. Rev. A*, vol. 49, no. 3, pp. 2117–2132, 1994.

[96] W. Becker, S. Long, and J. K. McIver, "Modeling Harmonic-generation By A Zero-range Potential," *Phys. Rev. A*, vol. 50, no. 2, pp. 1540–1560, Aug. 1994.

[97] P. Colosimo, G. Doumy, C. I. Blaga, J. Wheeler, C. Hauri, F. Catoire, J. Tate, R. Chirla, a. M. March, G. G. Paulus, H. G. Muller, P. Agostini, and L. F. DiMauro, "Scaling strong-field interactions towards the classical limit," *Nat. Phys.*, vol. 4, no. 5, pp. 386–389, Mar. 2008.

[98] A. Kästner, U. Saalmann, and J. Rost, "Electron-Energy Bunching in Laser-Driven Soft Recollisions," *Phys. Rev. Lett.*, vol. 108, no. 3, p. 33201, Jan. 2012.

[99] K. Zhang, Y. H. Lai, E. Diesen, B. E. Schmidt, C. I. Blaga, J. Xu, T. Gorman, F. Legare, U. Saalmann, P. Agostini, J. M. Rost, and L. F. DiMauro, "Universal pulse dependence of the low-energy structure in strong-field ionization," *Phys. Rev. A*, vol. 21403, no. 1, pp. 1–5, 2016.

[100] Y. Huismans, A. Rouzee, A. Gijsbertsen, J. H. Jungmann, A. S. Smolkowska, P. S. W. M. Logman, F. Lepine, C. Cauchy, S. Zamith, T. Marchenko, J. M. Bakker, G. Berden, B. Redlich, A. F. G. van der Meer, H. G. Muller, W. Vermin, K. J. Schafer, M. Spanner, M. Y. Ivanov, O. Smirnova, D. Bauer, S. V Popruzhenko, and M. J. J. Vrakking, "Time-Resolved Holography with Photoelectrons," *Science (80-.).*, vol. 331, no. 6013, 2011.

[101] D. D. Hickstein, P. Ranitovic, S. Witte, X.-M. Tong, Y. Huismans, P. Arpin, X. Zhou, K. E. Keister, C. W. Hogle, B. Zhang, C. Ding, P. Johnsson, N. Toshima, M. J. J. Vrakking, M. M. Murnane, and H. C. Kapteyn, "Direct Visualization of Laser-Driven Electron Multiple Scattering and Tunneling Distance in Strong-Field Ionization," *Phys. Rev. Lett.*, vol. 109, no. 7, pp. 1–5, Aug. 2012.

[102] S. Popruzhenko, G. G. Paulus, and D. Bauer, "Coulomb-corrected quantum trajectories in strong-field ionization," *Phys. Rev. A*, vol. 77, no. 5, pp. 1–7, May 2008.

[103] S. V. Popruzhenko and D. Bauer, "Strong field approximation for systems with Coulomb interaction," *J. Mod. Opt.*, vol. 55, no. 16, pp. 2573–2589, Sep. 2008.

[104] D. B. Milošević, "Reexamination of the improved strong-field approximation: Low-energy structures in the above-threshold-ionization spectra for short-range potentials," *Phys. Rev. A*, vol. 88, no. 2, p. 23417, Aug. 2013.

[105] C. D. Lin and J. Xu, "Imaging ultrafast dynamics of molecules with laser-induced electron diffraction.," *Phys. Chem. Chem. Phys.*, vol. 14, no. 38, pp. 13133–45, Oct. 2012.

[106] D. G. Arbó, S. Nagele, X. M. Tong, X. Xie, M. Kitzler, and J. Burgdörfer, "Interference of electron wave packets in atomic ionization by subcycle sculpted laser pulses," *Phys. Rev. A - At. Mol. Opt. Phys.*, vol. 89, no. 4, p. 43414, Apr. 2014.

[107] G. G. Paulus, W. Becker, and H. Walther, "Classical rescattering effects in two-color above-threshold ionization.," *Phys. Rev. A*, vol. 52, no. 5, pp. 4043–4053, Nov. 1995.

[108] W. Becker, S. P. Goreslavski, D. B. Milošević, and G. G. Paulus, "Low-energy electron rescattering in laser-induced ionization," *J. Phys. B At. Mol. Opt. Phys.*, vol. 47, no. 20, p. 204022, 2014.

[109] V. S. Popov, "Tunnel and multiphoton ionization of atoms and ions in a strong laser field (Keldysh theory)," *Physics-Uspekhi*, vol. 47, no. 9, pp. 855–885, Sep. 2004.

[110] X. M. Tong and C. D. Lin, "Empirical formula for static field ionization rates of atoms and molecules by lasers in the barrier-suppression regime," *J. Phys. B At. Mol. Opt. Phys.*, vol. 38, no. 15, pp. 2593–2600, Aug. 2005.

[111] O. I. Tolstikhin, T. Morishita, and L. B. Madsen, "Theory of tunneling ionization of molecules: Weak-field asymptotics including dipole effects," *Phys. Rev. A - At. Mol. Opt. Phys.*, vol. 84, no. 5, pp. 1–5, 2011.

[112] L. Arissian, C. Smeenk, F. Turner, C. Trallero, a. V Sokolov, D. M. Villeneuve, a. Staudte, and P. B. Corkum, "Direct Test of Laser Tunneling with Electron Momentum Imaging," *Phys. Rev. Lett.*, vol. 105, no. 13, p. 133002, Sep. 2010.

[113] L. Holmegaard, J. L. Hansen, L. Kalhøj, S. Louise Kragh, H. Stapelfeldt, F. Filsinger, J. Küpper, G. Meijer, D. Dimitrovski, M. Abu-samha, C. P. J. Martiny, and L. Bojer Madsen, "Photoelectron angular distributions from strong-field ionization of oriented molecules," *Nat. Phys.*, vol. 6, no. 6, pp. 428–432, May 2010.

[114] S. D. Khan, Y. Cheng, M. Möller, K. Zhao, B. Zhao, M. Chini, G. G. Paulus, and Z. Chang, "Ellipticity dependence of 400 nm-driven high harmonic generation," *Appl. Phys. Lett.*, vol. 99, no. 16, p. 161106, 2011.

[115] M. Möller, Y. Cheng, S. D. Khan, B. Zhao, K. Zhao, M. Chini, G. G. Paulus, and Z. Chang, "Dependence of high-order-harmonic-generation yield on driving-laser ellipticity," *Phys. Rev. A - At. Mol. Opt. Phys.*, vol. 86, no. 1,

pp. 1–5, 2012.

[116] S. Skruszewicz, J. Tiggesbäumker, M. Arbeiter, T. Fennel, and D. Bauer, "Two-Color Strong-Field Photoelectron Spectroscopy and the Phase of the Phase," vol. 43001, no. July, pp. 1–6, 2015.

[117] Z. Chen, A. T. Le, T. Morishita, and C. D. Lin, "Quantitative rescattering theory for laser-induced high-energy plateau photoelectron spectra," *Phys. Rev. A - At. Mol. Opt. Phys.*, vol. 79, no. 3, pp. 1–18, 2009.

[118] J. Xu, C. I. Blaga, A. D. DiChiara, E. Sistrunk, K. Zhang, Z. Chen, A.-T. Le, T. Morishita, C. D. Lin, P. Agostini, and L. F. DiMauro, "Laser-Induced Electron Diffraction for Probing Rare Gas Atoms," *Phys. Rev. Lett.*, vol. 109, no. 23, p. 233002, Dec. 2012.

[119] J. Xu, C. I. Blaga, K. Zhang, Y. H. Lai, C. D. Lin, T. a Miller, P. Agostini, and L. F. DiMauro, "Diffraction using laser-driven broadband electron wave packets.," *Nat. Commun.*, vol. 5, p. 4635, Jan. 2014.

[120] M. G. Pullen, B. Wolter, A.-T. Le, M. Baudisch, M. Hemmer, A. Senftleben, C. D. Schröter, J. Ullrich, R. Moshammer, C. D. Lin, and J. Biegert, "Imaging an aligned polyatomic molecule with laser-induced electron diffraction," *Nat. Commun.*, vol. 6, p. 7262, 2015.

[121] W. Becker and D. B. Milošević, "Above-threshold ionization for very low electron energy," *J. Phys. B At. Mol. Opt. Phys.*, vol. 48, no. 15, p. 151001, 2015.

[122] W. Quan, Z. Lin, M. Wu, H. Kang, H. Liu, X. Liu, J. Chen, J. Liu, X. He, S. Chen, H. Xiong, L. Guo, H. Xu, Y. Fu, Y. Cheng, and Z. Xu, "Classical Aspects in Above-Threshold Ionization with a Midinfrared Strong Laser Field," *Phys. Rev. Lett.*, vol. 103, no. 9, pp. 1–4, Aug. 2009.

[123] A. Kästner, U. Saalmann, and J. M. Rost, "Energy bunching in soft recollisions revealed with long-wavelength few-cycle pulses," *J. Phys. B At. Mol. Opt. Phys.*, vol. 45, no. 7, p. 74011, Apr. 2012.

[124] L. Guo, S. S. Han, X. Liu, Y. Cheng, Z. Z. Xu, J. Fan, J. Chen, S. G. Chen, W. Becker, C. I. Blaga, a. D. DiChiara, E. Sistrunk, P. Agostini, and L. F. DiMauro, "Scaling of the Low-Energy Structure in Above-Threshold Ionization in the Tunneling Regime: Theory and Experiment," *Phys. Rev. Lett.*, vol. 110, no. 1, p. 13001, Jan. 2013.

[125] G. Paulus, F. Lindner, H. Walther, a. Baltuška, E. Goulielmakis, M. Lezius, and F. Krausz, "Measurement of the Phase of Few-Cycle Laser Pulses," *Phys. Rev. Lett.*, vol. 91, no. 25, pp. 1–4, 2003.

[126] D. B. Milošević, G. G. Paulus, D. Bauer, and W. Becker, "Above-threshold ionization by few-cycle pulses," *J. Phys. B At. Mol. Opt. Phys.*, vol. 39, no. 14, pp. R203–R262, Jul. 2006.

[127] K. Zhang, Y. H. Lai, E. Diesen, B. E. Schmidt, C. I. Blaga, J. Xu, T. T. Gorman, F. Légaré, U. Saalmann, P. Agostini, J. M. Rost, and L. F. Dimauro, "Universal pulse dependence of the low-energy structure in strong-field ionization," *Phys. Rev. A - At. Mol. Opt. Phys.*, vol. 93, no. 2, pp. 1–4, 2016.

[128] X. M. Tong, Z. X. Zhao, and C. D. Lin, "Theory of molecular tunneling ionization," *Phys. Rev. A*, vol. 66, no. 3, pp. 1–11, 2002.

[129] T. K. Kjeldsen and L. B. Madsen, "Strong-field ionization of diatomic molecules and companion atoms: Strong-field approximation and tunneling theory including nuclear motion," *Phys. Rev. A - At. Mol. Opt. Phys.*, vol. 71, no. 2, pp. 1–10, 2005.

[130] A. N. Pfeiffer, C. Cirelli, M. Smolarski, D. Dimitrovski, M. Abu-samha, L. B. Madsen, and U. Keller, "Attoclock reveals natural coordinates of the laser-induced tunnelling current flow in atoms," *Nat. Phys.*, vol. 8, no. 1, pp. 76–80, 2011.

[131] P. Schwerdtfeger, "Table of experimental and calculated static dipole polarizabilities for the electronic ground states of the neutral elements (in atomic units)," *Seattlecentral.Edu*, 2014.

[132] V. P. Shevelko and a. D. Ulantsev, "Static multipole polarizability of atoms and ions in the Thomas-Fermi model," *J. Russ. Laser Res.*, vol. 19, pp. 275–282, 1979.

[133] A. A. Radzig and B. M. Smirnov, *Reference Data on Atoms, Molecules and Ions*. 1985.

[134] T. Brabec, M. Ivanov, and P. Corkum, "Coulomb focusing in intense field atomic processes.," *Phys. Rev. A*, vol. 54, no. 4, pp. R2551–R2554, Oct. 1996.

[135] G. G. Paulus, F. Grasbon, H. Walther, P. Villoresi, M. Nisoli, S. Stagira, E. Priori, and S. De Silvestri, "Absolute-phase phenomena in photoionization with few-cycle laser pulses.," *Nature*, vol. 414, no. 6860, pp. 182–184,

References

Nov. 2001.

[136] A. Guisti-Suzor, F. H. Mies, L. F. DiMauro, E. Charron, and B. Yang, "Dynamics of H 2 + in intense laser fields," *J. Phys. B At. Mol. Opt. Phys.*, vol. 28, no. 3, p. 309, 1995.

[137] A. Rudenko, B. Feuerstein, K. Zrost, V. L. B. De Jesus, T. Ergler, C. Dimopoulou, C. D. Schröter, R. Moshammer, and J. Ullrich, "Fragmentation dynamics of molecular hydrogen in strong ultrashort laser pulses," *J. Phys. B At. Mol. Opt. Phys.*, vol. 38, no. 5, pp. 487–501, 2005.

[138] A. D. Bandrauk and M. L. Sink, "Photodissociation in intense laser fields: Predissociation analogy," *J. Chem. Phys.*, vol. 74, no. 2, p. 1110, 1981.

[139] J. H. Posthumus, J. Plumridge, L. J. Frasinski, K. Codling, E. J. Divall, a J. Langley, and P. F. Taday, "Slow protons as a signature of zero-photon dissociation of H +," *J. Phys. B At. Mol. Opt. Phys.*, vol. 33, pp. 563–569, 2000.

[140] L. J. Frasinski, J. Plumridge, J. H. Posthumus, K. Codling, P. F. Taday, E. J. Divall, and A. J. Langley, "Counterintuitive alignment of H2+ in intense femtosecond laser fields," *Phys. Rev. Lett.*, vol. 86, no. 12, pp. 2541–2544, 2001.

[141] P. Q. Wang, a M. Sayler, K. D. Carnes, J. F. Xia, M. a Smith, B. D. Esry, and I. Ben-Itzhak, "Highlighting the angular dependence of bond softening and bond hardening of H + 2 in an ultrashort intense laser pulse," *J. Phys. B At. Mol. Opt. Phys.*, vol. 38, no. 15, p. 73002, 2005.

[142] S. Chelkowski, T. Zuo, and O. Atabek, "Dissociation, ionization, and Coulomb explosion of H2+ in an intense laser field by numerical integration of the time-dependent Schrodinger equation," vol. 52, no. 4, 1995.

[143] L. Yue and L. B. Madsen, "Inter- and intracycle interference effects in strong-field dissociative ionization," *Phys. Rev. A*, vol. 93, no. 3, p. 31401, 2016.

[144] V. Mosert and D. Bauer, "Dissociative ionization of H2+ : Few-cycle effect in the joint electron-ion energy spectrum," *Phys. Rev. A*, vol. 92, no. 4, p. 43414, 2015.

[145] M. F. Kling, C. Siedschlag, A. J. Verhoef, J. I. Khan, M. Schultze, T. Uphues, Y. Ni, M. Uiberacker, M. Drescher, F. Krausz, and M. J. J. Vrakking, "Control of Electron Localization in Molecular Dissociation," vol. 312, no. 2006, pp. 246–248, 2006.

[146] V. Wanie, H. Ibrahim, S. Beaulieu, N. Thiré, B. E. Schmidt, Y. Deng, A. S. Alnaser, I. V Litvinyuk, X.-M. Tong, and F. Légaré, "Coherent control of D 2 /H 2 dissociative ionization by a mid-infrared two-color laser field," *J. Phys. B At. Mol. Opt. Phys.*, vol. 49, no. 2, p. 25601, 2016.

[147] P. Wang, A. M. Sayler, K. D. Carnes, B. D. Esry, and I. Ben-itzhak, "Disentangling the volume effect through intensity-difference spectra: application to laser-induced dissociation of H2+," *Opt. Lett.*, vol. 30, no. 6, pp. 664–666, 2005.

[148] Y. Weijun, R. Alheit, and G. Werth, "Vibrational population of H2 + after electroionization of thermal H2," *Zeitschrift für Phys. D Atoms, Mol. Clust.*, vol. 28, no. 2, pp. 87–88, 1993.

[149] M. D. Feit, J. A. Fleck, and A. Steiger, "Solution of the Schrödinger equation by a spectral method," *J. Comput. Phys.*, vol. 47, no. 3, pp. 412–433, 1982.

[150] T. E. Sharp, "Potential-energy curves for molecular hydrogen and its ions," *At. Data Nucl. Data Tables*, vol. 2, no. C, pp. 119–169, 1970.

[151] D. R. Bates, "The Oscillator Strength of H2+, 1sσ—2pσ," *J. Chem. Phys.*, vol. 19, no. 9, p. 1122, 1951.

[152] D. E. Ramaker and J. M. Peek, "Dipole Strengths Involving the Lowest Twenty Electronic States of H2+," vol. 5, no. 2, pp. 167–184, 1973.

[153] P. Schwendner, F. Seyl, and R. Schinke, "Photodissociation of Ar2+ in strong laser fields," *Chem. Phys.*, vol. 217, pp. 233–247, 1997.

[154] L. Yue, "personal communication," 2017.

[155] M. Plummer and J. F. McCann, "Complex-basis-function Floquet calculations of multiphoton ionization rates in hydrogen systems," *J. Phys. B At. Mol. Opt. Phys.*, vol. 28, no. 18, pp. 4073–4089, 1995.

[156] M. Plummer and J. F. McCann, "Orientation dependence of field ionization of the hydrogen molecular ion," *J.*

Phys. B At. Mol. Opt. Phys., vol. 30, pp. L401–L411, 1997.

[157] M. Plummer, J. F. McCann, and L. B. Madsen, "The calculation of multiphoton ionization rates of the hydrogen molecular ion," *Comput. Phys. Commun.*, vol. 114, no. 1--3, pp. 94–119, 1998.

[158] Möller, M and et al, "Strong-field Photoionization of the Hydrogen Molecular Ion by Intense Short-wave Infrared Fields," *Prep.*

[159] A. L'Huillier, L. A. Lompre, and G. Mainfray, "Multiply charged ions formed by multiphoton absorption processes in the continuum," *Phys. Rev. Lett.*, vol. 48, no. 26, pp. 1814–1818, 1982.

[160] L. Lompre, A. L'Huillier, G. Mainfray, and C. Manus, "Laser-intensity effects in the energy distributions of electrons produced in multiphoton ionization of rare gases," *J. Phys. B At. Mol. Opt. Phys.*, vol. 2, no. 12, pp. 1906–1912, 1985.

[161] S. Augst, D. Meyerhofer, D. Strickland, and S. Chin, "Laser ionization of noble gases by Coulomb-barrier suppression," vol. 8, no. 4, pp. 858–867, 1991.

[162] Z. Chang, *Fundamentals of Attosecond Optics*. CRC Press Taylor & Francis Group, 2011.

[163] A. M. Sayler, P. Q. Wang, K. D. Carnes, and I. Ben-Itzhak, "Determining intensity dependence of ultrashort laser processes through focus z -scanning intensity-difference spectra: application to laser-induced dissociation of H + 2," *J. Phys. B At. Mol. Opt. Phys.*, vol. 40, no. 22, pp. 4367–4378, Nov. 2007.

[164] J. R. Hiskes, "Dissociation of Molecular Ions by Electric and Magnetic Fields," vol. 122, no. 1928, 1961.

[165] F. Grossmann, *Theoretical Femtosecond Physics*. Springer International Publishing, 2013.

[166] D. J. Tannor, *Introduction to Quantum Mechanics a Time-Dependent Perspective*. University Science Books, 2007.

[167] R. S. Mulliken, "Intensities of Electronic Transitions in Molecular Spectra VII. Conjugated Polyenes and Carotenoids," *J. Chem. Phys.*, vol. 7, no. 5, p. 364, 1939.

[168] P. Atkins and J. de Paula, *Physical Chemistry*. Oxford University Press, 2014.

Appendix

A1 Intensity Control for High-Power Few-Cycle Pulses

Since the early days of strong-field physics [1] [159] [160] [4], it is well known that typical measurements average over the inhomogeneous intensity distribution in a focused laser beam [161]. Thus, directly comparing measurements and theoretical results makes it either necessary to disentangle these averaging effects in measurements, see e.g. ref. [147], or to take the averaging into account for theoretical simulation. Similarly, if the intensity dependence is investigated by a measurement and compared to simulations, the experimental strategy for controlling the intensity should be taken into account by the simulations or disentangling techniques need to be applied in the measurement.

As the laser pulses in strong-field laser physics, often exploit non-linear optical processes to generate the desired laser pulses, controlling the peak intensity, I_0, in a continuous and structured way over a large range without changing other parameters such as the pulse duration, τ, or the geometry of the focus is a non-trivial task. Further, the typically large bandwidths and high powers even in the collimated beams present additional challenges.

In the following sections, an experimental method for controlling the peak intensity of high-power few-cycle pulses in a structured way in a relatively simple and cheap experimental setup is presented. It is used in the second measurement of this thesis, chapter 5, where an intensity dependent measurement on strong-field fragmentation of the hydrogen molecular ion is done.

Before we turn to details of the setup for intensity control, equations that describe the intensity distribution around the focal spot within the M^2-model of laser beams is given in section A1.1. From this, one can get an impression on options for changing the peak intensity within a given interaction volume, $V_{int}(x, y, z)$, where the target atoms or molecules are distributed with constant density, $\varrho(x, y, z) = \varrho_0$. Afterwards, the setup is introduced in section A1.3.

A1.1 Intensity Distribution around the Focal Spot in the M^2-Model

The intensity distribution of laser beam which is focused by a lens or a mirror with the focal length, f, has the intensity distribution,

$$I(r, z) = I_0 \left[\frac{w_{0_{Focus}}}{w_{Focus}(z)} \right]^2 \exp\left(\frac{-2r^2}{w_{Focus}^2(z)} \right). \tag{A.1}$$

Here, the laser pulse propagates along the z-axis and $r = \sqrt{x^2 + y^2}$ is the radial coordinate in cylindrical coordinates. The quantity, $w_{0_{Focus}}$ is the radius of the focal spot which depends on f, the wavelength, λ, and on the radius of the collimated beam at the position of the lens, w_{Lens},

$$w_{0_{Focus}} = \frac{f M^2 \lambda}{\pi w_{Lens}}. \tag{A.2}$$

The number M^2 is the beam quality parameter which is slightly larger than 1 one for typical lasers with good beam quality. Behind the lens, the radius of the beam, $w_{Focus}(z)$, behaves as,

$$w_{Focus}(z) = w_{0_{Focus}}\sqrt{1 + (z/z_{r_{Focus}})^2}. \tag{A.3}$$

The quantity, $z_{r_{Focus}} = \pi w_{0_{Focus}}^2/M^2\lambda$, is the Raleigh range of the beam. The radius of curvature of the wave front, $R_{Focus}(z)$, is

$$R_{Focus}(z) = z\left[1 + \frac{z_{r_{Focus}}}{z}\right]^2. \tag{A.4}$$

Last but not least, the peak intensity, I_0, of the beam of an ideal Gaussian pulse with the duration, τ, and pulse energy, ε is [162]

$$I_0 = \frac{1.88}{\pi}\frac{\epsilon}{\tau\,w_{0_{Focus}}^2}. \tag{A.5}$$

Strictly speaking, equations (A.1) to (A.5) are limited to a monochromatic approximation such that when working with broad, more precise considerations should be done. Further, if measurements with stable carrier-envelope phase (CEP) or CEP sensitive processes are investigated, it might necessary to consider the electric field distribution in the focus. Independent of the previous remarks, equations (A.1) to (A.5) shows not only that for a measurement, several options to change the peak intensity exist but also demonstrates that the shape and the extension of the interaction volume, $V_{int}(x, y, z)$, plays a role. Consequently, different methods for varying the intensity, cause convolutions of the experimental observables with the intensity distribution of various kinds and complexity [163]. For example, if one has a thin target, where V_{int} is approximately restricted to the xy-plane at fixed $z = z_T$, moving the position of the lens with respect to z_T allows to change the highest intensity in the volume, $I_{max} = \max(I(x, y, z = z_T))$. However, in such an approach not only I_{max} is changed but also the overlap between the target and laser beam is changed, which influences the convolution between the intensity distribution in the focal volume and experimental observables.

The method to change the intensity here, relies on controlling rather the pulse energy, ϵ, while the overlap between laser beam and target volume is not changed. For such a scenario, the frequency of intensities in the focal volume in dependence of the peak intensity is discussed in the next chapter for different target geometries.

A1.2 Frequency of Intensities in the Focal Volume for Different Target Geometries

In order to illustrate the frequency of intensities in the focal volume as function of peak intensity for different target geometries, we start by using a Monte-Carlo simulation. Such an approach is fast, relatively simple, flexible and robust. The idea is to generate i uniformly distributed "particles" within a given interaction region, $V_{int}(x, y, z)$ where the density of target atoms or molecules is assumed to be constant. Afterwards, equations (A.1) to (A.5) are used to calculate I_i, for each of the "particles" at the position x_i, y_i, z_i, for a given geometry of the focal spot, which is characterized by, the peak intensity, I_0, the spot size, $w_{0_{Focus}}$ and the Rayleigh range, $z_{r_{Focus}}$, From this ensemble, I_i, a histogram is calculated.
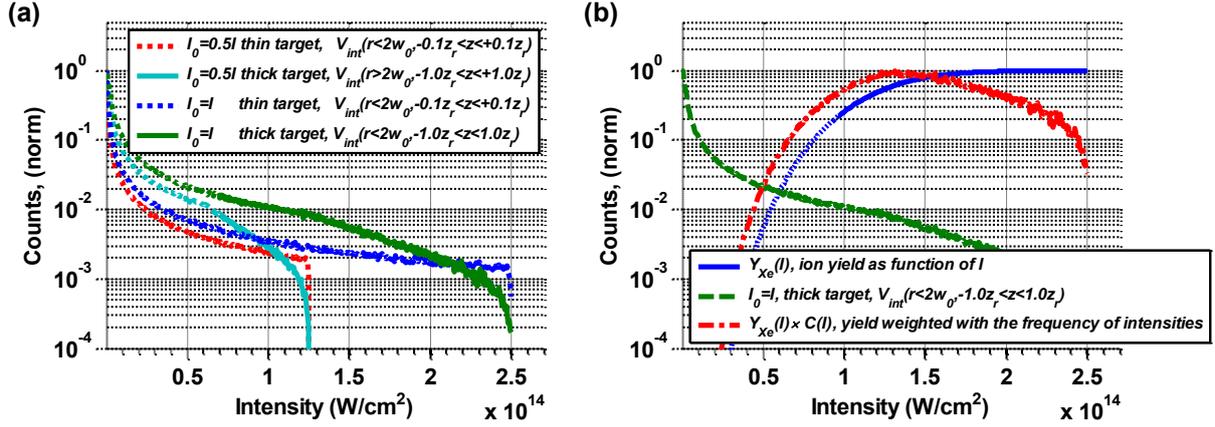
Figure A.1 Illustration of volume averaging.

(a) the frequency of intensities within the focal volume for two values of the peak intensity I_0. Different target geometries are compared (thin target – dotted and thick target - line). The comparison is done for two intensities. (b) Frequency of intensities and the intensity dependent ion yield as an example how volume effects influence the distribution of intensities that contribute to the observables in a measurement. The red curve illustrates that the intensity with the highest frequency is not the peak intensity.

Different interaction volumina, $V_{int}(x, y, z)$, are compared in Figure A.1. It shows the results of such a calculation. The first geometry is a thin target where the distribution of target particles has constant density in a narrow range around, $-0.1z_{r\,Focus} < z < 0.1z_{r\,Focus}$. Such an assumption is realistic for e.g. an ion or molecular beam target with a limited extension along the propagation direction of the laser, z. The second case shows a thick target geometry. Here, the target particles are assumed to be uniformly distributed in the range, $-1z_{r\,Focus} < z < 1z_{r\,Focus}$. This is realistic for an extended target if e.g. the whole vacuum chamber is filled with the target particles. For both cases, the histogram is compared for the two different values of the peak intensity. One can see that increasing the peak intensity, I_0, not only increases the frequency of high intensities but also increases the frequency of lower intensities. This in turn. changes the weight of the different intensities for the experimental observables. These effects need to be taken into account if e.g. intensity dependent measurements are compared to theoretical calculations.

In Figure A.1 (b) illustrate the volume averaging effects at the example of strong-field photoionization of Xenon by 3-cycle, 1780-nm pulses. The measurement is a convolution between the ionization probability, of Xenon as function of intensity, $Y_{Xe}(I)$, see the blue curve Figure A.1, and the volume of the corresponding intensity in the target, see the green dotted curve Figure A.1. With which frequency different intensities contribute to the final measurement result is given by the red curve. As a consequence, the dominating intensity contribution in this measurement would be significantly lower than the peak intensity. It illustrated the influence of focal volume.

Appendix

A1.3 Setup for Intensity Control of High-Power Few-Cycle Pulses

Here we present an experimental setup which allows to control the pulse energy of high-power broadband few-cycle pulses without changing the geometry of the focal spot.

The setup is shown in Figure A.2. The laser beam comes from the left, is transmitted through a $\lambda/2$-plate and reflected off a broadband Brewster polarizer. Changing the projection on the s-polarization of the Brewster plate's front surface by changing the angle of the $\lambda/2$-plate with respect to the incoming linear polarization allows to control the pulse energy behind the plate as the plate primarily reflects s polarization. A thin transmitting polarizer with high contrast over a broad bandwidth, ensures to maintain a linear polarization state after the setup by absorbing the residual p-component.

The operation principle of the setup is very similar to a Brewster polarizer or thin-film polarizer. However, instead of using the transmission for experiment, the reflection is used to minimize the amount of transmitting optics in the beam path. A few options exist for choosing this Brewster plate. One option is very similar to a thin film polarizer. A glass substrate with a polarization selective coating might be used. In this case, however, it is necessary to design this coating with respect to the spectral phase after the reflection. In addition, if a transmitting substrate is used, one needs to suppress the reflections from the back surface of the plate. This can e.g. be done using an anti-reflection coating by designing the Brewster plate with a small wedge.
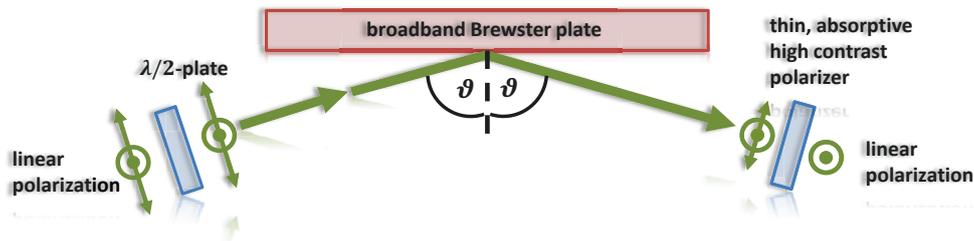

Figure A.2 Illustration of an arrangement for reflective intensity control of high-power few-cycle pulses
The linearly polarized laser beam is coming from the left. A $\lambda/2-$plate is used to control the ratio between s & p polarization on the surface of the broadband Brewster plate. The angle of incidence on the plate, ϑ, is chosen close to Brewster's angle for the center wavelength of the beam. Thus, the reflectivity can be controlled by adjusting the angle of the $\lambda/2-$plate which changes the ratio between s & p polarization on the plate. The thin, absorptive broadband polarizer is used suppress any p-polarization after the Brewster plate. This is necessary in order to keep the polarization state after this setup independent of the angle of the $\lambda/2-$plate.

The option, which we use here is a thick, absorbing or partly absorbing material with relatively high reflectivity. If the material is chosen appropriately, no special coating is required. It turns out that materials can be found which have properties in terms of bandwidth and reflectivity particularly for wavelength in the range of the HE-TOPAS-C.

In order to find appropriate materials for the Brewster plate, the Fresnel equations can be used to calculate the reflection coefficients for s-polarization, r_s, and p-polarization, r_p, at different angle of incidence of, ϑ, and in dependence of the wavelength. Thereby, the assumption of equal permeability, $\mu_{r_1} \approx \mu_{r_2}$, are used to calculate the reflection coefficients for s-polarization, r_s, and p-polarization, r_p, at different angle of incidence of, ϑ, and in

dependence of the wavelength. The result of such a calculation in dependence of the wavelength for an optimized angle of incidence is shown in Figure A.3. Particularly, Germanium (Ge) shows a high and flat reflectivity curve at a reasonable contrast between s- and p-component for an angle of incidence of $\vartheta = 80°$. The contrast, r_s/r_s, is better than 2-3 % for wavelength higher than 0.6 μm. Thus it is particularly well suited for wavelength that are higher than that. The Zinc selenide (ZnSe) plate has already high contrast for shorter wavelength in the visual spectral range such that it is suitable for few-cycle pulses in the visible and near-infrared spectral range. However, the reflectivity is less. Both materials are standard optical materials and thus, available from many vendors.
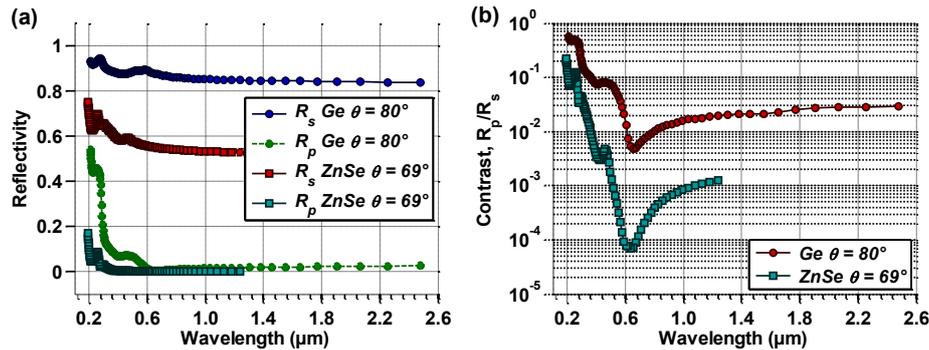

Figure A.3 Reflectivity and contrast of Brewster plates for intensity control

In (a), the calculated reflectivity of a polished Germanium (Ge) surface and a polished zinc selenide (ZnSe) surface as function of wavelength is shown for different incident polarization states. The contrast, $c = R_p/R_s$ between the reflectivity of the p- and the s-component is shown in (b). The angle of incidence, ϑ, has been optimized for a reasonable compromise between reflectivity, contrast and size.

Figure A.3 also demonstrates the necessity of cleaning the polarization with a high-contrast polarizer after the Brewster plate. If the $\lambda/2$-plate is adjusted such that only little energy is transmitted through the setup, most of the energy before the Brewster plate is rotated onto its p-plane. Although the reflection for p-polarization is small compared to the reflection of s-polarization, due the large amplitude going in p, p and s components can have similar amplitude behind the Brewster plate. Thus, the direction of the linear polarization is changed. Potentially, even elliptically polarized light might be produced. Cleaning the polarization state using the high-contrast polarizer ensures that the effect of rotated polarization is suppressed.

A2 Theoretical Description of the Hydrogen Molecular Ion

In this chapter, the theoretical description of the hydrogen molecular ion, H_2^+, is reviewed starting from the Hamiltonian of the system. The derivations follows [74] and uses similar notation. We introduce the coordinate system and the Hamiltonian in A2.1; apply the Born-Oppenheimer approximation in A2.2 and use the method of linear combination of atomic orbitals to illustrate an approximation of the electronic and nuclear Eigenstates in A2.3. Last but not least we discuss the effect of a static external field in A2.4.

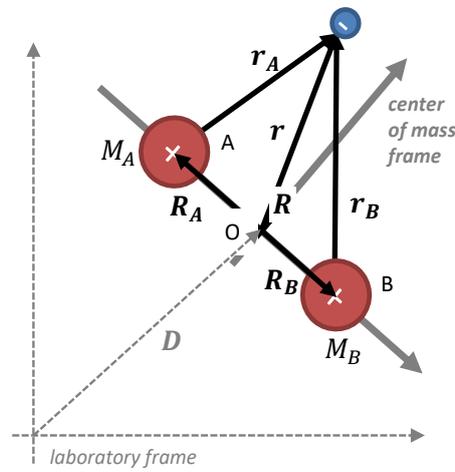### A2.1 Introduction of the Coordinate System and the Hamiltonian

Figure A. 4 The coordinate system H_2^+

Neglecting rotations and translations of the molecule and going directly to it's center of mass frame, the Hamiltonian of system consists of the kinetic energy of the electron, T_e, and the nuclei, T_N, as well as of the total potential energies, $V = V_{eN} + V_N$. The potential energies occur due to Coulombic interactions between the electron and nuclei, V_{eN}, both nuclei, V_N. The terms are [164],

$$T_e = -\frac{\hbar^2}{2m_{er}}\nabla_r^2, m_{er} = m_e \frac{M_A + M_B}{M_A + M_B + m_e} \qquad \rightarrow -\frac{1}{2}\nabla_r^2$$

$$T_N = -\frac{\hbar^2}{2\mu}\nabla_R^2, \mu = \frac{M_A M_B}{M_A + M_B} = \frac{m_p}{2} \qquad \rightarrow -\frac{1}{2\mu}\nabla_R^2 \tag{A.6}$$

$$V = \frac{1}{(4\pi\epsilon_0)}\left[-\frac{Q_A q_e^2}{|r - R_A|} - \frac{Q_B q_e^2}{|r - R_B|} + \frac{Q_A Q_B q_e^2}{|R|}\right] \rightarrow \left[-\frac{1}{|r - R_A|} - \frac{1}{|r - R_B|} + \frac{1}{|R|}\right]$$

. Thereby, the conversion from SI-units to atomic units is implemented using, $m_e = \hbar = 1/4\pi\epsilon_0 = q_e = 1$. The symbols denote, m_e the electron mass, $\hbar$ being reduced Planck's constant, q_e the elementary charge, Coulomb's constant, $1/4\pi\epsilon_0$, M_A denotes the mass of nucleus A, M_B the mass of nucleus B. Both masses are equal to the proton

mass $M = M_A = M_B = m_p \approx 1836 \cdot m_e$. The and charges of the nuclei are, $Q_A q_e = Q_B q_e = q_e = 1$, for protons. The quantities, μ and m_{er} are the reduced masses of the electron and the protons. Thereby, it is now common to use $m_{er} \approx m_e$. The position vectors are, $\boldsymbol{r}$ to the electron and $\boldsymbol{R_A}$ and $\boldsymbol{R_B}$ to both protons such that $\boldsymbol{R} = \boldsymbol{R_A} - \boldsymbol{R_B}$ stands for the relative vector between the nuclei with the length R. The full Hamiltonian, H, of the H_2^+ molecular ion within the center of mass frame in atomic units is then,

$$H(\boldsymbol{R}, \boldsymbol{r}) = T_e + V_{eN} + T_N + V_N = -\frac{1}{2}\nabla_r{}^2 - \frac{1}{|\boldsymbol{r_A}|} - \frac{1}{|\boldsymbol{r_B}|} - \frac{1}{2\mu}\nabla_R{}^2 + \frac{1}{|\boldsymbol{R}|} \tag{A.7}$$

, with $\boldsymbol{r_A} = \boldsymbol{r} + \boldsymbol{R}/2$ and $\boldsymbol{r_B} = \boldsymbol{r} - \boldsymbol{R}/2$. We chose the coordinate system is such that the direction of the $\boldsymbol{R}$-vector is fixed in space and points along the z-axis. The nuclear geometry is then purely characterized by the scalar R.

Thus, the time-independent Schrödinger equation (TISE) in full electronic and nuclear coordinates is

$$H(R, \boldsymbol{r})\psi(R, \boldsymbol{r}) = \tilde{E}\psi(R, \boldsymbol{r}) \tag{A.8}$$

with $\tilde{E}$ being an Eigen energy of the system to the Eigen function $\psi(R, \boldsymbol{r})$. In order to construct a solution to this problem, the TISE for the electronic Hamiltonian, $H_e = T_e + V_{eN}$ at fixed internuclear distance, R, is considered first, i.e.

$$H_e(R; \boldsymbol{r})\varphi(R; \boldsymbol{r}) = [T_e + V_{eN}]\varphi(R; \boldsymbol{r}) = E_e(R)\varphi(R; \boldsymbol{r}). \tag{A.9}$$

Equation (A.9) reflects that one searches an Eigen energy for the electron, $E_{en}(R)$, together with the corresponding electronic Eigen function $\varphi(R; \boldsymbol{r})$ for a fixed nuclear geometry, which is fully characterized by the distance R. It is clear that for a fixed distance, R, a set of electronic Eigen energies, $E_{en}(R)$, and, corresponding Eigen functions, $\varphi_n(R; \boldsymbol{r})$, exists. Thereby, the $\varphi_n(R; \boldsymbol{r})$ form a complete electronic Basis set. Thus, it can be used to describe any electronic wave function using a proper superposition of these Eigen functions, $\varphi_{arb}(R; \boldsymbol{r}) = \sum_n c_n \varphi_n(R; \boldsymbol{r})$. Thereby, the electronic energy can always be calculated using the energy expectation value, $E_e(R) = \int d\boldsymbol{r}\, \varphi_{arb}{}^*(R; \boldsymbol{r}) H_e \varphi_{arb}(R; \boldsymbol{r}) / |\varphi_{arb}(R; \boldsymbol{r})|^2$.

Next, $\varphi_n(R; \boldsymbol{r})$ with the energy, $E_{en}(R)$, is used in the Ansatz,

$$\psi(R, \boldsymbol{r}) = \sum_n \varphi_n(R; \boldsymbol{r})\chi_n(R), \tag{A.10}$$

for the full Eigenfunction, $\psi(R, \boldsymbol{r})$. This means that one searches for a solution to the full problem, that is product of electronic Eigen functions $\varphi_n(R; \boldsymbol{r})$ which depend parametrically on the nuclear coordinate R and corresponding nuclear functions $\chi_n(R)$. The nuclear wave function is thereby dedicated to the corresponding electronic state. One might state that the $\chi_n(R)$ plays the role of a complex valued $R-$dependent weight. Using this Ansatz in the full TISE yields the following calculation

$$H(R, \boldsymbol{r})\left[\sum_n \varphi_n(R; \boldsymbol{r})\chi_n(R)\right] = \tilde{E}\left[\sum_n \varphi_n(R; \boldsymbol{r})\chi_n(R)\right], \tag{A.11}$$

with $H(R, \boldsymbol{r}) = H_e + H_N = T_e + V_{eN} + T_N + V_N$ being the full Hamiltonian. Plugging in and considering only one electronic level yields

$$\sum_n [T_e + V_{eN} + T_N + V_N][\varphi_n(R; \boldsymbol{r})\chi_n(R)]$$
$$= \sum_n (T_e[\varphi_n(R; \boldsymbol{r})\chi_n(R)] + V_{eN}(\boldsymbol{r})[\varphi_n(R; \boldsymbol{r})\chi_n(R)] + T_N[\varphi_n(R; \boldsymbol{r})\chi_n(R)] \tag{A.12}$$
$$+ V_N(R)[\varphi_n(R; \boldsymbol{r})\chi_n(R)]) = \tilde{E}[\varphi_n(R; \boldsymbol{r})\chi_n(R)].$$

Using the electronic solution (A.9) and that V_N depends on the nuclear coordinates only, simplifies this to

$$\sum_n E_e(R) \cdot \varphi_n(R; \boldsymbol{r})\chi_n(R) + \sum_n V_N(R) \cdot \varphi_n(R; \boldsymbol{r})\chi_n(R) + \sum_n T_N[\varphi_n(R; \boldsymbol{r})\chi_n(R)]$$
$$= \tilde{E}[\varphi_n(R; \boldsymbol{r})\chi_n(R)]. \tag{A.13}$$

Inserting the derivatives and applying the product rule exemplary for one summand in the last term of the left hand side (l.h.s.) yields,

$$T_N[\varphi_n(R; \boldsymbol{r})\chi_n(R)] = -\frac{1}{2\mu}\{\nabla_R[(\nabla_R\varphi_n(R; \boldsymbol{r}))\chi(R) + \varphi_n(R; \boldsymbol{r})(\nabla_R\chi(R))]\}$$
$$= -\frac{1}{2\mu}\left[\left(\nabla_R{}^2\varphi_n(R; \boldsymbol{r})\right)\chi_n(R) + 2(\nabla_R\varphi_n(R; \boldsymbol{r}))(\nabla_R\chi_n(R)) + \varphi_n(R; \boldsymbol{r})\left(\nabla_R{}^2\chi_n(R)\right)\right], \tag{A.14}$$

such that the full problem reads,

$$H(R, \boldsymbol{r})[\varphi(R; \boldsymbol{r})\chi(R)]$$
$$= \sum_n \{E_{en}(R) + V_N(R)\}[\varphi_n(R; \boldsymbol{r})\chi_n(R)]$$
$$+ \sum_n \left\{-\frac{1}{2\mu}\left[\left(\nabla_R{}^2\varphi_n(R; \boldsymbol{r})\right)\chi_n(R) + 2(\nabla_R\varphi_n(R; \boldsymbol{r}))(\nabla_R\chi_n(R))\right.\right.$$
$$\left.\left. + \varphi_n(R; \boldsymbol{r})\left(\nabla_R{}^2\chi_n(R)\right)\right]\right\} \tag{A.15}$$
$$= \tilde{E}[\varphi(R; \boldsymbol{r})\chi(R)].$$

So far, the result (A.15) is exact and equivalent to the full TISE in (A.8). However, by using (A.10) and (A.9) in (A.8) one imagines that the solution to (A.8) has a structure where the $\varphi_n(R; \boldsymbol{r})$s depend only parametrically on the nuclear coordinate.

A2.2 Application of the Born-Oppenheimer Approximation

In the next step, the Born-Oppenheimer (BO) approximation is applied by neglecting the first two terms in (A.15). These terms contain derivatives of the electron wave-function $\varphi(R; \boldsymbol{r})$ with respect to the nuclear coordinates, i.e. $\nabla_R{}^2\varphi(R; \boldsymbol{r})$ and $\nabla_R\varphi(R; \boldsymbol{r})$. This is justified as the motion of the nuclei is due their higher mass orders of magnitude slower compared to the motion of the electron. Also the change of $\varphi_n(R; \boldsymbol{r})$ with respect to a change of the nuclear coordinate is assumed to be small. Thus, these terms can be neglected in many relevant situations. Neglecting them yields an approximate expression for the full time-independent problem,

$$H(R, \boldsymbol{r})[\varphi(R; \boldsymbol{r})\chi(R)] \approx \sum_n \varphi_n(R; \boldsymbol{r})\left\{E_{en}(R) + V_N(R) - \frac{1}{2\mu}\left[\left(\nabla_R{}^2\chi_n(R)\right)\right]\right\}[\chi_n(R)]$$
$$\sum_n \varphi_n(R; \boldsymbol{r})\{E_{en}(R) + V_N(R) + T_N\}[\chi_n(R)] \approx \tilde{E}\left[\sum_n \varphi_n(R; \boldsymbol{r})\chi_n(R)\right]. \tag{A.16}$$

Thereby, the terms have been written in suggestive order [165]. By multiplication of the whole equation with $\varphi_n{}^*(R; \boldsymbol{r})$ and integrating over electronic coordinates, $\boldsymbol{r}$, yields the TISE for nuclear problem on the nth BO-potential, $U_n(R) = E_{en}(R) + V_N(R)$,

$$\{E_{en}(R) + V_N(R) + T_N\}\chi_n(R) = \{U_n(R) + T_N\}\chi_n(R) = \tilde{E}\chi_n(R). \tag{A.17}$$

Thereby, one uses the orthogonality of the electronic problem, i.e. that $\int \varphi_m{}^*(R; \boldsymbol{r})\varphi_n(R; \boldsymbol{r})\,d\boldsymbol{r} = 0$ for $n \neq m$. Equation (A.17) is the TISE for the internuclear distance R in an effective potential, i.e. the Born-Oppenheimer (BO-

potential), $U_n(R)$, if the electron is in the nth Eigenstate. Thereby, $U_n(R)$, contains the electron-nuclei as well as electron-electron forces via $E_{en}(R)$ as well as nuclei-nuclei forces, $V_N(R)$.

Similar to the electronic TISE, again a complete basis set of Eigen functions, $\chi_{nv}(R)$ that solves (A.17) with Eigen energies, $\tilde{E}_{nv}$ can be found for each electronic Eigenstate n. If $U_n(R)$ has a local minimum a stable chemical bond with localized Eigen functions and corresponding Eigen energies that are called vibrational levels can be formed. If $U_n(R)$ has no local minimum, the problem in (A.17) does not support bound states. Thus, no stable chemical bond occurs and the molecule would dissociate, i.e. the internuclear distance, increases but the electron still remains in a bound state.

Similarly to the electronic states, one might use these Eigen functions $\chi_{nv}(R)$ to describe an arbitrary nuclear wave function on the nth electronic potential via superposition, $\chi_{narb}(R) = \sum_{nv} g_{nv}\chi_{nv}(R)$. If the molecule, however, populates several electronic states the full wave function reads, $\psi(R, \mathbf{r}) = \sum_n \varphi_n(R; \mathbf{r})\chi_n(R) = \sum_n \varphi_1(R; \mathbf{r})\chi_1(R) + \varphi_2(R; \mathbf{r})\chi_2(R) + \cdots$, and several $U_n(R)$ play a role, such that (A.17) becomes several BO TISEs.

Altogether, the previous consideration yields the following procedure and physical picture to find an approximate Eigen function, $\psi(R, \mathbf{r})$, with the Eigen energy, $\tilde{E}$, of the total system. One, (i) needs to solve the electronic TISE, i.e. (A.9), with R being fixed but a parameter for the electronic problem. This yields an effective electronic potential, which the electron produces for the nuclei, $E_{en}(R)$. This potential changes if one choses another Eigen state of the electron. It is this energy, $E_{en}(R)$, which measures the binding energy of the electron if the two nuclei are at the fixed position, R. (ii) Second, using the found $E_{en}(R)$ together with $V_N(R)$ by combining them to the BO potential $U_n(R)$ yields a second TISE for the nuclear Eigen function, $\chi_{nv}(R)$, and the total energy Eigen energy $\tilde{E}$, i.e (A.17). A full Eigenstate is then, $\psi(R, \mathbf{r}) = \varphi_n(R; \mathbf{r})\chi_{nv}(R)$ and has the Eigen energy, $\tilde{E}_{nv}$. It is the electronic potential which mediates forces between electron and nuclei. For a general situation, the molecule is not necessarily in one electronic state, such that (A.17) represents a system of equations.

The BO-approximation is central for arriving at this physical picture. It allows to separate the electronic and the nuclear problem. This is very powerful and yields very good results in many situation. But it fails under certain circumstances which are shortly mentioned here. It might be necessary to improve the BO-approximations in situations where: (i) The electronic presence of probability is –somewhat unclear-, i.e. in regions where several electronic wave functions yield similar or even the same energy but have different electronic wave functions (degeneracy). In this case, the electronic potential is not well defined and can thus, be more sensitive to changes of the nuclear geometry. (ii) In situations where the relative motion of the nuclei is substantial, e.g. in high-energy atom-molecule collisions. (iii) Last but not least, it is clear that the BO approximation might yield unreasonable results when the electron is slow/moves on the same time scale as the nuclei. Under such circumstances, it is unreasonable to neglect the second derivatives in (A.15)

Next, electronic and nuclear Eigen states are obtained within the method of linear combination of atomic orbitals in order to familiarize with the physical picture.

A2.3 Using Linear Combination of Atomic Orbitals to Illustrate the Approximate Electronic an Nuclear Eigenstate within the Born-Oppenheimer Approximation of H_2^+

In order to familiarize with the previously introduced concepts, of electronic wave function, nuclear wave function, Born-Oppenheimer (BO) potential and BO Schrödinger equation, a full solution to the TISE of H_2^+ is reviewed here. Therefore, the method of linear combination of atomic orbitals (LC) is used as it allows to perform many calculations in an analytical manner. The consideration follow refs [74] [166] [165].

As stated before, one starts at (A.9) by solving the electronic problem for fixed inter nuclear distance R, i.e. one needs to solve $H_e(R; \boldsymbol{r})\varphi(R; \boldsymbol{r}) = E_e(R)\varphi(R; \boldsymbol{r})$. Within the LC method, one uses a superposition of two hydrogen 1s wave functions, which are separated by the internuclear distance, R. Each wave function of the hydrogen atom has the form, $\alpha_{1s}(r) = \pi^{-1/2}\exp(-\tilde{r})$ with $\tilde{r} = \sqrt{x^2 + y^2 + z^2}$ being the radius in spherical coordinates. As the molecule's internuclear axis is kept fixed along the z-direction, cylindrical coordinates are appropriate to give an approximate expression for the R-dependent electronic Eigen functions. One is the gerade electronic LC wave function, $\varphi_{gLC}(R; \rho, z)$,

$$\varphi_{gLC}(R; \boldsymbol{r}) = \frac{1}{\sqrt{2}}[\alpha_{1s}(\boldsymbol{r}_A) + \alpha_{1s}(\boldsymbol{r}_B)]$$

$$\varphi_{gLC}(R; x, y, z) = \frac{1}{\sqrt{2\pi}}\left[e^{-\sqrt{x^2+y^2+(z+R/2)^2}} + e^{-\sqrt{x^2+y^2+(z-R/2)^2}}\right] \tag{A.18}$$

$$\varphi_{gLC}(R; \rho, z) = \frac{1}{\sqrt{2\pi}}\left[e^{-\sqrt{\rho^2+(z+R/2)^2}} + e^{-\sqrt{\rho^2+(z-R/2)}}\right].$$

The other is the ungerade electronic wave function, $\varphi_{uLC}(R; \rho, z)$,

$$\varphi_{uLC}(R; \boldsymbol{r}) = \frac{1}{\sqrt{2}}[\alpha_{1s}(\boldsymbol{r}_B) - \alpha_{1s}(\boldsymbol{r}_A)]$$

$$\varphi_{uLC}(R; x, y, z) = \frac{1}{\sqrt{2\pi}}\left[e^{-\sqrt{x^2+y^2+(z-R/2)^2}} - e^{-\sqrt{x^2+y^2+(z+R/2)^2}}\right] \tag{A.19}$$

$$\varphi_{uLC}(R; \rho, z) = \frac{1}{\sqrt{2\pi}}\left[e^{-\sqrt{\rho^2+(z-R/2)^2}} - e^{-\sqrt{\rho^2+(z+R/2)}}\right].$$

These two functions are assumed to be reasonable approximate expression for the two lowest electronic Eigen energy states. In Figure A.5, two-dimensional cuts through the electron density of $\left|\varphi_{gLC}(R; \rho, z)\right|^2$ and $|\varphi_{uLC}(R; \rho, z)|^2$ are shown. For the gerade case, electron density occurs between the nuclei while for the ungerade case, no electron density can be found between the nuclei. This leads to the formation of the molecular bond in the first case but not in the second.
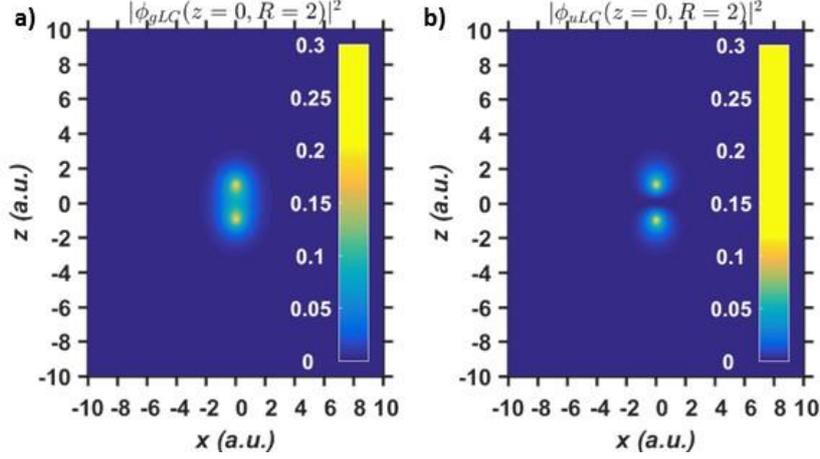
Figure A.5 Electron density of the gerade and the ungerade electronic wave function for H_2^+ obtained within the LC method

a) shows a cut through the electron density, $|\varphi_{gLC}(R=2; x, y=0, z)|^2$, of the gerade electronic wave function obtained within the LC method. Significant electron density is found within the nuclei such that a molecular bond is formed. b) shows a cut through the electron density, $|\varphi_{uLC}(R=2; x, y=0, z)|^2$. In this case, the electron density between the two nuclei is zero and thus, no molecular bond is formed.

The R-dependence is illustrated in Figure A.6. There, cuts through the real part of both states are shown together with the fixed nuclear potential along the z-coordinate of the system for some R. By scanning R, each of the electronic Eigen states, $\varphi_{gLC}(R; \rho, z)$ and $\varphi_{uLC}(R; \rho, z)$ produces an the R-dependent electronic Eigen energy curve, $E_{egLC}(R)$ and $E_{euLC}(R)$. Without going into detail further, but following the calculation [74]. Calculating $E_{egLC}(R)$ and $E_{euLC}(R)$ analytically yields the following expressions for electronic Eigen energy curves,

$$E_{e\,g,uLC}(R) = -\frac{1}{R} - \frac{1}{2} + \frac{1}{R}\frac{(1+R)e^{-2R} \pm (1-2R^2/3)e^{-R}}{1 \pm (1+R+R^2/3)e^{-R}}. \tag{A. 20}$$

The corresponding Born-Oppenheimer potential, $U(R)$, is then, $U_{g,uLC}(R) = E_{e\,g,uLC}(R) + 1/R$,

$$U_{g,uLC}(R) = -\frac{1}{2} + \frac{1}{R}\frac{(1+R)e^{-2R} \pm (1-2R^2/3)e^{-R}}{1 \pm (1+R+R^2/3)e^{-R}} \tag{A. 21}$$

. Both are curves are shown in Figure A.6. e). $U_{gLC}(R)$, has a minimum close to $R_{eqLC} \approx 5/2$ while the BO potential, $U_{uLC}(R)$, is a monotonically decreasing function. Thus, a stable chemical bond with several bound vibrational states exist on the $U_{gLC}(R)$ curve only. This has been as expected from the distribution of the electron density in Figure A.5. Figure A.6 f) illustrates the electronic Eigen energy curves, $E_{eg}(R)$ and $E_{eu}(R)$ from a numerically exact solution, of the electronic problem together with the resulting BO potentials, $U_g(R)$ and $U_u(R)$, and the probability of nuclear wave function, $|\chi(R)|^2$ which was obtained by numerical solution the TISE on $U_g(R)$.
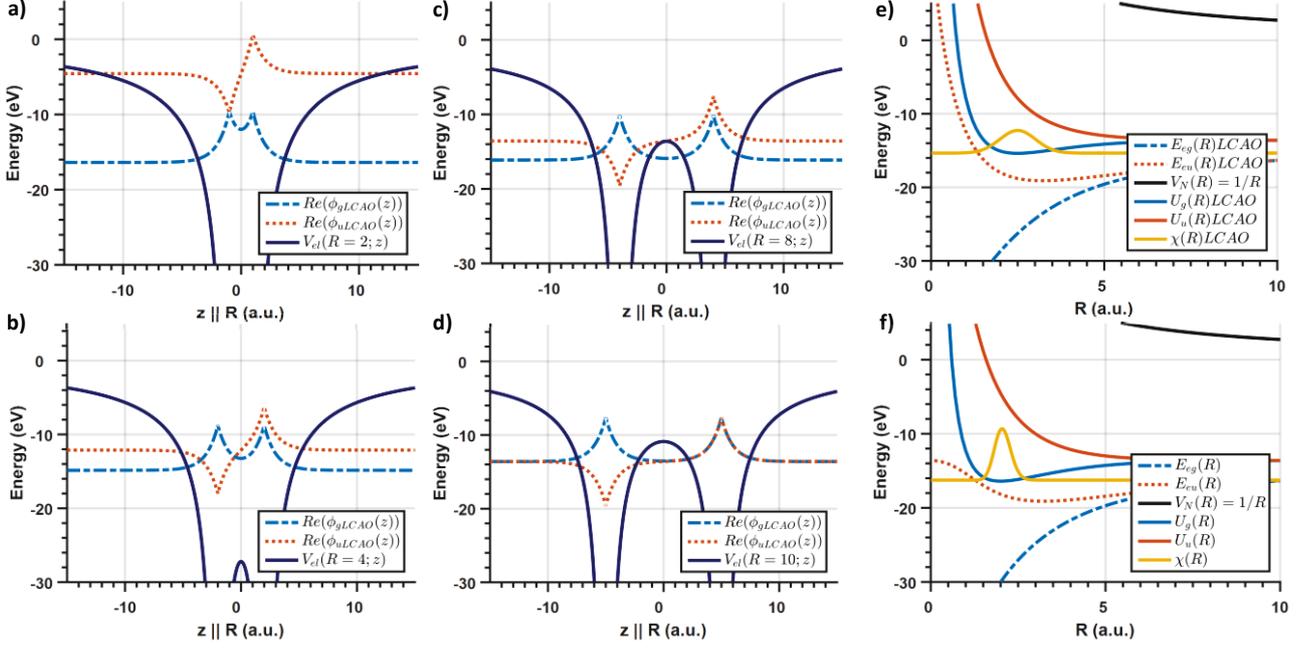
Figure A.6 Linear combination of atomic orbitals to find an approximate ground state wave function for H_2^+

a)-d) illustrate the cuts through the gerade and the ungerade electronic wave-function for different inter nuclear distances within the LCAO method. e) shows the electronic energies $E_{egLC}(R)$ and $E_{euLC}(R)$ as function of R obtained based on the LC electronic wave functions as well as the nuclear potential $V_N(R) = 1/R$. Adding $E_{egLC}(R)$ and $V_N(R)$ gives the Born-Oppenheimer (BO) potentials, $U_{gLC}(R)$ and $U_{uLC}(R)$ the LCAO approximation which are shown in addition. Also shown is $\left|\chi_{g0LC}(R)\right|^2$ of the nuclear groundstate eigen function $\chi_{g0LC}(R)$ if the BO potential is approximated using a second order Taylor series around the equilibrium distance, $R_{LCAO} \approx 2.5$. f) shows the same curves as e) but with the electronic eigen energy curves from a numerically exact solution of the electronic problem, $E_{eg}(R)$ and $E_{eu}(R)$. The vibrational ground state, $|\chi(R)|^2$, has been found by solving the TISE on $U_g(R)$ numerically.

In order to find an approximate expression for the vibrational wave function, $\chi_{gLC}(R)$, the analysis is continued by approximating $U_{gLC}(R)$ using a Taylor series up to quadratic order around $R_{eqLC} \approx 5/2$, i.e. $U_{gLC}(R) \approx U_{gLC}(R_{eqLC}) + \frac{1}{2}\partial^2 U_{gLC}(R)/\partial R^2\big|_{R_0}(R - R_{qLC})^2$. As R_{eqLC} is close to a minimum, the first derivative is zero. Using MATLAB's symbolic functions tool box one finds $\partial^2 U_{gLC}(R)/\partial R^2\big|_{R_{eqLC}} \approx 0.0619$ and $U_{gLC}(R_{qLC}) \approx -0.5648$ such that the approximated BO potential is

$$U_{gLC}(R) \approx -0.5648 + \frac{1}{2}0.0619\left(R - R_{qLC}\right)^2 = E_{eR_{LC}} + \frac{1}{2}k_{LC}^2\left(R - R_{qLC}\right)^2. \tag{A.22}$$

Finding the nuclear ground state wave function means to solve,

$$\left(-\frac{1}{2\mu}\left(\nabla_R{}^2\chi_{g1LC}(R)\right) + E_{eR_{LC}} + \frac{1}{2}k_{LC}^2\left(R - R_{eqLC}\right)^2\right)\chi_{g1LC}(R) = \tilde{E}_{nvLC}\chi_{g1LC}(R), \tag{A.23}$$

which is the BO-TISE for the nuclear part of the wave function, i.e. (A.17). First, the constant part is split of using $E_{vLC} = \tilde{E}_{nvLC} - E_{eqR_{LC}}$. Introducing, $\kappa_{LC}^2 = k_{LC}^2/\mu$, yields the nuclear TISE, which has the form as a harmonic oscillator,

$$\left(\frac{1}{2\mu}\nabla_R{}^2\chi(R) + \frac{1}{2}\mu\kappa_{LC}^2\left(R - R_{qLC}\right)^2\right)\chi_{g1LC}(R) = E_{vLC}\chi_{g1LC}(R) \tag{A.24}$$

. It's Eigen energies are,

$$E_\nu = \kappa_{LC}\left(\nu + \frac{1}{2}\right) = \frac{k_{LC}}{\sqrt{\mu}}\left(\nu + \frac{1}{2}\right) \quad \nu = 0,1,2,\dots \quad . \tag{A.25}$$

The corresponding wave function of the nuclear ground state is a Gaussian centered around R_0, i.e.

$$\chi_{g0LC}(R) = \left(\frac{\mu\kappa_{LC}}{\pi}\right)^{1/4} e^{-\frac{1}{2}\mu\kappa_{LC}(R-R_{eqLC})^2} = \left(\frac{\sqrt{\mu}k_{LC}}{\pi}\right)^{1/4} e^{-\frac{1}{2}\sqrt{\mu}k_{LC}(R-R_{eqLC})^2}. \tag{A.26}$$

The full electronic and nuclear wave function of the vibrational and electronic ground state within the approximation from above reads, $\psi_{g1LC}(R,\boldsymbol{r}) = \varphi_{gLC}(R;\boldsymbol{r})\chi_{g1LC}(R)$, i.e.

$$\psi_{g1LC}(R,\rho,z) = \left(\frac{\sqrt{\mu}k_{LC}}{\pi}\right)^{1/4} e^{-\frac{\sqrt{\mu}k_{LC}}{2}(R-R_{qLC})^2} \frac{1}{\sqrt{2\pi}}\left[e^{-\sqrt{\rho^2+(z-R/2)^2}} + e^{-\sqrt{\rho^2+(z+R/2)^2}}\right]. \tag{A.27}$$

From $\psi(R,\rho,z)$, one might see that the nuclear wave function kind of weights the contribution of the R-dependent electronic wave functions.

The vibrational ground state adds about energy $E_{\nu=0} = 0.001\ a.u. = 0.0272$ eV to the approximate total energy of the system, i.e.

$$\tilde{E}_{n\nu LC} = E_{\nu LC} + E_{eqR_{LC}} \approx -0.5658\ \text{a. u.} \approx 15.40\ \text{eV}. \tag{A.28}$$

The total energy, $\tilde{E}_{n\nu LC}$, is the energy that is approximately needed in order to separate all three particles, i.e. to go from a stable H_2^+ molecular ion in its vibrational ground state to two protons and a free electron, $H_2^+ \to p^+ + p^+ + e^-$. The energy that is needed in order to separate a hydrogen atom from the H_2^+ molecule, i.e. to dissociate it, $H_2^+ \to H + p^+$, is

$$D_{\nu LC} = \tilde{E}_{n\nu LC} - E_{e\,gLC}(R \to \infty) = -0.5658 - \frac{1}{2} \approx 0.0658\ \text{a. u.} \approx 1.79\ \text{eV}. \tag{A.29}$$

In Figure A.6 f), this result is compared with a calculation that uses the exact BO potential of the real H_2^+ molecule. First, the LC result yields wrong equilibrium distance, i.e. $R_{eqLC} \approx 5/2$ compared to $R_{equ} = 2$. Second, the dissocation energy, $D_{LC} = 1.77$ eV, is smaller compared to $D = 2.79$ eV. The shape of the LC nuclear wave function is a lot wider compared to the exact ground state nuclear wave function. As the consideration illustrates, these differences originate from constructing the molecular electronic wave function, $\varphi(R;\boldsymbol{r})$, as superposition of exact atomic wave functions. This procedure causes an erroneous probability of presence for the electron and in turn, causes an erroneous electronic potential, $E_e(R)$. Finally it leads to a slightly wrong BO potential, $U(R)$, which establishes an erroneous nuclear wave function. For comparisons of experimental and theoretical data one should use the exact BO potential instead of the LC results

Reviewing the LC method in combination with approximating BO potential by a quadratic function around the equilibrium distance is very useful to illustrate the physical picture of a chemical bond. Phenomenologically, the chemical bond might be summarized as follows. An electron around two protons has a probability of presence which is described by the electronic wave function, $\varphi(R;\boldsymbol{r})$. It forms an electronic potential, $E_e(R)$, such that the two protons can be bound together although their positive charges without the electron would repel each other. For H_2^+ this is only possible if the electronic wave function, $\varphi(R;\boldsymbol{r})$, is in the ground state as the BO potential, i.e. $E_e(R) + 1/R$, has a minimum in this case. From this perspective, it seems to be reasonable that modifying $\varphi(R;\boldsymbol{r})$ by e.g. applying a static external field yields a modified $E_e(R)$ and thus a changed $U(R)$, which in turn yields an effect on the nuclear wave function, $\chi(R)$, such that e.g. the equilibrium distance is changed. Changing the nuclear wave function reacts back on the electronic wave function as the electron wave function rearranges due to the new

position of the nuclei. Now, imagine a quasi-static but rapidly oscillating field where the $\varphi(R;\boldsymbol{r})$ follows the field almost instantaneously, very rich effects on the nuclear wave function, $\chi(R)$, can be expected.

The effect of an external field on the electronic states and thus on the BO potential is illustrated in the next section.

A2.4 Two-Level Perturbation Theory Applied to H_2^+ in Static External Electric Field
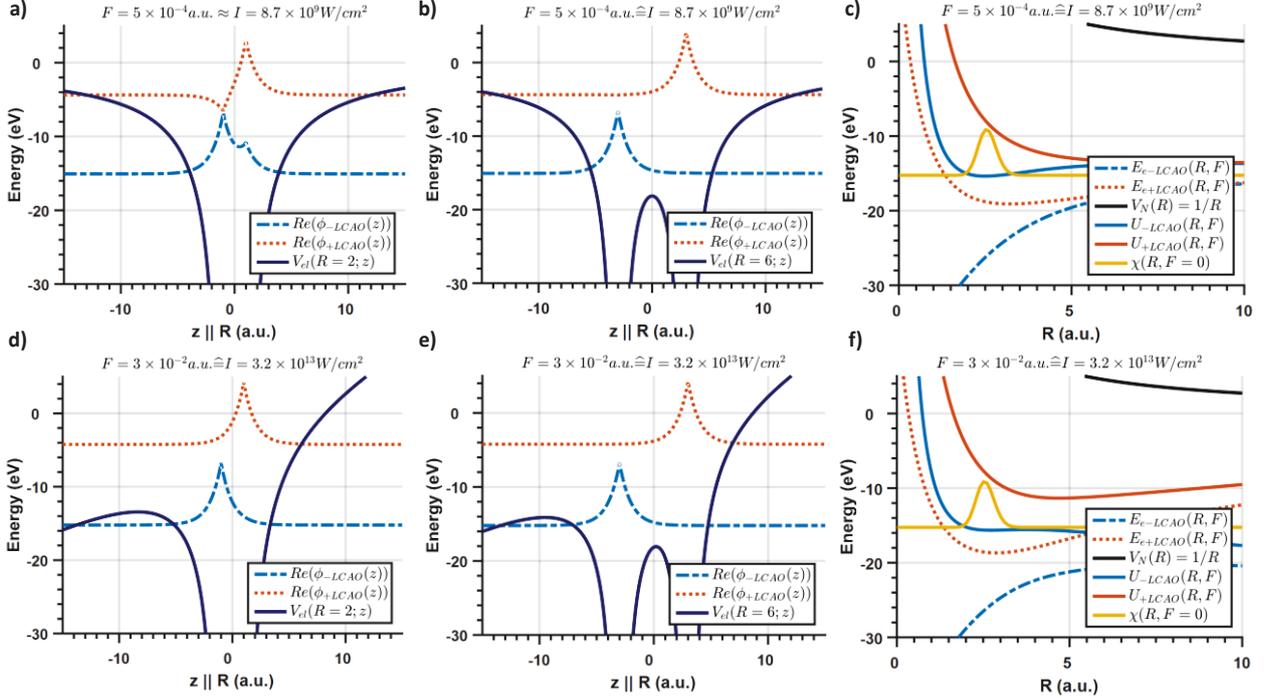

Figure A. 7 Influence of a static electric field on the electronic wave function within the perturbation theory

a), b), d) and e) illustrate a cut through the $\varphi_{-LC}(R;z,F)$ and the $\varphi_{+LC}(R;z,F)$ electronic wave functions in a static external field obtained based on the field-free LCAO solutions and within perturbation theory of a two-level system. The wave functions are shifted in energy such that their baseline match the energy Eigen values, E_{e-LC} and E_{e+LC} as calculated based on (A.33). For weak fields and small distances, i.e. a) and b), the cut resembles the mixing of the field-free wave function. For the strong field case, d) and e), the +-state lies energetically above the barrier and would thus ionize very quickly. The electronic ground state, however, is still bound but could tunnel through the potential barrier similarly to the situation in an atom. c) and f) shows the resulting BO potentials in the field. The +-state is bend up while the −-state is bend down. Increasing the field strength, increases the strength of the bending,

Here, the electronic problem of H_2^+ within a static external electric field is solved, using a two-level model and first order perturbation theory as detailed in A3. Although it is generally not necessary, the field-free solution to the electronic problem are assumed to be the LC wave functions as used in A2.3. In this way, the analysis can be done with analytical expression to a large extend and is useful for illustrations and for getting insight. However, for the comparisons to experimental data always use the exact electronic Eigen energies, i.e. $E_g(R)$ and $E_u(R)$.

Adding a static electric field of the strength, $F = F\boldsymbol{e}_z$, adds

$$V_F(\boldsymbol{R},\boldsymbol{r},F) = F(Q_A\boldsymbol{R_A} + Q_B\boldsymbol{R_B} - \boldsymbol{r})\boldsymbol{e_z} \tag{A.30}$$

to the Hamiltonian of the field free problem (A.7). Using the simplifications, $Q_A = Q_B$ and $\boldsymbol{R_A} = -\boldsymbol{R}/2 = -\boldsymbol{R_B}$, as H_2^+ is a diatomic molecule yields,

$$H(\boldsymbol{R},\boldsymbol{r},F) = -\frac{1}{2\mu}\nabla_R{}^2 + \frac{1}{|\boldsymbol{R}|} - \frac{1}{2}\nabla_r{}^2 - \frac{1}{|\boldsymbol{r_A}|} - \frac{1}{|\boldsymbol{r_B}|} + \boldsymbol{r}F$$

$$H(\boldsymbol{R},\boldsymbol{r},F) = T_N + V_N + T_e + V_{eN} + V_{eF} = H_N + H_e^0 + V_{eF} = H_N + H_e^0 + H_e'F. \tag{A.31}$$

Working along the lines of the BO-approximation by considering the electronic problem with fixed nuclei and applying perturbation theory for the influence of the static field yields the Schrödinger equation,

$$H_e(R;\boldsymbol{r},F)\varphi(R;\boldsymbol{r},F) = (H_e^0 + H_e'F)\varphi(R;\boldsymbol{r},F) = E_e(R,F)\varphi(R;\boldsymbol{r},F). \tag{A.32}$$

Here F takes the role of the perturbation, λ, in A3. Continuing within the two-level LC model by assuming that the field-free solution of the unperturbed system are given by the LC wave functions $\varphi_{gLC}(R;\boldsymbol{r})$ and $\varphi_{uLC}(R;\boldsymbol{r})$ in (A.18) and (A.19) yields the exact solution for the two-level Eigen energies in the field,

$$E_{e\pm LC}(R,F) = \frac{1}{2}\left(E_{e_{gLC}}(R) + E_{e_{uLC}}(R)\right) \pm \frac{1}{2}\sqrt{\left(E_{e_{gLC}}(R) - E_{e_{uLC}}(R)\right)^2 + 4F^2|\langle g_{LC}|\boldsymbol{r}|u_{LC}\rangle|^2}. \tag{A.33}$$

Thereby, the expression for the perturbed energies in (A.49) has been applied with $H_{11} = \langle g_{LC}|H_e^0 + H_e'F|g_{LC}\rangle = E_{e_{gLC}}(R)$ and $H_{22} = \langle u_{LC}|H_e^0 + H_e'F|u_{LC}\rangle = E_{e_{uLC}}(R)$ because, $\langle g_{LC}|H_e'|g_{LC}\rangle = \langle u_{LC}|H_e'|u_{LC}\rangle = \langle g_{LC}|\boldsymbol{r}|g_{LC}\rangle = \langle u_{LC}|\boldsymbol{r}|u_{LC}\rangle = 0$ and $H_{12} = \langle g_{LC}|H_e^0 + H_e'F|u_{LC}\rangle = \langle g_{LC}|H_e^0|u_{LC}\rangle + F\langle g_{LC}|\boldsymbol{r}|u_{LC}\rangle = F\langle g_{LC}|\boldsymbol{r}|u_{LC}\rangle$. The new Eigen states of H_2^+ in the field are found by evaluating,

$$\rightarrow \zeta = \frac{1}{2}\text{atan}\left(-2\frac{F|\langle g_{LC}|\boldsymbol{r}|u_{LC}\rangle|}{E_{e_{gLC}}(R) - E_{e_{uLC}}(R)}\right) \tag{A.34}$$

and using it in the expressions,

$$\varphi_{-LC}(R;\boldsymbol{r},F) = \cos\zeta\,\varphi_{gLC}(R;\boldsymbol{r}) + \sin\zeta\,\varphi_{uLC}(R;\boldsymbol{r})$$

$$\varphi_{+LC}(R;\boldsymbol{r},F) = -\sin\zeta\,\varphi_{gLC}(R;\boldsymbol{r}) + \cos\zeta\,\varphi_{uLC}(R;\boldsymbol{r}). \tag{A.35}$$

. It is common to approximate further the transition dipole matrix element, $d(R) = \langle g|\boldsymbol{r}|u\rangle$, of H_2^+ [167] [151]

$$d_{LC}(R) = \langle g_{LC}|\boldsymbol{r}|u_{LC}\rangle \approx \frac{R}{2}\left(\frac{1}{\sqrt{1-(e^{-R}(1+R+R^2/3))^2}}\right). \tag{A.36}$$

With (A.33) to (A.35) one has exact expressions for the electronic Eigen energy and wave function of a two-level model of H_2^+ in an external field with the LC approximation using the field-free Eigen functions as basis set.

Figure A. 7 illustrates the influence of the static laser field on the electronic wave function together with the field's effect on the BO potential. The shown curves have been calculated using (A.33) with potentials as given in the

caption. Our consideration shows that the field leads to a changed electronic wave function, which leads to a modification of the R—dependent electronic energy curves. Thereby, the φ_{-LC}-state, i.e. the electronic ground state in the field causes a BO potential, which favors an increase of the inter nuclear distance, R. It can thus, induce a stretching motion for the nuclei as the binding region is widened due to the static external field. In addition, a tunneling barrier is formed. If the electron is, however, in the first excited electronic state in the field, i.e. in the φ_{+LC}-state, the corresponding BO potential curve bends up. If the field is strong enough, the corresponding BO potential forms a minimum towards which the nuclear wave function might be pushed such that R might be reduced, see Figure A. 7 f).

The analysis of the electronic wave functions can be continued by considering several limiting cases that are discussed in A3. For small R, $E_{e_{uLC}}(R) - E_{e_{gLC}}(R)$, is large such that the approximation of a *non-degenerate system* can be used. Using (A.53) yields approximate wave functions,

$$
\varphi_{-LC}(R; \boldsymbol{r}, F) \approx \varphi_{gLC}(R; \boldsymbol{r}) - \frac{F\langle g_{LC}|\boldsymbol{r}|u_{LC}\rangle}{\Delta E_{e_{ugLC}}(R)} \varphi_{uLC}(R; \boldsymbol{r})
$$

$$
\varphi_{+LC}(R; \boldsymbol{r}, F) \approx \varphi_{uLC}(R; \boldsymbol{r}) + \frac{F\langle g_{LC}|\boldsymbol{r}|u_{LC}\rangle}{\Delta E_{e_{ugLC}}(R)} \varphi_{gLC}(R; \boldsymbol{r})
$$

(A.37)

, with $\Delta E_{e_{ugLC}}(R) = E_{e_{uLC}}(R) - E_{e_{gLC}}(R)$. The energy correction in first order perturbation theory is zero. Thus, first non-zero energy corrections are quadratic in the field, i.e.

$$
E_{e_-}(R, F) \approx E_{e_{gLC}}(R) \rightarrow E_{e_-}(R, F) \approx E_{e_{gLC}}(R) - \frac{(F\langle g_{LC}|\boldsymbol{r}|u_{LC}\rangle)^2}{\Delta E_{e_{ugLC}}(R)}
$$

$$
E_{e_+}(R, F) \approx E_{e_{uLC}}(R) \rightarrow E_{e_+}(R, F) \approx E_{e_{uLC}}(R) + \frac{(F\langle g_{LC}|\boldsymbol{r}|u_{LC}\rangle)^2}{\Delta E_{e_{ugLC}}(R)}.
$$

(A.38)

The *system is degenerate* for large distances as, $E_{e_{uLC}}(R) \approx E_{e_{gLC}}(R) \approx -1/2$, such that the energies of $|+\rangle$ and $|-\rangle$ are approximately,

$$
E_{e_\pm}(R, F) = -\frac{1}{2} \pm F|\langle g_{LC}|\boldsymbol{r}|u_{LC}\rangle|,
$$

(A.39)

and the corresponding states in the field are

$$
\varphi_{-LC}(R; \boldsymbol{r}, F) \approx \frac{1}{\sqrt{2}}\Big(\varphi_{gLC}(R; \boldsymbol{r}) - \varphi_{uLC}(R; \boldsymbol{r})\Big)
$$

$$
\varphi_{+LC}(R; \boldsymbol{r}, F) \approx \frac{1}{\sqrt{2}}\Big(\varphi_{gLC}(R; \boldsymbol{r}) + \varphi_{uLC}(R; \boldsymbol{r})\Big).
$$

(A.40)

A compromise between *non-degenerate system* and *strictly degenerate system* might be given using (A.56). It yields for the energies at intermediate R where the electronic *system is nearly degenerate*,

$$
E_{e_{-LC}}(R, F) \approx E_{e_{gLC}}(R) - F\langle g_{LC}|\boldsymbol{r}|u_{LC}\rangle
$$

$$
E_{e_{+LC}}(R, F) \approx E_{e_{uLC}}(R) + F\langle g_{LC}|\boldsymbol{r}|u_{LC}\rangle.
$$

(A.41)

As the Eigen functions in the field, one might use expressions (A.19) in this case, too.
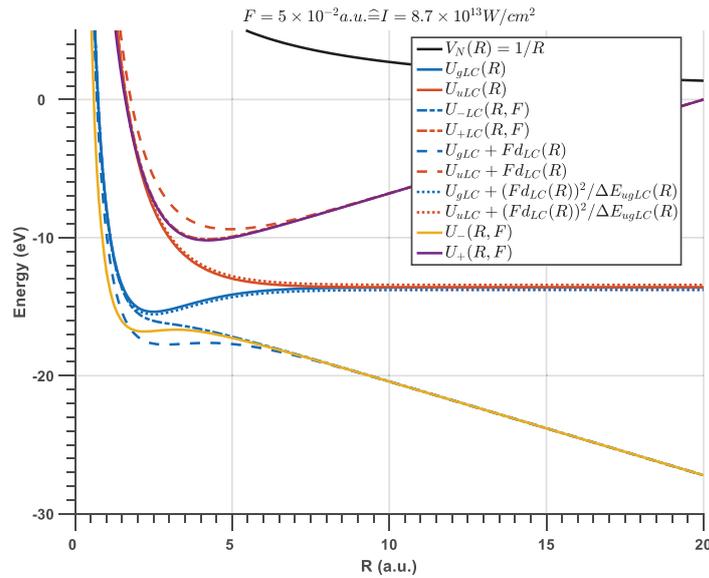
Figure A.8 Influence of approximate expressions for electronic Eigen energies in the field and on the BO potential
Various approximations to calculate the BO curves in the field within the LC method are compared. Altogether, the approximate curves in comparison behave as expected. In addition, more realistic BO curves in the field, i.e. $U_+(R,F)$ and $U_-(R,F)$ are shown. They have been calculated based on the exact field free BO curves, $U_g(R)$ and $U_u(R)$, in combination with (A.35) where the LC transition dipole matrix element has been used.

We compare the influence on the BO potential of the approximate expressions for the Electronic eigen energy curves in the field obtained within the LC method in Figure A.8. Altogether, the difference between the exact solution, (A.33), and the approximate expressions, (A.38), (A.39) and (A.41), as function of R behave as expected. At small R, (A.38) fits extremely well and better than (A.39) and (A.41). At large R, however, it does not reproduce the behavior of the exact solution. In this region, (A.39) fits the exact solution extremely well. The compromise between the cases of (A.38) and (A.39), i.e. (A.41) the solution for a nearly degenerate system, matches the exact solution reasonably well over a large range of R. However, the match is not perfect particularly close to the equilibrium distance R.

Besides this comparison of different expressions for the BO potential within the LC method Figure A.8 contains a more realistic BO curve in the laser field, i.e. $U_+(R,F)$ and $U_-(R,F)$. For these curves, the exact field free BO potentials, $U_g(R)$ and $U_u(R)$, have been used together with LC transition dipole matrix element, $d_{LC}(R)$ to calculate the BO curves in the field using (A.36). It is this model of the electronic structure of H_2^+ that is used to describe the ionization dynamics, which are compare to the measurement results in chapter 5. For the transition dipole moment at small Rs around the equilibrium distance we used more exact calculations, see chapter 5.3.

Independent on the details of the used approximations for the BO potential or the coupling in the field, one might draw the following picture of the interaction between H_2^+ and a static external electric field F. The external field changes the probability of presence of the electron (expressed by finding the new Eigenstates in the field as superposition of the field-free Eigenstates). This affects the BO potential curves to which the nuclear wave function reacts.

A3 Perturbation Theory of Two-Level Systems

Here we summarize central results of two-level perturbation theory in order to have them at hand for the one-dimensional two-level model of strong-field photoionization of H_2^+. The considerations follows [168].

A3.1 Time-Independent Perturbation Theory

After the previous review of the H_2^+ molecule within the LC approximation, perturbation theory of a two-level system is reviewed here. The results of the calculations here are the more general basis for the calculations in the previous chapter.

Consider a two-level system with the perturbation free Hamiltonian, H^0, that has the two eigenstates, $|1\rangle$ and $|2\rangle$ with corresponding eigenfunctions, ψ_1 and ψ_2, and the Eigen energies, E_1 and, E_2. Introducing the perturbation, $\lambda H'$, of strength λ one hopes that the superposition,

$$\psi = a_1 \psi_1 + a_2 \psi_2 = a_1 |1\rangle + a_2 |2\rangle = |\psi\rangle, \tag{A.42}$$

solves the problem

$$H|\psi\rangle = [H^0 + \lambda H']|\psi\rangle = E|\psi\rangle. \tag{A.43}$$

Thereby, $|\psi\rangle$ is Eigen state of the perturbed system with the corresponding Eigen energy, E. Using the Ansatz (A.42) in (A.43) yields

$$a_1(H - E)|1\rangle + a_2(H - E)|2\rangle = 0. \tag{A.44}$$

Multiplication of once with $\langle 1|$ and once with $\langle 2|$ gives

$$\langle 1|a_1(H - E)|1\rangle + \langle 1|a_2(H - E)|2\rangle = 0$$
$$\langle 2|a_1(H - E)|1\rangle + \langle 2|a_2(H - E)|2\rangle = 0. \tag{A.45}$$

By employing $\langle 1|2\rangle = \langle 2|1\rangle = 0$ and $\langle 1|1\rangle = \langle 2|2\rangle = 1$ and denoting, $H_{12} = \langle 1|H|2\rangle$ one arrives at

$$\rightarrow a_1\langle 1|H|1\rangle - a_1 E \langle 1|1\rangle + a_2\langle 1|H|2\rangle - E\langle 1|2\rangle = 0$$
$$\rightarrow a_1\langle 2|H|1\rangle - a_1 E \langle 2|1\rangle + a_2\langle 2|H|2\rangle - a_2 E\langle 2|2\rangle = 0. \tag{A.46}$$

This is a system of equations for the coefficients,

$$a_1(H_{11} - E) + a_2 H_{12} = 0$$
$$a_1 H_{21} + a_2(H_{22} - E) = 0. \tag{A.47}$$

The Eigen values are found by searching for roots of the determinant of the matrix,

$$\begin{vmatrix} H_{11} - E & H_{12} \\ H_{21} & H_{22} - E \end{vmatrix} = 0 \tag{A.48}$$
$$\rightarrow (H_{11} - E)(H_{22} - E) - H_{12}H_{21} = E^2 - E(H_{11} + H_{22}) + H_{11}H_{22} - H_{12}H_{21} = 0.$$

The solutions are,

$$E_{\pm} = \frac{1}{2}(H_{11} + H_{22}) \pm \sqrt{\left(\frac{H_{11} + H_{22}}{2}\right)^2 - H_{11}H_{22} + H_{12}H_{21}}$$

$$E_{\pm} = \frac{1}{2}(H_{11} + H_{22}) \pm \frac{1}{2}\sqrt{(H_{11} - H_{22})^2 + 4H_{12}H_{21}} \tag{A.49}$$

$$H_{12} = H_{21}^* \rightarrow H_{12}H_{21} = |H_{12}|^2$$

$$E_\pm = \frac{1}{2}(H_{11} + H_{22}) \pm \frac{1}{2}\sqrt{(H_{11} - H_{22})^2 + 4|H_{12}|^2}.$$

With this, one has expressions for the perturbed Eigen energies, E_+ and E_-.

Next, expressions for the corresponding perturbed Eigen states, $|+\rangle = a_1|1\rangle + a_2|2\rangle$ and $|-\rangle = b_1|1\rangle + b_2|2\rangle$ need to be found. Expressing the coefficients in the form of sine- and cosine-like functions, following [168],

$$|-\rangle = \cos\zeta\,|1\rangle + \sin\zeta|2\rangle$$
$$|+\rangle = -\sin\zeta\,|1\rangle + \cos\zeta|2\rangle. \tag{A.50}$$

It ensures that they are orthonormal as, $\langle-|+\rangle = -\sin\zeta\cos\zeta + \cos\zeta\sin\zeta = 0$ and $\langle+|+\rangle = \cos^2(\zeta)\langle 1|1\rangle + \sin^2(\zeta)\langle 2|2\rangle = 1 = \langle-|-\rangle$. The perturbed Eigenstates are then found by setting up the matrices $\boldsymbol{U}$ and $\boldsymbol{U}^{-1}$ and constructing the matrix equation,

$$\begin{pmatrix} E_- & 0 \\ 0 & E_+ \end{pmatrix} = \boldsymbol{U}^{-1}\boldsymbol{H}\boldsymbol{U} = \begin{pmatrix} \cos\zeta & \sin\zeta \\ -\sin\zeta & \cos\zeta \end{pmatrix}\begin{pmatrix} H_{11} & H_{12} \\ H_{21} & H_{22} \end{pmatrix}\begin{pmatrix} \cos\zeta & -\sin\zeta \\ \sin\zeta & \cos\zeta \end{pmatrix} = \begin{pmatrix} a & b \\ c & d \end{pmatrix}$$

$$a = H_{11}\cos^2\zeta + H_{22}\sin^2\zeta + 2H_{12}\cos\zeta\sin\zeta$$
$$b = H_{12}(\cos^2\zeta - \sin^2\zeta) + (H_{22} - H_{11})\cos\zeta\sin\zeta$$
$$c = H_{12}(\cos^2\zeta - \sin^2\zeta) + (H_{22} - H_{11})\cos\zeta\sin\zeta$$
$$d = H_{22}\cos^2\zeta + H_{11}\sin^2\zeta - 2H_{12}\cos\zeta\sin\zeta. \tag{A.51}$$

Solving $b = c = 0$ yields,

$$H_{12}(\cos^2\zeta - \sin^2\zeta) + (H_{22} - H_{11})\cos\zeta\sin\zeta = 0$$
$$\rightarrow \frac{H_{22}}{(H_{22} - H_{11})} = \frac{-\cos\zeta\sin\zeta}{\cos^2\zeta - \sin^2\zeta} = -\frac{1}{2}\tan(2\zeta) \rightarrow -\frac{2H_{22}}{(H_{22} - H_{11})} = \tan(2\zeta) \tag{A.52}$$
$$\rightarrow \zeta = \frac{1}{2}\operatorname{atan}\left(-\frac{2H_{12}}{H_{22} - H_{11}}\right).$$

For a *non-degenerate system*, where the energy difference, $E_2 - E_1$, is large, the term $2H_{12}/(H_{22} - H_{11})$ becomes small such that one approximates, $\tan(2\zeta) \approx 2\zeta \rightarrow \zeta \approx -H_{22}/(H_{22} - H_{11})$. Thus, using $\cos\zeta \approx 1$ and $\sin\zeta \approx \zeta$, yields,

$$|-\rangle \approx |1\rangle - \frac{|H_{12}|}{H_{22} - H_{11}}|2\rangle$$
$$|+\rangle \approx |2\rangle + \frac{|H_{12}|}{H_{22} - H_{11}}|1\rangle. \tag{A.53}$$

And the new states are dominated by old states but mixed with a contribution from the other state that is inversely proportional to the energy difference. Thereby, the energies remain approximately unchanged, $E_- \approx E_1$ and $E_+ \approx E_2$ for Hamiltonian perturbing which fulfills, $\langle 2|H'|2\rangle = \langle 1|H'|1\rangle = 0$. The first non-zero correction to the energy in this case occurs if the second order correction is considered. It is [168]

$$E_- \approx E_1 - \frac{|H_{12}|^2}{E_2 - E_1}$$
$$E_+ \approx E_2 + \frac{|H_{12}|^2}{E_2 - E_1}. \tag{A.54}$$

The second order correction to the wave function can be found e.g. in ref. [168].

For a *degenerate system* where $H_{22} - H_{11} \approx 0$, i.e. $E_1 \approx E_2$ one has $\tan(2\zeta) \rightarrow -\infty$ such that $\zeta = -\pi/4$ and the perturbed Eigen states are a complete mixture of the unperturbed states

$$|-\rangle = \frac{1}{\sqrt{2}}(|1\rangle - |2\rangle) \tag{A.55}$$

$$|+\rangle = \frac{1}{\sqrt{2}}(|1\rangle + |2\rangle).$$

In this case, the corrected energies are

$$E_\pm = \frac{1}{2}(H_{11} + H_{22}) \pm H_{12}. \tag{A.56}$$

As $H_{22} \approx H_{11}$ one might write, $E_\pm = H_{11} \pm H_{12}$.

One might consider the case of a *nearly degenerate system* where the approximation $(H_{11} - H_{22})^2 \approx 0$, is used instead of $H_{22} - H_{11} \approx 0$. Using $H_{11} + H_{22} \approx 2H_{11} \approx 2H_{22}$ but accounting for the difference between H_{11} and H_{22} yields,

$$E_{11-} = H_{11} - H_{12}$$
$$E_{22+} = H_{22} + H_{12}. \tag{A.57}$$

A reasonable approximation for the wave functions in this case is to as it avoids the divergence in (A.54). It represents an equal mix of the states without perturbation. This approximation might be used if one seeks an approximate expression for a compromise between the two limiting cases.

A3.2 Time-Dependent Perturbation Theory

Time-dependent first-order perturbation theory is shortly reviewed here and later specified for a two-level system [168]. One starts at the time-dependent Schrödinger equation (TDSE),

$$i\frac{\partial}{\partial t}\psi(t) = H(t)\psi(t) = i\frac{\partial}{\partial t}|\psi(t)\rangle = H(t)|\psi(t)\rangle, \tag{A.58}$$

with the explicitly time-dependent Hamiltonian, $H(t) = H^0 + H'(t)$. It consist of a time-independent part, H^0, and the time-dependent perturbation, $H'(t)$, of strength λ, i.e. $H'(t) = \lambda H''(t)$. The wave function, $\psi(t)$ can be expressed as superposition of a chosen complete set of orthonormal Eigen states of the unperturbed Hamiltonian H^0,

$$|\psi(t)\rangle = \psi(t) = \sum_n a_n(t)\psi_n(\boldsymbol{r}) = \sum_n a_n(t)|n\rangle, \tag{A.59}$$

where the coefficients, $a_n(t)$, are time-dependent while the wave functions, $\psi_n(\boldsymbol{r})$, respectively the states $|n\rangle$ are time-independent. Thereby, $\sum_n |a_n(t)|^2 = 1$ ensures the normalization of $\psi(t)$. Using, in the TDSE yields,

$$i\sum_n \frac{\partial}{\partial t}[a_n(t)|n\rangle] = i\sum_n \frac{\partial}{\partial t}a_n(t)|n\rangle = [H^0 + H'(t)]\sum_n a_n(t)|n\rangle$$
$$i\frac{\partial}{\partial t}\sum_n a_n(t)|n\rangle = \sum_n H^0 a_n(t)|n\rangle + \sum_n H'(t)a_n(t)|n\rangle \tag{A.60}$$

, and multiplication with $\langle m|$ brings in matrix form,

$$i\langle m|\frac{\partial}{\partial t}\sum_n a_n(t)|n\rangle = \langle m|\sum_n H^0 a_n(t)|n\rangle + \langle m|\sum_n H'(t)a_n(t)|n\rangle$$
$$i\frac{\partial}{\partial t}\sum_n a_n(t)\langle m|n\rangle = \sum_n a_n(t)\langle m|H^0|n\rangle + \sum_n a_n(t)\langle m|H'(t)|n\rangle \tag{A.61}$$
$$i\sum_n S_{mn}\frac{d}{dt}a_n(t) = \sum_n a_n(t)H^0_{mn} + \sum_n a_n(t)H'_{mn}(t)$$

, where the abbreviations, $S_{mn} = \langle m|n \rangle = \int \psi_m^*(r)\psi_n(r)dr$ is called the overlap integral (reff tannor), and $H_{mn}^0 = \langle m|H^0|n \rangle = \int \psi_m^*(r)[H^0\psi_n(r)]dr$ and $H_{mn}'(t) = \langle m|H'(t)|n \rangle = \int \psi_m^*(r)[H'(t)\psi_n(r)]dr$ are matrix elements as the interpretation of (A.61) as matrix equation illustrates,

$$i\frac{d}{dt}\sum_n a_n(t)S_{mn} = \sum_n a_n(t)H_{mn}^0 + \sum_n a_n(t)H_{mn}'(t)$$

$$\rightarrow i\begin{bmatrix} S_{11} & S_{12} & \cdots \\ S_{21} & S_{22} & \cdots \\ \vdots & \vdots & \ddots \end{bmatrix}\begin{bmatrix} \dot{a}_1 \\ \dot{a}_2 \\ \vdots \end{bmatrix} = \begin{bmatrix} H_{11}^0 & H_{12}^0 & \cdots \\ H_{21}^0 & H_{22}^0 & \cdots \\ \vdots & \vdots & \ddots \end{bmatrix}\begin{bmatrix} a_1 \\ a_2 \\ \vdots \end{bmatrix} + \begin{bmatrix} H_{11}'(t) & H_{12}'(t) & \cdots \\ H_{21}'(t) & H_{22}'(t) & \cdots \\ \vdots & \vdots & \ddots \end{bmatrix}\begin{bmatrix} a_1 \\ a_2 \\ \vdots \end{bmatrix} \tag{A.62}$$

$$\rightarrow i\begin{bmatrix} S_{11}\dot{a}_1 + S_{12}\dot{a}_2 + \cdots \\ S_{21}\dot{a}_1 + S_{22}\dot{a}_2 + \cdots \\ \vdots \end{bmatrix} = \begin{bmatrix} H_{11}^0 a_1 + H_{12}^0 a_2 + \cdots \\ H_{21}^0 a_1 + H_{22}^0 a_2 + \cdots \\ \vdots \end{bmatrix} + \begin{bmatrix} H_{11}'(t)a_1 + H_{12}'(t)a_2 + \cdots \\ H_{21}'(t)a_1 + H_{22}'(t)a_2 + \cdots \\ \vdots \end{bmatrix}$$

. Using that $S_{mn} = 0$ and $H_{mn}^0 = 0$ for $m \neq n$ as the chosen complete basis set is orthonormal and in addition, plugging in that the basis is are Eigen functions of H^0 that fulfill, $H_{nn}^0 = E_n$, yields

$$i\frac{d}{dt}\begin{bmatrix} a_1 \\ a_2 \\ \vdots \end{bmatrix} = \begin{bmatrix} E_1 a_1 \\ E_2 a_2 \\ \vdots \end{bmatrix} + \begin{bmatrix} H_{11}'(t)a_1 + H_{12}'(t)a_2 + \cdots \\ H_{21}'(t)a_1 + H_{22}'(t)a_2 + \cdots \\ \vdots \end{bmatrix}$$

$$i\frac{d}{dt}\begin{bmatrix} a_1 \\ a_2 \\ \vdots \end{bmatrix} = \begin{bmatrix} [E_1 + H_{11}'(t)] & H_{12}'(t) & \cdots \\ H_{21}'(t) & [E_2 + H_{22}'(t)] & \cdots \\ \vdots & \vdots & \ddots \end{bmatrix}\begin{bmatrix} a_1 \\ a_2 \\ \vdots \end{bmatrix}. \tag{A.63}$$

This result is further simplified by approximating the system with two levels and considering a perturbation which fulfills, $H_{nn}'(t) = 0$. Using both, one arrives at the matrix equation that is appropriate to describe the interaction of a two-level model, e.g. H_2^+, in a time-dependent external field,

$$i\frac{d}{dt}\begin{bmatrix} a_1 \\ a_2 \end{bmatrix} = \begin{bmatrix} H_{11}^0 & H_{12}' \\ H_{21}' & H_{22}^0 \end{bmatrix}\begin{bmatrix} a_1 \\ a_2 \end{bmatrix}. \tag{A.64}$$

Equation (A.64) represents a system of a linear differential equations for the time-dependent coefficients, a_1 and a_2.

Solving (A.63) and (A.64) respectively is appropriate to describe two-level dynamics such as Rabi cycling of a two-level atom in an external laser field. Thereby, the chosen Eigenstates depend the spatial coordinate, r, of the electron only. The system is then fully characterized by $\psi(t) = a_1(t)\psi_1(r) + a_2(t)\psi_2(r)$ where it is stressed again that $\psi_1(r)$ and $\psi_2(r)$ are time-independent Eigenstates of the perturbation free problem. For molecular dynamics, however, $\psi(t)$, depends on the electronic and the nuclear coordinates, i.e. $\psi(t, r, R)$. It makes the problem a bit more complicated but does not change much on the principle. The TDSE reads,

$$i\frac{\partial}{\partial t}|\psi(t, r, R)\rangle = i\frac{\partial}{\partial t}\sum_n |\varphi_n(R; r)\rangle|\chi_n(R, t)\rangle = H(t)\sum_n |\varphi_n(R; r)\rangle|\chi_n(R, t)\rangle = H(t)|\psi(t, r, R)\rangle, \tag{A.65}$$

where the time dependence is written suggestively into the nuclear part of the wave function, $\chi_n(R, t)$. The electronic Eigenstates, $|\varphi_n(R; r)\rangle = |n\rangle$, are used as the basis for the electronic problem and are time-independent similar to simpler case before. Multiplication from the left with another electronic Eigenstate, $\langle \varphi_m^*(R; r)| = \langle m|$, yields,

$$i\langle m|\frac{\partial}{\partial t}\sum_n |\varphi_n(R; r)\rangle|\chi_n(R, t)\rangle = \langle m|H(t)\sum_n |n\rangle|\chi_n(R, t)\rangle$$

$$i\sum_n \langle m|n\rangle\frac{d}{dt}|\chi_n(R, t)\rangle = \langle m|H(t)\sum_n |n\rangle|\chi_n(R, t)\rangle \tag{A.66}$$

$$i\sum_n S_{mn}\frac{d}{dt}|\chi_m(R, t)\rangle = \sum_n H_{mn}(t)|\chi_n(R, t)\rangle = \sum_n [H_{mn}^0 + H_{mn}'(t)]|\chi_n(R, t)\rangle.$$

Next one uses that the electronic basis set is orthogonal, i.e. $\langle m|n\rangle = 0 = H^0_{mn}$ for $m \neq n$, and plugs in that $H^0_{nn}(R) = E_{en}(R)$ yields the electronic Eigen energy curve, $E_{en}(R)$. Further, the perturbation is assumed to fulfill, $H'_{mn}(t) = 0$ for $m = n$. One arrives at the TDSE for the nuclei where several BO-potential curves, U_n, are coupled by the time-dependent perturbation, $H'_{12}(R,t)$

$$
i\frac{d}{dt}\begin{bmatrix}\chi_1(R,t)\\\chi_2(R,t)\\\vdots\end{bmatrix} = \begin{bmatrix}H^0_{11}(R) & H'_{12}(R,t) & \cdots\\H'_{21}(R,t) & H^0_{22}(R) & \cdots\\\vdots & \vdots & \ddots\end{bmatrix}\begin{bmatrix}\chi_1(R,t)\\\chi_2(R,t)\\\vdots\end{bmatrix}
$$

$$
i\frac{d}{dt}\begin{bmatrix}\chi_1(R,t)\\\chi_2(R,t)\\\vdots\end{bmatrix} = \begin{bmatrix}T_N + E_{e2}(R) + V_N(R) & H'_{12}(R,t) & \cdots\\H'_{21}(R,t) & T_N + E_{e2}(R) + V_N(R) & \cdots\\\vdots & \vdots & \ddots\end{bmatrix}\begin{bmatrix}\chi_1(R,t)\\\chi_2(R,t)\\\vdots\end{bmatrix} \tag{A.67}
$$

$$
i\frac{d}{dt}\begin{bmatrix}\chi_1(R,t)\\\chi_2(R,t)\\\vdots\end{bmatrix} = \begin{bmatrix}T_N + U_1(R) & H'_{12}(R,t) & \cdots\\H'_{21}(R,t) & T_N + U_2(R) & \cdots\\\vdots & \vdots & \ddots\end{bmatrix}\begin{bmatrix}\chi_1(R,t)\\\chi_2(R,t)\\\vdots\end{bmatrix}.
$$

The operator, T_N, stands for the kinetic energy of the nuclei, $T_N = \nabla_R^2/2\mu$, with μ being the effective mass of the nuclei. For a two-level system, this simplifies to

$$
i\frac{d}{dt}\begin{bmatrix}\chi_1(R,t)\\\chi_2(R,t)\end{bmatrix} = \begin{bmatrix}T_N + U_1(R) & H'_{12}(R,t)\\H'_{12}(R,t) & T_N + U_2(R)\end{bmatrix}\begin{bmatrix}\chi_1(R,t)\\\chi_2(R,t)\end{bmatrix}. \tag{A.68}
$$

(A.68) is formally integrated in order to illustrate the effect of coupling the nuclear wave functions on two BO potentials, i.e.

$$
\chi_1(R,t_1) = -i\int_{t_0}^{t_1}[T_N + U_1(R)]\chi_1(R,t')dt' - i\int_{t_0}^{t_1}H'_{12}(R,t')\chi_2(R,t')dt'
$$
$$
\chi_2(R,t_1) = -i\int_{t_0}^{t_1}H'_{12}(R,t')\chi_1(R,t')dt' - i\int_{t_0}^{t_1}[T_N + U_2(R)]\chi_2(R,t')dt'. \tag{A. 69}
$$

Specifying the coupling as dipole interaction, $H'_{12}(R,t) = H'_{21}(R,t) = E(t)d_{12}(R)$, with the field, $E(t)$ and the transition dipole matrix element, $d_{12}(R)$, yields

$$
\chi_1(R,t_1) = -i\int_{t_0}^{t_1}[T_N + U_1(R)]\chi_1(R,t')dt' - i\int_{t_0}^{t_1}E(t')d_{12}(R)\chi_2(R,t')dt'
$$
$$
\chi_2(R,t_1) = -i\int_{t_0}^{t_1}[T_N + U_2(R)]\chi_2(R,t')dt' - i\int_{t_0}^{t_1}E(t')d_{12}(R)\chi_1(R,t')dt'. \tag{A.70}
$$

The nuclear wave function on each of the BO curves consist of a summand which is representative for the field free evolution of the nuclear wave function on the respective BO potential, i.e. the first summand in (A.70). In addition, there is a second summand which can be understood as a copy of the nuclear wave function on the other BO curve. The strength of the generated copy is proportional to the strength of the electric field, $E(t)$, and the transition dipole matrix element, $d_{12}(R)$. Further it scales with the complex amplitude of the wave function on the other surface. Due the complexity of $\chi_1(R,t')$ and $\chi_2(R,t')$, the contribution from the copy can interfere with the part of the wave function which is already on the respective BO potential. Thus, the coupling can lead to an enhancement (constructive interference) or suppression (destructive interference) of the probabilities on each of the curves, $|\chi_1(R,t')|^2$ or $|\chi_2(R,t')|^2$.

A4 Split-Step Method for Numerical Solution of the Time-Dependent Schrödinger Equation

Here we shortly review the split-step for numerical solution of the time-dependent Schrödinger equation (TDSE). It is introduced following the description in [166] in A4.1. Afterwards, it is demonstrated how it is applied to the coupling of several BO-potentials in A4.2.

A4.1 The Split-Step Method for Numerically Solving the TDSE

The split-step method [149] [166] is used for numerical solution of the time-dependent Schrödinger equation on a grid. For the time-evolution of the wave function, $\psi(x,t)$, on a single time- and space dependent potential, $V(x,t)$, reads

$$i\frac{\partial}{\partial t}\psi(x,t) = H(x,t)\psi(x,t) = \left[\frac{1}{2m}\nabla^2 + V(x,t)\right]\psi(x,t)$$

$$i\frac{\partial}{\partial t}\psi(x,t) = \left[\frac{p^2}{2m} + V(x,t)\right]\psi(x,t) = [T + V(x,t)]\psi(x,t).$$

(A.71)

It has the formal solution,

$$\psi(x,t) = e^{-iH(x,t)t}\psi(x,t=0).$$

(A.72)

$\psi(x,t)$ as well as the potential $V(x,t)$ are represented on a spatial grid with N points between the starting point, x_b, and the endpoint, x_e. Thus, the x-step width is, $\Delta x = (x_e - x_b)/N$, which leads to the discretization in momentum space, $\Delta p = 2\pi/\Delta x N$, and a momentum range between $-p_m = -\pi/\Delta x$ and $p_m = +\pi/\Delta x$.

Using the symmetrized split step algorithm, the wave function at the time, $t + \Delta t$, is approximated by numerical calculation,

$$\psi(x, t + \Delta t) \approx e^{-iV(x,t)\Delta t/2}iFFT\left[e^{-iT\Delta t}FFT\left[e^{-iV(x,t)\Delta t/2}\psi(x,t)\right]\right]$$

(A.73)

, starting from the innermost brackets. Thereby, FFT stands for the fast-fourier-transform operation, which is a numerical method to calculate the discrete Fourier transformation. It's inverse operation is denoted by $iFFT$. The Fourier transformation connects the wave function in real space representation, $\psi(x,t)$, with its momentum space $\psi(p,t)$, i.e. $\psi(p,t) = [\int \psi(x,t)\exp(-ipx)dx]/\sqrt{2\pi}$. Repeating the full operation until, $t_k = k\Delta t$, yields the wave function on the x-grid and p-grid at every time, t_k between the starting time, t_0 and an end time, t_{end}. In Fourier space, the momentum propagator is $T = p^2/2m$ with m being the mass of the particle.

At every time-step, observables of interest such as the probability distribution $|\psi(x,t)|^2$ or expectation values of, e.g. the position operator $x_{exp}(t) = \int \psi^*(x,t)x\psi(x,t)dx$ or the momentum operator, $p_{exp}(t) = \int \psi^*(p,t)p\psi(p,t)dp$, can be calculated and saved for later analysis and interpretation of the numerical results. Similarly, it is possible to calculate projections, $c(t)$, onto e.g. an Eigenstate of interest using $c_n(t) = \int \psi_n^*(x)\psi(x,t)dx$. In the example, $\psi_n(x)$, denotes e.g. an Eigenstate of e.g. the time-independent Hamiltonian. This enables to evaluate time-dependent population, $P_n(t) = |c_n(t)|^2$, of the nth Eigenstate of the system. An important observable that is used to check the reasonability of the calculation is the norm wave function $n(t)$. The norm of

the wave function on the grid is $n_{grid}(t) = \int \psi^*(x,t)\psi(x,t)dx$. It should be $n(t) = 1$ over the whole calculation unless there are understandable and justified reasons why it is not.

An imaginary boundary is applied in the region around the boundaries of the x-grid. This avoids that parts of the wave function that are reflected from the boundaries of the grid perturb the calculation. The boundary, $V_{im}(x)$, has $\cos^2$ -shape and reads, $V_{im}(x) \sim -10i\cos^2([\pi/2x_w][x - x_{b/e} + x_w])$ for $x < x_b + x_w$; $x > x_e - x_w$ and 1 otherwise. Thereby, x_w is an adjustable width, which is chosen appropriately. The imaginary boundary is used in the following way. After propagating $\psi(x,t)$ using (A.73), one calculates, $\psi'(x, t + \Delta t) = \exp[-1i\Delta t V_{im}(x)] \psi(x, t + \Delta t)$, at every time step Δt. The next propagation step is done using $\psi'(x, t + \Delta t)$. It is clear that this procedure, causes a loss of probability at every time step. This lost probability has the norm, $n_{im}(\Delta t) = |\psi(x, t + \Delta t)|^2 - |\psi'(x, t + \Delta t)|^2$. The time-dependent evolution of the absorbed norm is then $n_{im}(t) = \sum n_{im}(\Delta t)$. With absorbing boundaries, not $n(t) = 1$ needs to be constant but, $n'(t) = n(t) + n_{im}(t) = 1$. A similar approach for checking the norm can be used if other loss channels such as ionization are included. However, it is important to have a comprehensive understanding of these loss channels.

In order to check the convergence and stability of the numerical solution, it is common to repeat the calculation several times using different sizes, $x_e - x_b$ and number of points, N, on the grid and different sizes of the time step Δt. If reducing the number of grid points does not change the result of the calculation anymore, the numerical result can be accepted as having converged.

A4.2 The Split-Step Method for Coupled Potentials

Having shortly reviewed the split-step method for time-evolution of the wave function, $\psi(x,t)$ on a single time- and space dependent potential, $V(x,t)$, the method is extended to the case where several such potentials, $V_l(x,t)$, are coupled. Such a scheme is needed if e.g. several electronic levels of a molecule are coupled by an external laser field as it is e.g. the case for a two-level model of H_2^+ in chapter 5.3. The consideration is done specifically for a two-level model here. However, it is straightforward to extend it to more levels.

In order to illustrate the idea of the scheme, the TDSE of a two-level system in matrix, i.e., (A.64) is considered first [153] [166],

$$i\frac{d}{dt}\begin{bmatrix}a_1\\a_2\end{bmatrix} = \begin{bmatrix}H_{11} & H_{12}\\H_{21} & H_{22}\end{bmatrix}\begin{bmatrix}a_1\\a_2\end{bmatrix} \to i\frac{d}{dt}\begin{bmatrix}a_1\\a_2\end{bmatrix} = \begin{bmatrix}H_{11}^0 & H_{12}'\\H_{21}' & H_{22}^0\end{bmatrix}\begin{bmatrix}a_1\\a_2\end{bmatrix} \to i\frac{d}{dt}\boldsymbol{A}(t) = \boldsymbol{H}(t)\boldsymbol{A}(t)$$

$$\to \boldsymbol{A}(t) = \exp\left(-i\int_{t_0}^t \boldsymbol{H}(t')dt'\right)\boldsymbol{A}(t_0). \tag{A.74}$$

For a numerical solution of this problem one writes,

$$\to \boldsymbol{A}(t + \Delta t) = \exp(-i\boldsymbol{H}(t)\Delta t)\boldsymbol{A}(t_0) = \exp\left(-i\begin{bmatrix}T + V_{11} & V_{12}\\V_{21} & T + V_{22}\end{bmatrix}\Delta t\right)\boldsymbol{A}(t_0). \tag{A.75}$$

Where the expression, $\exp(-i\boldsymbol{H}(t)\Delta t)$, represents the matrix exponential which is the first term in a so-called Magnus expansion. Although it is not necessary, one has renamed, $H_{11}^0 = T + V_{11}$, being the time-independent Hamiltonian and $V_{21}(t) = V_{21}$ as well as $V_{12}(t) = V_{12}$ being the time-dependent perturbation that couples the states 1 and 2 within first order time-dependent perturbation theory. The introduced error due to using only the first

order in the Magnus expansion is sufficiently small if Δt is sufficiently small, see [166]. Next one splits, the matrix exponential similarly to (A.73).

$$\rightarrow \; \boldsymbol{A}(t + \Delta t)$$
$$= \exp\left(-i \begin{bmatrix} V_{11} & V_{12} \\ V_{21} & V_{22} \end{bmatrix} \frac{\Delta t}{2}\right) iFFT\left[\exp\left(-i \begin{bmatrix} T & 0 \\ 0 & T \end{bmatrix} \Delta t\right)\right] FFT\left[\exp\left(-i \begin{bmatrix} V_{11} & V_{12} \\ V_{21} & V_{22} \end{bmatrix} \frac{\Delta t}{2}\right) \boldsymbol{A}(t_0)\right]. \tag{A.76}$$

The used algorithm would be the same as in (A.73), however, the part of the propagation step which is done in real space, i.e. $\exp(-iV(x,t)\Delta t/2)\psi(x,t)$, has become a matrix exponential now, i.e. $\exp(-i\boldsymbol{W}\Delta t/2)$, with $\boldsymbol{W}$ being not necessarily a diagonal matrix. For the relevant cases there is a transformation, $\boldsymbol{U}$, which transforms $\boldsymbol{W}$ to a diagonal matrix, $\boldsymbol{D} = \boldsymbol{U}^{-1}\boldsymbol{W}\boldsymbol{U}$, of which the matrix exponential can be calculated by,

$$\rightarrow \; \exp(-i\boldsymbol{D}\Delta t/2) = \begin{pmatrix} \exp(-id_1\Delta t/2) & 0 \\ 0 & \exp(-id_2\Delta t/2) \end{pmatrix}, \tag{A.77}$$

, with d_1 and d_2 being the entries of $\boldsymbol{D}$. Thus, the operation (A.76) can be done in the following way,

$$\rightarrow \; \boldsymbol{A}(t + \Delta t) = \boldsymbol{U}\exp\left(-i\boldsymbol{D}\frac{\Delta t}{2}\right)\boldsymbol{U}^{-1}iFFT\left[\exp(-i\boldsymbol{T}\Delta t)FFT\left[\boldsymbol{U}\exp\left(-i\boldsymbol{D}\frac{\Delta t}{2}\right)\boldsymbol{U}^{-1}\boldsymbol{A}(t_0)\right]\right]. \tag{A.78}$$

This result is not limited to two levels and can be used for any diagonalizable matrix, $\boldsymbol{W}$. However, it means that one need to calculate the transformation $\boldsymbol{U}$ at every time step. As demonstrated in A3 and in [153] [166], the transformation and the diagonal matrix can be calculated analytically exact for a two-level system which makes the calculation particularly robust and fast for the case of a two-level system.

Similarly to the extension of the simple two-level problem to the coupling of several BO-potentials in (A. 63), the scheme can be extended to include the dependence on the nuclear coordinate by making the transformation, $\boldsymbol{U} = \boldsymbol{U}(R)$, as well as the diagonal matrix $\boldsymbol{D} = \boldsymbol{D}(R)$ R-dependent, i.e.

$$\begin{bmatrix} \chi_1(R, t + \Delta t) \\ \chi_2(R, t + \Delta t) \end{bmatrix} =$$
$$\exp\left(-i\boldsymbol{D}(R)\frac{\Delta t}{2}\right)\boldsymbol{U}^{-1}(R) \times iFFT\left[\exp(-i\boldsymbol{T}\Delta t)FFT\left[\boldsymbol{U}(R)\exp\left(-i\boldsymbol{D}(R)\Delta t\frac{\Delta t}{2}\right)\boldsymbol{U}^{-1}(R)\begin{bmatrix} \chi_1(R, t) \\ \chi_2(R, t) \end{bmatrix}\right]\right], \tag{A.79}$$

written explicitly for two-levels here. As written here, the scheme is appropriate to solve the TDSE on several electronic levels. Extending it to more than two BO-potentials is straight forward, however, $\boldsymbol{D}$ and $\boldsymbol{U}$ are not analytically exact available anymore and must be found by numerical means.

Mentioned strategies to check the convergence and reasonability of the numerical results remain the same as for the propagation on a single electronic state. One varies the temporal and spatial grid until the result of the calculation does not change anymore. Thereby, the calculation is continued for a time-interval after the laser pulse is over until all observables have converged.

Ehrenwörtliche Erklärung

Ich erkläre hiermit ehrenwörtlich, dass ich die vorliegende Arbeit selbstständig, ohne unzulässige Hilfe Dritter und ohne Benutzung anderer als der angegebenen Hilfsmittel und Literatur angefertigt habe. Die aus anderen Quellen direkt oder indirekt übernommenen Daten und Konzepte sind unter Angabe der Quelle gekennzeichnet.

Bei der Auswahl und Auswertung folgenden Materials haben mir nachstehend aufgeführte Personen in der jeweils beschriebenen Weise entgeltlich/unentgeltlich geholfen.

1. Dr. A. Max Sayler Englischkorrekturen

Weitere Personen waren an der inhaltlich-materiellen Erstellung der vorliegenden Arbeit nicht beteiligt. Insbesondere habe ich hierfür nicht die entgeltliche Hilfe von Vermittlungs- bzw. Beratungsdiensten (Promotionsberater oder andere Personen) in Anspruch genommen. Niemand hat von mir unmittelbar oder mittelbar geldwerte Leistungen für Arbeiten erhalten, die im Zusammenhang mit dem Inhalt der vorgelegten Dissertation stehen.

Die Arbeit wurde bisher weder im In- noch im Ausland in gleicher oder ähnlicher Form einer Prüfungsbehörde vorgelegt.

Die geltende Promotionsordnung der Physikalisch-Astronomischen Fakultät ist mir bekannt.

Ich versichere ehrenwörtlich, dass ich nach bestem Wissen die reine Wahrheit gesagt und nichts verschwiegen habe.

Ort, Datum   Unterschrift